Characterization of Superelastic Nitinol Wire for Application to Aortic Stent Graft Design

Robbie Brodie

2018

A thesis submitted in fulfilment of the requirements for the Degree of Doctor of Philosophy

Declaration

This thesis is the result of the author's original research. It has been composed by the author and has not been previously submitted for examination which has led to the award of a degree.

The copyright of this thesis belongs to the author under the terms of the United Kingdom Copyright Acts as qualified by University of Strathclyde Regulation 3.50. Due acknowledgement must always be made of the use of any material contained in, or derived from, this thesis.

Signed:

Date:

Acknowledgements

Abstract

Aortic stent graft devices are required to treat patients with life-threatening vascular disease. These devices depend on superelastic Nitinol material for their ability to be delivered through a minimally invasive endovascular approach and then to self-expand for long-term implantation at the target site. In this safety-critical application, Nitinol stent components are subjected to challenging in-service conditions in terms of thermo-mechanical loading. Characterization of the material's response to these loading conditions is therefore essential for its safe and effective implementation in the design of medical devices.

This thesis reports material characterization work performed on superelastic Nitinol stent wire under conditions relevant to its in-service application. The product life cycle of Nitinol stent graft components is investigated, highlighting the importance of the material's bending behaviour and the associated tensile and compressive mechanical responses.

With tensile behaviour and test methods already well established for Nitinol, the work first focuses on developing a method for compressive testing of representative Nitinol wire material, building on a previous method to enable testing to higher strains. This allows characterization of the material in compression for thermo-mechanical loading representative of large compaction deformations, in-vivo cycling and different temperatures seen during production, sterilization and implantation. The results also allow a clear understanding of the material's tension-compression stress-strain asymmetry, which is essential to understanding its bending behaviour. This investigation concludes with a feasibility study into a novel compression test method developed by the author, using short wire samples with high-resolution 'microtester' equipment to obtain improved results.

The work then focuses on development of a test method for bend testing of thin Nitinol wires to investigate the load response to in-service deformations at relevant test

temperatures. This allows characterization of the wire's load-history dependent bending response, whereby the force exerted at a given deflection during unloading depends on the maximum deflection during loading, with interesting application possibilities for stent components. The testing also allows the material's temperature dependence, cyclic behaviour and large deformation response in bending to be studied.

Following this, full-field strain measurement of thin Nitinol wires in bending is presented, achieved through application of 3-D microscopic Digital Image Correlation (DIC) technology. The development of a novel test method, together with extensive data analysis, provides results for characterization of the material's complex bending behaviour, allowing new insight to its tension–compression asymmetry, localised deformation, load-unload strain hysteresis and load-history dependence of strain state in bending. This testing provides useful quantitative characterisation data including neutral axis eccentricity at high bend deformations.

Finally, Abaqus FEA software is used to investigate the effectiveness of its in-built superelastic constitutive model for representing the Nitinol stent wire's bending behaviour, and ultimately its suitability for use in stent design and analysis. The uniaxial stress-strain test results are used for input to the model, and then bending simulation results are compared against the experimental results, both in terms of force and strain outputs. Key findings include the model's inability to represent the strain localisation seen in bending experiments, leading to under-representation of the maximum strains for 'intermediate' bend deflections, and also the model's under-representation of unloading forces at these deflections (unless input parameters are adapted to compensate). Despite these limitations of the model, the cyclic stiffness and strain changes in bending are shown to be reasonably well represented, validating it for its primary use in fatigue analysis of stent components.

Contents

List of Figures

List of Tables

Nomenclature

3PB	3 Point-Bend
ΔD	Delta Deflection, referring to small bend deflection changes
$\Delta\varepsilon$	Delta Strain, referring to small (normal) strain changes
$\Delta\sigma$	Delta Stress, referring to small (normal) stress changes
AAA	Abdominal Aortic Aneurysm
Af	Austenite finish temperature of Nitinol
Anaconda	Vascutek's stent graft product for treatment of AAA
at%	Atomic percentage of Nickel or Titanium in Nitinol
CAD	Computer Aided Design
CoC	Certificate of Conformance
COF	Chronic Outward Force
DMEM	Design, Manufacture & Engineering Management (University of Strathclyde)
DIC	Digital Image Correlation
Exx	Normal (axial) strain following rigid body motion removal (in DIC)
FDM	Fused Deposition Modelling (3D printing method)
FE	Finite Element
FEA	Finite Element Analysis

FOV	Field of View
ID	Inner Diameter
k	Gradient of Exx (from DIC results) across planar section of bending wire from intrados to extrados.
L-D	Load-Deflection
NiTi	Nitinol
NiTi#1	Binary Nitinol material supplied by Fort Wayne Metals
OD	Outer Diameter
R	Radius of curvature of bend, inversely proportional to k
RRF	Radial Resistive Force
SEM	Scanning Electron Microscopy
Vx, Vy, Vz	x (axial), y (transverse) or z components of displacement vector V (in DIC)
wt%	Weight percentage of Nickel or Titanium in Nitinol

Chapter 1: Introduction

1.1 Context

The nickel titanium alloy Nitinol has found widespread application as a medical implant material in the field of endovascular stents. Stent products are designed for delivery within a low-profile catheter to a diseased site within a patient's vascular system, where they can be deployed and expanded to perform a life-saving function. Typically these devices are used to treat arterial aneurysms and occlusions.

Nitinol has the ability to undergo large recoverable strains, and it is this 'superelastic' behavior, together with its excellent biocompatibility, that sets it apart as the material of choice for self-expanding stent products. While a large number of self-expanding Nitinol stent designs are available on the market, they all rely on the same underlying mechanism: superelastic Nitinol in bending.

One such design is the Anaconda stent graft, manufactured by Vascutek Ltd. This product is designed to treat Abdominal Aortic Aneurysms (AAAs), and utilizes a patented ring stent design. This stent, made by winding a thin Nitinol wire into a ring bundle, uses the large deformation bending of Nitinol to allow compaction into a small delivery catheter and then expansion at an implant site where it applies a radial force to seal and anchor against the artery inner wall. Further details of the device's design and function are given in the 'Background' section of Chapter 2.

In order to analyze and optimize the performance of endovascular products, stent graft designers need to understand the bending behavior of their specific Nitinol material as it relates to their particular application. For this reason, Vascutek established a collaborative project with the University of Strathclyde in order to characterize the bending behavior of the Nitinol wire used for their stent graft products.

In simple terms, when a structure is deformed in bending, the material towards its inner bend surface (intrados) is compressed while the material towards its outer bend surface (extrados) is tensioned. (There may also be shear stresses in the material, depending on how the structure is constrained and loaded). Therefore, in order to characterize the bending behavior of Nitinol wire, it is important to characterize the contributing tensile and compressive properties. As will be discussed in Chapter 2, the open literature indicates that the mechanical behaviour of Nitinol in compression is very different from that in tension, leading to complexities in stresses and strains during bending. It is therefore imperative that both the tensile and compressive properties are studied in order to understand the bending behavior of superelastic Nitinol components.

Tensile testing of superelastic Nitinol is commonly performed, and there is a great deal of published literature available regarding the mechanical response of Nitinol wires to tensile loading. Indeed, a standard test method for tension testing of superelastic Nitinol materials is available (ASTM F2516). In Vascutek's case, they have an internal procedure for tensile testing of their stent wire, and hold a considerable database of tensile stress-strain results (both from in-house testing and from supplier certification).

However, compressive testing of medical-grade superelastic material to large strains is a greater challenge, and no standard method exists. Far less literature is available on this topic, and there is little published information that can be directly applied by device designers in their application of the material. In Vascutek's case, they currently hold no compressive stress-strain data for their specification of Nitinol material, and all mechanical property specifications are currently based on tensile properties, despite the knowledge that the material's compressive properties will be considerably different.

Clearly, then, there is a need for characterization of compressive and bending behavior of superelastic Nitinol wire that is relevant to its application in stent graft components.

Another important factor in designing stent components is the growing use of Finite Element Analysis (FEA) tools as part of the design process. It is now expected that

regulatory submissions for new endovascular products will include FEA studies on critical components to support the durability safety case. Within commonly used FEA software packages such as Abaqus, constitutive models for Nitinol material are available that require input of numerous parameters for the thermo-mechanical properties. The accuracy of these inputs as well as the availability of experimental test results for model validation are vital to ensure reliable FEA simulations can be performed.

In order to support the growing FEA requirements of the stent device industry, it is necessary to obtain accurate and robust experimental data that can be used for input to and validation of the Nitinol material models used for simulations of their stent graft components.

1.2 Objectives

The main objective of this work is to perform experimental testing on superelastic Nitinol material representative of the stent wire used for self-expanding stent graft devices, in order to characterize its behavior in compression and bending under conditions that are relevant to its in-service application. This will allow improved understanding of the structural behavior of stent graft products, enabling future analysis and optimization of designs.

With Finite Element Analysis becoming more and more instrumental for the understanding and optimization of stent components, another objective of the present work is to provide experimental material test data for input to and validation of FEA models. In the knowledge that FE-based constitutive models can never perfectly capture a material's behaviour, an important part of the validation activity will be to evaluate the capabilities and limitations of existing models in relation to the design of stent components.

1.3 Thesis Layout

In Chapter 2, a Background section explains the application and design of stent graft products and the required material specification for the Nitinol components, using Vascutek's Anaconda device as a case study. This includes a summary of the product's in-service life cycle, describing the conditions that the Nitinol components will be subjected to. This helps to focus the subsequent investigations on areas that are relevant to device application.

The Literature Review then explores important experimental considerations when working with Nitinol, and looks at how previous investigators have approached compressive and bend testing of the material. The results from these tests are considered for any useful qualitative information they can provide about the material behavior. The review also includes a brief look at constitutive modelling of Nitinol for FEA, focusing on a material model that is widely used in industry for design of stent devices.

The literature review also highlights novel areas of investigation for the present work, including the use of Digital Image Correlation to measure superelastic strains during bending of thin Nitinol wires.

In chapter 3, uniaxial compressive testing of representative Nitinol wire is reported. This testing uses specially sourced material samples with test equipment at University of Strathclyde. The test regime is designed to obtain material data relevant to compaction, thermal processing, deployment and in-vivo loading of stent graft components. The compressive results are compared against existing tensile test results from Vascutek's database, in order to gain a good understanding of the tensile – compressive asymmetry of the material. The understanding of both tensile and compressive properties are applied later to the analysis of bending behavior.

Chapter 4 then reports on 3-Point Bend Load-Deflection tests performed on thin wire material, using University of Strathclyde's Bose 3200 machine for its low load cell capability. 3-Point bending was chosen as the approach most representative for

Vascutek's stent components in service, and again the test regime was designed to be relevant to device application. In particular, the unloading forces in bending are relevant to understanding the forces exerted by the material in a stent when deployed in the body.

In chapter 5, 3-Point Bend testing is again performed but this time using 3D Digital Image Correlation (DIC) to measure the surface strains during bending. Here, the development of a suitable test method is described for this novel application of DIC, and then the testing outputs are processed to obtain useful strain vs deflection results. These results are then analyzed using knowledge gained from the previous chapters to understand the stress-strain behavior of the material within the wire during superelastic bending. This analysis is used to explain load history effects in bending that had been highlighted by previous investigators at University of Strathclyde during FEA studies of Nitinol beams.

DIC is also used to measure strains on 'Free-Bend' samples, in order to measure the full cross-sectional strain distribution for a given bend radius, including the neutral axis position.

In chapter 6 the tensile, compressive and bending behavior data from the experimental testing are used for input to and validation of FE-based models. Here, Abaqus is used with its built-in Nitinol constitutive model. Following comparison of experimental results with simulation results, limitations of the FEA constitutive material model are discussed together with applicability to the design of Nitinol components for stent graft products.

The FEA model of the Nitinol wire in bending is then used to perform additional studies of superelastic bending behavior to supplement the knowledge gained during experimental testing.

Chapter 7 provides the main conclusions of the study and proposes recommendations for future studies with specific focus on the needs of stent graft devices.

Chapter 2: Background and Literature Review

The practical application of the present work is to provide nitinol wire material characterization information for the design of stent graft components. This chapter aims to lay the foundations for this work, by giving background information on the following:

- The application and design of stent graft devices, using the Vascutek Anaconda device as a case study
- The nitinol material specification used for components of these devices
- The 'Product Life Cycle' of the nitinol components

Based on this background, the literature review then focuses on relevant work reported by previous investigators, in order to guide experimental testing and simulation work that will improve the understanding of Nitinol-based stent graft products and allow optimization of future designs.

2.1 Background

2.1.1 Stent Graft Design and Application: the Vascutek 'Anaconda' Device

In order to give the background to the present work in terms of stent graft design and application, a case study of one representative device will be used: Vascutek's Anaconda stent graft.

The Anaconda device is designed to treat Abdominal Aortic Aneurysm (AAA). An aneurysm is a local 'ballooning' of the vessel under blood pressure, caused by thinning and weakening of the vessel walls due to disease. If left untreated, there is a danger that the aneurysm will rupture which can lead to death within minutes.

The Anaconda stent graft is a modular conduit used to treat aneurysmal aorta by forming a seal in healthy artery above and below the aneurysm region, providing an alternative conduit for blood via the polyester graft material. The aneurysmal vessel walls outside the graft conduit are thereby excluded from blood pressure, and so the danger of rupture is averted. Over time, the unpressurized aneurysm will typically shrink in size.

Figure 2-1 below shows the blood flow through a patient's abdominal aorta before and after treatment with the Anaconda device, from CT scan images. The 'Pre-implant' image shows clearly the aneurysmal ballooning of the vessel under blood pressure. The 'Post-Implant' image shows the metal stent components of the device, which are sewn to the graft fabric, extending between the abdominal aorta and the left and right common iliac vessels below, with blood now flowing through the device. Note that contrast agent is injected into the blood to allow visualization using CT. Therefore, regions of the aorta where there is no blood flow do not show up in the reconstruction images – such as the aneurismal sac region in the 'post-implant' image.

Pre-Implant

Post-Implant
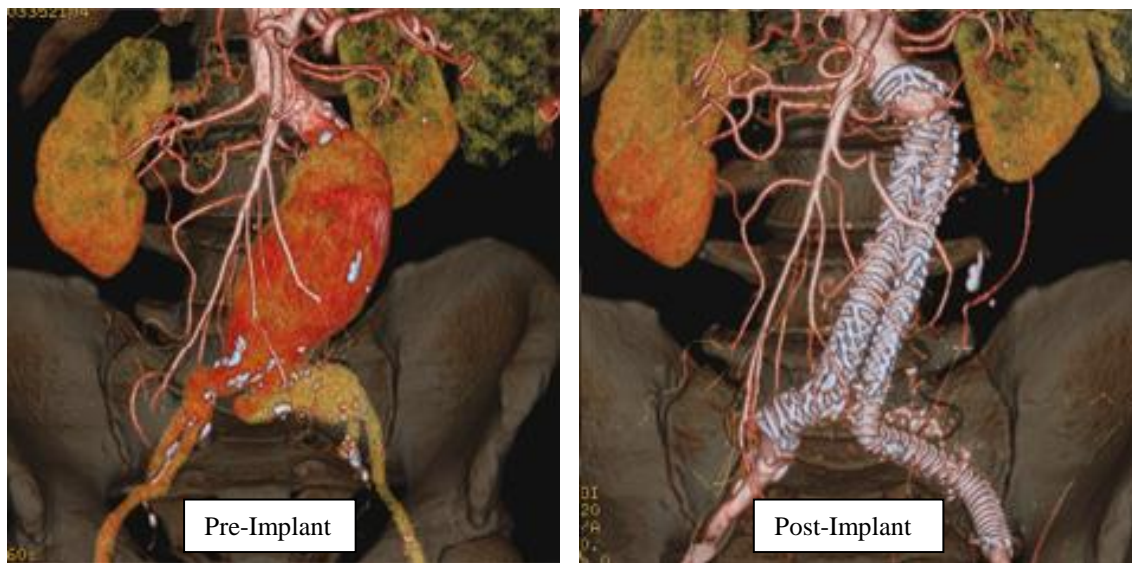
Figure 2-1: 3D reconstruction images of patient's abdominal aorta before and after implanting an Anaconda stent graft device. Courtesy of Dr P Bungay, Derby, UK.

Figure 2-2 shows an Anaconda device deployed in a glass model of an aneurysmal aorta. With reference to figure 2-2, the Anaconda device is a modular system consisting of a proximal body device and two distal leg devices. The body device has proximal ring stents that radially seal against the inner wall of the vessel lumen, and also has hook components that penetrate the vessel wall to provide anchoring against device migration.

Distally, the body device has a bifurcation with two limbs. The two modular leg devices are docked within the distal limbs of the bifurcate body device (again by stent ring radial force) and then seal distally in the left and right common iliac vessels. The graft fabric of the body and leg devices therefore extends from the aorta above the aneurysm region to the iliacs below the aneurysm and is held in place by the stents and hooks. This woven polyester fabric is impervious to blood as the blood flows through the device, and therefore the aneurysm is excluded.
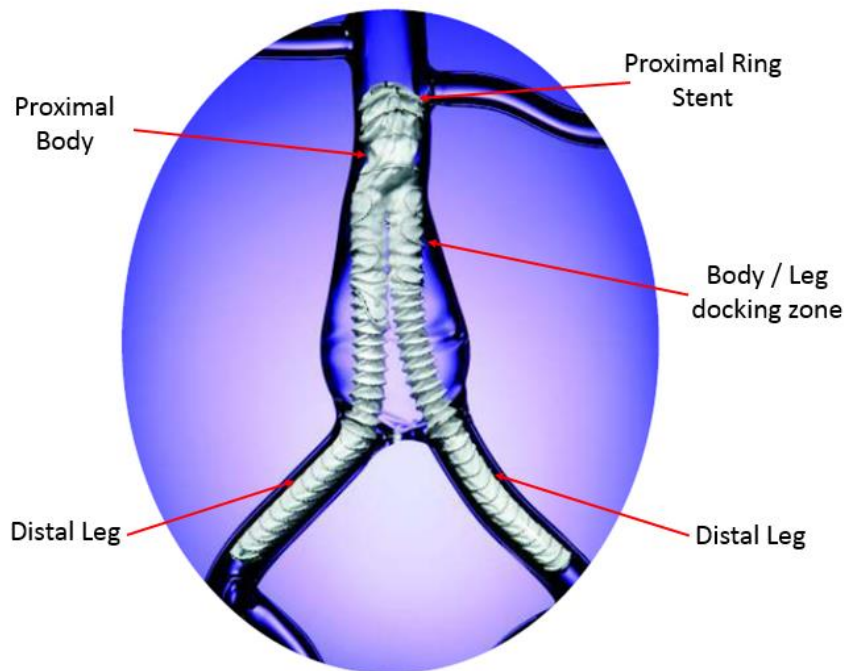
Figure 2-2: Anaconda device deployed in a glass model of an aorta.

A key feature of the Anaconda device is that it is designed for endovascular delivery. This means that instead of requiring open surgery to implant the device, it is delivered using a minimally invasive approach via a small incision in the groin into one of the iliac arteries. Figure 2-3 shows the tip and sheath of the delivery system that are designed for smooth, atraumatic delivery of the device to the implant site under fluoroscopic visualization. Figure 2-4 then shows a micro-CT reconstruction image of the proximal body device shape when it is compacted within this sheath.
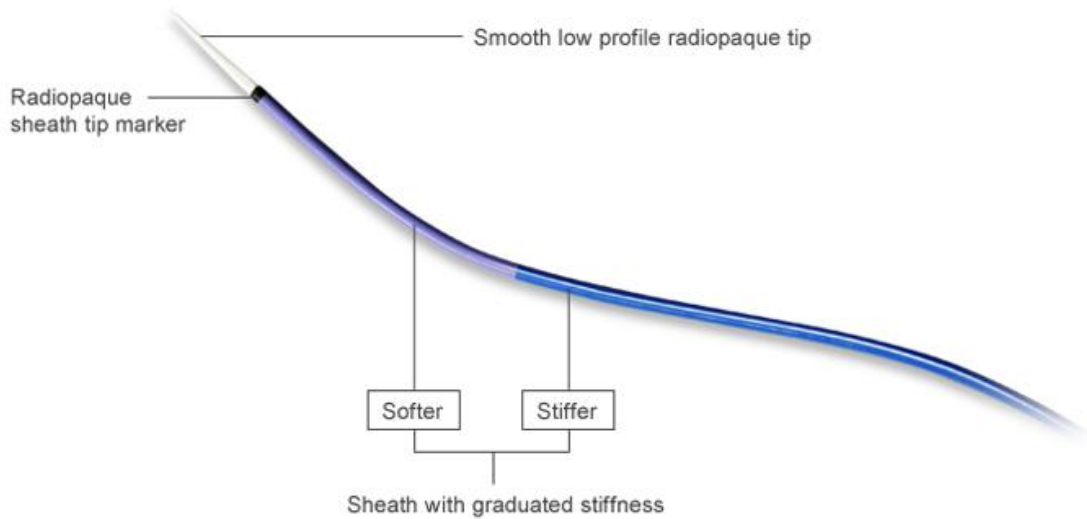
Figure 2-3: Anaconda delivery system tip and sheath

As can be seen in figure 2-4, the stent graft device fits inside the low profile sheath (23 Fr / 7.7 mm OD) by high deformation bending of the metal components (made from thin nitinol wire) into a compacted shape. For the ring stent components, this deformation occurs by being folded down into a steep 'saddle' shape. The hook components bend to a flatter shape against the sheath inner lumen wall. The graft fabric to which these metal components are sewn is also folded down during compaction. In this way, the whole body device is able to fit within the low profile sheath. Likewise, each leg device of the modular system is contained within a 18 Fr (6 mm) OD sheath for low profile delivery.

Once the compacted device has been delivered to the required implant site within the aorta, the device must then be unsheathed, positioned and then released from the delivery system so that it will remain in the aorta for long-term in-vivo service while the delivery system is removed from the patient. Figure 2-5 shows an Anaconda body device attached to its delivery system after unsheathing.
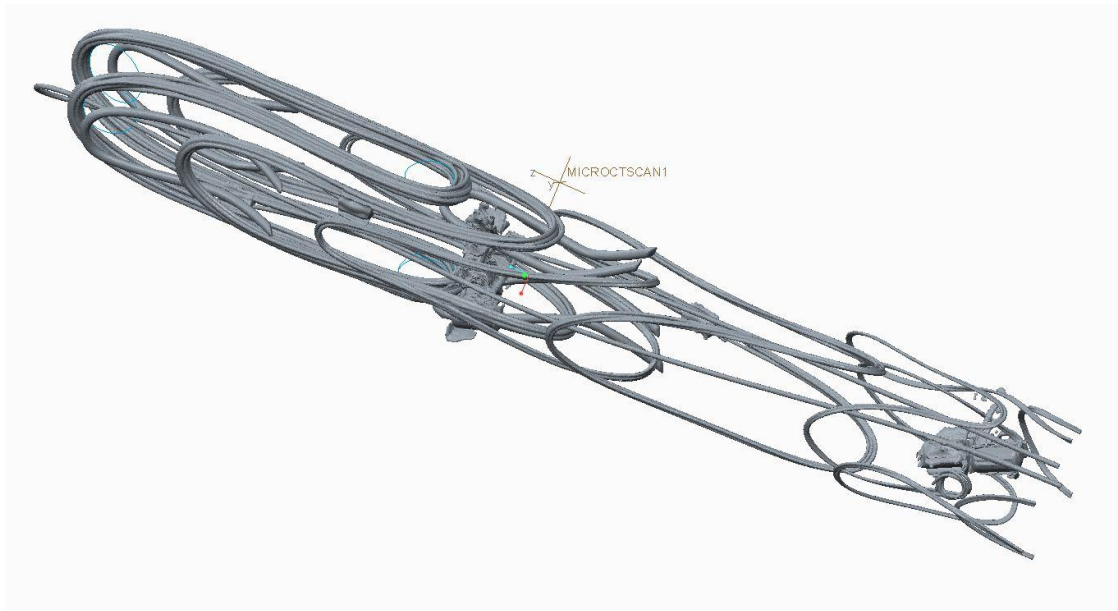
Figure 2-4: Micro-CT scan reconstruction of compacted Anaconda body device inside sheath
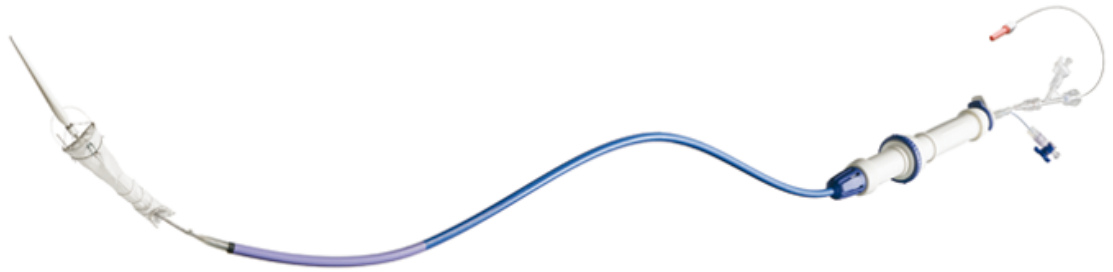
Figure 2-5: unsheathed Anaconda body device on its delivery system

As can be seen, when the device is unsheathed, the metal components recover their shape so that the device opens up. The requirement for components that can be highly deformed for endovascular delivery and then undergo 'self-expansion' during deployment is a key reason for the use of superelastic Nitinol material.

Once the Anaconda body device has been unsheathed, it can then be repositioned using controls on the delivery system handle, allowing the device to be accurately implanted at the desired site. Figure 2-6 shows how the proximal end of the device can be collapsed for repositioning and then re-opened when positioning is complete. As can be seen, collapse of the device involves the stent ring components being deformed into a steeper saddle shape, while re-opening unloads these components to a shallow saddle shape for contact and sealing with the vessel walls.

Deployed   Collapsed   Re-deployed
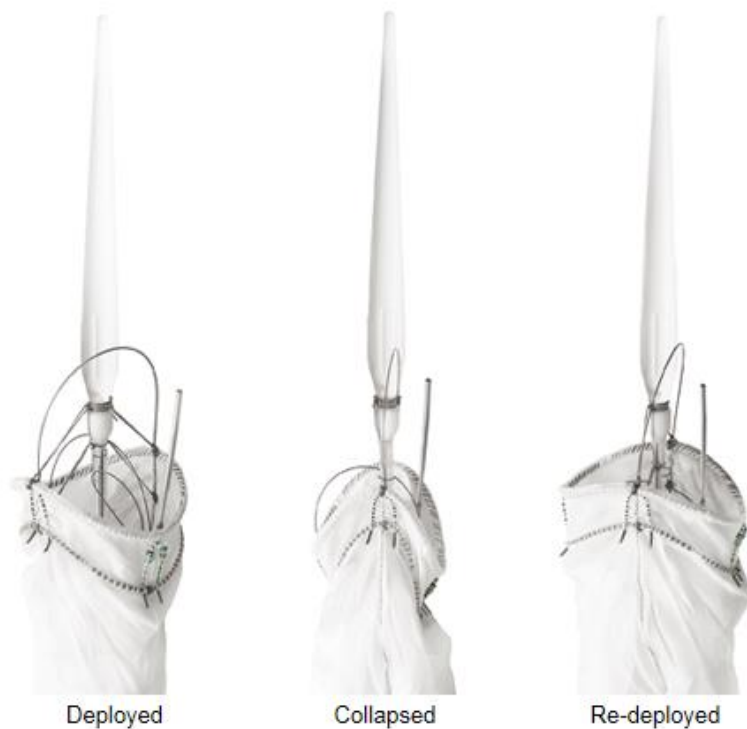
Figure 2-6: collapse and re-opening of the Anaconda body device during re-positioning

Figure 2-7 helps to clarify the design and function of the Anaconda device by showing labelled components. Table 2-1 then explains the function of each labelled component.
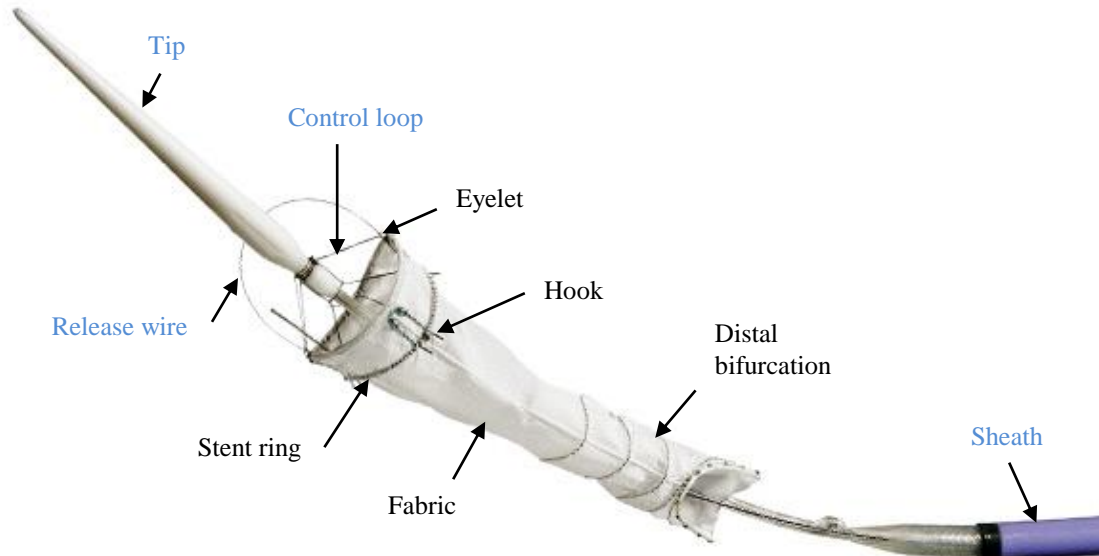
Figure 2-7: Anaconda stent graft device, with key functional components labelled

Component	Function
Tip	At the leading end of the delivery system, this ensures safe passage of the delivery system over a guidewire through the endovascular approach. The tip has a smooth, bullet-shaped profile and has flexibility to allow passage through tortuous anatomy without trauma to the vessel wall. The injection molded tip component is made from 80 % pebax plastic / 20 % barium sulphate material, for flexibility and radiopacity.
Sheath	During system assembly, the sheath is pulled over the device for compaction and is then attached to the delivery system handle, so that the folded device is held deformed within the sheath for endovascular delivery. In the procedure, the sheath is retracted by the clinician to deploy the self-expanding stent graft at the implant site. The sheath is made from pelprene with a stainless steel braid for flexibility with torqueability and kink resistance. It has a hydrophylic external coating for endovascular passage, and an internal PTFE layer to minimize device compaction and deployment forces.
Control loop	Control loops are part of the delivery system assembly, used to attach the device to the delivery system until final device release. Each control loop passes through an eyelet on the device, and is locked in place by a removable release wire. These loops are made from Polyethylene braid to provide tensile strength.

Component	Function
Eyelet	The device has eyelets sewn to the fabric at peak and valley positions of the 'saddle' shaped rings. Each eyelet is made from monofilament sewn onto the fabric, providing attachment points for the device to the delivery system via the control loops.
Release wire	There are 2 release wires in the delivery system that 'lock' the device to the delivery system by passing through the control loops that have been passed through the device eyelets. These release wires can be pulled out from the delivery system handle to release the device from the system. The delivery system can then be removed from the patient, leaving the implanted device in the vessel. The release wires are made from mechanically polished Nitinol wire to accommodate the large strains experienced in compaction and to allow for low-friction withdrawal.
Stent ring	The stent rings are made from multiple turns of thin straight-set Nitinol wire. They are designed to fold down into a compact shape for delivery within a sheath, and then to self expand at the implant site with adequate radial force. The main function of the top 2 stent rings is to hold the device in sealing contact with the vessel wall, so that blood will flow through the device without leaking past the device into the aneurysm sac. The rings also provide radial force to push the hooks into the vessel tissue for device anchoring. All stent rings on a device also have the function of holding the graft fabric open, providing a patent lumen for the blood to flow though. The stent rings have a Chemically Etched surface finish for corrosion resistance.
Hook	Hooks are sewn onto the fabric at the proximal end of the device, with points protruding at the 2nd ring peak and valley positions. Together with the sealing rings radial force, these hooks act to anchor the device in the vessel, preventing axial migration of the device over time. The hooks are made from Nitinol to accommodate large strains during compaction. They are Electro-Polished for corrosion-resistance.
Fabric	The woven polyester fabric is impervious to blood and has sufficient strength to maintain integrity under blood pressure, providing a conduit for blood flow through the aorta and iliacs in order to exclude the surrounding aneurysm.
Distal bifurcation	The fabric body has a distal bifurcation, providing docking zones for the two leg devices to attach to the body. These leg devices will provide a conduit between the body device and the common iliac arteries. Ring stents sewn onto the tubular leg fabric hold the graft material patent and allow distal sealing with the iliac vessels.

Table 2-1: description of the design and function of Anaconda system components labelled in Figure 2-7

2.1.2 Superelastic Nitinol Material for Stent Components

Nitinol is a binary Nickel Titanium Alloy, with near-equiatomic percentages of nickel and titanium. It has useful 'Superelastic' and 'Shape Memory' behaviours that depend on underlying phase changes within the material, controlled by temperature or stress. Therefore, Nitinol is considered a 'smart material'.

The two main phases of Nitinol material in service are Austenite and Martensite. The austenite phase has a cubic atomic structure and is stable at temperatures above the material's 'Austenite Finish' (Af) temperature. The martensite phase has a monocilic crystal structure and is stable at temperatures below the material's 'Martensite Finish' (Mf) temperature or at temperatures above Af when sufficient stress is applied ('Stress-Induced Martensite'). Between Mf and Af temperatures, the material is either martensite or austenite depending on its temperature history, or is in transition between the two phases. For the Nitinol material used in Vascutek's stent graft devices (Fort Wayne Metals NiTi#1 – see Appendix 1 for specification), the Af temperature is in the range $12C \leq Af \leq 18C$, the Mf temperature is typically ≤ -100 C, and Stress-Induced Martensite occurs at > 500 MPa tension at room temperature. For the present work, we are interested in the material behaviour above Af temperature (from Af up to approximately Af + 60 C), where superelasticity occurs.

One of the main commercial applications of Nitinol is in stent graft components, as it can be processed to meet the following requirements:

- Superelasticity for compaction and self-expansion
- High unloading stresses to give ring radial force for sealing and vessel damping
- Stiffness to limit deformation under in-vivo pulsatile loading conditions
- Biocompatibility
- Corrosion resistance for long-term implantation
- Fatigue resistance for long-term pulsatile in-vivo loading conditions
- Kink resistance to avoid damage during compaction

The first three of these characteristics are most relevant to the present work, and will now be considered in greater detail.

Superelasticity

The superelastic effect is the ability of Nitinol to transform from its austenite phase to its Martensite phase in a given temperature range (the 'superelastic window') when stress is applied to achieve a large recoverable deformation. When the stress is reduced, the phase change is then reversed with Martensite material transforming back to Austenite, and the large transformation strain is recovered. In this way, large deformations such as those seen during device compaction can be achieved without plastic deformation, and can then be fully recovered when the device self-expands during deployment. Figure 2-8 shows a typical 'superelastic' stress-strain graph for nitinol in its 'superelastic window' temperature range, where the material has been loaded in tension to 6% strain, then fully unloaded for strain recovery. The material has then been pulled to failure at approximately 12% elongation. The schematic diagrams accompanying the graph depict how the material phase changes from cubic austenite to detwinned martensite without plasticity to achieve a large recoverable transformation strain during loading.

The uniaxial tensile stress-strain curve for superelastic Nitinol material has a characteristic 'flag' shape, with the following key features that are typically considered when specifying Nitinol for stent graft devices: the initial modulus (or 'austenite elastic modulus'); the loading stress plateau; the unloading modulus; the unloading stress plateau. These features are highlighted on a typical Nitinol stress-strain curve in fig 2-9.
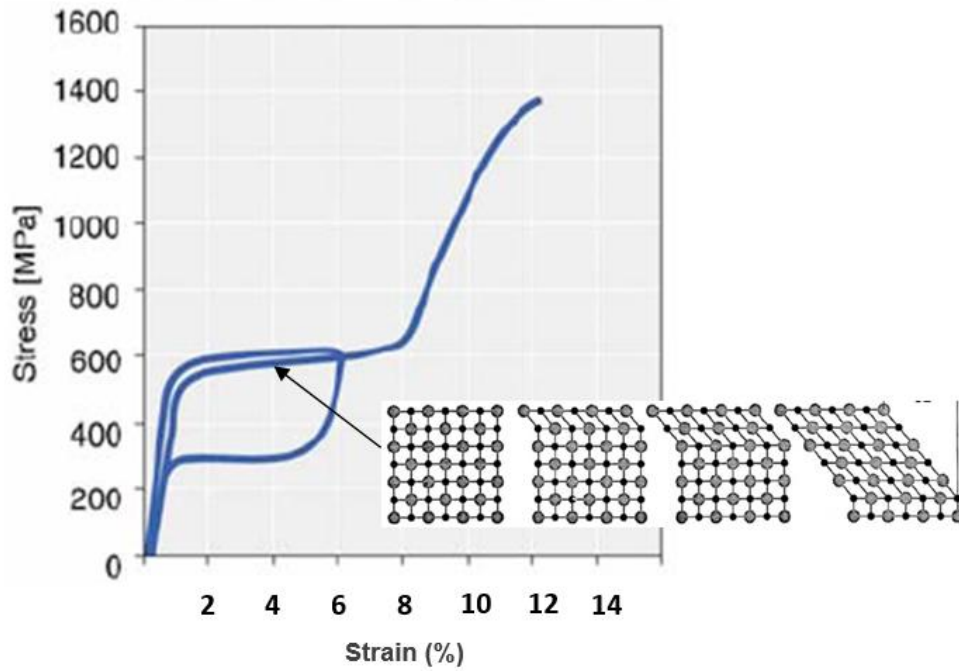
Figure 2-8: Typical stress-strain curve for superelastic Nitinol in uniaxial tension with schematic diagram depicting Austenite to Martensite phase change in the material during reversible 'transformation strain' deformation
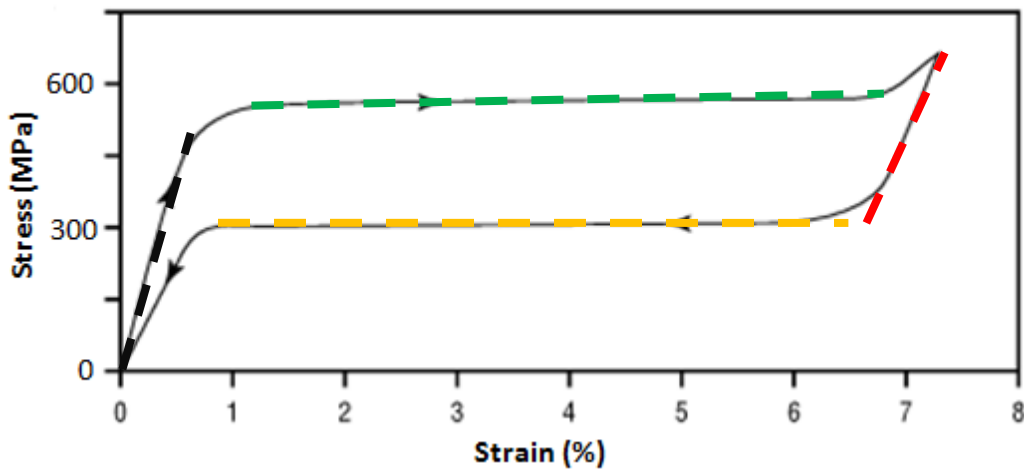
Figure 2-9: stress-strain load-unload graph for superelastic nitinol in tension, with overlay of dashed lines showing key features: initial modulus (black), loading stress plateau (green), unloading modulus (red), unloading stress plateau (orange)

The superelastic effect is temperature dependent, occuring only within a temperature range above the material's Af temperature, known as the 'superelastic window' range. Below Af, but above Mf, austenite phase will transform to martensite under stress (Stress-Induced Martensite or 'SIM') but will not reverse-transform to austenite when the stress is removed. Therefore, the material exhibits SIM without superelasticity at certain temperatures. (Note that the resulting residual strain could still be recovered by heating the material to above its Af temperature – ie. there is still no plasticity involved in the deformation). As temperature increases above the Af temperature, the loading and unloading plateau levels increase, as it takes higher stress to transform austenite to martensite and vice-versa at higher temperatures. With increasing temperatures and transformation stress levels, there is also increased plastic deformation that occurs, meaning increased permanent set upon unloading. The maximum temperature at which Martensite can be stress-induced is known as the 'Martensitic Deformation' temperature (Md), beyond which austenite elasticity will be followed by plastic deformation of the austenite material, with no 'SIM' phase change occuring. For Vascutek's NiTi#1 wire, the 'superelastic window' is in the range 12 C to approximately 70 C.

Unloading Stresses

When Nitinol material is unloaded, such as when a stent is deployed from the delivery sheath, it will follow a certain stress-strain path that depends on its level of compaction strain. In general, the material can follow two types of unloading stress-strain path:

1. Linear elastic unloading: from 'compaction' strains < ~1.2 %
2. Non-linear 'superelastic' unloading: from compaction strains > ~1.2 %

These two paths are illustrated in figure 2-10. Path 'A' represents nitinol material that has reached a large transformation strain during compaction and is unloaded to a lower 'reverse transformation' strain during deployment. Path 'B' represents nitinol material that has experienced only small strains during compaction, remaining in its austenite phase, and has then been unloaded to a lower 'elastic' strain during deployment. These

scenarios will occur for material at different regions of a stent when it is unsheathed and deployed into a vessel, with the stent component attaining a final 'oversize' shape inside the vessel.
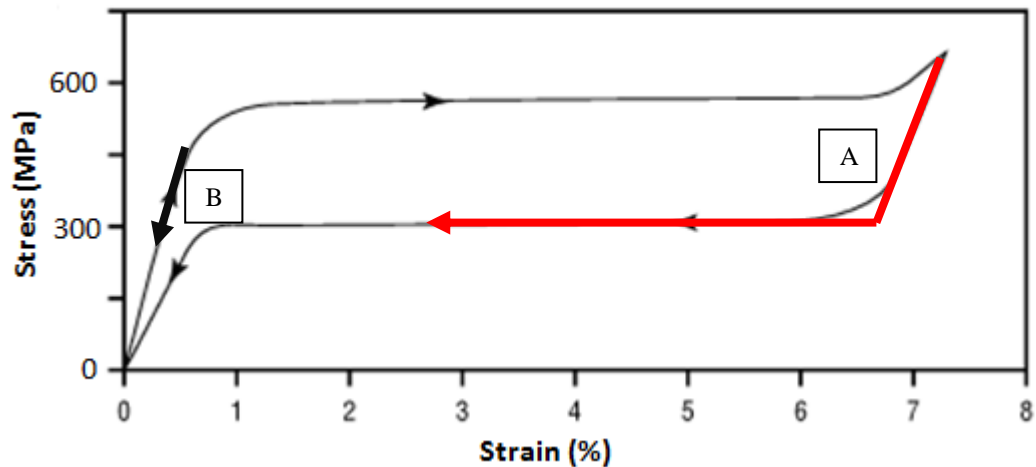
Figure 2-10: stress-strain load-unload graph for superelastic nitinol in tension, with overlay of unload paths 'A' and 'B' illustrating 'superelastic' unloading and 'linear elastic' unloading respectively.

Vascutek's Anaconda stent graft devices come in a range of sizes, and during clinical planning the correct size is chosen to treat the particular patient according to their aorta inner diameter. The aim is to provide a device where the stent ring will have an oversize of 10 – 20 % within the aorta at the landing zone. Therefore, when a stent ring is deployed in-vivo, it expands to an 'oversize' saddle shape where it is in contact with the vessel inner wall. The vessel wall constrains the stent from opening further into a flat ring shape. In this equilibrium state, a stent's radial force is known as its 'Chronic Outward Force' (COF). Figure 2-11, provided by Vascutek Ltd, is an illustration of the Anaconda stent graft device deployed in-vivo, showing the proximal sealing rings exerting Chronic Outward Force on the vessel.
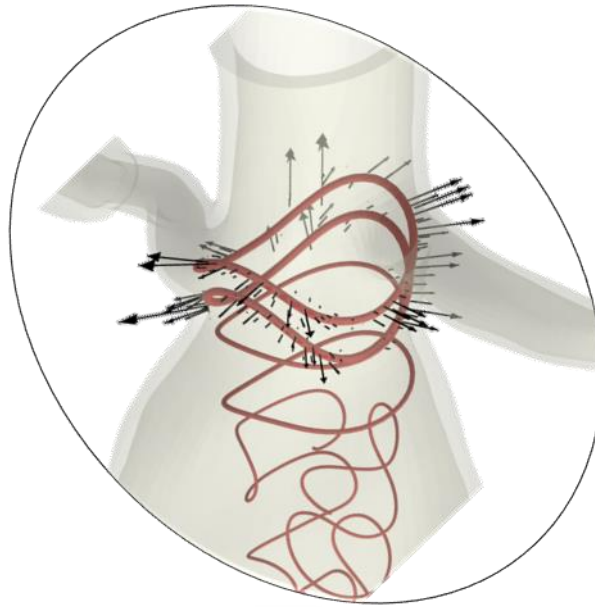
Figure 2-11: illustration of Anaconda stents deployed in vessel, depicting the proximal rings exerting Chronic Outward Force on the vessel walls. Courtesy of Vascutek Ltd

In this deployed position, the stent ring's nitinol material is at a certain strain depending on its position in the ring – higher strains near outer bend surfaces of peaks and valleys; lower strains at intermediate axial positions and near the wire's centerline.

This unloading strain state determines the stress state of the saddle-shaped ring, which determines the radial force (COF) exerted on the vessel. This can be understood as follows: at a particular unloading strain, the nitinol material is at a certain stress (as can be seen in figure 2-10). The stress level of that material and its distance from the neutral axis contributes to the internal moment of a given cross-section of the wire in bending. The sum of all these internal moments around a wire turn determines the radial force of a single wire strand. The sum of these wire strand radial forces gives the ring radial force (COF).

For a stent graft device, it is desirable to maximize the radial force (COF) of the proximal rings for three reasons:

1. Sealing performance
2. Migration resistance
3. Vessel damping and reduced diametric strain: aortic vessel exhibits 'hyperelastic' behavior radially, where it stiffens as its diameter increases under radial force. A ring with higher radial force will therefore move the vessel to a larger diameter, higher stiffness state. Diametric strain due to pulsatile loading will then be reduced, meaning that the fatigue loading on the ring will be reduced.

To maximize radial force of a stent without compromising the low-profile configuration for compaction, it is required to specify a material that has high stresses at unloading strains. To achieve this, the following specifications of superelastic nitinol material are desirable:

- High initial linear elastic modulus

- High loading stress plateau

- Low 'unloading' moduli (note: unloading modulus depends on 'compaction' strain history, as will be explained in '2.2: Literature Review')

- High unloading stress plateau

These characteristics aim at ensuring the material when unloading in a stent remains at its highest possible stress state for the 'deployed' oversize position. For Vascutek's NiTi#1 wire, the following specifications have been agreed with the supplier to ensure suitable radial force can be achieved by the ring stents in service:

- At 37 C, load plateau @ 4 % strain must be > 560 MPa

- At 37 C, unload plateau @ 4 % strain must be > 250 MPa

Vascutek's existing wire specification does not include initial modulus or unloading moduli – this may be an area for quality control improvement in future.

As has previously been stated, Nitinol's stress-strain response is highly temperature dependent. Increasing the temperature above Af increases the initial modulus and upper and lower stress plateau levels. Therefore, the unloading stress state of the wire at body temperature (37 C) can also be maximized by lowering the Af temperature specification. However, research has shown that a large gap between Af temperature and test temperature has a negative impact on fatigue life. For these reasons, the following specification has been considered optimal for Vascutek's NiTi#1 wire:

- 12 C ≤ Af ≤ 18 C (due to processing limitations, it is not feasible to specify a tighter Af temperature range than this)

Material Stiffness

When Nitinol material is reloaded from a 'deployed' position, it takes a different path from its unloading path during deployment. This is illustrated in figure 2-12, where nitinol material has been unloaded from a 'compaction' strain of 7 % to a 'deployed' strain of 2 % in tension. It is then re-loaded to a strain of 2.2 %.

The modulus of this re-load path determines the resistance of the material to loading deformation from this 'deployed' strain state. In terms of ring stent design, this 're-load' stiffness determines the deployed stent's resistance to deformation by the vessel walls under pulsatile blood pressure loading conditions, known as the 'Radial Resistive Force' (RRF) of a stent. Increased Radial Resistive Force will minimize cyclic deformation under pulsatile loading, and therefore maximize fatigue life of a ring stent.

For this reason, it is desirable to maximize the re-load stiffness in the Nitinol specification. This re-load stiffness is also known as the 'cycling modulus' of the material, and is related both to the austenite elastic modulus and the martensite elastic modulus. At present, Vascutek does not specify these parameters for its NiTi#1 wire, but this may be an area for quality control improvement in future.
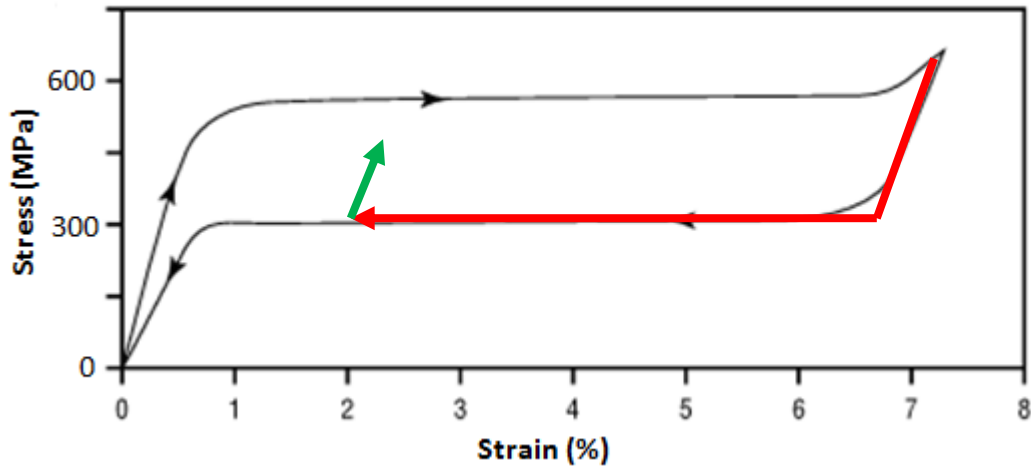
Figure 2-12: stress-strain load-unload graph for superelastic Nitinol in tension, with overlay of unload path (red) and re-load path (green)

2.1.3 Product Life Cycle of Nitinol Components

In order to better understand the requirements of Nitinol material in stent graft devices, and for research effort to have practical application, it is useful to consider the Product Life Cycle of a device. Table 2-2 below outlines the main steps in the Product Life Cycle of the Vascutek Anaconda stent graft, and shows the thermo-mechanical processing experienced by the ring stent and hook Nitinol components at each stage.

Product Life Cycle step	Nitinol wire processing
1. Device manufacture at room temperature (RT)	**Rings**: As-received straight-set NiTi wire (ø 0.1 – 0.24mm, NiTi#1 – see Appendix 1) wound into ring bundle with multiple wire turns, ends joined by Tantalum crimp. Rings sewn onto fabric with suture. Ring wire is in bending, with maximum strains < initial elastic limit.
	Hooks: As-received NiTi wire (diameter 0.45mm, NiTi#1 – see Appendix 2) heat set into shape, electro-polished, cut and filed to size and sewn onto fabric with suture. Hook is undeformed.

Product Life Cycle step	Nitinol wire processing
2. Device Assembly to delivery system at RT	**Rings**: deformed into slight saddle shape by attachment to delivery system at peak and valley eyelets (see figure 2-7). Collapse to steep saddle shape and opening of ring following attachment (see figure 2-6): wire bends at peaks and valleys with maximum strains > initial elastic limit, causing material phase change (max ε > 1.2% in tension and compression).
3. Device compaction in sheath at RT (up to 3x)	**Rings**: Compaction into sheath via introducer funnel: bends wire at peak and valley regions (see figure 2-4) with maximum strains beyond the loading transformation plateaus (>7.5% tension, > 4% compression). Device may be unsheathed and re-compacted twice more – causing 'large strain' cycling of the material.
	Hooks: compaction into sheath via introducer funnel bends the wire at the 'kick' hinge points with maximum strain in loading transformation region (max ε > 1.2% in tension and compression). (Note: 'kick' hinge bend direction in compaction is opposite to bend direction during in-vivo operation). Hook wire also bends (to a lesser extent) at the arch region (see compacted hook components in figure 2-4). Device may be unsheathed and re-compacted twice more – causing 'large strain' cycling of the material.
4. Product sterilization – RT to 53C and back to RT (up to 3x)	**Rings and hooks**: stresses increase in strained nitinol material due to temperature increase and then decrease when returned to room temperature. Sterilization may be repeated twice more – causing thermal cycling of the material.
5. Endovascular delivery of compacted device to implant site at body temperature (37C)	**Rings and hooks**: stresses increase in strained nitinol material due to temperature increase from RT to 37C.

Product Life Cycle step	Nitinol wire processing
6. Unsheathing of device at implant site (at 37C)	**Rings**: wire at peak and valley positions rapidly reduces its bend curvature as ring expands, and some material unloads along 'unloading modulus' and then along unloading plateau (see path A in figure 2-10). Final unloading strains (and bend curvatures) depend on whether user holds device in 'collapsed' position via control collar or not during unsheathing. (See 'collapsed' device in figure 2-6).
	Hooks: hook wire fully unloads upon unsheathing, with some material unloading along 'unloading modulus', then along 'unloading plateau' and finally with austenite elasticity. Hook material is at zero strain following unsheathing, even if device is held 'collapsed'.
7. Repositioning of device by collapse / re-open (at 37C) (see figure 2-6)	**Rings**: Collapse to steep saddle shape: peak and valley material loads with maximum strains beyond initial elastic limit, causing material phase change (max $\varepsilon > 1.2\%$ in tension and compression). Re-opening of ring: peak and valley material unloads along the 'unloading modulus' and then the 'unload plateau'. Repeated collapse-open repositioning cycles will subject the outer and inner bend material to 'intermediate strain' $\Delta\varepsilon$ cycling. There is no limit set on this, but it is unlikely that repositioning will exceed 3 cycles during a procedure. Note that the material will always be 'unloading' following the repositioning (collapse / re-open) cycle.
	Hooks: if the hooks penetrate the vessel walls during this repositioning stage, it is possible that the hook 'kick' hinge points could undergo load / unload bending cycles if the user pushes, pulls and twists the delivery system prior to collapsing. Otherwise, the hooks remain undeformed during this stage.

Product Life Cycle step	Nitinol wire processing
8. Release of device from delivery system at implant site (by pulling out release wires – see figure 2-7) (at 37C)	**Rings**: wire continues to unload, reducing bend curvatures, until the ring contacts the vessel walls and the ring's Chronic Outward Force matches the radial resisting force of the vessel. The final 'mean strain' state of the material will depend on the ring oversize in the vessel – which depends on the vessel ID and vessel compliance relative to the ring size and radial force.
	Hooks: the sharp points of the hooks pierce the vessel walls and the hooks penetrate the vessel until the rings contact the vessel walls. At this stage, where there is no pressure differential between the blood inside and outside the graft, there is minimal 'migration force' loading on the hooks and the material in the 'hinge' regions is under minimal strain.
9. Long term implantation with excluded aneurysm and pulsatile blood pressure loading (at 37C)	**Rings**: wire is cyclically loaded and unloaded in bending with small $\Delta\mathcal{E}$ levels about a mean strain, with cycling 'from below' (i.e. from the unload plateau). The magnitude of the $\Delta\mathcal{E}$ cycles depends on the stented vessel's diametric strain under pulsatile blood pressures. Cycling rate is approximately 1 cycle per second. Note that over time the mean and delta strains may change as the ring opens out further due to vessel creep and / or re-modeling.
	Hooks: a pressure differential develops between the blood inside the sealed graft and the 'excluded' vessel outside. This leads to cyclic 'migration' forces on the hooks about a mean force. The hooks undergo maximum bending strains at the 'kick' hinges as the device moves relative to the embedded hook legs. Previous FEA suggests that the maximum cyclic strains caused by this pulsatile loading are below the threshold for phase transformation, with the material remaining fully austenite and deforming elastically.

Table 2-2: Product Life Cycle of Vascutek Anaconda stent graft, describing the thermo-mechanical processing experienced by the ring and hook Nitinol components at each stage

The background section has considered the function of superelastic nitinol wire in stent graft devices for treating Abdominal Aortic Aneurysm (AAA), with particular focus on Vascutek's Anaconda device. In order to better understand this application of Nitinol, material characterization testing and FEA simulation is to be performed for Vascutek's NiTi#1 wires. Prior to undertaking these activities, a literature review will be performed with focus on the following relevant areas for Nitinol:

- Effects of material processing history
- Temperature dependence
- Strain rate dependence
- Compressive and tensile testing techniques
- Compressive and tensile stress-strain characteristics
- Bend testing techniques
- Bend behavior characteristics
- Load path history effects in bending
- Cycling effects on material properties
- Constitutive Modelling of superelastic Nitinol for FEA

2.2 Literature Review: Characterisation of Superelastic Nitinol Material

The behaviour of self-expanding stent structures in service is dependent on the mechanical response of superelastic nitinol material in bending, which in turn is largely dependent on the material response under tensile and compressive loading. A literature review was conducted to consider previous investigations into these mechanical behaviours of nitinol. (Note that consideration of shear / torsional responses of Nitinol, while relevant to in-service bending behaviour of stents, are beyond the scope of this project). A central aim of this literature review was to provide a solid basis for planning, executing and analysing material characterization testing on Vascutek's nitinol wire. Therefore, the literature review was conducted with three major objectives in mind:

- To understand how to perform mechanical characterization testing for small diameter superelastic Nitinol wire, representative of stent material in tension, compression and bending
- To understand the general qualitative mechanical behaviours of superelastic nitinol material in tension, compression and bending
- To gain knowledge of the FEA-based constitutive models commonly used in design of superelastic Nitinol components, considering their capabilities in describing relevant superelastic material behaviours.

The findings of the literature review are presented in three main parts:
- '**2.2.1: Experimental testing considerations for Nitinol'** looks at key issues for sample sourcing and test set-up based on Nitinol's sensitivity to processing history and temperature.
- '**2.2.2: Compressive, Tensile and Bend Testing of Nitinol**' presents a review of the material characterization test methods and results published by previous investigators.
- '**2.2.3: Superelastic Constitutive Models for Nitinol'** presents a brief review of the literature on superelastic Nitinol constitutive modelling, focusing on the model that will be used for FEA in Chapter 6 of the thesis.

2.2.1 Experimental Testing Considerations for Nitinol

2.2.1.1 Sample Material Properties: Processing History Dependence

The sensitivity of Nitinol's material properties to its processing history, as reported in the literature, was considered in order to understand the requirements for test sample sourcing.

Processing Steps for Nitinol wire material

Biscarini et al (1) outline the main steps involved in processing raw nickel and titanium material to a finished superelastic wire product. These are:

- *Melting:* high purity raw materials (Ti sponge, electrolytic grade Ni) in desired amounts are melted and then cooled into an ingot, using Vacuum Induction Melting (VIM) or Vacuum Arc Melting (VAR) or both. Re-melting of the ingot is performed to ensure good microstructural homogeneity. The output from this step is an ingot with the desired Ni Ti composition, as well as trace elements including carbon and oxygen which lead to the presence of 'melt inclusions' in the material.

- *Hot Working:* the ingot is hot-worked in multiple cycles at elevated temperatures (typically 750 – 950 C) through large deformations (> 90 %) to achieve a first shape (e.g. Rod). This step achieves a microstructure exhibiting improved workability (greater ductility) compared to the 'as-cast' ingot microstructure.

- *Cold Working (CW):* a series of cold work steps move the first shape (e.g. Rod) towards the target shape (e.g. Round wire) with desired physical / mechanical properties. 30-50 % cold work (reduction in cross section area) is typical for each CW step, with intermediate annealing at 600-800 C for stress relief between steps. The annealing steps cause recrystallization and growth of the austenite grains, minimizing work hardening due to dislocations. For round wires, Cold Working involves drawing through a series of dies.

- *Shape Setting:* Heat treatment(s) after the last Cold Work step are used to set the final desired shape (e.g. Straight set wire) and to optimize the transformation and mechanical properties of the nitinol.

Pelton et al (2) further focus on the optimization of superelastic medical grade nitinol wire by cold working, continuous strain-age annealing, and additional ageing treatments. Continuous strain-age annealing involves pulling the cold worked wire through a furnace at a given applied strain and speed. In order to achieve straightened wire with superelastic properties, they report using 30 –50 % cold work and then continuous strain-age annealing at 450-550 C under stress of 35-100 MPa.

Effects of Processing History on Mechanical Properties

Shaw and Kyriakides (3) describe the microstructural aspects of the transformation mechanisms in nitinol to give an understanding of the macroscopic phenomena, such as superelasticity. They note that the properties of the material, and therefore the macroscopic thermo-mechanical behaviour, can be altered significantly by small changes in the processing parameters such as alloy composition and thermomechanical treatments, including cold working, annealing and thermal cycling. Specific examples of processing effects on final properties from the literature are given below.

Pelton et al (2) performed different ageing heat treatments on Ti - 50.8 at% Ni wire to investigate the effect of heat set processing on the transformation temperatures and mechanical properties of the finished wire product. Wire samples were aged between 300 – 550 C for 2-180 minutes. It was found that the ageing heat treatments had the following effects: Af temperature increased for temperatures up to 500 C and decreased between 500 C and 550 C ageing temperatures; loading plateau stress slightly decreased for temperatures up to 500 C, with more rapid decrease at 550 C; UTS increased for temperatures up to 450 C and decreased for 500 C and 550 C ageing temperatures. The paper also investigates the effect of processing on the fatigue resistance properties of Nitinol wire, and shows that superelastic wires processed to have Af temperature closer to (but still below) the test temperature had improved fatigue resistance.

Nemat-Nasser and Guo (4) performed uniaxial compressive testing on superelastic Nitinol rods (Ø4.75 mm x 5 mm) that had undergone different heat treatments, with 30 minute dwells at the following temperatures: 300 C, 450 C, 550 C, 600 C, 650 C. Their results of quasi-static compressive testing of these samples at 23 C show changes in the superelastic curve shape due to heat treatment processing, with decreasing transformation stresses and increased recoverable strain as heat treat temperature increases, and changing hysteresis loop area (dissipated energy) for different ageing

processes (decreasing for low to mid ageing temperatures, increasing for mid to high temperatures).

Schaffer and Plumley (5) investigated the effects of different final cold work draws on the tensile and fatigue properties of Ti – 50.9 at% Ni wires, with final diameter 0.32 mm. They report that increased final cold work gives increased upper plateau stress, increased load-unload hysteresis and increased UTS for the superelastic wire samples following heat treatment (490 C for 15 mins). They also found an improvement in fatigue life for lower cold work samples (20 - 30 % CW) at alternating strains > 1% in Rotary Bend Fatigue Tests.

Reasons for Processing History Effects

The processing steps from raw material melt to finished nitinol material produce a particular polycrystalline microstructure in the finished material. This microstructure includes grains of a particular size and crystal structure / phase, inclusions from the melt, dislocations from the cold work steps and precipitates from the various heat treatments. It is the particular composition and directionality of this finished material microstructure (as well as its surface finish) that provide the macroscopic mechanical properties. Some examples of how the microstructure can affect the material behaviour are given below.

For as-received superelastic nitinol material used in medical devices, grain sizes are typically in the range 10 – 100 nm (refs: 6-9). In the paper by Mehta et al (6), where stent specimens are annealed at 850 C for 30 minutes in order to grow grains to sizes of 20-50 µm suitable for strain measurement, it states "it is well known that thermomechanical processing of nitinol strongly affects grain size and thus the resulting mechanical properties". Pelton (7) gives clear evidence of this, presenting tensile stress-strain curves together with TEM microstructure images for both annealed and stress-relieved wire samples, showing that the 'annealed' microstructure has a higher initial modulus up to 0.5 % strain before 'yielding' with no further stress increase, while the nano-grain

'stress-relieved' structure (typical grain size 75 nm) continues to increase its stress up to 1.3% strain where it reaches its transformation plateau.

As well as grain size, Fonte and Saigal (10) show that the directionality or 'crystallographic texture' of the microstructure, due to drawing and thermomechanical conditioning processes, have a strong effect on nitinol properties such as recovery strain and strength levels.

Further, Perry et al (11) showed the effect of heat treatment on the presence of R-phase in nitinol material, and its resulting effect on initial elastic modulus. Two heat treatments 'A' (325 C for 60 minutes, then water quench) and 'B' (500 C for 30 minutes, then water quench) were used, where samples treated with A exhibited a strong R-phase component while samples treated with B did not. Load vs strain plots for tensile and compressive surfaces of bending samples showed that 'heat treatment A' samples had a 'sigmoidal' shaped initial elastic region with lower effective modulus in tension, while 'B' samples had a linear elastic modulus with little tensile-compressive asymmetry in this region. This clearly shows that the presence of R-phase following processing has a considerable effect on the initial elastic behaviour of nitinol.

Pelton et al (2) consider the effect of ageing heat-treatments on the microstructure. They describe the formation of precipitates within the TiNi matrix of Ti - 50.8 at% Ni wire at 300-500 C ageing heat treatments, while at higher 'annealing' temperatures (500-550 C) there is diffusion of the Ni and Ti atoms in the matrix, with dissolving of precipitates. These changes in the microstructure are responsible for the macroscopic wire property changes described previously (evidenced by differences in Af temperature, loading plateau stresses and UTS).

Fonte and Saigal (10) further explain the effects of precipitates within the material microstructure. They explain that heat treating between 400 C and 500 C, required to

maximize superelasticity, causes Ti_3Ni_4 precipitation. These precipitates act as nucleation sites for stress-induced martensite and obstacles to dislocation motion, decreasing the critical stress for phase transformation – the loading plateau level – and increasing the critical stress for dislocation motion – and therefore the UTS. Formation of nickel-rich precipitates due to the heat treatment shifts the Ni:Ti ratio by reducing the nickel content of the matrix, and therefore increases the Af temperature.

As has been shown, the properties of a finished nitinol material specimen are dependent on its polycrystalline microstructure, which in turn is dependent on the precise conditions of each step in its processing history. For this reason, in order to obtain useful results for analysis and design of stent components, it is vital to perform material characterization testing on specimens that have undergone equivalent processing history to the material that will be used in service.

2.2.1.2   Testing Temperature

Churchill et al (12) emphasize the importance of temperature control and monitoring when performing material characterization testing on nitinol. They explain that, unlike conventional metals, a small change in specimen temperature can significantly influence the results of experiments on nitinol. This is demonstrated by a series of isothermal uniaxial tensile tests on 0.762 mm superelastic wire with active Af temperature of 0 C (i.e. full superelastic strain recovery at all temperatures > 0 C) for the temperature range -50 to 70 C, with 10 C increments. In the 'superelastic window' of 0 to approximately 50 C, the results show an increase in modulus and upper and lower plateau stress levels with increasing temperature. They show that in this 'superelastic' temperature range, there is a linear increase of upper and lower plateau stresses of 6.7 MPa/C (which for a typical stent material represents an increase of approximately 1.4 % and 2.8 % for upper and lower plateau values respectively, relative to the room temperature values). It is important to note also that there is clear evidence of R-phase in the initial elastic loading curves at certain temperatures, with an initial lower modulus due to the R-phase,

followed by a steeper 'austenite elasticity' slope. In their results, this R-phase is only present at temperatures below the superelastic window, but it is known that this can commonly occur in the temperature range 20 – 40 C for binary nitinol (13) and can exacerbate the temperature sensitivity of nitinol test results.

Pelton et al (2) report similar results from their tensile testing of superelastic Ti - 50.8 at% Ni wire at different temperatures between -100 and 200 C. Their wire again had an active Af of 0 C and exhibited a 'superelastic window' of 0 to 60 C. In this superelastic range, there was a linear stress rate of 6.1 MPa/C for both loading and unloading. The paper states that this lies within the typical range for Nitinol alloys of 3-20 MPa/C. Again there is evidence in some of the curves (at 0 C and 10 C test temperatures) of R-phase affecting the initial elastic modulus. In their paper on the same topic presented at SMST 2000 (ref 14), Pelton et al also show an interesting graph of Initial Elastic Modulus plotted against test temperature for the same wire – shown in figure 2-13 below. This graph shows a sharp increase in the initial modulus with increasing temperature in the superelastic window (0 to 60 C).
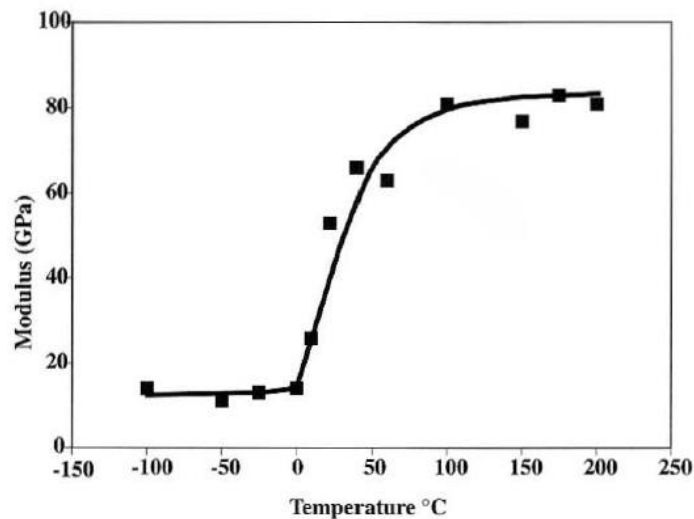
Figure 2-13: Effect of test temperature on initial elastic modulus, taken from figure 5 of ref (14)

As well as tensile testing, Siddons and Moon (15) show that compressive testing of nitinol is also sensitive to test temperature. The 'first cycle' graphs presented for compressive testing of superelastic Nitinol tubing (OD 3.17 mm, ID 2.50 mm) at 19 C and 37 C show that the higher temperature leads to higher phase transformation stresses both in loading and unloading, each increasing by approximately 120MPa from 19 to 37 C, both in tension and in compression.

It is clear that special attention must be given to controlling and monitoring the test temperature when performing mechanical testing on Nitinol. Where temperature control and monitoring for the test specimen are limited, the results must be interpreted with caution.

2.2.1.3   Testing Strain Rate

The sensitivity of nitinol's mechanical response to temperature changes leads to another important consideration for testing: the strain rate. Zurbitu et al (16) explain that the stress-induced martensite transformation (austenite to martensite) is exothermic, while the reverse transformation is endothermic. This means that, unless the strain rate is kept low enough to allow heat transfer via the specimen surface with the surrounding environment, the specimen temperature will increase during loading and decrease during unloading. These temperature changes will, in turn, affect the upper and lower plateau stresses respectively. If the strain rate is low enough, there is enough time for complete heat transfer with the surroundings, and the temperature does not significantly change in the specimen. The deformation process can then be considered isothermal.

Shaw and Kyriakides (3) show the extent to which an ambient medium and strain rate affect Nitinol's mechanical response in uniaxial tensile testing. They performed tests on 1.07mm nitinol wire above its active Af temperature (in its superelastic state) in both water and air at 4 different stain rates. The results are summarized in Table 2-3, and indicate that for tensile testing of this wire diameter in water, strain-rates should not

exceed 4×10^{-4} s^{-1} to avoid significant influence on the transformation stress values, while for testing in air, the maximum strain rate to avoid any effects on the transformation stress results is 4×10^{-5} s^{-1}.

These results are referenced extensively in the literature as a basis for tensile test set-ups. For instance, Zurbitu et al (16) quote 10^{-4} s^{-1} as an upper limit for isothermal mechanical testing. Churchill et al (12) describe using a very slow strain rate (5×10^{-5} s^{-1}) when performing uniaxial tensile tests on 0.762 mm superelastic nitinol wire in air, in order to avoid self heating / cooling during phase transformation. For tensile testing of their Shape Memory wire (1.016 mm diameter, active Af approximately 45 C) they used a liquid bath and higher strain rate of 4×10^{-4}s^{-1}, due to the increased thermal conductivity of liquid over air.

Although widely referenced, it should be noted that the results of ref (3) are for 1.07 mm diameter wire, and that thinner wire specimens can be tested at higher strain rates due to the greater ratio of surface area to internal material for heat transfer. This is seen in the ASTM F2516-07 standard (17), which includes a table showing maximum loading rates for tensile testing of nitinol specimens. Table 2-4 summarizes the ASTM F2516 recommendations for crosshead speed vs specimen diameter, and shows the equivalent strain rate for each speed (for 150 mm gage length).

Note that for tubing, the standard states that *d* should be calculated as (outer diameter) – (inner diameter). A higher strain rate can be used for tubing than for wire of the same OD, as the tube has smaller volume for heat generation and greater surface area for heat transfer.

Global strain rate	Stress-induced phase change	Peak temp change I		Global transformation stress change relative to 'fundamental stress-strain response' (%)	
		Water	Air	water	Air
4×10^{-5} s^{-1}	A – M	0	0.5	0	0
	M – A	0	-0.5	0	0
4×10^{-4} s^{-1}	A – M	1	6	+4.3%	+15%
	M – A	-1	-6	-3.3%	-16%
4×10^{-3} s^{-1}	A – M	7	12 (after reaching 'peak', remains at 'peak' temp for duration of loading)	+9%	+34%
	M – A	-4	-11 (after reaching 'valley' remains at 'valley' temp for duration of unloading)	-18%	-36%
4×10^{-2} s^{-1}	A – M	9	Linear increase from test temp to t + 28C during phase change	+20%	No 'plateau' – stress increases positively throughout loading: 'homogenous deformation' due to numerous nucleation sites and propagation of many interface fronts at higher temp & strain rate
	M – A	-5	Linear decrease from t + 28C to t - 6C during phase change	-22%	No 'plateau' - stress decreases negatively throughout unloading

Table 2-3: Summary of results from Shaw and Kyriakides (3) showing effect of ambient medium and strain rate on uniaxial tensile stress-strain results for Nitinol wire

d, diameter (mm)	First cycle (load to 6% strain and unload)		Second cycle (load to failure)	
	Crosshead speed (mm/min per mm gage length)	Equivalent global strain rate for 150mm gage length (s^{-1})	Crosshead speed (mm / min per mm gage length)	Equivalent global strain rate for 150mm gage length (s^{-1})
d ≤ 0.2	0.08	1.33×10^{-3}	0.8	1.33×10^{-2}
0.2 < d ≤ 0.5	0.04	6.67×10^{-4}	0.4	6.67×10^{-3}
0.5 < d ≤ 2.5	0.02	3.33×10^{-4}	0.2	3.33×10^{-3}
d > 2.5	0.01	1.67×10^{-4}	0.1	1.67×10^{-3}

Table 2-4: Recommended strain rates for uniaxial tensile testing of Nitinol, taken from
ASTM F2516-07 (17)

Another important point to note when considering Ref (3) results is that the specimen temperature changes and related stress changes only occur during the exothermic / endothermic forward and reverse phase change deformations. The specimen temperature during initial elastic deformation in loading and final elastic unloading is constant at the ambient temperature for all the strain rates and both ambient mediums. Also, the initial elastic modulus is not affected by the strain rate or medium.

Considering strain-rate effects for nitinol structures in bending, Reedlunn et al (18) explain that strain rate sensitivity in bending is far less than in uniaxial tension, as the latent heat exchanges are spread along the length of the bending beam and only the outer fibre is experiencing the maximum strain rate. In contrast, for uniaxial tension, the latent heat exchanges are concentrated at the transformation front.

For compressive testing on nitinol, Chen et al (19) report quasi-static compressive testing of Ǿ6.35 mm x 12.7 mm SE508 rod (Af 5-18 C; superelastic range 15-150 C) at a strain rate of 10^{-3} s^{-1} at room temperature. The results show clear superelastic behaviour with full strain recovery up to the peak test strain of 3.2 %. At much higher

strain rates ($81 - 750$ s^{-1}) used for the dynamic testing, the stress-strain response was considerably different with different superelastic curve shape and large permanent set.

Nemat-Nasser and Guo (4) also performed quasi-static compressive testing on superelastic NiTi rod (Ǿ4.75 mm x 5 mm, heat treated at 500 C for 30 mins, tested at 23 C) at strain rates of 10^{-3} s^{-1} and 10^{-1} s^{-1}. Their results show small differences in terms of higher loading transformation stresses and lower unload transformation stresses with the higher strain rate. They also performed dynamic compressive load-unload testing at much higher strain rates ($440 - 4200$ / s) which again showed considerably different behaviour, with the explanation that deformation occurs by dislocation-based slip plasticity at the very high strain rates, as opposed to the diffusionless phase transformation of SIM and superelasticity.

As has been seen, the strain rate, in conjunction with the geometry of the specimen and the ambient medium, must be carefully considered when performing mechanical testing on nitinol material. Where time limitations preclude very low strain-rate testing, the information provided in the above literature review can provide useful guidance in interpreting results and identifying possible error.

Having looked at the importance of controlling strain rate when performing material characterisation for Nitinol, it is also useful to consider how strain rates might affect the stresses within an arterial stent device in-vivo, where it is subject to dynamic pulsatile loading. For fatigue safety, the Nitinol components of these devices need to be designed to withstand 400 million pulsatile cycles (for 10 years implantation at 70 heart beats per minute), meaning that the maximum cyclic delta strains in the components need to be very low to avoid fatigue fracture. For such small strain excursions, the material deformation is purely elastic, with no phase change and therefore no associated self-heating / cooling effects. The in-vivo cyclic mechanical response of the nitinol components can therefore be considered strain-rate independent.

2.2.1.4 Conclusions: Experimental Testing Considerations for Nitinol

The following must be carefully considered when performing mechanical characterization testing for nitinol material:

- Processing history equivalence of test sample material vs in-service material
- Test temperature: chosen to match in-service conditions, with careful control and monitoring during testing
- Strain rate: suitable for the test sample geometry and ambient medium, and appropriate to the intended strain-rate(s) of the in-service component material

The following items should be stated when reporting results of mechanical testing on Nitinol:

- Material composition (Ti - at% Ni or Ti - wt% Ni)
- Any known details of processing history (e.g. final cold work %; final heat treatment conditions, subsequent machining and surface finishing)
- Active Af temperature
- Sample geometry
- Test temperature
- Test medium (e.g. Air or water)
- Test strain rate

2.2.2 Compressive, Tensile and Bend Testing of Nitinol

2.2.2.1 Uniaxial Compression Testing: Experimental Set-Up Considerations

It is well known that uniaxial compression testing has inherent difficulties, particularly due to buckling, shear and friction. As explained in ref (20), the mode of deformation in compression testing will depend on the sample geometry and the contact surface friction. The information from (20) offers a useful 'rule of thumb' for compressive test set-up, and is summarized in Table 2-5.

Sample Length / Diameter ratio (L/D)	Contact surface friction	Deformation mode
> 5	all friction conditions	buckling
2.5 - 5	all friction conditions	Shearing
2.0 – 2.5	Friction present	Double barrelling
< 2.0	Friction present	Barrelling
< 2.0	No friction	Homogenous compression

Table 2-5: Effect of Sample Length : Diameter ratio and end-surface friction on deformation mode for compressive testing, taken from (20)

For material characterization of nitinol used for medical device implants, the challenges of compression testing are exacerbated by the requirement to test with 'equivalent process history' samples to the low profile material used in devices, and by the desire to test to large superelastic strains (> 5.5 %) that are likely to be seen in-service. A review of the literature shows that two approaches have generally been taken for uniaxial compression testing of superelastic nitinol.

The first approach is to use large diameter samples to achieve suitable L/d ratio without the requirement for any additional test support structures. This approach clearly compromises on the 'equivalent processing history' requirement, and therefore the results cannot be taken as fully representative for use in implantable medical device design. Details of exemplar test set-ups are given below.

Nemat-Nasser and Guo (4) used ø4.75mm x 5mm superelastic nitinol rod samples for uniaxial compression testing. In order to reduce end friction of the samples during deformation (and therefore minimize barrelling effects), the sample ends were polished prior to final sample heat treatment and then the ends were greased before testing.

Chen et al (19) used ø6.35 mm x 12.7 mm cylindrical samples machined from ø7.94 mm rod stock (the machined smaller diameter is required to keep the compressive loads within the tester's load cell limits). The samples were heat-treated for superelasticity following machining. Strain measurement was performed using both an extensometer and a strain gauge on each sample.

Liu et al (21) used ø6.7mm binary NiTi bar with 10 – 20 mm lengths. They describe using a 'standard method' for compression testing whereby the sample was placed in a cylinder and the compression load was transmitted via a piston. High pressure lubricant was applied to the loading surfaces to reduce friction forces. Deformation strain was measured with an LVDT (linear variable differential transformer).

The second approach to compression testing seen in the literature is to use a larger L/d ratio, but with some form of lateral support to prevent column buckling. This approach then allows smaller diameter samples and / or longer sample lengths to be used. The use of a greater L/d ratio is desirable to reduce the impact of end effects on the compression results. As described by Painting (22), 'barrelled' samples have non-uniform stress and strain distributions towards the ends. Painting explains that, among other consequences, frictional end effects can lead to high values for compressive E results.

Reedlunn et al (18) performed uniaxial compression testing on NiTi tubing with OD 3.176 mm and ID 2.54 mm (Af: 19 C; test temperature 23 C). They used a sample length of 41.59 mm, and held this at either end in the blind hole of a cylinder (hole diameter 3.2 mm, hole length 15.9 mm, cylinder diameter 25.4 mm), leaving a free length of 9.38 mm between these holders. This gives a *free length: diameter* ratio of 2.95:1. Buckling was further prevented by careful alignment of the grips. The contained ends of the specimen were coated with a light oil to facilitate free sliding in the grips. In order to measure strain, a length of the sample in the central free portion was painted with a speckle pattern for DIC measurement (see later *'Experimental Strain Measurement Methods'*

section 2.2.2.7 for more on DIC). This meant that the axial compressive strain in this central portion, away from the ends, could be taken from the averaged full-field strains over the DIC gage length. Using this set-up, they achieved strains of 4 % load and unload without evidence of buckling in the results. With a slightly modified set-up (L=40.83; L_f=7.87; L_f/d=2.48) they tested to 5 % load and unload without evidence of buckling. In terms of accuracy of strain results, Reedlunn compares the DIC strains measured in the free length with the 'grip' strains calculated from the crosshead movement (δ/L) and shows that the grip strain is consistently higher. This shows that there is some error in the grip strain calculation, attributed to 'specimen settling' in the grips. DIC measurement at the free length gives more accurate compressive strain results.

Siddons and Moon (15) used tubing of 3.17 mm OD, 2.50 mm ID, 42 mm long, held in specially adapted pin chucks with flat steel inserts to support the tubing against buckling, leaving a free length of 7 mm in the centre of the tubing. The chucks were tightened so that the flat inserts just contacted the test piece without gripping it. Crosshead movement was used to measure displacement and calculate nominal strain. Their results show maximum nominal strains of 6 % - although these are based on crosshead motion of the grips and therefore may be higher than reality, as seen in Reedlunn's results.

Henderson et al (23) performed compression tests on wire diameters of 1, 1.8 and 2.4 mm, where the wires were sourced to meet equivalent tensile specifications to implantable wire material in the diameter range 0.1 to 0.24 mm. They developed special holders for these samples, as shown in figure 2-14 together with the set-up dimensions in the accompanying table.
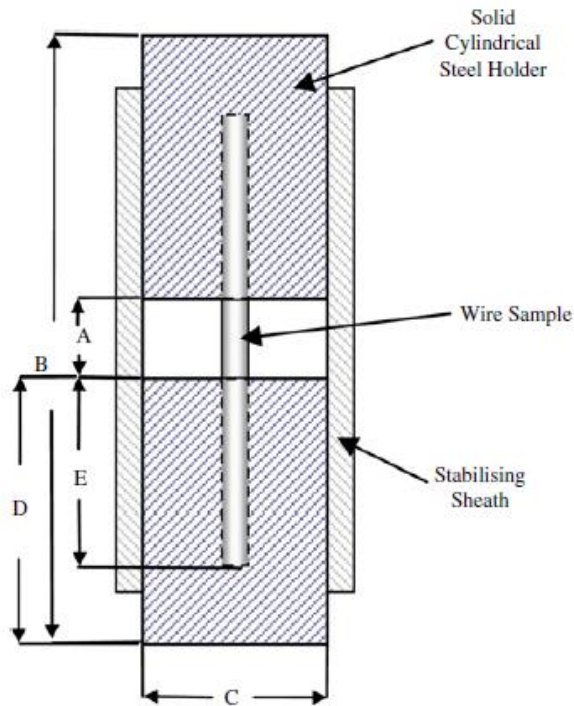
Test rig size (mm)	1	1.8	2.4
A (mm)	1.5	2	2.5
B (mm)	44	60	60
C (mm)	20	20	20
D (mm)	22	33	33
E (mm)	10	18	23

Figure 2-14: Schematic and dimension details for compression test set-up used by Henderson et al (23)

Again, the set-up is designed to use a long specimen length supported against buckling by holders, leaving a short free length in the centre, with L_f/d values of 1.5, 1.11 and 1.04 for the 1, 1.8 and 2.4 mm samples. The diameter of the blind hole in each rig has been designed to allow for some expansion of the wire due to Poisson's effect. Unlike the previous set-ups described, there is also an outer stabilising sheath designed to aid in alignment of the top and bottom support cylinders. With this set-up, Henderson reports results up to 4 % nominal strain (again calculated from crosshead displacement). The maximum strain here was limited by the short free length for compression between grips.

2.2.2.2 Uniaxial Compression Testing: Qualitative Features of Results and Compressive – Tensile Asymmetry

Using results from published research, it is important to understand the qualitative features of superelastic nitinol material in compression, and particularly their differences from tensile test results. While quantitative values differ considerably, the main qualitative features are fairly consistent throughout the literature and are outlined below.

Figure 2-15, taken from ref (18), shows both tensile and compressive results from the uniaxial testing performed by Reedlunn et al.

With reference to the loading behavior seen in figure 2-15, the initial modulus in compression is a straight line up to a strain of approximately 1 %. The initial tensile modulus is initially the same (showing no evidence of R-phase in this region) up to approximately 0.5 % strain, after which the slope reduces. This behavior in tension is also reported by Schaffer and Plumley (5) and is attributed to stress-induced R-phase.

An inflection point in the compression results then shows that the critical stress has been reached for stress-induced martensite. This critical stress is considerably higher than the tensile stress for SIM, which again occurs at around 1 % strain. Austenite to martensite transformation in compression then occurs up to approximately 3.5 %, with a positive slope as stress continues to increase with strain. In contrast, the loading plateau in tension is flatter and longer, extending beyond 6 % strain.

Between 3.5 and 4 % compressive strain, there is another inflection point as the stress begins to increase and then increases linearly with a steep slope (similar to the initial modulus) as strain increases. This shows that deformation is no longer primarily by phase transformation but by martensite elasticity and by plastic slip beyond 4 % compressive strain. Similarly, the tensile stress begins to increase beyond the end of its (longer) plateau, though with a lower modulus.
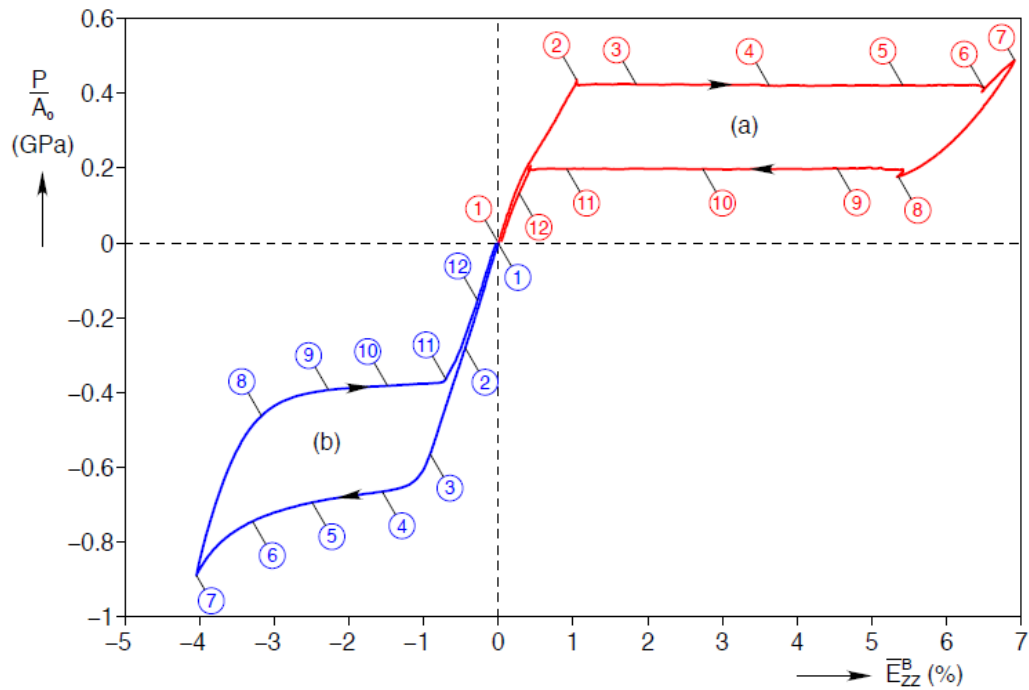
Figure 2-15: Mechanical response of tube specimens during (a) tension experiment and (b) compression experiment, taken from figure 4 of ref (18). The circled numbers correspond to strain field images shown in ref (18), which are not reproduced here.

Considering the unloading behavior seen in figure 2-15, the unload modulus is steeper than the load modulus beyond the end of the plateau, both for compression and tension. This 'linear elastic' unload continues down to about 3.5 % strain in compression, beyond which unloading continues along an unloading plateau as reverse phase transformation (martensite to austenite) occurs at this stress level. This 'plateau' has a slight slope, as stress reduces with decreasing strain – unlike tensile unloading where the unload plateau is flat. For compression, the unloading plateau extends from approximately 3.5 % down to 0.6 %, while the tensile unload plateau is from approximately 5.5 % to 0.6 % strain. Below these strains, unloading is linear elastic for both tension and compression as the material is fully austenite (apart from any plasticity which causes some residual strain).

Reedlunn's results (18) and Henderson's results (23) show both the loading and unloading plateau stresses to be higher in compression than in tension. The tension-compression asymmetry of nitinol is generally attributed to the fact that a different martensite 'variant' will form for a given crystal (grain) within the material during tensile phase transformation than during compressive phase transformation (18). The tensile variant can accommodate larger strains by twin boundary motion (24), with lower stress required to move these twin boundaries than for the compressive variant (15).

Reedlunn's compressive results to both 4 % and 5 % maximum strains show another important feature of nitinol uniaxial stress-strain curves: the effect of plasticity. The sample that has been strained to 5 % strain, and therefore has experienced some plastic deformation, unloads along a lower stress plateau than the sample strained to 4 % maximum – as seen in the blue curves of figure 2-16.

This behavior can also be seen in the work of Chen et al (19) where they loaded a single sample to increasingly large maximum compressive strains and then unloaded. At the lower maximum strains, within the SIM mode of deformation, the material unloads along a similar stress plateau each time. Once larger maximum strains are reached, beyond the SIM plateau, the material unloads along a lower plateau. This same behavior is well known for uniaxial tensile testing of superelastic nitinol, and can be clearly seen in the results of Rebelo et al (25) – as shown in figure 2-17.

Another important finding from Reedlunn's work using a full-field strain measurement technique (DIC) is that it shows compressive strain fields to be nearly homogenous during uniaxial loading and unloading. This is very different from full-field strain results for uniaxial tensile testing, where strain localization is seen as transformation fronts propagate through the material during loading, and then the process is essentially reversed during unloading.
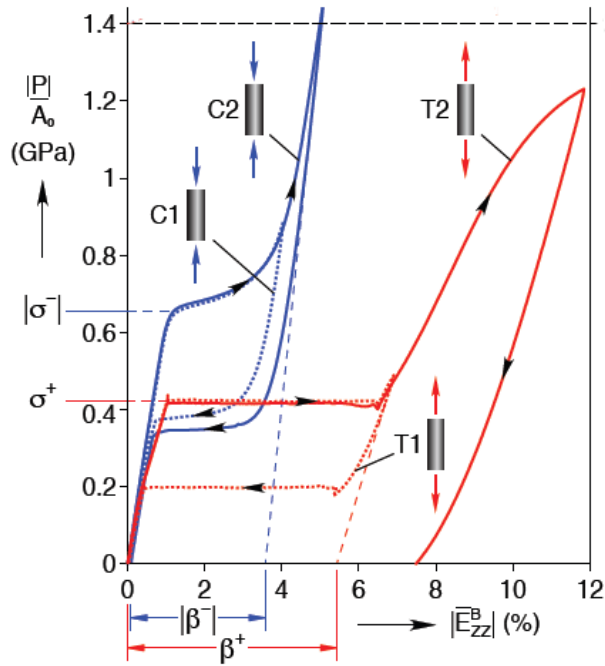
Figure 2-16: Blue stress-strain curves show the different unloading paths taken for NiTi tube loaded to 4 % (C1) and 5 % (C2) maximum compressive strains, as tested by Reedlunn et al. Tension curves (red) are also included but not discussed here. From ref (18), figure 8.
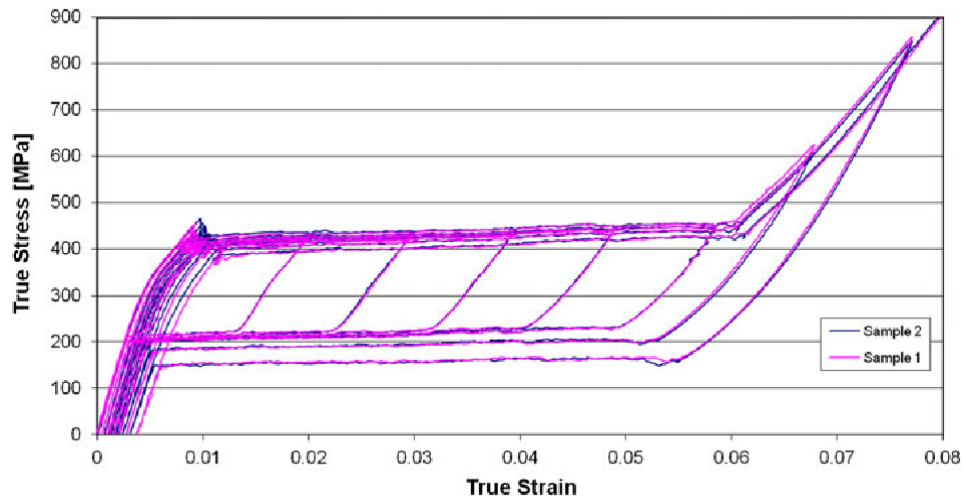
Figure 2-17: Preload effects on NiTi tubing material in uniaxial tension as tested by Rebelo et al, taken from figure 2 of ref (25).

Reedlunn explains that the tensile 'localization' behavior is caused by grains in the material being aligned such that phase transformation in one grain (from austenite to martensite structure or vice versa) will apply stress to neighboring grains sufficient to cause their transformation, leading to a macroscopic front. For compression, however, the grain alignments mean that transformation is less likely to spread to neighboring grains without large stress increase – meaning that transformation is more diffuse throughout the material and strain increases more homogenously as stress increases.

2.2.2.3 Strain Localization of Nitinol in Uniaxial Tension

On the topic of strain localization of nitinol in uniaxial tension, it is useful to consider the results presented by Shaw and Kyriakides (3). A schematic of the test set-up and results graphs are reproduced in figure 2-18.

For this experiment, Shaw and Kyriakides used 1.017 mm binary nitinol wire with a length of 63.5 mm between the grips. The four local extensometers each had a gauge length of 2.5 mm and were spaced 12.5 mm apart. Each thermocouple was attached to the wire within the gauge length of an extensometer.

Of particular interest from these results are the 'strain history' plots in fig 2-18(b), showing local strain (primary vertical axis) against 'global strain' calculated from grip displacement (horizontal axis). In order to study the local strain history behavior, the curve (b) at location 4 from figure 2-18 is reproduced in figure 2-19 with the distinct regions numbered.
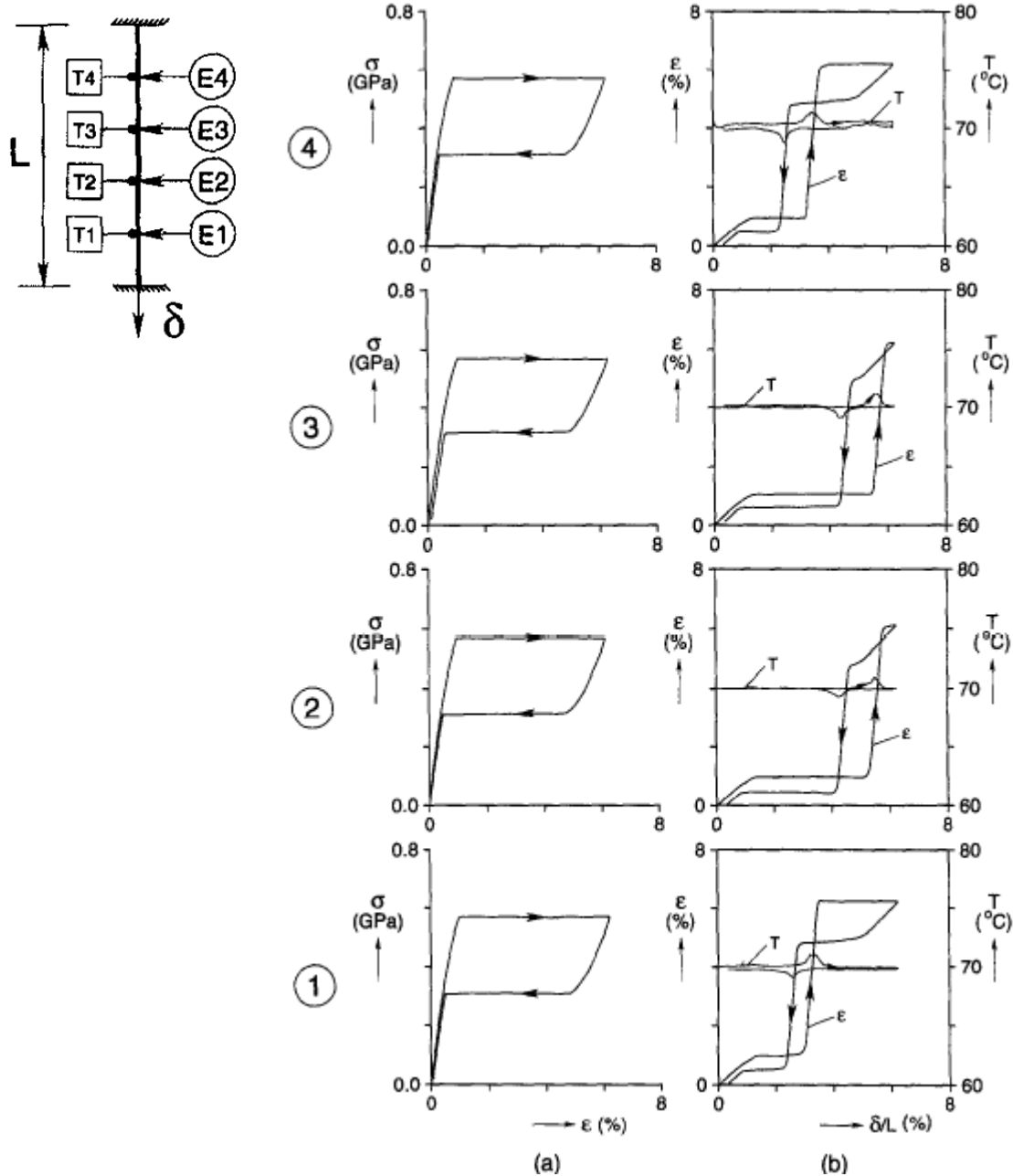
Figure 2-18: Reproduced from figure 10 of ref (3). Left: schematic of tensile test set-up for 1.017 mm nitinol wire in uniaxial tension, with 4 local extensometers and 4 thermocouples along the axial length. Right: results show (a) local stress-strain response at the 4 axial positions; (b) corresponding strain and temperature histories.
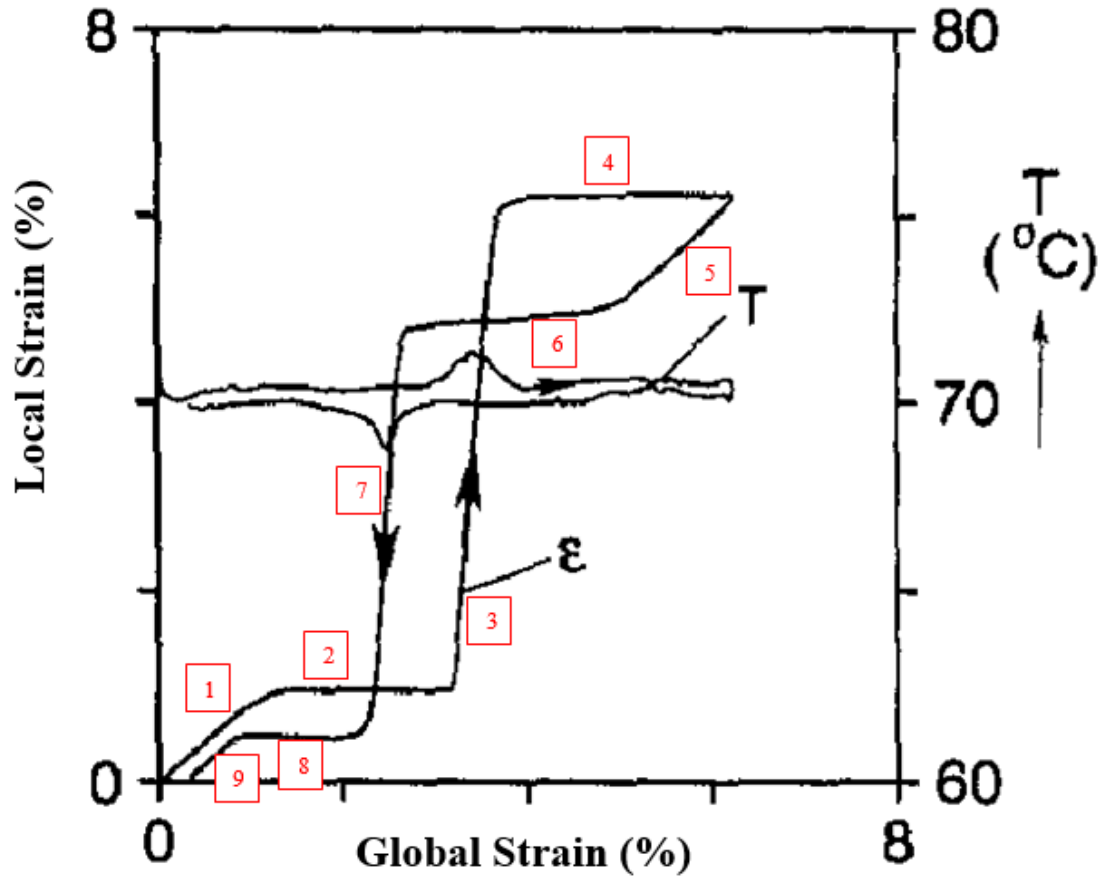
Figure 2-19: curve (b) location 4 from figure 2-18, with distinct regions of 'local strain vs global strain' curve numbered

With reference to figures 2-18 and 2-19, the local strain history behavior is described below, in the order in which it occurs.

In loading:

1) Initial linear increase in strain with global wire length increase, strain uniform along the wire – due to austenite elasticity

2) Local strain remains constant despite overall wire length increase. This is because global strain is increasing due to propagating transformation front(s) that nucleated elsewhere and have not yet reached this axial location

3) Local strain rapidly increases at this particular axial location as the transformation front passes through. The local material transforms from austenite to martensite structure and increases its strain disproportionately to the global strain of the wire

4) Local strain remains constant as the material has fully transformed to martensite in this axial position, while global strain increase is occurring by the transformation front(s) continuing to move along the wire.

In unloading:

5) Initial linear decrease in strain with global wire length decrease, uniform along the wire – due to martensite (and any remaining austenite) elasticity

6) The transformation front acts in reverse, meaning local strain remains constant at a given location until the front passes through.

7) As the front passes through, the local strain rapidly decreases as the material transforms from martensite to austenite. The material exhibits 'localization memory', whereby the last position to transform during loading will be the first to reverse-transform during unloading. Note that the reverse-transform occurs at a lower global strain than the loading transform, due to the effect of linear elastic martensite unloading on the global strain.

8) Following reverse transformation, the local strain remains constant until all material along the wire length has transformed back to the austenite parent phase, at which point the wire unloads uniformly with austenite linear elasticity (9).

These results show that, for nitinol in uniaxial tension, the method of strain measurement must be carefully considered for the required investigation. While cross-head displacement may give an 'average' (global) tensile strain of 5 % for the wire, the actual strains along the length of the wire may vary considerably from 1.5 % in some locations up to > 7 % at others due to the presence of local transformation fronts.

2.2.2.4 Bend Testing: Linear Elastic Beam Bending Theory

Review of the literature shows that there are a few key modes of bending commonly used for material characterization. In order to understand the key features of these bending modes, it is useful to consider beam bending theory for linear elastic materials before considering the more complicated case of Nitinol in bending. The basic features of these bending modes for linear elastic materials are outlined below. For useful beam bending descriptions and calculators, see refs (26) and (27).

Cantilever Bending
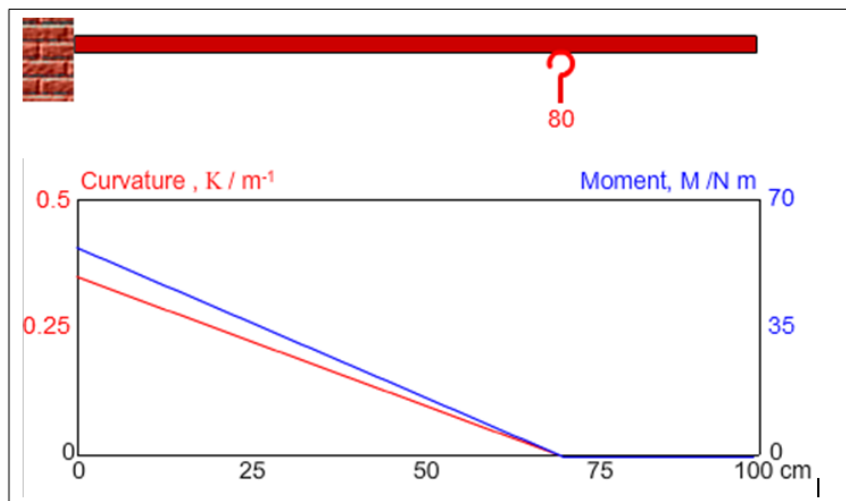
Figure 2-20: Cantilever beam bending example, showing moment and curvature distribution, taken from ref (26)

With reference to the example in figure 2-20 (taken from ref (26)), for a cantilever beam with a point load applied a distance 'X' from its free end, the moment M (in Nm) and curvature K (in m^{-1}) are 0 from the beam's free end up to X, and then increase linearly to maximum values at the fixed cantilever end.

3-Point Bending

For a simply supported beam with a centrally applied point load (i.e. symmetrical 3-point bending), the moment M and curvature K increase linearly from 0 at each support to maximum values at the centre load point (see example in figure 2-21, taken from ref (26)).
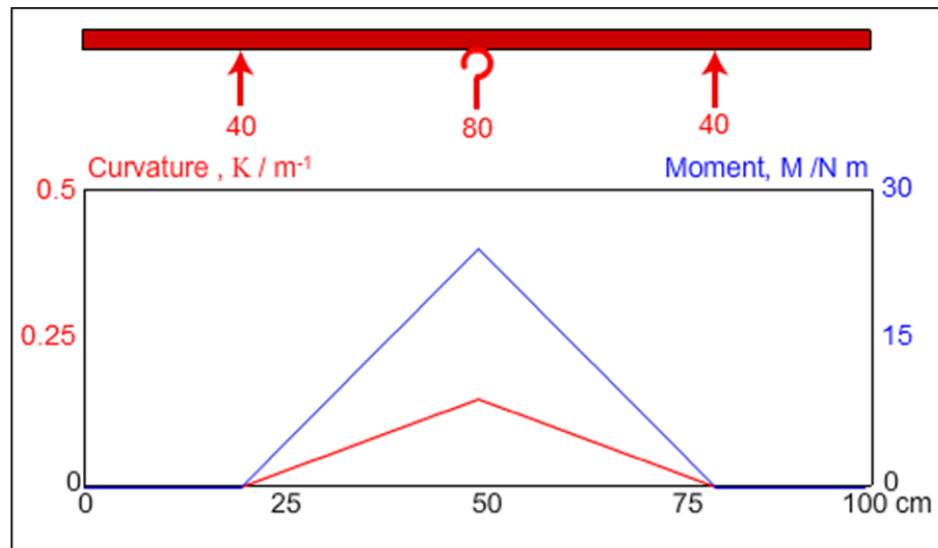
Figure 2-21: symmetrical 3-point bend example, showing moment and curvature distribution, taken from ref (26)

4-Point Bending

For a simply supported beam with 2 applied point loads equidistant from the centre (i.e. symmetrical 4-point bending), the moment M and curvature K increase linearly from 0 at each support to maximum values at each loading point, with moment M and curvature K constant at these maximum values between the loading points (see example in figure 2-22, taken from ref (26)). Due to the constant moment between the central pins of a beam in 4-point bending, the beam is in 'pure bending'. There is no shear force V (= $\delta M/\delta x$) between the central pins, the transverse planes are perpendicular to the axial direction of the bending beam and the maximum principal stresses and strains are in the axial direction.
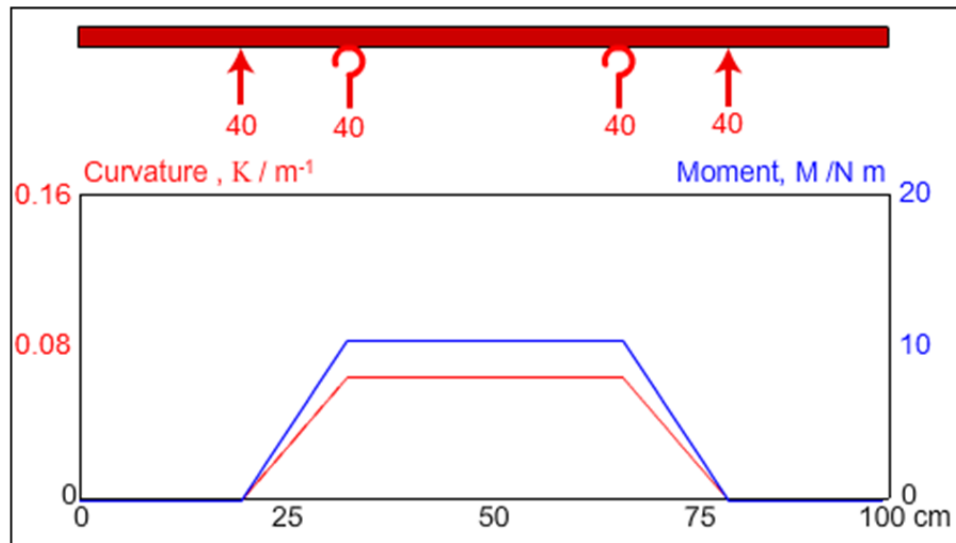
Figure 2-22: symmetrical 4-point bend example, showing moment and curvature distribution, taken from ref (26)

2.2.2.5 Experimental Bend Testing of Superelastic Nitinol

Reedlunn et al (18) performed 4-point bend testing at 23 C on superelastic Nitinol tubing (OD: 3.176 mm; ID: 2.54 mm) with Af temperature = 19 C. A custom 4-point bend fixture was used to apply a pure moment during bending (with no axial or shear loads) – allowing bending with a controlled radius of curvature along the measured length of the sample. Stereo Digital Image Correlation (DIC) was used for surface strain measurement. Their results show a number of interesting behaviours for nitinol in bending.

Firstly, they show results for 'normalised moment' vs 'dimensionless curvature' – see lower plot of figure 2-23. Details of how the applied moment 'M' value was calculated from measurement of applied load and rig geometry, as well as how the average curvature 'k' for the gage length was derived from measurements of cross-section rotation, are given in Ref (18). For the purposes of this literature review, it is the qualitative bending behavior shown by their moment-curvature results plot that is of

primary interest, giving a useful representation of bending stiffness. With reference to the lower plot of figure 2-23, during loading (increasing curvature) the applied moment increases linearly, then plateaus during a large curvature increase, and then increases again beyond the plateau. On unloading (decreasing curvature), there is hysteresis as the bending moment decreases linearly to a lower plateau, where the curvature reduces with almost no moment decrease, before a final linear decrease in applied moment as the tube straightens. Thus, the moment-curvature response for 4-point bending exhibits the same 'flag' shape as superelastic nitinol's uniaxial stress-strain response for loading and unloading.

Secondly, they plot neutral axis position (location relative to cross-section diameter where local axial strain is 0) against bend curvature – see upper red plot of figure 2-23, where Y_0 is cross-sectional distance from centre line toward intrados. The results clearly show the tensile-compressive asymmetry of nitinol, as the neutral axis is positioned nearer to the intrados than the extrados throughout bending, both during loading and unloading. As will be explained further in chapter 5 of this thesis, this neutral axis eccentricity allows equilibrium between the compressive forces on one side and the tensile forces on the other, and shows that the compressive stress is higher than the tensile stress for nitinol at a given strain magnitude.

The neutral axis position vs curvature plot is also interesting as it shows increasing tensile-compressive asymmetry up to the curvature where the applied moment plateau ends, at which point the neutral axis remains in the same position with further bending. On unloading, the neutral axis position (and t-c asymmetry) remains the same until a fairly low curvature, at which point it returns back towards the centre.
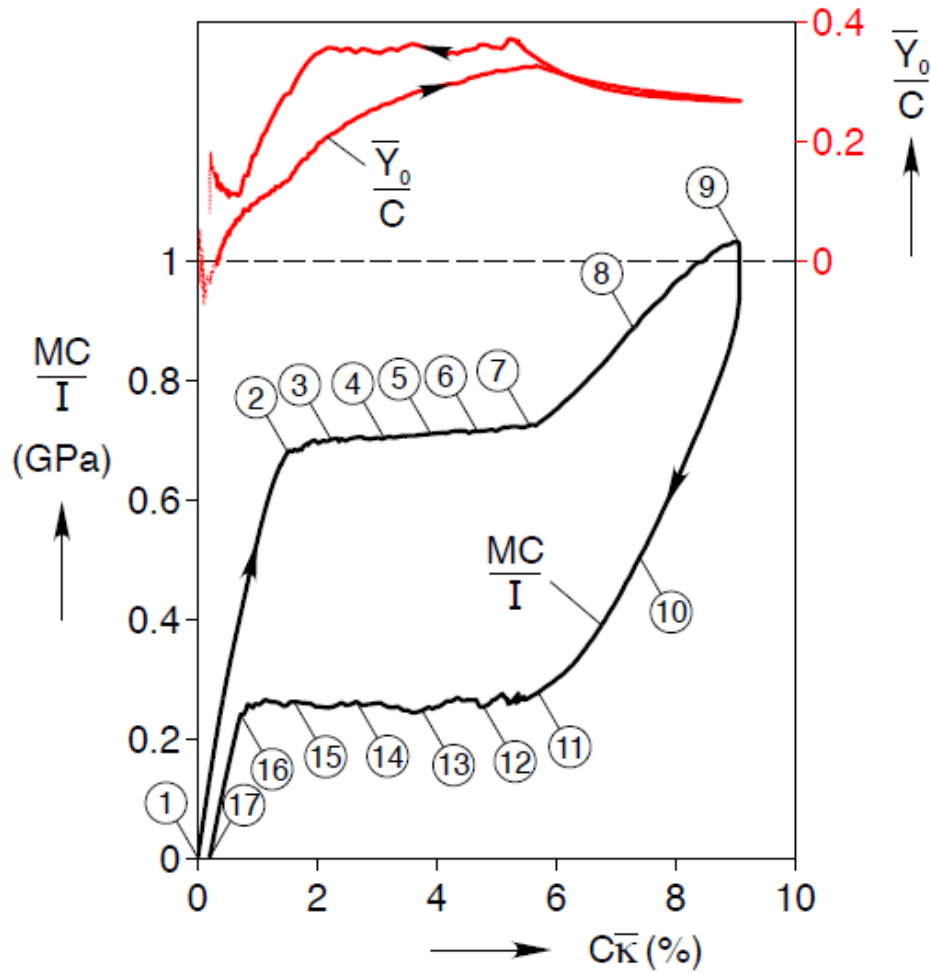
Figure 2-23: Lower plot: 'Normalised Moment' (related to outer fiber stress) vs 'dimensionless curvature' (related to outer fiber strain) plot for a single 4-point bend load-unload cycle of Nitinol tubing, taken from figure 10 of ref (18). 'M' is applied moment, 'C' is cross-sectional outer radius (= OD/2), I is area moment of inertia of cross- section and k is average curvature of gage length. The circled numbers correspond to strain field images shown in ref (18), which are not reproduced here. Upper Plot: Neutral axis position vs. dimensionless curvature.

One of the most interesting findings from the work of Reedlunn et al is the observation of strain localization in bending. They found that during bending with an applied 'pure moment', the compressive side had no evidence of localization, showing homogenous

strain for all curvatures in loading and unloading. On this side, the local DIC strain results for cross-sections fitted closely to the linear cross-sectional strain predicted by beam bending theory for the corresponding bend curvature. However, on the tensile side there was evidence of localization as high strain regions initiated at certain locations on the extrados and propagated diagonally ('wedge localizations') across the tube as bend curvature was increased. This produced local strains that do not match beam theory predictions, with non-linear cross-sectional strain plots showing that plane sections do not remain plane. It is important to note, however, that this only occurs at 'intermediate' curvatures, where beam theory predicts maximum strain levels in the 'transformation strain' region. At greater curvatures, where beam theory predicts maximum tensile strains exceeding phase transformation levels ($\geq$ 7%), the measured cross-sectional strains match the theory well and the plane sections are approximately planar. Also, they show that when the measured strain is averaged over a few diameters of length (as opposed to being taken at a single cross-section position), there is good agreement with beam theory strain calculation. The conclusion of their study on localization is that care must be taken when using beam theory to predict strains for superelastic nitinol in bending, as the averaged bending strains may under- or over-predict local strains by up to a factor of two.

When considering the application of these 'localization in bending' findings, it is important to remember that Reedlunn et al were using a 'pure bending' 4 Point Bend experimental set-up to impose a constant bend radius to the specimen along its measured length. With this set-up, the critical stress for transformation nucleation could occur at any point on the outer bend surface, depending on the particular alignment of crystal grains in the microstructure, and then propagate to neighboring grains that are not necessarily on the extrados – giving local strain results that do not match beam theory predictions. However, for other beam bending set-ups such as 3 Point Bending or cantilever bending, as well as many situations experienced in service, the beam will not be in pure bending but will have an 'apex' region where the applied moment /curvature

is at a maximum. In this case, the local applied moments would control the location of transformation nucleation (at the bend apex).

It should also be remembered that the bend testing by Reedlunn et al was performed on tubes of relatively large diameter, meaning that large tensile 'transformation' strains are reached with a fairly low cross-sectional strain gradient. For thin nitinol wires, however, there will be a much higher strain gradient across the cross section from compressive to tensile strains, meaning that transformation propagation / strain evolution with bending is more likely to be controlled by bend geometry than by local grain orientation.

Further to their investigation of beam-theory application for predicting local strains of nitinol in bending, Reedlunn et al investigated the effectiveness of beam theory for predicting global bending response and average neutral axis position during loading. They showed that using Euler-Bernoulli beam theory with an asymmetric material model (based on the uniaxial compression and tensile data) gave a good match to their experimental results for global bending during loading. They did not attempt to calculate the unloading responses using beam theory, as the path-dependent behavior in unloading involves far greater complexity.

Pelton et al (28) performed both 3- and 4- Point Bending experiments on nitinol wires, although they only report 3-Point Bend results for a ø1.5 mm wire with 20 mm span between supports. They imposed deflections up to 3.5 mm at the centre point, with LVDT deflection measurement. The resulting Load – Deflection curve, shown in figure 2-24 below, exhibits a 'superelastic flag' shape, with load-unload hysteresis involving upper and lower 'plateaus' (note, though, that these 'plateaus' are not flat). In order to investigate strains of tubes in bending, they used their 3-Point Bending L-D results to validate an asymmetrical nitinol constitutive model, which was then used in FEA analysis to simulate bending behavior and investigate strains.
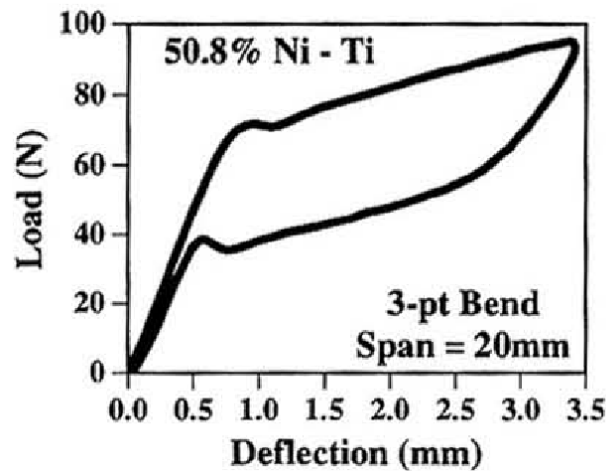
Figure 2-24: Load-Deflection curve of 1.5 mm wire in 3-point bending, taken from figure 1 of ref (28).

De La Flor et al (29) performed experimental cantilever bend testing on ø1 mm Nitinol wire, 60 mm long, using custom designed bending accessories for a Zwick 1445 Tensile Test Machine. Their results for load-deflection at different temperatures again show the stiff-compliant-stiff behavior during loading, involving a 'loading plateau' region. They do not present results for unloading. Similar to Reedlunn et al (18), they show that an asymmetrical constitutive model with different tensile and compressive properties can give a good prediction of the load-deflection response during bend loading.

Considering the experimental set-up for Nitinol in bending, ISO 15841 (30) is followed by a number of manufacturers as a method for 3-Point Bend testing of superelastic wires. The standard, designed to allow clinicians to make meaningful comparisons between wires used in orthodontics, describes the set-up and method for bend testing of 'type 2' wires, defined as 'wires not displaying linear elastic behavior during unloading at temperatures up to 50 C' – in other words, superelastic wires. (Note: wire diameter is not specified in the standard, but orthodontic arch wires are typically 0.3 – 0.55 mm in diameter). Details of the test method are summarized below:

Set-up:

- Symmetrical 3 Point Bend testing shall be used, with deflection by a centrally-placed indenter

- Span between supports = 10 mm

- Specimen length = 30 mm

- Radii of fulcrum and indenter = 0.10 ± 0.05 mm

- Cross-head rate (for deflection) = 7.5 ± 2.5 mm/min

- Test temperature = 36 ± 1 C

Procedure:

- Deflect wire to 3.1 mm (indenter displacement) then unload

- From Force − Deflection diagram, record force magnitudes during unloading at 3.0, 2.0, 1.0, 0.5 mm and permanent set after unloading.

Although aimed at the particular application of orthodontic wires, this standard offers useful general guidance for set-up of experimental bend tests to characterize thin superelastic nitinol wire.

2.2.2.6 Load Path History Effects in Bending

During its lifecycle, the nitinol wire in an endovascular stent component is compacted into a sheath by loading to a small bend radius, and is later deployed at an intended implant site by unloading to a larger bend radius. Once deployed, it may additionally be repositioned by further loading and unloading bending cycles. Thus, the bending nitinol material will be subjected to a particular loading and unloading history before reaching its final 'deployed' state in a blood vessel. It is therefore important to consider the effects of load path history on Nitinol's mechanical response in bending. The following sections will focus on 2 particular aspects:

- Load path history effects on force exerted during unloading

- Load path history effects on strain state during unloading

Load Path History Effects on Force Exerted during Unloading for Nitinol in Bending

Due to the stress hysteresis of nitinol's superelastic behavior, it is obvious that the material in bending will exert a greater force during loading than unloading for a given bend curvature. This basic load-path history effect is shown by the 4-Point Bend moment hysteresis curves presented by Reedlunn et al (18) and the 3-Point Bend Load-deflection curves by Pelton et al (28) – see figures 2-23 and 2-24 above for examples.

Less obvious are the path-dependent effects of plasticity on unloading of nitinol. The previously mentioned authors Rebelo et al (25) and Chen et al (19) have investigated path-dependent unloading effects on nitinol in uniaxial tension and compression. Their results show that the material will unload along the same lower stress plateau provided its maximum strain is within the upper stress plateau range (generally < 7 % in tension, < 4 % in compression). However, for increasingly large maximum strains beyond the upper plateau range, the material will unload along lower stress plateaus and exhibit greater permanent set.

Duerig et al (31) demonstrate the load-path history effect on unloading modulus for superelastic nitinol material in uniaxial tension. For superelastic wire tested at 40 C, they show that for maximum strains between 2 % and 8 %, the unloading modulus decreases with increased maximum strain – see figure 2-25. As a basic explanation, this reduction in unloading modulus with increasing transformation strain is attributed to the increasing volume fraction of martensite in the wire, with martensite having a lower effective modulus than austenite. Interestingly, unloading from beyond 8 % strain up to 12 %, there is an increase in the unloading modulus – a trend that they say is reproducible at all superelastic temperatures. The detailed investigation of these phenomena is beyond the scope of this review, and it is sufficient to note the general behavior of Nitinol in terms of its path-dependent unloading modulus.
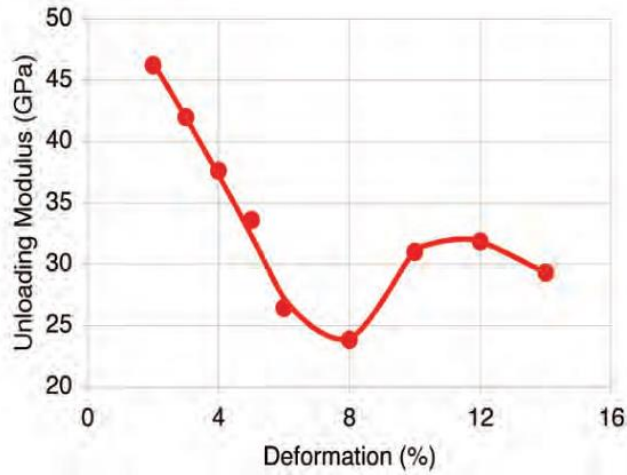
*Figure 2-25: Unloading modulus as a function of strain for superelastic NiTi wire –
taken from figure 5-2 in ref (31)*
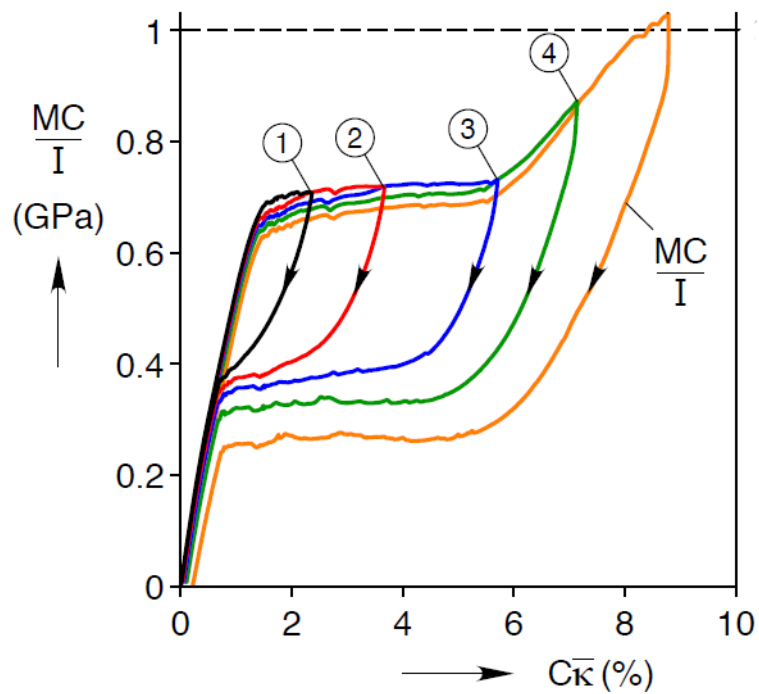
*Figure 2-26: 'Normalised Moment' versus 'dimensionless curvature' for incremental 4-
point bend load-unload cycling of Nitinol tubing, taken from figure 16 of ref (18). The
circled numbers correspond to strain field images shown in ref (18), which are not
reproduced here.*

For stent components, it is the path-dependent unloading behavior *in bending* that is of primary interest. Reedlunn et al (18) used their 4-Point Bend set-up to perform 5 cycles of loading and unloading on a tube sample, with increasing maximum curvature for each cycle. Their results are reproduced in figure 2-26.

In terms of path-dependent effects on unloading, the moment-curvature results of figure 2-26 show the following important features:

- Where unloading begins from within the upper plateau region, increasing maximum curvature leads to slightly decreased unloading plateau values.
- Where unloading starts from beyond the upper loading plateau, increasing maximum curvature leads to more dramatic reduction in the unloading plateau.

These findings are attributed to increasing levels of plasticity within the bending material's outer and inner fibers following larger maximum curvatures. The results are important as they suggest that the level of bend curvature experienced during compaction of a nitinol stent component may affect the subsequent force exerted by the component during unloading, thereby influencing the Chronic Outward Force exerted on the blood vessel for sealing, migration resistance and damping.

On the topic of plasticity effects, it is also important to note that the load history of nitinol components in bending can have a significant effect on fatigue resistance. Gupta (32) reports a collaborative project involving the FDA (Food and Drug administration) to look at the effects of pre-strain on fatigue life of nitinol wire. Here, Rotary Bend Fatigue testing was performed on 0.5 mm diameter wires following bending round mandrels to give 8 % or 10 % bending pre-strains. They also heated the strained samples to 60 C to simulate sterilization. Their results showed that the pre-conditioning of the material resulted in reduced rotary bend fatigue life, with most fatigue failures initiating at the compressive pre-strained surface. When assessing these results, it is important to consider the loading that the material was subjected to. The pre-conditioning step subjected the material at the intrados to compressive strains beyond the SIM plateau

limit, considered by Gupta et al to be damaging to the material. The rotary bend testing then subjected this 'damaged' material to alternating tensile and compressive loading, with the cyclic tensile loads enabling crack growth from any defects on the compressive pre-strain surface. This testing therefore shows that a high compressive pre-strain followed by cyclic tensile loading is detrimental to fatigue life. In terms of application to stent graft devices, this kind of loading could be relevant to the hook components of Vascutek's Anaconda device. For stent components, the compressive pre-strain material will undergo compressive-compressive in-vivo loading and therefore the results from ref 32 cannot be applied. Nevertheless, the conclusion from the Ref (32) study is important, not least due to the direct involvement of the FDA in this work:

"The present study underscores the importance of accounting for mechanical history in the design of implants, particularly as ever smaller catheters are adopted for device delivery."

Load Path History Effects on Strain State during Unloading for Nitinol in Bending

Van Zyl et al (33) used Finite Element Analysis simulation of a nitinol beam in cantilever bending to investigate the load history dependency of final strain state for a given bend deflection. They used a rectangular beam model (60w x 40t x 400l (in mm)) with the asymmetric Shape Memory Alloy (SMA) model available in Ansys Finite Element Analysis (FEA) software. One end of the beam was fixed, and a vertical line displacement was applied to the other end to load it in the following way:

- Initial load displacement of 30 mm
- Additional load displacement to a maximum displacement in the range 37.5 to 52.5 mm
- Unload to 30 mm displacement

Stress (maximum first principle stress) and strain (total mechanical strain) measurements were taken for a single element at the root location of the beam, outer fiber position. The graph in figure 2-27, taken from ref (33), shows the key results from this study. This graph shows that the 'maximum tensile strain' element has a higher strain for a given

beam end displacement following a larger maximum displacement in the load-unload history. As the final beam end displacement is the same in each case (30 mm), this suggests that the beam is taking a different shape depending on the loading history.
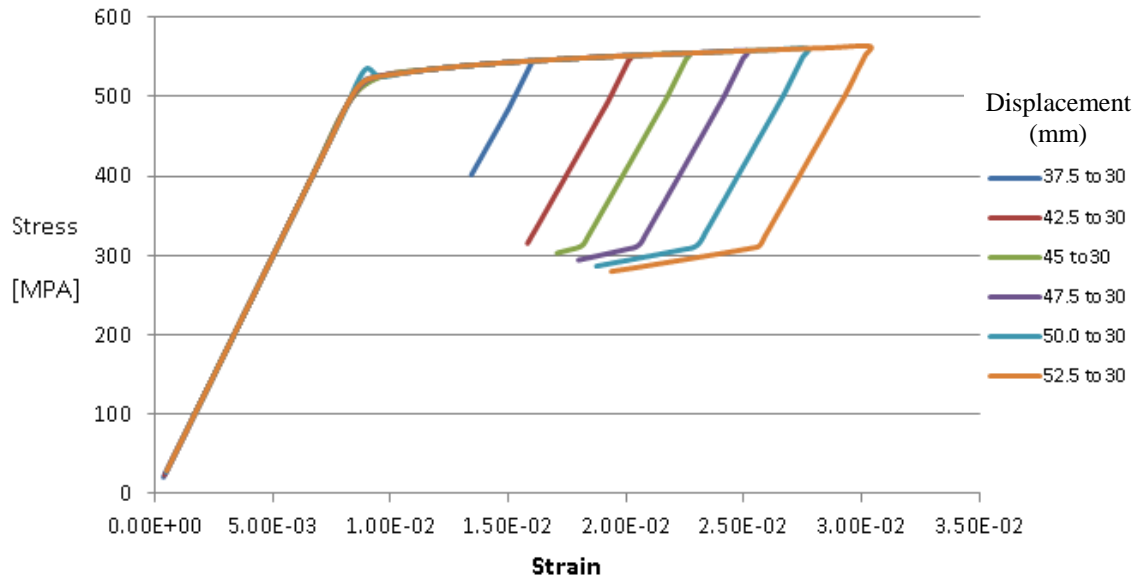
Figure 2-27: stress-strain measurements for root location, outer fiber of simulated NiTi cantilever beam in bending, to investigate final strain as a result of load history (from ref 33).

Van Zyl considered the underlying constitutive model used for the Ansys SMA material to propose an explanation for the load history dependence of strain. However, no experimental work was carried out to validate the FE analysis. Indeed, a review of the literature on nitinol structures in bending has yielded no experimental investigation of this particular phenomenon. It is therefore an objective of the present work to experimentally investigate the load path history effects on unloading strain state for nitinol beams in bending.

2.2.2.7 Experimental Strain Measurement Methods for Nitinol in Bending

In order to experimentally investigate the strain of nitinol material in bending, it is necessary to identify a suitable method of strain measurement. The available methods are highly dependent on the geometry of the structure to be measured. As it is a central objective of the present work to characterize 'equivalent' material to that used in-service for nitinol stent components, it is desirable to find a method capable of measuring axial strains for wire in the diameter range 0.1 to 1 mm. Additionally, the method should be capable of measuring recoverable axial strains from 0 to 10 %. With such a challenging specification, initial enquiries revealed that traditional strain gauge measurement methods would not be feasible. Even if a small enough gauge with large recoverable strain range could be found, the information gained would be limited to very few strain locations. Therefore, a review of more contemporary strain measurement methods was conducted.

Three potential methods were found that have previously been used for strain measurement of Nitinol to superelastic strains:

- Digital Image Correlation (Ref 34)
- Moire Interferometry (Ref 11)
- X-Ray Diffraction (Ref 6)

Consideration of cost, equipment availability, ease of use and ease of results interpretation showed that Digital Image Correlation (34) was the most feasible method for the present investigation.

Digital Image Correlation (DIC)

Reedlunn et al (34) give an in-depth explanation of the DIC technique, which uses image-matching algorithms to track the local displacements of random speckle patterns on the surface of a sample during deformation. These surface displacements can then be used to calculate local surface strains, and to measure the full-field strain of the surface at a given deformation. In this way, DIC is a non-contact method that uses digital images

of a sample at different deformations to calculate strains. While some material samples may have a naturally occurring random surface pattern that can be used for DIC, others may require surface preparation. Reedlunn describes using an airbrush paint method suitable for surface preparation of thin nitinol wires.

In ref (34), Reedlunn et al describe using 3D DIC to measure the surface strains of ø 0.762 mm superelastic nitinol wire during cyclic uniaxial tensile loading and unloading. 3D DIC uses 2 CCD (Charge Coupled Device) cameras and additional calibration and image correlation techniques to calculate the specimen surface profile and the strain distributions thereon. The method allowed them to study the strain localization and cyclic behavior of nitinol in considerable detail. They also performed validation of the method, using a laser extensometer for global strain measurement of the sample to show good agreement with the averaged DIC results.

While Reedlunn's work shows the feasibility of DIC for strain measurement on thin wires (34) and, separately, its usefulness for studying superelastic strains in bending (18), no examples of DIC application to thin wires (< 1 mm) in bending were found in the published literature. DIC was therefore identified as an interesting and novel approach for characterization of Vascutek's stent wire. Chapter 5 of this thesis gives details of the microscopic 3D DIC approach used for experimental study of ø 0.45 mm superelastic wire in bending.

2.2.2.8 Stress-strain response of Superelastic Nitinol in cycling

As shown by the 'Product Life Cycle' (table 2-2) in the 'Background' section 2.1.3 of this chapter, the Nitinol material will experience a high degree of cyclic loading in its application to endovascular stent components. It is therefore important to review the available literature on Nitinol's mechanical response to cycling.

Siddons and Moon (15), Henderson et al (23) and Reedlunn et al (34) have all investigated the effects of 'full superelastic' cycling of nitinol (with loading to the end of the transformation plateau and fully unloading for each cycle). They show major changes in the stress-strain response from the 1st cycle ('virgin material') to the 25th cycle and beyond, with eventual stable response at higher cycle numbers. In particular, this 'large strain' cycling results in decreasing loading plateaus, a smaller hysteresis loop between loading and unloading and a large amount of permanent set, for both tensile and compressive uniaxial cycling.

However, superelastic Nitinol material does not undergo this level of 'large strain', high cycle loading in service for stent components. For the stent rings of the Anaconda device, there will be a maximum of 3 compaction-deployment cycles, meaning a maximum of 3 'large strain' cycles. For this small number of cycles, there is still some reduction in the upper plateau and a small amount of permanent set (ref 34), but the changes are small compared to the high cycle number effects, and there is no observed change to the unloading plateau. This can be seen in figure 2-28, reproduced from Reedlunn (34).

Considering the in-service behavior of nitinol for stent components (Table 2-2), the 'intermediate strain' $\Delta\varepsilon$ cycles experienced during collapse-reposition-open of the device are likely to be small in number (≤ 3). For stents under pulsatile deformations, it is the 'small $\Delta\varepsilon$' cycling behavior ($\Delta\varepsilon < 1\%$) that will have the greatest bearing on long-term performance, including fatigue resistance. Therefore, the focus of this literature review is on the small $\Delta\varepsilon$ response at representative 'in-vivo' mean strains.
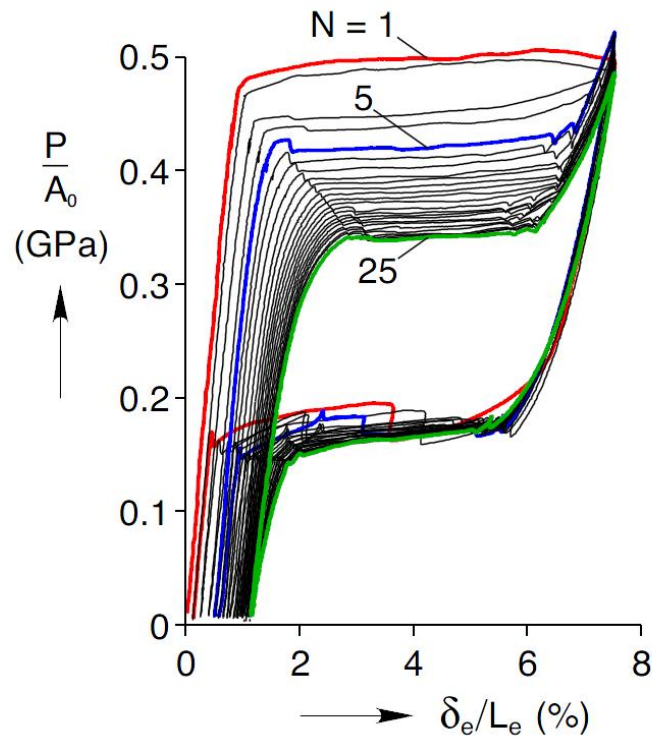
Figure 2-28: mechanical response of superelastic wire to 25 uniaxial tensile load-unload cycles in room temperature air (22C), taken from figure 7 of ref (34).

Pelton (7) performed uniaxial tensile testing on tensile samples machined from superelastic wire with 3 mm diameter gage. The samples were processed in two different ways prior to testing:

- 'annealed' samples were heat treated at 900 C for 30 minutes, giving final Af of -15 C
- 'stress-relieved' samples were heat treated at 500 C for 10 minutes, giving final Af of 20 C (typical of stent material processing)

Room Temperature tensile testing was then performed on the different samples, with loading to 1.5 % mean strain and then cycling with $\Delta\varepsilon = 0.5$ % peak-to-peak (1.25 to 1.75 % ε) for 100 cycles. During testing, Transmission Electron Microscopy (TEM) was used to investigate the material microstructure. For the annealed material, where the microstructure is initially amorphous, the stress-strain results show that the cycling

modulus (and therefore $\Delta\sigma$) increases while the hysteresis decreases with cycling. The TEM explains this, showing that the microstructure consists of a high density of dislocations which show increasing 'work-hardening' with cycling. For the stress-relieved material, where microstructure consists of small grains of approximately 75nm width, the cyclic stress-strain curves show minimal hysteresis and no change in modulus during cycling, although there is a drop in the stress levels from 1st cycle down to a stable level after 5 cycles. (Note, though, that this cycling occurred from the upper plateau, which tends to show this 'softening' behavior when the $\Delta\epsilon$ level is large enough). The TEM investigation after cycling showed no change in the microstructure for this material. The conclusion from this work was that thermal processing is important to the cyclic behavior and therefore the fatigue behavior of superelastic Nitinol, with optimized thermo-mechanically treated microstructures giving stable and predictable cyclic behavior for small $\Delta\epsilon$s.

This has positive implications for characterization of Vascutek's Nitinol material, as the wire used for Anaconda stent components is of the 'stress-relieved, nano grain size' microstructure type (9) shown by Pelton's TEM images (7). This means that the wire's long-term, small $\Delta\epsilon$ cyclic behavior will be stable and can therefore be reliably characterized from testing to a small number of cycles.

Rebelo et al (35) investigated the effects of cyclic loading on superelastic nitinol tubing in uniaxial tension. They used 3.125 mm OD x 2.15 mm ID tubing, length 130 mm, heat treated to give active Af temp of 27 C, and performed testing at 37 C in air with strain rate of 10^{-3} s^{-1} and with 25 mm gage length extensometer for strain measurement and control. For each mean and delta strain level, tests were performed with cycling both 'from above' – with direct loading to the mean strain followed by 100 $\Delta\epsilon$ cycles – and 'from below' – with loading to 6 % strain, unloading to the mean strain and then 100 $\Delta\epsilon$ cycles. Table 2-6 below summarizes the tests performed. Figure 2-29 then shows the 'set 3' results from ref (35).

		Mean Ɛ	ΔƐ (peak to peak)
Set 1	From above	2 %	1 %
	From below	2 %	1 %
Set 2	From above	2 %	1.6 %
	From below	2 %	1.6 %
Set 3	From above	3 %	1.2 %
	From below	3 %	1.2 %
Set 4	From above	4 %	1.6 %
	From below	4 %	1.6 %

Table 2-6: Test sets performed by Rebelo et al (35) to investigate cycling effects on nitinol in uniaxial tension
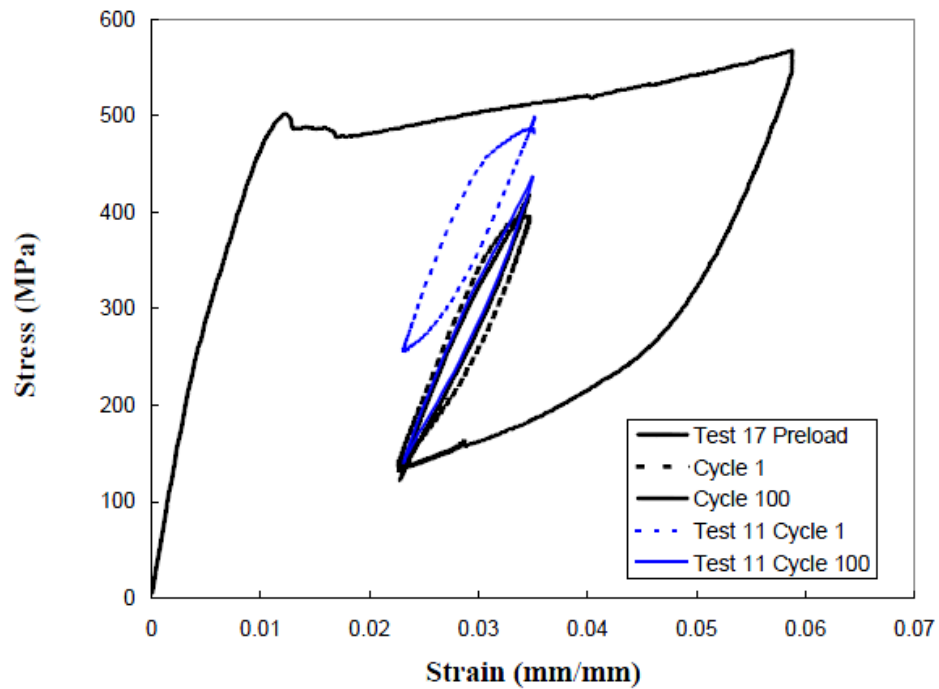
Figure 2-29: Test results of 3 % Mean, 1.2 % peak-to-peak alternating strains cycling 'from above' (blue) and 'from below' (black) – taken from figure 5 of ref (35).

It should be noted that all these tests subjected the nitinol material to relatively large $\Delta\varepsilon$ values, and as such there was some load-unload hysteresis evident in the cycle curves for all test sets. An interesting finding from the results is that the 'from below' cycling remained at approximately the same upper and lower stress levels throughout cycling, whereas the 'from above' results showed decreasing stress levels during cycling ('softening') until the cycles stabilized at levels close to the 'from below' results (see example in figure 2-29 above). In fact, it was found that for these $\Delta\varepsilon$ levels, the 'from above' cycling material responses tended to merge with the 'from below' response, showing path-independence for the high-cycle behavior. The other important finding was that for the lower $\Delta\varepsilon$ tests ($\Delta\varepsilon$= 1 % or 1.2 %), the cycle shape and modulus remained stable throughout cycling, while for the higher $\Delta\varepsilon$ tests there was a clear change in shape of the hysteresis loop from 1 to 100 cycles. This work suggests, then, that for low $\Delta\varepsilon$ cycles at mean strains reached during unloading, the cyclic response can be assumed to be stable from the 1st cycle onwards.

Further evidence of this is given by Schlun et al (36). They performed uniaxial tensile testing according to ASTM F2516-06 at 37C in a water bath on dog-bone samples laser cut from nitinol tubing and processed in an identical manner to laser-cut stents. As in the previous case, they performed $\Delta\varepsilon$ cycling at a given mean strain both 'from above' (during loading) and 'from below' (during unloading). Their results for $\Delta\varepsilon$ = 0.4 % (peak to peak) at 2 % mean strain are shown below in figure 2-30.

These results show no changes during 100 cycles. At this $\Delta\varepsilon$ level there is no load-unload hysteresis loop present and the cyclic modulus remains the same during cycling. It is interesting to note that in this case, there was no drop in stress levels for the 'from above' cycling, which may be due to the lower $\Delta\varepsilon$ cycling performed here compared to Pelton's (7) or Rebelo's (35) cyclic testing. It is also important to note that their results show a higher cyclic modulus for the 'from below' cycling, meaning these cycles undergo a greater $\Delta\sigma$ for the same $\Delta\varepsilon$ than the 'from above' cycles.
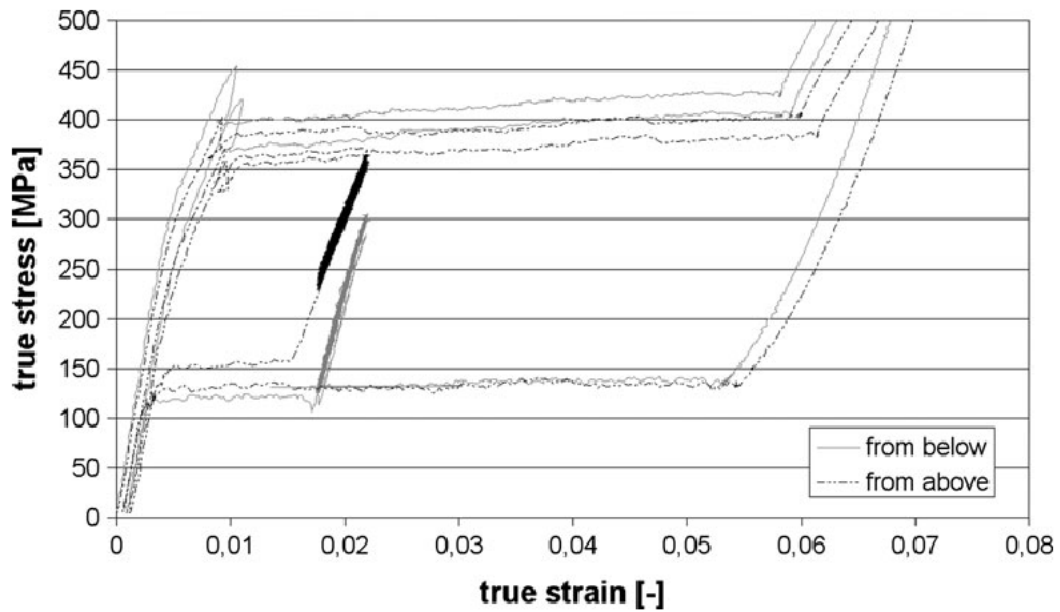
Figure 2-30: Test results of 2 % Mean, 0.4 % peak-to-peak alternating strains cycling 'from above' (black) and 'from below' (grey) – taken from figure 5 of ref (36).

For $\Delta\mathcal{E}$ = 2 % (peak to peak) with mean strain of 3 %, they obtained similar results to Rebelo (35), with a similar change in the hysteresis loop shape with cycling until a stable shape is reached at 90 cycles.

Launey et al (37) performed tension-tension fatigue testing on 0.25 mm nitinol wire samples (45 % CW, Af = 17±3 C) at 37 C test temperature following tensile pre-straining, to investigate the effects of pre-straining, mean strain and delta strain on fatigue life of nitinol. The key finding from their work is that phase change during cycling is detrimental to fatigue life, and therefore nitinol components for use in high-cycle applications should be designed to avoid phase change during cycling. In terms of their tensile stress-strain results, they showed that phase change is seen by hysteresis in the cyclic behavior. Therefore, long-term fatigue safety is indicated by an absence of load-unload stress hysteresis in cycling. In relation to these findings, they also show that a greater gap between loading and unloading plateau stresses (greater 'large strain'

hysteresis) allows a higher $\Delta\varepsilon$ fatigue limit, and that large tensile pre-strains (beyond the transformation plateau) can in fact increase this fatigue limit by lowering the unloading plateau. However, as has previously been seen in the analysis of Gupta et al (32), the effect of high pre-strain on subsequent fatigue life depends on the direction of loading for each step. In the Ref (32) study, high compressive pre-strains were detrimental to rotary bend (alternating tensile-compressive loading) fatigue life. In terms of application to endovascular stent components, it would be useful to see results for cyclic bending fatigue of Nitinol following pre-strain bending in the same direction. No such studies were found in the current literature review.

In summary, a number of investigators have considered the uniaxial tensile stress-strain behavior of superelastic nitinol under small $\Delta\varepsilon$ cycling conditions. However, no previous results could be found in the published literature for mechanical response of nitinol in bending or compression during small $\Delta\varepsilon$ cycling (despite a large volume of work on cyclic fatigue characterization for bending components). Therefore, it is an intention of the present experimental work to include small $\Delta\varepsilon$ cycling in the compression and bending characterization testing of nitinol wires.

2.2.2.9 Conclusions: Compressive, Tensile and Bend Testing of Nitinol

Tensile testing of Nitinol wire material has been widely investigated and reported, with a wealth of information on testing techniques and results available in the literature. On the other hand, there is little published research on compressive and bend characterization of nitinol wire material.

Compressive testing of wire samples has inherent set-up difficulties related to buckling. It has, however, been shown that larger diameter samples in the diameter range 1-2 mm can be processed to give similar mechanical properties to thin nitinol wire (diameter < 0.5 mm), opening up the possibility of investigating compressive properties of nitinol wire material under uniaxial loading. Where lateral supports are used to prevent buckling

of longer samples, care should be taken in using crosshead displacement to calculate strain, as this has been shown to overestimate strain values. If shorter samples are to be used to avoid buckling, high resolution displacement control and measurement test equipment would be required, and end friction difficulties must be resolved.

Information on compressive testing of larger rod and tube nitinol samples is more widely available, and provides the following characteristics for superelastic nitinol in compression:

- The initial elastic modulus is constant up to the transformation stress, and is generally higher than the effective initial tensile modulus (up to the tensile transformation stress). This can be attributed to the effect of stress-induced R-phase in tensile loading, which does not occur in compression.

- The transformation stresses in compression are higher than in tension, both for loading and unloading.

- The loading and unloading plateaus in compression have a low effective modulus but are not flat, as in tension. Stress increases with strain in loading and decreases with strain in unloading, even during phase transformation.

- Loading and unloading 'plateaus' are shorter in compression than in tension, meaning there is less transformation strain.

- Unloading stress plateaus are load-path independent both for tension and compression providing the maximum loading strain lies within the loading plateau.

- Unloading stress plateaus are load-path dependent both for tension and compression if the maximum loading strain is beyond the end of the loading plateau. In this case, the unloading plateau decreases with increasing maximum strain. This is attributed to the presence of plastic dislocations within the material following large strains.

- In uniaxial compression, deformation during phase transformation is essentially homogenous throughout the material. This is different from uniaxial tension,

where strain localisation occurs as phase change nucleates at a discrete location and then propagates as a front along the length of the material.

- Small $\Delta\mathcal{E}$ cyclic behavior during unloading of nitinol in compression has not been reported in the literature. For understanding of in-vivo stent behavior, it would be useful to investigate the stress-strain path of this cycling behavior, including the 'compressive cycling modulus' (which will have an influence on the stent's Radial Resistive Force). A number of investigations have been performed for $\Delta\mathcal{E}$ cyclic behavior of nitinol in tension, with results suggesting that the material response will remain stable from the initial cycle providing the $\Delta\mathcal{E}$ is small.

For bend testing, common approaches to material characterisation include 3-point bending, 4-point bending and cantilever beam bending. These different approaches give different distributions of curvature and moment along the length of a test sample, and an appropriate method should be chosen for investigation of in-service bending behaviour.

Again, little published information is available for thin nitinol wire (< 0.5 mm diameter) in bending. However, a number of investigations for thicker nitinol beams have been reported, providing the following characteristics for superelastic nitinol in bending:

- The neutral axis is eccentric for superelastic nitinol in bending, and is located towards the inner (compressive) bend surface. The neutral axis eccentricity results from the tensile-compressive asymmetry of Nitinol's stress-strain behaviour.
- In bending, superelastic nitinol shows the characteristic load-unload 'flag' shape for moment vs curvature, similar to the curve shape seen for stress vs strain for uniaxial tensile and compressive testing. As would be expected, this shows that stiff-compliant-stiff behaviour and 'moment' hysteresis occur in bending due to the phase change effects.

- Strain localization can occur in bending when the outer tensile material is in the unstable phase-change state, meaning that plane sections do not remain plane and local tensile strains do not match beam theory predictions. This has only been demonstrated for large diameter tubing in 4-point bending. It is considered that localization effects may be less evident or even absent for thin wires in bending with applied localised moments – as for 3-point bending and in-service stent rings.

- When the outer tensile material is beyond the unstable phase-change condition (> 7.5 % strain), local bending response is well predicted by beam theory, with plane sections.

- Global bending response of nitinol in loading is predicted well using beam theory with an asymmetric material model.

- FEA simulation has demonstrated that in bending, the final strain state of a nitinol beam during unloading is dependent on its load-path history.

This literature review has provided useful general information on the macroscopic tensile, compressive and bending behaviours of superelastic nitinol material due to the elastic, stress-induced phase change and plastic response of its microstructure to mechanical loading. The review has also highlighted the dependence of these properties on processing history and service temperature. However, this general information lacks the detail required to characterise the particular Nitinol material used for a specific manufacturer's stent graft components, both in terms of quantitative data and also in terms of the particular conditions that the material will be subjected to in service. In order to obtain material characterisation results that are useful for the design and analysis of stent graft products, and in particular Vascutek's products, it is therefore necessary to perform compressive and bend testing on wire material of a representative specification with test conditions appropriate to the intended use, which can then be used together with existing knowledge of the material's tensile behaviour. In terms of performing these

compressive and bending tests, the knowledge gained from this Literature Review will provide useful guidance.

This review has also highlighted a number of areas where no previous work has been published, providing clear opportunities for novel investigation as part of the planned project work. In particular, the work will involve novel experimental investigation of the following areas:

- the load-path dependence of strain for bending nitinol beams during unloading
- strain measurement of thin Nitinol wire in bending, using Digital Image Correlation (DIC)

These investigations will provide useful insights to the deformation behaviour of stent graft components during compaction and deployment, which in turn will help in analysis and optimisation of component design.

2.2.3 Superelastic Constitutive Models for Nitinol

As described in the introduction (Chapter 1), FEA has become a vital tool for stent graft development for the analysis and optimization of superelastic Nitinol components. An intention of the present work is to apply the results from physical tests on Nitinol wire to calibrate and validate a superelastic material model commonly used in industry, in order to evaluate its effectiveness in describing bending behavior for superelastic stents. With this purpose in mind, a review of the literature on superleastic Nitinol constitutive models was undertaken to understand the ability of these models to describe the relevant material behaviours.

A constitutive model is the mathematical description of a material's response to various loadings. In the case of Shape Memory Alloys, the material's responses to applied stresses or strains and to temperature changes are of primary interest. Many constitutive models have been proposed to describe Nitinol's superelastic, temperature-dependent and shape memory behaviours, falling into the broad categories of microscopic

(modelling of molecular-level phenomena), mesoscopic (modelling on the lattice particle scale) and macroscopic (modelling of homogenized material response) (38). Macroscopic models are also known as phenomenological models, and are generally the only viable option for engineering application to design and analysis of structural components due to their relative computational efficiency. For Nitinol, a number of macroscopic models have been developed to capture the phenomenological effects of superelasticity. However, one particular model has been adopted more widely than any other, largely due to its commercial availability within Finite Element Analysis (FEA) software packages such as Abaqus and Ansys: the Auricchio-Taylor model. This is the material model that will be used for FEA of superelastic Nitinol wire in the present work, as will be reported in Chapter 6. This constitutive model is described below.

2.2.3.1 Auricchio-Taylor Superelastic Model in Abaqus

Within Abaqus, a built-in superelastic material model is available, based on the macromodel proposed by Auricchio and Taylor to describe finite strain superelastic behaviour (42). To understand how this model was developed, it is useful to trace its evolution through the literature.

Lubliner (39) originally described an inelastic material model based on the concept of 'Generalized Plasticity', suitable for describing non-linear features not covered by classical plasticity, and allowing straight-forward numerical implementation. Lubliner and Auricchio (40) then used this 'Generalized Plasticity' framework to develop a 1-D constitutive model to describe shape memory alloys that undergo solid state phase transformations to give superelastic behaviour. This was then developed by Auricchio, Taylor and Lubliner (41) into a 3D isotropic model for superelastic behaviour, including description of 3 phase transformations (austenite to single variant (detwinned) martensite; detwinned martensite to austenite; and martensite re-orientation), temperature dependence of transformation stresses and tension-compression asymmetry features. Importantly, this work also included numerical implementation within a Finite

Element (FE) setting, with some experimental validation of the results, and included simulations to demonstrate applicability to superelastic device design. Next came the seminal paper from Auricchio and Taylor (42) describing the extension of the 3D model to finite-strain superelastic behaviour, an important development due to the large deformations typically required for superelastic components and devices. Again, the paper described numerical implementation in an FE setting with examples of validation and application. Auricchio and Sacco (43, 44) then developed the model by allowing for different elastic properties for the austenite and martensite phases, and also proposed an additional superelastic beam model, based on Euler-Bernoulli beam theory. In 2001, Auricchio published a paper (45) describing a refined version of the model as a robust and efficient solution algorithm for use in FE, to enable application to device design. Here he demonstrates the efficacy of the model using a number of 1-D and 3-D problems of varying complexity. Rebelo et al (46) then implemented the 'Auricchio-Taylor' model within Abaqus, available as user-defined material subroutines (UMAT for Abaqus/Standard and VUMAT for abaqus/Explicit) in Abaqus version 6.4 (2003) and then as built-in user material models for both Abaqus Standard and Explicit from version 6.5 (2005) onwards. Rebelo also extended the model to allow for some plasticity features (post-transformation hardening curve, permanent set) to be captured, available as the SuperElastic-Plastic model in more recent versions of Abaqus. Additionally, certain user subroutines have been developed that can be used as add-ons to improve the modelling of cyclic behaviour (35) and plasticity effects (47).

The 'Abaqus Auricchio-Taylor' (AAT) model is now widely used in the design of superelastic Nitinol components and devices within the medical device industry. Examples of its application for medical device simulations are given in refs (48-50). Two key reasons explain the model's widespread uptake by industry:

- Verification and Validation evidence: as an in-built model within Abaqus, it is supported by a great deal of verification and validation evidence (for example, see (51) and (52) for early experimental validation studies) and so is recognised

by regulatory authorities as a suitable constitutive model for superelastic Nitinol, albeit with certain limitations

- Ease of use: the input parameters required by the user to calibrate the model for their specific material are easily obtained from simple uniaxial stress-strain test results. Many other thermo-mechanical models have been developed (a detailed description of available models is provided by Lagoudas in ref (50)) but these are typically more involved than the AAT model for calibration.For example, in ref (51) the AAT model was chosen over the 'Qidwai-Lagoudas' model due to the perceived ease of model parameter calibration. (It should be noted that simplifications are possible for the Qidwai-Lagoudas making it simpler to calibrate, as used in ref 52). The simplicity of input parameters, together with the availability as an in-built user material, mean that the AAT model is accessible to a wide user base.

A detailed description of the Auricchio-Taylor constitutive model is beyond the scope of this review, and the reader is referred to ref (48) for a clear, concise summary of the theory including equations.

Briefly, the model uses stress (tensor) and temperature as control variables, and detwinned martensite fraction (scalar) and strain (tensor) as internal variables. For the superelastic model, any strain increment is decomposed into a linear elastic part and a stress-induced transformation part. Following standard plasticity rules, a transformation potential is calculated from the stress using a Drucker-Prager formulation (with stress separated into pressure and deviatoric stress components) and is used to derive the change in martensite fraction and the transformation strain increment. This transformation only occurs within certain stress thresholds, which are different for forward (Austenite to detwinned Martensite) and reverse (detwinned Martensite to Austenite) transformations, providing the model with stress hysteresis. The stress thresholds are input by the user, based on uniaxial tests, and the model includes a shift of

stress thresholds as a linear function of the temperature relative to the reference temperature. The model can accommodate non-proportional loading conditions, as any changes in stress direction produce martensite re-orientation with negligible additional effort.

The austenite and martensite are both assumed to follow isotropic linear elasticity, and different elastic properties can be input by the user for each (again based on uniaxial test results). During the phase transformation, where there is a mixture of the two phases, elastic properties (Young's Modulus, Poisson's ratio) are calculated from the elastic constants of each following the rule of mixtures, according to the fraction of martensite present.

Finally, a difference in response for tension and compression is enabled for the model by inputting a different transformation start stress threshold in compression and by specifying a value for volumetric transformation strain, thereby adjusting the angles used in the Drucker-Prager transformation equations to give different compressive behaviour. It is interesting to note that for development of the original Auricchio-Taylor model described in (42), different models were assessed for the phase change evolution, including an exponential form and a linear form. The exponential form (with suitable parameter inputs) gave considerably better results for accurately capturing the stress-strain behaviour as the material initially transitions from Austenite to Martensite and vice-versa. However, the A-T model implemented in Abaqus uses the linear form, likely chosen for its simplicity and requirement for fewer user input variables.

The Abaqus Superelastic model has also been extended to include certain features of plasticity for cases of loading beyond the end of the transformation plateau. Here, as well as elastic and transformation strain components, the total strain increment additionally comprises a plastic part. The plastic strain increment is calculated using a flow rule and

hardening model. A useful summary of how the Superelastic-Plastic model works is given in (47).

One final point on the A-T Superelastic model relates to the experimental validations of this model that are reported in literature. A large number of 3- and 4-point bending tests of Nitinol wires and tubes have been performed with comparison against simulations using the model (for example, (41), (42), (52), (53)). However, in all these cases the bending behaviour is validated in terms of load-deflection response, with no validation of the accuracy of strain results. For design and analysis of superelastic stent components, the material strains due to bending are of great importance in order to assess compaction and cyclic fatigue performance. Therefore, it is an aim of the present work to use strain results from experimental Nitinol wire bend tests for comparison with bending simulation results from the Abaqus A-T Superelastic model, as will be reported in Chapter 6.

2.2.3.2 Looking Forward: the Souza-Auricchio Model

The Auricchio-Taylor model described above, based on General Plasticity theory, was focused on superelasticity modelling. In the concluding remarks of ref (45), Auricchio states that future work will involve development of a model for both superelastic and shape memory behaviours. From that time on (2001) it is noticeable in his publications that Auricchio changes his attention to a different modelling approach, based on the publication of Souza et al (54), which describes a model developed within the theory of irreversible thermodynamics, using a free energy density function. With Auricchio himself moving on from the A-T model he developed to focus his attention elsewhere, it makes sense to include a brief overview of the alternative model he has been developing since the watershed of 2001. This will give some idea of the state-of-the-art in this field, and it may well be that such a model will in future supersede A-T as the industry model of choice for superelastic Nitinol. A description of the model is given below, in the context of a brief survey of its evolution through the literature.

In 1998, Souza et al (54) proposed a new model to describe superelastic and shape memory behaviour for 3-D media under small deformations. The model uses a free energy density function including terms for elastic energy, thermal deformation, transformation strain energy and chemical energy. Total strain and absolute temperature are the control variables, while the transformation strain tensor is the only internal variable to describe phase transformation effects. The model is based on a few simple, physically justified assumptions. For example, the transformation strain is assumed to be deviatoric as SMA phase transformations take place under near-isochoric conditions. The transformation strain magnitude is limited according to the maximum transformation strain seen in uniaxial tensile testing.

Auricchio and Petrini (55) saw the potential of this as a simple, effective and robust model and worked on improvements and methods to implement it in an FE context, leading to their 2002 publication. In 2004 (56), they described a simple modification to the model to enable a more effective, robust algorithm for implementing the numerical model. In 2007, Auricchio et al (57) extended the model to include plasticity effects including deformation accumulation due to fatigue. In 2009, Auricchio et al (58) included differences between austenite and martensite properties, and in 2011 Arghavani, Auricchio et al (59) developed the 3-D model for finite strain to allow for large deformation problems. Here they also included algorithms for implementation in FE, with examples showing improved efficiency of this model over previous versions. Barrera et al (60) in 2014 showed developments for improved plasticity and functional fatigue modelling. Finally, Urbano and Auricchio (61) published in 2015 to show improvements allowing more accurate modelling of the macro stress-strain behaviour beyond the end of the transformation plateau, describing martensite transformation of unfavourably oriented grains after the main plateau.

Petrini's 2017 presentation (62) gives a good overview of the model, its improvements over time and some recent applications. Of particular interest is the comparison of the state-of-the-art version with the Abaqus A-T Superelastic-Plastic model, showing that the new model is more effective in describing the qualitative macro stress-strain effects of plasticity (including reduced unload plateaus) and functional fatigue. This is in addition to the new model's ability to describe shape memory behaviours, which the A-T model cannot.

Ref (63) from 2010 gives an interesting example of the application of the Souza-Auricchio model to stent device deployment modelling. Here, an ad-hoc algorithm describing the particular material's behaviour was implemented into the Abaqus/Standard code using a user material subroutine (UMAT). It should be noted that there is not presently a commercially available UMAT for the Souza-Auricchio constitutive model.

2.2.4 Summary of Research Priorities from Literature Review

The preceding literature review has highlighted some notable gaps in knowledge, which the current research must seek to address in order to achieve the objective of superelastic Nitinol wire characterization for application to stent graft design. The research priorities that have been highlighted from this are given below:

- the only information found on compressive characterization testing of thin superelastic Nitinol wire (as opposed to other material forms with unrepresentative processing history) was from the investigation by Henderson et al (23) at University of Strathclyde, and this did not focus on the relevant in-service conditions for stent graft products. The current work must therefore aim to develop a suitable test method and obtain compressive stress-strain results for Nitinol wire representative of stent material and its in-service conditions.

- No experimental information was found for the mechanical response of thin Nitinol wire (in the range 0.1 to 0.45mm) tested in bending under the loading regimes most relevant to the in-service conditions of stent material (including large 'compaction' bend deformations and cyclic deformations representative of in-vivo pulsatile loading). Current work should therefore seek to obtain results for Nitinol wire's load response to bending deformations representative of in-service stent conditions.

- No previous experimental work to measure superelastic strains of thin Nitinol wire in bending could be found, providing an exciting opportunity for novel investigation in the present work.

- No experimental investigations of the effect of loading history on final strain state of Nitinol during unloading in bending were found. This interesting phenomena, reported by van Zyl et al (33) through FEA simulation work, requires an explanation in order to understand what effect it may have on stent component behaviour.

- Finally, no studies could be found on the accuracy of FEA-based Nitinol constitutive models (and in particular the widely-used Auricchio-Taylor model in Abaqus) for representing the strain state of superelastic Nitinol wire in bending. This should be addressed in the current work by using data from experimental strain measurement of Nitinol wire in bending for validation of FEA simulations using the Abaqus superelastic constitutive model.

Chapter 3: Compression Testing

3.1 Background

In order to understand the behaviour of superelastic nitinol wire for application to implantable stent graft components, it is important to characterise the material's mechanical response to compressive loading. In service, these implantable components will be subjected to large tensile and compressive strains in bending during endovascular delivery. Characterisation of the tensile response of nitinol wires to these high strains is well-known, with a well-defined method described in standard ASTM F2516-07 (Ref 17). However, compressive testing of thin nitinol wires to typical service strains is more difficult to achieve, with no standard method available. Chapter 2 (Literature Review) described some of the experimental approaches that have been used by investigators to study nitinol in compression, together with their limitations.

Having considered various approaches, it was decided to follow the compression testing approach developed by Henderson et al (ref 23) for the following reasons: availability of the equipment; past experience of University technicians with the test method; ability to use representative 'wire' sample material with equivalent processing history to device material; proven success in achieving results up to compressive strains of 4% without buckling. Using this approach, further work was required to overcome limitations of the previous study (23) so that useful data could be gathered on compressive Nitinol behavior relevant to stent graft design. In particular: Henderson's testing did not involve full phase transformation to the end of the loading plateau in compression, being limited to 4% maximum strain; testing was only performed at a single test temperature of Af + 30 C; only large strain cycling (between 0.01% and 4% strain, 50 cycles) was performed, with no medium or small strain cycling which are important to characterize for stent design and analysis; the published study gives very little detail of the results, showing only a single cycle graph from the compression testing.

It was therefore decided to use Henderson's approach as a basis, and to expand on that previous work to study a number of compressive characteristics relevant to the functioning of stent graft nitinol components.

3.2 Objectives

The overall objective for this piece of work is to obtain compressive stress-strain data for representative Nitinol material at conditions relevant to stent graft application.

In order to achieve this objective, the following sub-objectives were identified for compression testing:

- Characterize the stress-strain response up to 6 % compressive strain at room temperature, representing anticipated conditions during device compaction
- Investigate the effect of three load-unload cycles to 6 % compressive strain at room temperature, representing anticipated 'worst case' cycling during compaction
- Characterize the stress-strain response at different 'in service' temperatures: room temperature (17 to 25 C), body temperature (37 C) and sterilization temperature (55 C)
- Investigate the effect of loading history on the unloading stress-strain path in compression at 37 C: this is important to understand for stent components in bending, where different regions of the material will experience different load-unload paths during compaction and deployment
- Characterize the cycling behaviour for small and medium $\Delta\varepsilon$ load-unload cycling 'from below' (i.e. from the unloading stress-strain plateau) at 37 C: this is important for understanding the material response to in-vivo pulsatile loading, which is a key consideration for fatigue safety and device durability.

Another aim of this work is to gain understanding of the tensile – compressive asymmetry of the Nitinol material, which will allow informed analysis of its behaviour in bending. This will be achieved by comparing the compressive test results with existing tensile results (from Vascutek's database).

3.3 Equipment and Method

3.3.1 Sample Holder

As described in ref (23), Henderson designed three different compression sample holders, to accommodate three wire diameters: 1 mm, 1.8 mm and 2.4 mm (see figure 2-14 of Chapter 2 for details). Henderson explains how these holders were designed to limit transverse movement of the wire sample, thereby preventing buckling, while allowing for expansion of the sample due to Poisson's effect. Therefore, the fit between sample and holder bore was precisely defined. These same holders were available at the time of testing, and were used to investigate whether higher strains could be achieved without buckling using longer material samples. Initial investigation showed that the 1mm sample holder could be used with a sample length of 19.5 mm to achieve a maximum compressive nominal strain of 6 % (where nominal strain is defined as crosshead movement / original sample length). This holder was therefore deemed suitable for the planned compressive testing, avoiding the need for new equipment. Figure 3-1 shows a photograph and dimensioned schematic of the sample holder, comprising upper and lower steel holders and a steel stabilising sheath, with the Nitinol wire sample material.

3.3.2 Uniaxial Testing Machine

The testing was performed on a Zwick 2061 static uniaxial testing machine with 10 kN load cell and with an environmental chamber capable of achieving the target range of room temperature up to 55 C. The tests were run using 'DMG Rubicon 825 version 1.71 Control Interface' software. Figure 3-2 shows a photograph of the compression test set up on the machine.

Label	Dimension (mm)
A	2
B	47
C	20
D	22.5
E	8.75
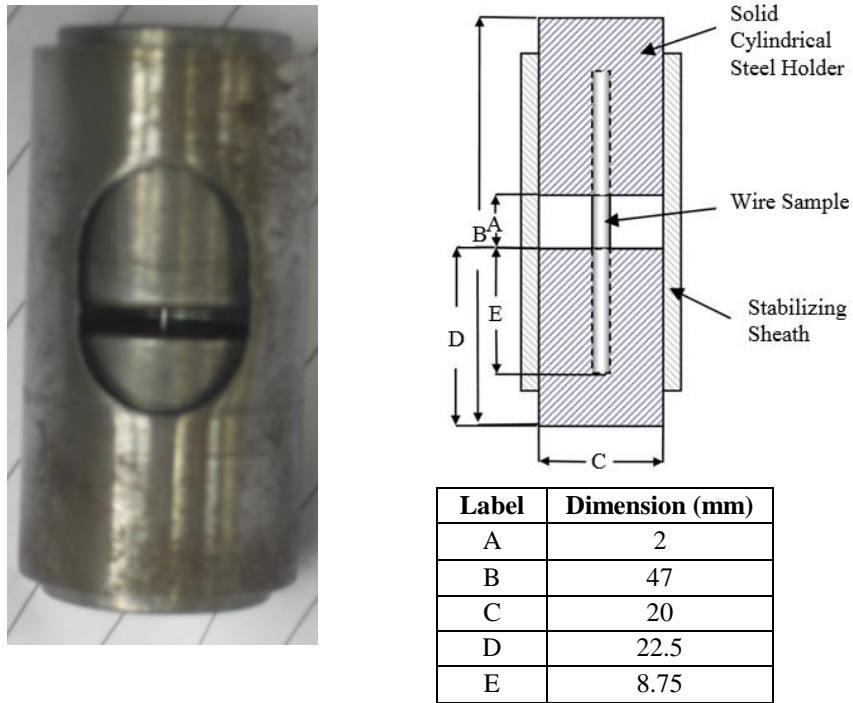
Figure 3-1: 1mm wire compression sample in holder – photograph and cross-section schematic with dimensions
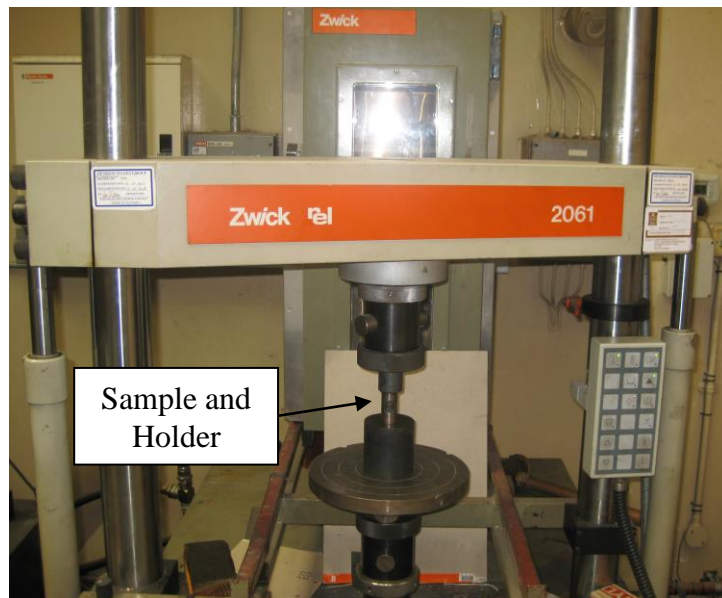
Figure 3-2: Compression test sample in holder on Zwick 2061 machine

3.3.3 Test Conditions

The compression testing was conducted in air, with temperature control provided by the environmental chamber with thermostat. Test temperature was monitored using a thermocouple in contact with the exposed sample length between the holders. The test temperature was specified to be within $\pm$ 1C of target temperature. For elevated temperatures, a minimum dwell time of 5 minutes was used prior to testing.

The testing was performed under displacement control, with a 100N initial load ('pre-load') condition. In terms of strain rate, test speeds were chosen to maximise the number of tests that could be performed in the available time while minimising the risk of adiabatic heating effects on the results. For large cycle tests, strain rates were used ranging from $3.33*10^{-4}$ s^{-1} for small strain excursion tests to $2*10^{-3}$ s^{-1} for testing to 6 % nominal strain. These speeds were considered acceptable as previous investigators (refs (4) and (19)) have successfully performed quasi-static compressive testing on much larger diameter samples at a strain rate of 10^{-3} s^{-1}, meaning that the chosen rates should be suitable for testing 1mm diameter wire. For the '$\Delta\varepsilon$ cycle tests' (100 cycles), strain rates ranged from $2*10^{-3}$ s^{-1} for small $\Delta\varepsilon$ cycles to $4*10^{-3}$ s^{-1} for large (2% peak-to-peak) $\Delta\varepsilon$ cycles. For all these tests, the strain rates were relatively high due to time constraints for the testing. As seen in the literature review, this may affect the results by increasing the upper plateau stresses and reducing the lower plateau stresses. This will need to be considered when analysing the compression test results and it is recommended that lower strain rates be used for future testing.

3.3.4 Test Sample Material

The superelastic nitinol components in Vascutek's stent graft devices are made from Fort Wayne NiTi#1 etched wire in the diameter range 0.1 to 0.45mm (see Appendices 1 and 2 for specifications). In order to obtain wire samples with equivalent processing history and mechanical performance to the device material while having suitable thickness for the proposed compressive testing, Fort Wayne Metals were asked to produce 1mm wire

to meet the standard Vascutek wire specification for mechanical performance (see Appendix 1). This specification is based around the uniaxial tensile performance of the material, and it was assumed that adherence to the standard processing steps and specification would provide material with equivalent microstructure and therefore equivalent compressive characteristics to the thinner wires.

Figure 3-3 shows stress-strain results of tensile testing at 37 C in air (using ASTM F2516-07 with exceptions) for 3 different nominal wire diameters: 1 mm, 0.45 mm and 0.14 mm. These results are taken from the supplier's Certificate of Conformance (CoC) data for the wire batches. The two smaller sizes are representative of the range of wires used in Vascutek's stent graft components. Note that the true stress and true strain have been plotted here, found using the following equations:

$$\varepsilon_{true} = \ln(1 + \varepsilon_{nom})$$
$$\sigma_{true} = \sigma_{nom} * (1 + \varepsilon_{nom})$$

[Note: In the reported results, true stress and strain plots are used where quantitative values are of primary importance, such as when identifying inputs for constitutive models. Engineering (or 'nominal') stress and strain plots are used where the qualitative data is of primary importance.]

The results of figure 3-3 show a good match for tensile test results between the wires up to approximately 8 % strain, showing that the 1mm sample wire can be considered equivalent to the material used for Vascutek's stent graft components in terms of mechanical properties.
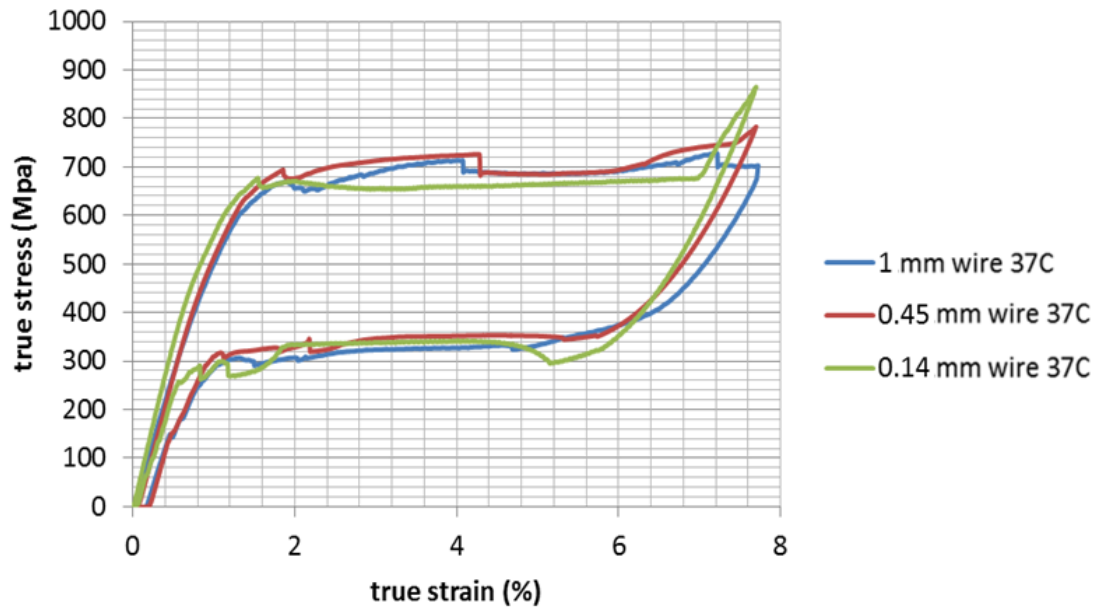
Figure 3-3: Stress-Strain plots for uniaxial tensile testing at 37 C of 1 mm wire (Lot F5928420), 0.45 mm wire (Lot F5298520) and 0.14 mm wire (Lot F5208630), from Fort Wayne Metal's CoC data

Table 3-1 gives key characteristics from the Certificate of Conformance for each of the wire lots, again showing clear equivalence of the 1 mm wire to the smaller diameter wires. All wires are 'NiTi#1 Straight Annealed' type, with 'Etched' surface finish.

Having established equivalence of the material, it was requested that the 1 mm samples be supplied in 19.5 mm lengths, with the ends precision cut perpendicular to the axial direction. This was achieved using EDM. It was considered that the Heat Affected Zone associated with the EDM cut (in the order of 10μ deep) would be negligible in relation to the sample length and would therefore have no effect on the tested material properties.

Nominal diameter	Measured diameter (mm)	Lot no.	Material composition*	Cold work	Active Af temperature** (C)	Upper plateau stress @ 4% strain (MPa)	Lower plateau stress @ 4% strain*** (MPa)
1mm	0.9992	F5928420	Ti – 55.94wt%Ni	44%	14.1	666	316
0.45mm	0.4506	F5298520	Ti – 55.89wt%Ni	43.6%	14.3	710	345
0.14mm	0.1392	F5208630	Ti – 55.96wt%Ni	46.2%	17	634	331
* With ASTM F2063-05 specifications for medical-grade Binary Nitinol material							
** Measured on finished wire by Bend and Free Recovery testing, as per ASTM F2082							
***Following 8% maximum nominal strain							

Table 3-1: Comparison of material characteristics from Certificates of Conformance of different diameter wires, showing equivalence of 1 mm wire to smaller wires

3.3.5 Test Plan

Table 3-2 below outlines the tests undertaken on the 1 mm x 19.5 mm NiTi wire samples in order to meet the objectives for compressive testing.

[It should be noted that the 'Room Temperature' (RT) test sets 1 – 3 were not performed in the environmental chamber but at the ambient temperature of the laboratory, which was measured to be 17 C, as stated in the table. This is 6 C cooler than the 23 C clean room temperature where Vascutek's stent grafts are manufactured. Using the findings of the literature review in Chapter 2, this may lead to loading and unloading stress plateau values here that are approximately 40 MPa lower than would be seen were the tests performed at 23 C.

The higher temperature tests (37 C and 55 C) were performed in the environmental chamber.]

Test Set	Temp (C)	Description	Displacement Steps	Speed (mm/s)	Strain Rate (s⁻¹)	No. Samples
1	17 (RT)	Load to 6% ε, unload to 0 (1 cycle)	100N initial load	0.039	$2*10^{-3}$	3 (1a, 1b, 1c)
			Load to 1.17mm in 30s			
			Unload to 0 in 30s			
2	17 (RT)	Load to 6% ε, unload to 0 (3 cycles)	100N initial load	0.039	$2*10^{-3}$	3 (2a, 2b, 2c)
			Load to 1.17mm in 30s, Unload to 0 in 30s (x 3 cycles)			
3	17 (RT)	Load to 4% ε, unload to 0 (3 cycles)	100N initial load	0.026	$1.33*10^{-3}$	3 (3a, 3b, 3c)
			Load to 0.78 mm in 30s, Unload to 0 in 30s (x 3 cycles)			
4	37	Load to 6% ε, unload to 0 (1 cycle)	100N initial load	0.039	$2*10^{-3}$	3 (4a, 4b, 4c)
			Load to 1.17mm in 30s			
			Unload to 0 in 30s			
5	55	Load to 5.5% ε, unload to 0 (1 cycle)	100N initial load	0.0357	$1.83*10^{-3}$	3 (5a, 5b, 5c)
			Load to 1.07mm in 30s			
			Unload to 0 in 30s			
6	37	Load to 5.5% ε, unload to 0 (1 cycle)	100N initial load	0.0357	$1.83*10^{-3}$	3 (6a, 6b, 6c)
			Load to 1.07mm in 30s			
			Unload to 0 in 30s			
7	37	Load to 4% ε, unload to 0 (1 cycle)	100N initial load	0.026	$1.33*10^{-3}$	3 (7a, 7b, 7c)
			Load to 0.78mm in 30s			
			Unload to 0 in 30s			
8	37	Load to 3% ε, unload to 0 (1 cycle)	100N initial load	0.0195	$1*10^{-3}$	1
			Load to 0.585mm in 30s			
			Unload to 0 in 30s			
9	37	Load to 2% ε, unload to 0 (1 cycle)	100N initial load	0.013	$6.67*10^{-4}$	1
			Load to 0.39mm in 30s			
			Unload to 0 in 30s			

Table 3-2: uniaxial compression test sets (continued on next page)

Test Set	Temp (C)	Description	Displacement Steps	Speed (mm/s)	Strain Rate (s^{-1})	No. Samples
10	37	Load to 1% ε, unload to 0 (1 cycle)	100N initial load	0.0065	3.33*10^{-4}	1
			Load to 0.195mm in 30s			
			Unload to 0 in 30s			
11	37	Load to 5.5% ε, unload to 3% ε, then 100 cycles with 2% Δε (peak to peak)	100N initial load			3 (11a, 11b, 11c)
			Load to 1.07mm in 30s	0.0357	1.83*10^{-3}	
			Unload by 0.485mm in 15s	0.0323	1.66*10^{-3}	
			Load by 0.195mm in 5s	0.039	2*10^{-3}	
			Unload by 0.39mm in 5s, Load by 0.39mm in 5s (x 100 cycles)	0.078	4*10^{-3}	
			Unload to 0 in 15s	0.039	2*10^{-3}	
12	37	Load to 5.5% ε, unload to 3% ε, then 100 cycles with 1% Δε (peak to peak)	100N initial load			3 (12a, 12b, 12c)
			Load to 1.07mm in 30s	0.0357	1.83*10-3	
			Unload by 0.485mm in 15s	0.0323	1.66*10-3	
			Load by 0.097mm in 3s	0.0323	1.66*10-3	
			Unload by 0.195mm in 3s, Load by 0.195mm in 3s (x 100 cycles)	0.065	3.33*10-3	
			Unload to 0 in 15s	0.039	2*10-3	
13	37	Load to 5.5% ε, unload to 3% ε, then 100 cycles with 0.4% Δε (peak to peak)	100N initial load			3 (13a, 13b, 13c)
			Load to 1.07mm in 30s	0.0357	1.83*10-3	
			Unload by 0.485mm in 15s	0.0323	1.66*10-3	
			Load by 0.039mm in 2s	0.0195	1*10-3	
			Unload by 0.078mm in 2s, Load by 0.078mm in 2s (x 100 cycles)	0.039	2*10-3	
			Unload to 0 in 15s	0.039	2*10-3	

Table 3-2: uniaxial compression test sets (continued from previous page)

3.4 Results and Discussion

3.4.1 'Compaction Strain' Compressive Testing

Test set 1 was performed to characterize the stress-strain response up to 6 % compressive strain at room temperature, representing anticipated conditions during device compaction. The results for the 3 samples are plotted in figure 3-4.

Eng Strain (%)
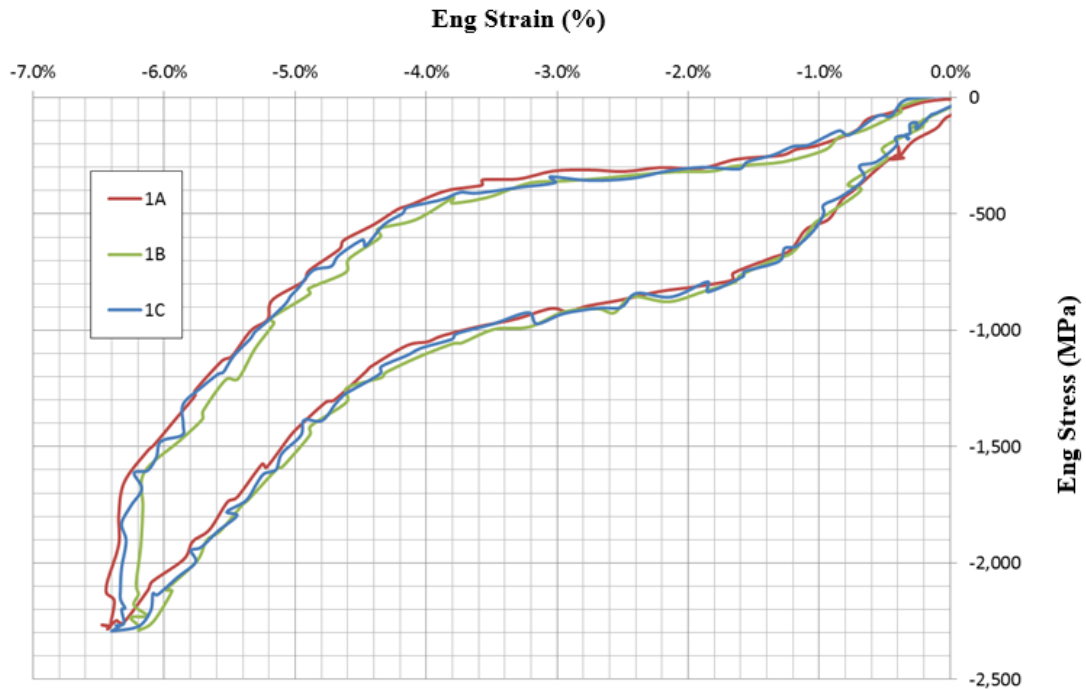
Figure 3-4: Test set 1 stress-strain results: 1 mm wire, single load-unload cycle to 6 % compressive strain, at 17 C (3 samples: 1A, 1B, 1C)

The compressive stress-strain plot of figure 3-4 shows the following features in loading:

- Initial linear elastic modulus up to 1.3 % strain
- Upper loading 'plateau' beyond the initial modulus up to 4 % strain. This 'plateau' region is not flat in compression, with a stress increase of approximately 200 MPa over the 2.7 % transformation strain interval. Within this plateau region, compressive deformation mainly takes place by reversible stress-induced phase change from austenite to martensite crystal structure. As explained

in section 2.2.2 of Chapter 2, in compression this phase change is diffuse throughout the material (unlike in tension, where there is localization of phase change).

- Beyond 4 % strain, there is a '2nd linear modulus' up to 6 % nominal strain. This 2nd modulus region is attributed to deformation by martensite elasticity as well as some plasticity once the material has fully transformed from austenite to martensite. (Note: due to the 100 N pre-load condition used to initiate displacement control, the samples were actually compressed to slightly higher nominal strains than the 6 % target values. All compressive results plots presented in this chapter have been positioned to the origin (rather than the 100 N pre-load position), giving maximum nominal strains that are approximately 0.2 to 0.4 % higher than the target strains.)

The figure 3-4 results show the following features for unloading:

- The plots show a vertical drop in the stress at constant strain when changing direction from loading to unloading. This behavior was consistently seen when the compression stress-strain data was plotted, and is attributed to friction effects due to test rig misalignment in the set-up. It is therefore not a characteristic of the Nitinol mechanical response itself. This issue is discussed in detail in section 3.4.5 later in this chapter. However, the central finding for interpreting the compressive results is that the test rig friction increases the measured force during loading and decreases the measured force during unloading – thereby affecting the stress values plotted. The results shown here are therefore useful qualitatively for showing characteristic behaviours of the material under different loading conditions, as well as giving a quantitative 'outer bound' for the stress-strain path in compression. Further, the 'Friction Effect Investigation' (section 3.4.5) culminates in plotting of 'corrected' compressive results that can be used to extract mechanical property values for the material.

- Following the vertical stress drop, the results show a near-linear unload modulus from the maximum strain down to a lower 'unload plateau' at approximately 3.6 %. This unloading region is attributed to deformation recovery by martensite elasticity

- The unload 'plateau', from 3.6 % to 1 % strain, is not flat in compression. The stress decreases by approximately 200 MPa over the 2.6 % reverse transformation strain interval. In this unload 'plateau' region, there is reverse phase change from martensite to austenite crystal structure as compressive stress decreases.

- At 1 % strain, the material mainly consists of austenitic NiTi as well as plastic dislocations due to the large loading strain excursion. Unloading to zero stress occurs by austenite elasticity, showing a linear final unload modulus. The presence of plasticity means that this modulus is lower than the initial loading modulus, and also results in residual strain (approximately 0.3 % following the 6 % maximum strain load-unload cycle).

Figure 3-5 shows load-unload tensile test results for the 0.45 mm wire (Lot F5298520) at Room Temperature, allowing consideration of the material's tensile-compressive asymmetry by comparison with figure 3-4.

Comparing the results of figure 3-5 with those of figure 3-4:

- The 'effective' initial modulus in tension is lower than in compression, and in tension this initial loading region shows some non-linearity. This is attributed to the presence of R-phase (see refs (5), (11) for similar R-phase effects) for this material at room temperature, which has lower tensile stiffness than austenite NiTi but similar compressive stiffness.

- Stress induced martensite is initiated at a lower stress level in tension than in compression. In tension, the 'loading plateau' is then almost flat, with phase change continuing at near constant applied stress. As discussed previously, in

tension this phase change initiates locally and propagates through the material with a transformation front. In compression, phase change is diffuse, occurring more evenly throughout the material.
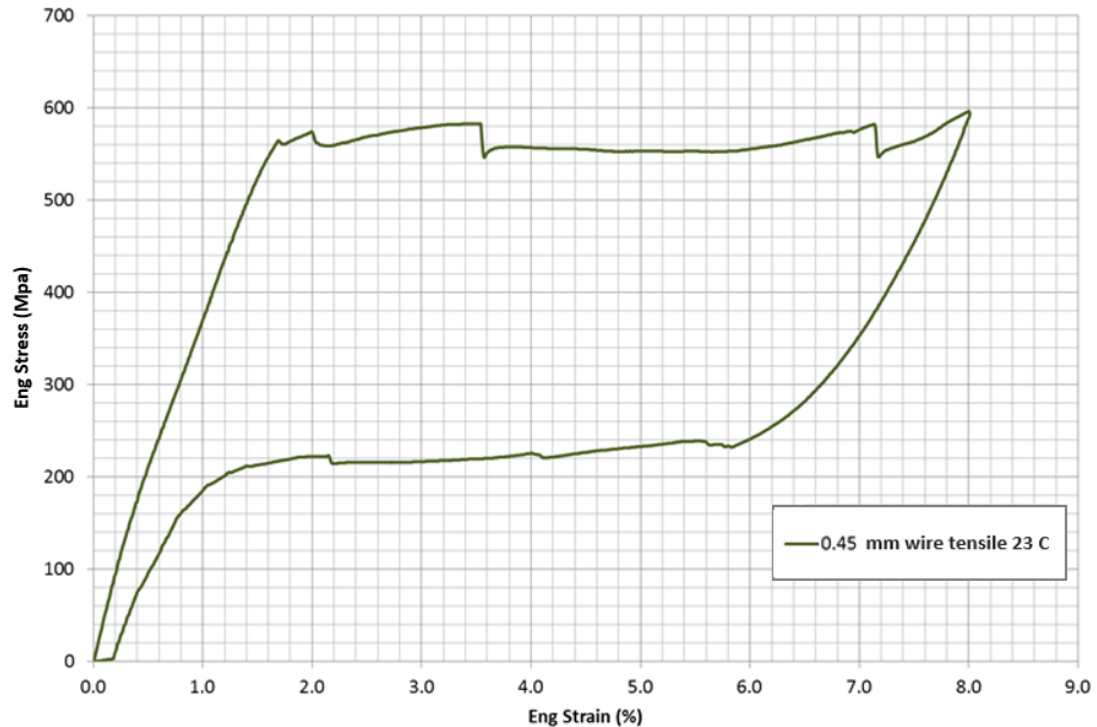
Figure 3-5: Uniaxial tensile stress-strain results: 0.45 mm wire (Lot F5298520), single load-unload cycle to 8 % tensile strain, at 23 C (1 sample)

- The phase-change 'plateau' region is shorter in compression than in tension. Beyond this transformation strain region, the material undergoes increasing plastic deformation. This means that the NiTi wire material has greater recoverable strain in tension (up to 8 %) than in compression (up to 4 %).
- For unloading, the material shows stress hysteresis for both tension and compression, with strain recovery occurring at lower stress levels. For each case, the material unloads from its maximum strain with martensite elasticity until it

reaches a critical stress for reverse phase change. This occurs at a higher stress in compression than in tension.

- In tension, strain recovery by reverse phase change then occurs at a near constant stress level, giving a flat 'unload plateau'. This phase change occurs with localization, as transformation front(s) act in reverse. In compression, the 'unload plateau' is not flat as the reverse phase transformation occurs more evenly throughout the material.

- At approximately 1 % strain following unloading, reverse phase change is complete and the material is at similar stress both in tension and compression. Final unloading then occurs with austenite elasticity.

Test set 2 was performed to investigate the effect of three load-unload cycles to 6% compressive strain at room temperature, representing anticipated 'worst case' cycling during compaction. The results for one sample (2B) are plotted in figure 3-6. For clarity, the results from the other two samples are omitted from the plot, though these were seen to be very similar. Figure 3-7 then shows the same results as in figure 3-6, but with the residual strain from the previous cycle removed in each case. This allows easier observation of the effects of cycling on stress-strain behaviour. From cycle 1, the residual strain was 0.3%; from cycle 2, the additional residual strain was 0.25%.

The results in figure 3-6 show that in compression to maximum strains anticipated during compaction (approximately 6%), there is some permanent set in the material due to plasticity, giving residual strain of approximately 0.3% for each cycle. This means that when stent rings undergo three compaction cycles during 'worst-case' assembly, the wire material will experience some permanent set due to compressive loading at peak and valley inner bend surfaces. This plasticity will have the effect of lowering stresses during unloading of the material, thereby reducing radial force. Therefore, any radial force or sealing verification testing of components or devices should include compaction strain history.
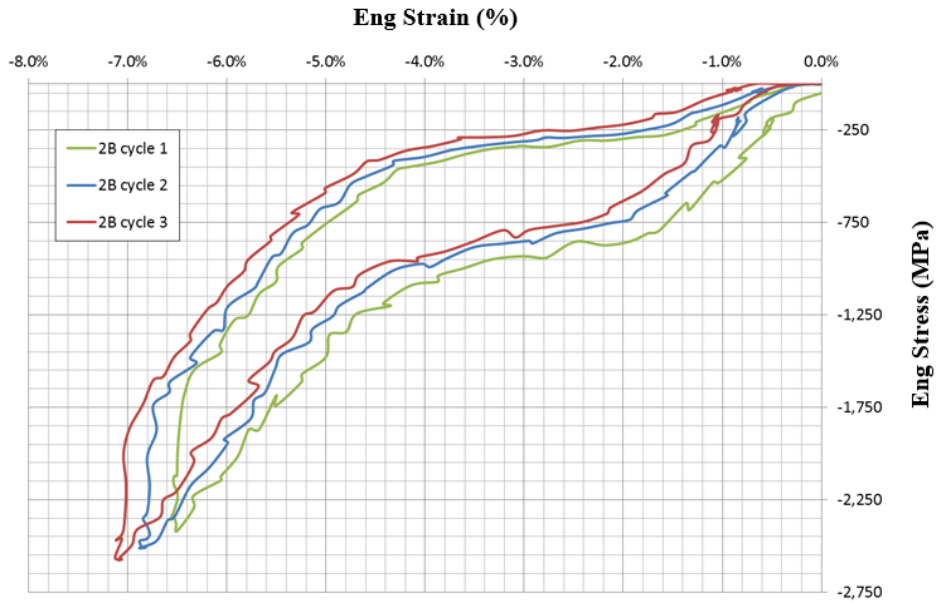
*Figure 3-6: Test set 2 stress-strain results: 1 mm wire, three load-unload cycles to 6 %
compressive strain, at 17 C (1 sample: 2B)*
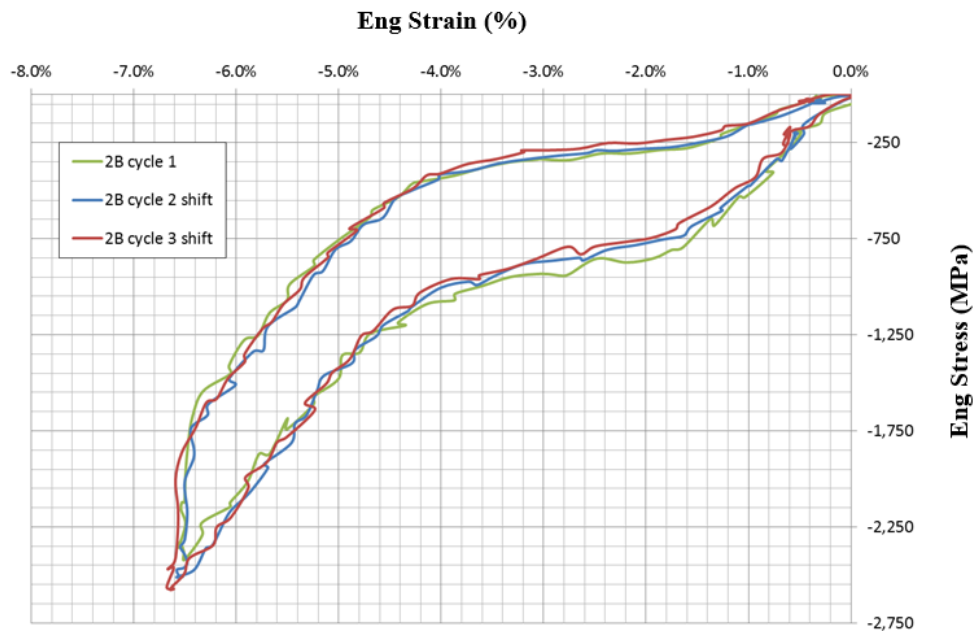
*Figure 3-7: Sample 2B stress-strain results, modified from figure 3-6 so that strain is
plotted from the origin for each cycle (ie. Residual strain from previous cycle removed)*

Figure 3-7, however, shows that this permanent set from previous cycles has little effect on the stress-strain response of subsequent cycles, meaning that the compressive stiffness of the wire material will not be affected by 'worst case' assembly involving 3 compaction cycles.

Figure 3-8 shows 3 load-unload cycles to 4 % compressive strain at 17 C room temperature (test set 3), to investigate the effects of 'worst case' 3 compaction cycles on material subjected to lower maximum transformation strains. Again, only one sample (3B) result is shown, as the results from the other two samples were almost identical. The plots in figure 3-8 show clearly that material experiencing maximum compressive strains of 4 % or less will fully recover its strain by superelasticity, with no evidence of plasticity. This can be seen by the fact that each curve follows the same stress-strain path and completes its unloading cycle at the origin.
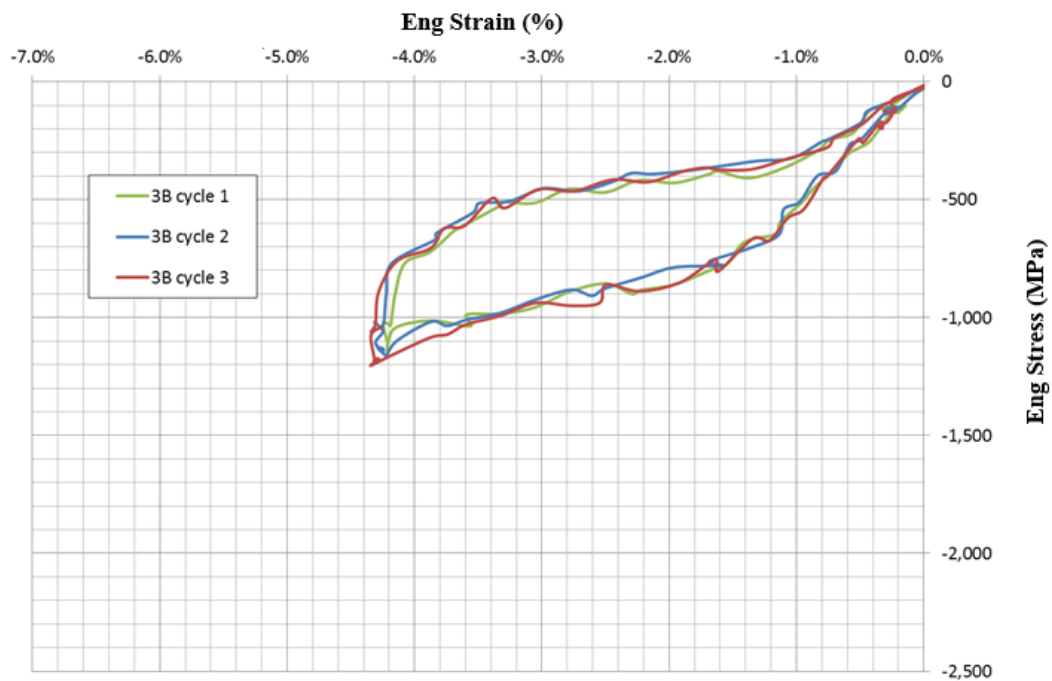
Figure 3-8: Test set 3 stress-strain results: 1 mm wire, three load-unload cycles to 4 % compressive strain, at 17 C (1 sample: 3B)

For comparison with these 'large cycle' compressive results, figure 3-9 then shows results from a uniaxial tensile investigation of 'compaction strain' cycling at room temperature (23 C) that was performed on the 0.45 mm NiTi#1 wire (Lot F5298520).
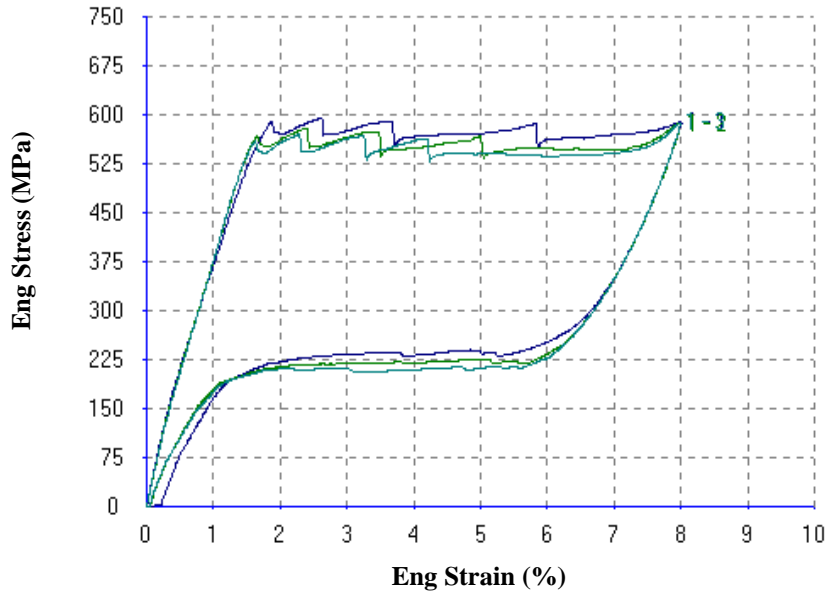
Figure 3-9: Uniaxial tensile stress-strain results: 0.45 mm wire (Lot F5298520), three load-unload cycles to 8 % tensile strain, at 23 C (1 sample)

The tensile test results in figure 3-9 show that in tension to high strains anticipated during compaction (approximately 8 %), there is little or no residual strain, suggesting minimal permanent set in the material due to plasticity. As with compression, we see that where maximum strain is limited to the 'phase transformation' plateau region the deformation is fully recoverable and subsequent cycles can achieve the same large recoverable strains. It is also interesting to note that there is a small decrease in the loading plateau stress level with each subsequent cycle (green cycles vs blue initial cycle in figure 3-9), as was expected from the Literature Review. This shows that, in tension, phase change is initiated at lower stress following a cycle where stress-induced martensite has occurred. In terms of stent graft device performance, this may lead to

slightly lower compaction forces for stent components following previous compaction cycles.

3.4.2 Temperature Dependence

Results from test sets 1 to 7 were used to characterize the compressive stress-strain response of the material at different 'in service' temperatures: room temperature (17 C), body temperature (37 C) and sterilization temperature (55 C). In order to make direct comparisons for both loading and unloading, the results have been grouped according to strain excursion. Figure 3-10 shows results from test sets 3 and 7, for testing to 4 % max ε at test temperatures of 17 C and 37 C. Figure 3-11 then shows results from test sets 1 and 4, for testing to 6 % max ε at test temperatures of 17 C and 37 C.
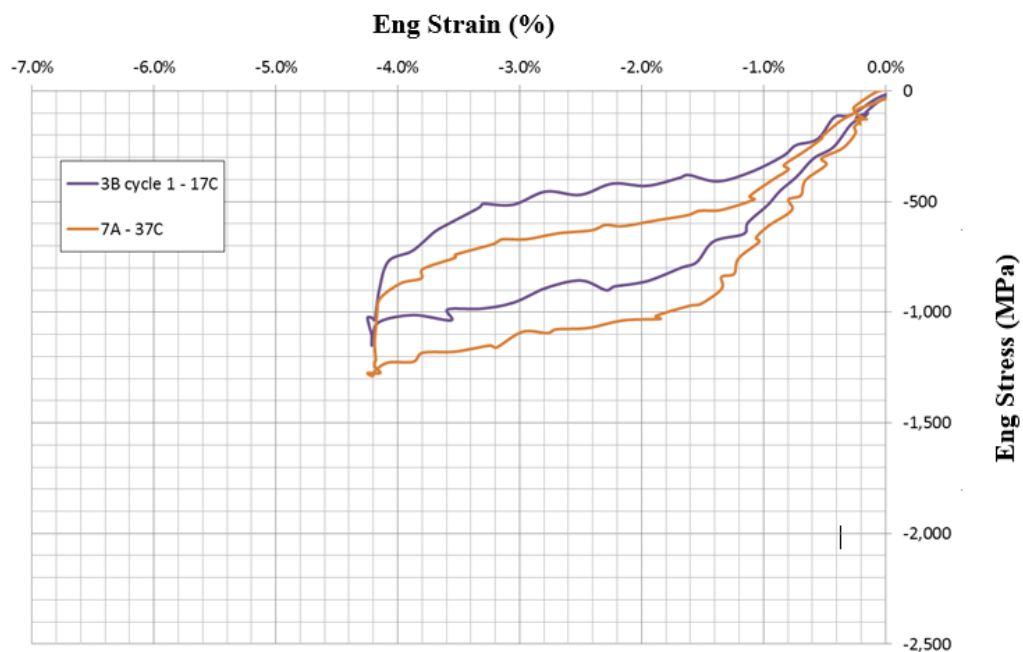
Figure 3-10: Effect of test temperature on stress-strain results from test sets 3 and 7: 1mm wire, single load-unload cycle to 4 % compressive strain, at 17 C (sample 3B) and 37 C (sample 7A)
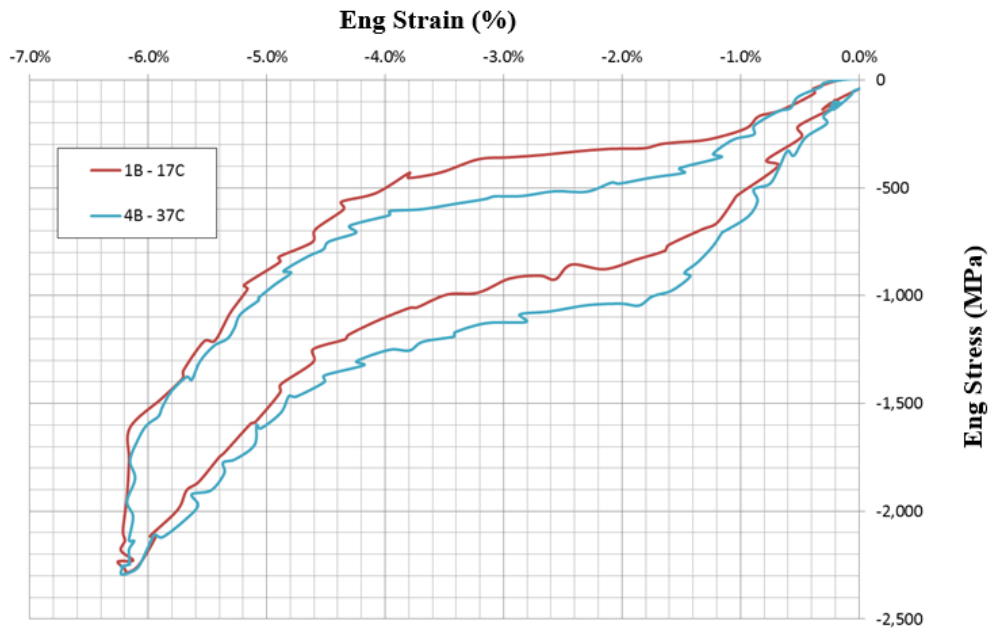
Figure 3-11: Effect of test temperature on stress-strain results from test sets 1 and 4: 1mm wire, single load-unload cycle to 6 % compressive strain, at 17 C (sample 1B) and 37 C (sample 4B)

The compressive results of figures 3-10 and 3-11 show an increase in initial modulus of 9 GPa from compression at room temperature to 37 C, and an increase in upper 'plateau' stresses of around 150 MPa (7.5 MPa/∘C). For unloading, the lower 'plateau' stresses are again approximately 150 MPa higher at 37 C than at 17 C, for both the 4 % and 6 % maximum strain tests.

Figure 3-12 shows results from test sets 5 and 6, for testing to 5.5 % max ε at test temperatures of 37 C and 55 C. The results of figure 3-12 show that the trends of increasing modulus (~0.5 GPa/∘C) and upper plateau level (~7.5 MPa/∘C) continue up to 55 C (maximum device sterilization temperature). However, in unloading there is less of a difference between the two curves. This is likely to be due to increased plasticity at the higher temperature (55 C) for material strained to 5.5 %, causing it to unload along a lower plateau. This increased plasticity at 55 C is also seen by the increased residual strain (~0.35 %) following unloading compared to the 37 C curve (~0.05 % residual

strain). It is expected that temperature comparison tests performed to < 4 % maximum strain would show considerably higher unloading stresses in the material at 55 C compared to 37 C, consistent with the temperature dependence results in loading.
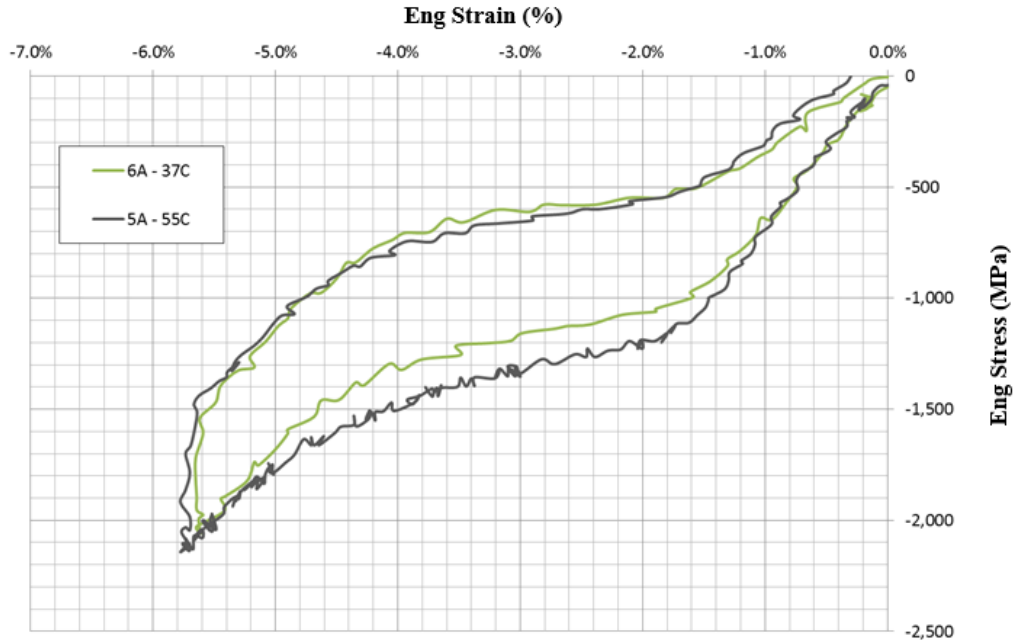
Figure 3-12: Effect of test temperature on stress-strain results from test sets 5 and 6: 1mm wire, single load-unload cycle to 5.5 % compressive strain, at 37 C (sample 6A) and 55 C (sample 5A)

Tensile tests on Vascutek's NiTi#1 wire have also been performed to investigate temperature dependence. Figure 3-13 shows results from tensile testing of 0.45 mm wire (Lot F5298520) at 23 C and at 37 C.

The tensile results of figure 3-13 show increased initial modulus from 42 GPa at 23 C to 56 GPa at 37 C (~1 GPa/∘C). The upper and lower plateau stress levels increase by about 100 MPa (~7.1 MPa/∘C) from 23 C to 37 C. For the large strain excursion tests (up to 8%), there is greater permanent set at 37 C (0.3 %) than at 23 C (< 0.2 %).
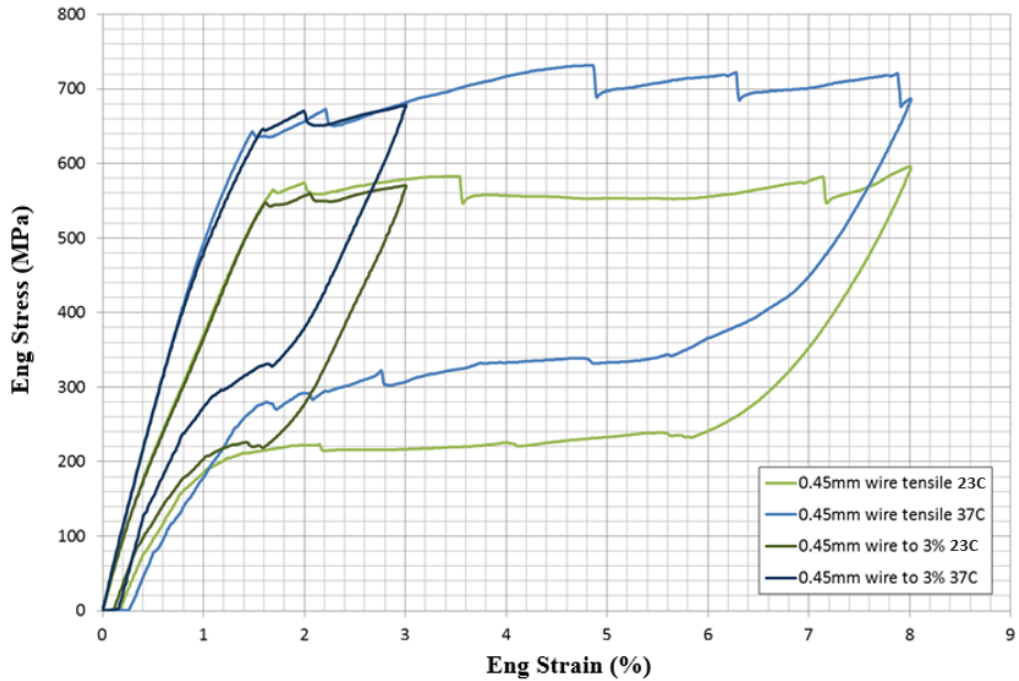
Figure 3-13: Effect of temperature on uniaxial tensile stress-strain results: 0.45 mm wire (Lot F5298520) for single load-unload cycles to 3 % and 8 % tensile strains, at 23C and 37 C (one sample for each curve)

Considering device performance, the temperature dependence investigation reported here leads to the following conclusions:

- Nitinol components will have lower bending stiffness at room temperature than at elevated temperatures, helping to minimize device compaction forces during assembly. The lower the assembly temperature, the lower the compaction force contribution from nitinol components on the device.

- Sterilization of compacted nitinol rings at 55 C is likely to cause some plasticity and permanent set at the high compressive strain regions (inner bend surfaces of peaks and valleys), which may affect reduction in stresses (and therefore radial force) during unloading. It is therefore recommended that relevant verification testing be performed at 37 C on components or devices that have undergone compaction strain and sterilization temperature (55 C) conditions.

- Stent components will have higher bending stiffness when implanted in the body (at 37 C) than at room temperature, due to the higher tensile and compressive moduli and stress plateaus. Therefore, as well as including suitable strain and temperature processing history, simulated use testing should be carried out at 37 C to represent in-vivo performance.

3.4.3 Load Path Dependence

Test sets 4 and 6 – 10 were used to investigate the effect of loading history on the unloading stress-strain path in compression at 37 C. The aim of this investigation was to gain insight to the behaviour of material within a bending stent graft component, where different regions are at different strains and therefore undergo different load-unload paths during compaction and deployment. Figure 3-14 shows an overlay of plots from the different test sets.
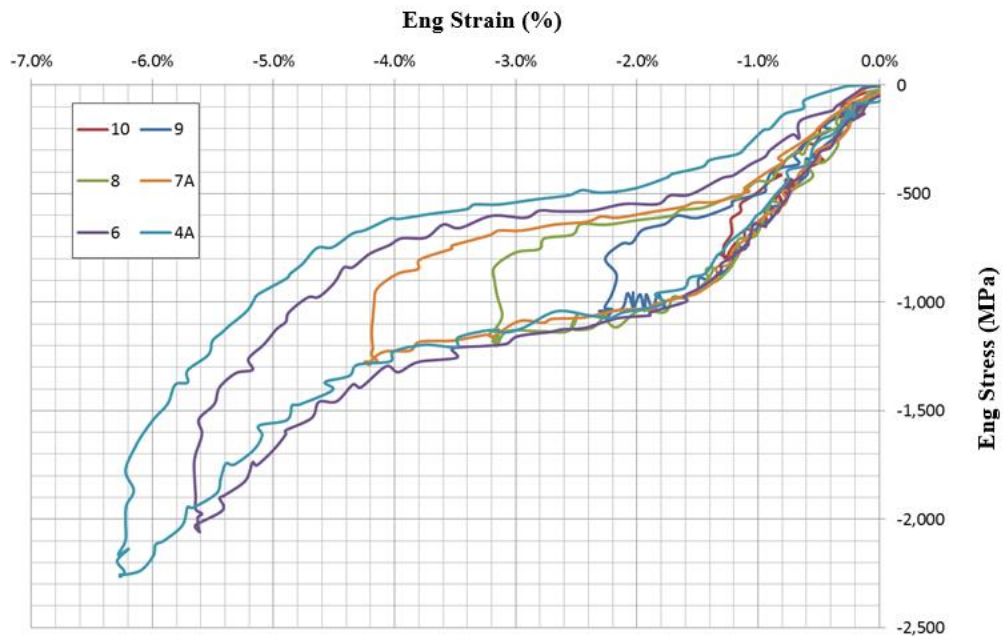
Figure 3-14: Stress-strain results from test sets 4, 6, 7, 8, 9 and 10: 1 mm wire, single load-unload cycles to various maximum compressive strains, at 37 C (one sample for each load-unload curve). Results show effects of loading history on unload path for superelastic Nitinol in compression

From figure 3-14 it can be seen that for all compressive transformation strains up to 4 %
in loading, the material unloads to a common unload plateau and then recovers its strain
with no permanent set. For increasing compressive strains beyond 4 % in loading, there
is decreasing unload plateau level and increased permanent set. Due to the test rig
friction effect, it is difficult to see the effect of increasing loading strains on unload
modulus in these results. However, in the 'corrected' results of the later 'Friction
Investigation' section (3.4.5) it can be seen that the unload modulus decreases slightly
with increasing strain up to 4%, and then increases between 4 % and 6 % loading strain
to a level similar to the initial austenite elastic modulus.

For comparison, figure 3-15 shows results from a uniaxial tensile investigation of load
path dependence at 37 C that was performed on Vascutek's 0.45 mm NiTi#1 wire.
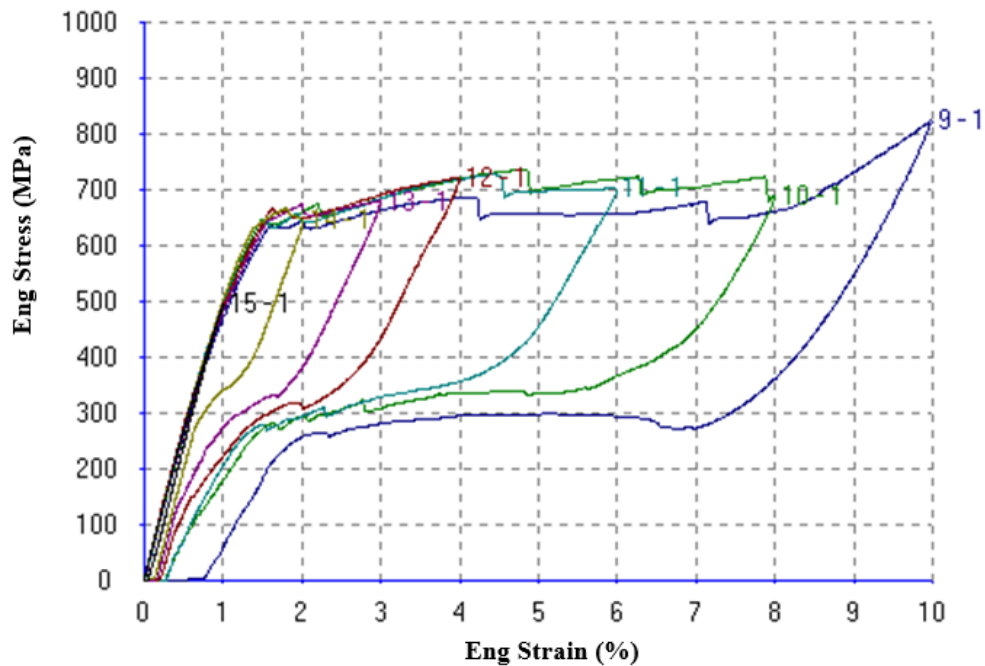
*Figure 3-15: Uniaxial tensile stress-strain results: 0.45 mm wire (Lot F5298520), single
load-unload cycles to various maximum tensile strains, at 37 C (one sample for each
load-unload cycle). Results show effects of loading history on unload path for
superelastic Nitinol in tension*

These tensile results show some similar behaviours for load-path dependence as were seen for compression:

When unloaded from increasing strains within the upper plateau region (up to 8 % tensile strain), the material unloads with decreasing modulus to a common unload plateau for superelastic strain recovery. There is minimal permanent set following strain recovery, showing that deformation is accommodated by elasticity and phase change up to 8 % tensile strain, with minimal plasticity.

For a higher maximum strain beyond the loading plateau (> 8 % strain), there is increased unload modulus and decreased unload plateau level during tensile unloading. There is also increased residual strain upon full unloading, showing that the material has undergone some plastic deformation and permanent set at this higher maximum strain level.

The above load-path dependence investigation for nitinol wire in compression and tension has implications for the behavior of stent components in bending.

Superelastic material in large deflection bending components will have complex stress distributions during unloading, with lower stresses in regions that have been subjected to maximum strains beyond the upper phase change plateau compared to those that have unloaded from within this upper plateau region. Further, regions that are unloading from strains beyond 1.4 % strain (i.e. that have undergone some level of phase change) may be at a lower stress level than regions that remained in the austenite elasticity region during loading, even though the former region is now at a higher strain. These complexities in stress state for a nitinol bending component during unloading mean that it is difficult to predict how uniaxial tensile and compressive stress-strain curve values will influence radial force of ring stents in service. Empirical testing at Vascutek (not reported here) suggests that initial elastic modulus of the material may have a greater influence on ring radial force and 'pulsatile loading' stiffness during unloading than the unload plateau stress level. This requires further investigation in order that an optimal wire specification might be identified in future.

Regions that have undergone strains beyond the upper plateau limit (> 4 % compression, > 8 % tension) in their loading history will experience some permanent set, which will affect subsequent unloading stress levels and may affect fatigue resistance.

Due to the load history dependence effects, nitinol stent components and devices should go through representative compaction loading history prior to verification testing.

3.4.4 ΔƐ Cycling in Compression

Test sets 11 − 13 (Table 3-2) were performed to characterize the cycling behaviour for different levels of ΔƐ load-unload cycling 'from below' (i.e. from the unloading stress-strain plateau) at 37 C. This is important for understanding the material response to in-vivo pulsatile loading, which is a key consideration for fatigue safety and device durability.

Figure 3-16 shows the results from test set 11 C (2 % Δε cycling 'from below'), with the 1st, 10th, 20th, 50th and 100th Δε cycle highlighted to investigate evolution and stabilization of the cyclic response. Results from one sample are plotted, as the other two sample results were seen to be almost identical.

Considering the figure 3-16 plots, it can be seen that each Δε load-unload cycle involves a hysteresis loop including upper and lower plateaus, showing that forward and reverse phase transformation is occurring for each cycle. As has been discussed in Section 2.2: Literature Review of Chapter 2, this would be expected to lead to low fatigue resistance.
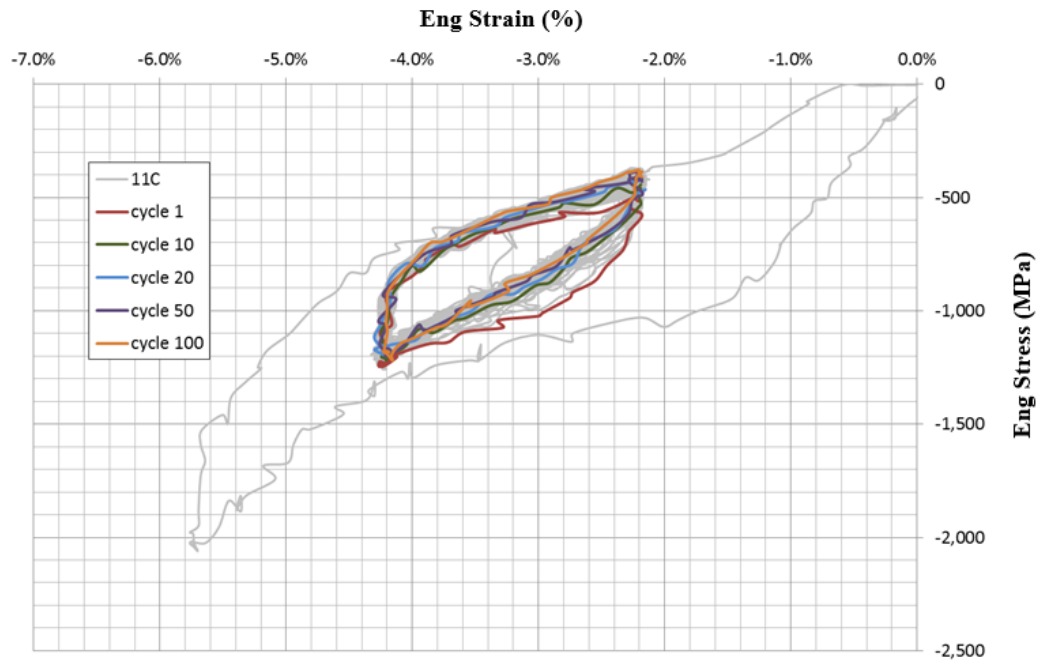
Figure 3-16: Cyclic stress-strain behavior of 1mm NiTi wire at 37 C in compression: 100 cycles at 2 % peak-to-peak Δε during unloading (Test Set 11, sample 11C)

Considering the different Δε cycles, cycle 1 shows an increase in stress up to a loading plateau that is lower than the upper plateau for the initial 'compaction' cycle (grey line), showing that phase change is being initiated at a lower stress when the material is re-loaded from the lower plateau. Unloading then involves an initial vertical stress drop, attributed to test rig friction (see Section 3.4.5 'Friction Investigation' for further analysis), and then unloading along a lower stress plateau similar to the original 'compaction' cycle level. (Note that removal of test rig friction from these results would be expected to reduce the loading modulus and upper plateau of each cycle and increase the lower plateau so that the hysteresis loop would be smaller.)

By cycle 10, the stress-strain path of the cycling material has changed, with a less pronounced loading 'plateau' rising to the same end point as cycle 1. This effect of larger Δε cycling was reported previously by Schlunn et al in ref (36). During unloading, there

is a slight drop in the plateau level compared to cycle 1. These behaviours show that the material undergoes cyclic softening between 1 and 10 cycles at this Δε level.

From cycles 10 to 100, the cyclic behavior is stable, with consistent load-unload paths.

Following the 100 cycles, the material then unloads to 0 stress along a lower stress plateau than was expected from the initial 'compaction cycle' path, and has increased residual strain (0.6 % compared with 0.05 % seen for sample 6A in figure 3-12). This shows that the cycling has caused permanent set in the material.

FE analysis of Vascutek's stent components (not reported here) suggests that the 2% Δε cycles are far higher than would be expected due to in-vivo pulsatile motion. These FE simulations suggest that maximum compressive Δε will be < 0.15% for a stent ring at worst-case pulsatile cycling conditions. In fact, the large 2% Δε cycles are more relevant to component behavior during repositioning of the device during the implant procedure, where there are unlikely to be more than three load-unload cycles. Therefore, it is considered that the test set 11 results (figure 3-16) are less relevant to high cycle fatigue performance of the implanted device.

Figure 3-17 shows results from test set 12 (1 % Δε cycling 'from below'), with the 1st, 10th, 20th, 50th and 100th Δε cycle highlighted to investigate evolution and stabilization of the cyclic response. Results from one sample (12C) are plotted, as the other two sample results were seen to be almost identical.

Here the results again show a hysteresis loop for each cycle, although there is no clear plateau during loading even for cycle 1. In unloading a lower plateau can be seen. Therefore, the hysteresis loops show evidence of phase transformation with each cycle. Again, there is a stress drop due to friction between loading and unloading for each cycle, which exaggerates the size of the hysteresis loops. The corrected results in figure

3-26 of the 'Friction Investigation' section below attempt to remove this friction effect, helping to clarify the material's cycling behavior.
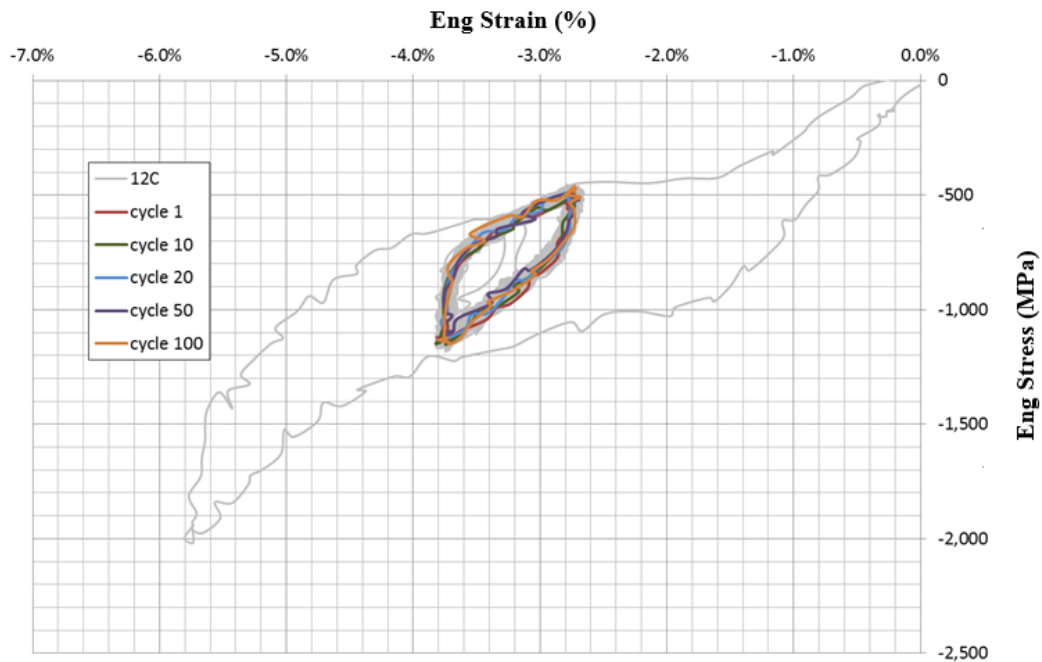
Figure 3-17: Cyclic stress-strain behavior of 1mm NiTi wire at 37 C in compression: 100 cycles at 1 % peak-to-peak Δε during unloading (Test Set 12, sample 12C)

An important finding from the above results is that the response is stable from 1 to 100 cycles, suggesting recoverable deformation with little permanent set at this Δε level. This is also seen in the minimal residual strain (0.3 %) following full unloading after 100 cycles. Again, though, this 1 % Δε cycle level is higher than anticipated for in-vivo pulsatile loading, and is therefore considered less relevant to high cycle fatigue performance of the implanted device.

Figure 3-18 shows results from test set 13 (0.4 % Δε cycling 'from below'), with the 1st, 10th, 20th, 50th and 100th Δε cycle highlighted to investigate evolution and stabilization of

the cyclic response. Results from one sample (13C) are plotted, as the other two sample results in the test set were seen to be almost identical.

Figure 3-18: Cyclic stress-strain behavior of 1mm NiTi wire at 37 C in compression: 100 cycles at 0.4 % peak-to-peak Δε during unloading (Test Set 13, sample 13C)

The figure 3-18 plot shows the stress-strain path that is taken by the Nitinol wire material when it is compressed to a high 'compaction' strain (5.5 %), unloaded to a 'deployment' strain (~ 3 %) and then re-loaded to a slightly higher strain (~ 3.4 %) before undergoing 0.4 % unload-load cycles. The path the material takes as it is re-loaded between the 'deployment' strain of 3 % and the higher strain of 3.4 % demonstrates stiff elastic deformation, rather than the compliant deformation seen during reverse phase change (lower stress plateau). This is an important characteristic of nitinol for designing fatigue-safe stent components, providing the component with radial resistive stiffness to limit cyclic deformation due to vessel pulsatile loading.

In terms of the effects of cycling on the material, figure 3-18 shows that at 0.4 % $\Delta\varepsilon$ level, the response is stable from cycles 1 to 100. This is important, as it means the material's relevant compressive stress-strain behavior for loading and unloading due to pulsatile motion can be characterized from a single load-unload $\Delta\varepsilon$ cycle.

Considering the cyclic path shape in figure 3-18, each load-unload cycle includes a loop. However, the vertical stress drop at the start of unloading for each cycle suggests that this loop is purely a result of test rig friction. Figure 3-27 in the 'Friction Investigation' section shows the 'corrected' results, where the cycles show linear elastic loading and unloading at this $\Delta\varepsilon$ level. These results show that for stent components under anticipated pulsatile loading conditions ($\Delta\varepsilon \leq 0.15$ %), the material will load and unload with linear elasticity and will not undergo phase change with each pulsatile cycle. These characteristics are desirable for fatigue resistance. Again, the stability of the cycling and the low residual strain (~0.1 %) following full unloading show that this level of $\Delta\varepsilon$ cycling causes little or no permanent set in the material.

For comparison, figures 3-19 and 3-20 show tensile stress-strain plots for Vascutek's NiTi#1 wire material including $\Delta\varepsilon$ cycling 'from below' during unloading.

From figure 3-19 it can be seen that at 1 % $\Delta\varepsilon$ cycling 'from below' there is a hysteresis loop including plateaus beyond 0.5 % $\Delta\varepsilon$ in loading and unloading. This suggests that for $\Delta\varepsilon > 0.5$ %, phase change is occurring. It is also interesting to note that the upper plateau of the cycling material is lower than the original upper plateau of the 'compaction' cycle. As with the compressive tests, this shows that the phase change is being initiated in tension at a lower stress when the material is re-loaded from the lower plateau.
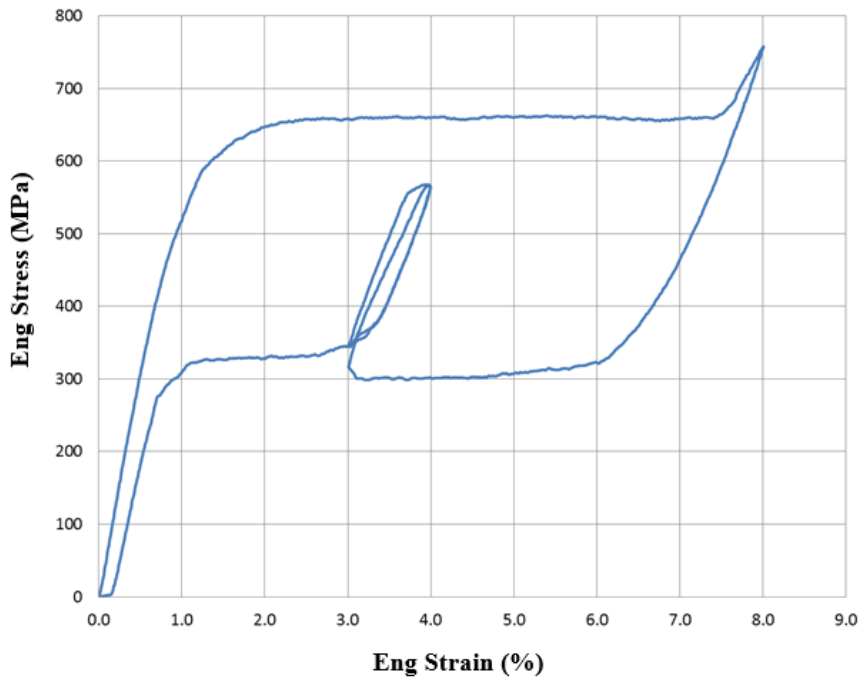
Figure 3-19:   Uniaxial tensile stress-strain plot with single 1 % peak-to-peak Δε load-unload cycle during unloading: 0.14 mm wire (Lot F5208630) at 37 C
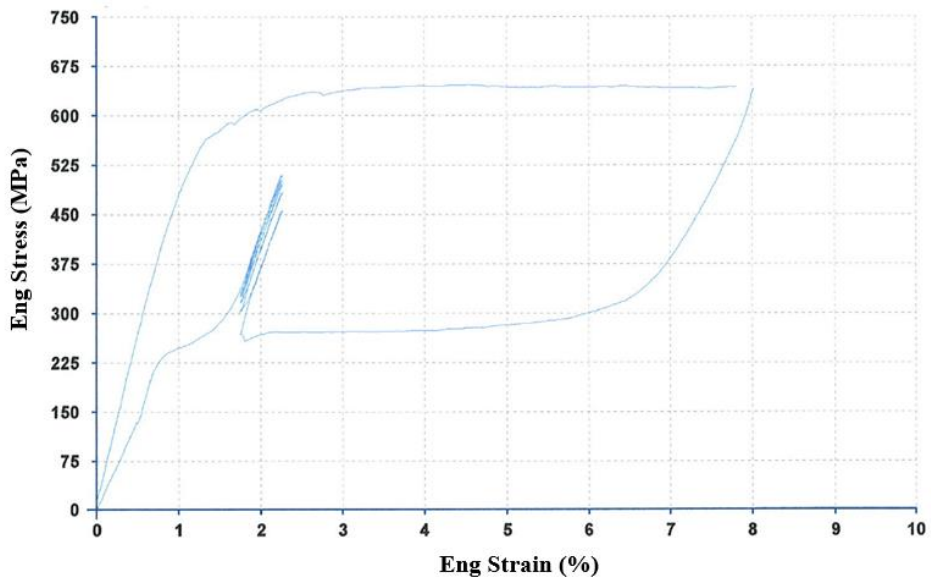
Figure 3-20:   Uniaxial tensile stress-strain plot with ten 0.5 % peak-to-peak Δε load-unload cycles during unloading: 0.22 mm wire (Lot F5204730) at 37 C

In this test, only one $\Delta\varepsilon$ cycle was performed in order to establish the maximum $\Delta\varepsilon$ before phase change is initiated – found to be 0.5 %. Therefore, no conclusions about cyclic stability can be drawn. However, it can be seen even from this single cycle that some cyclic 'hardening' is occurring, as final unload to 0 follows a slightly higher unload stress plateau path than that seen prior to the $\Delta\varepsilon$ cycle.

Figure 3-20 shows uniaxial tensile testing performed previously at Vascutek with 0.5 % $\Delta\varepsilon$ cycling 'from below'. Ten $\Delta\varepsilon$ cycles were used prior to final unloading. The results show that at this $\Delta\varepsilon$ level, all cycles have the same cycling modulus with a value between the initial austenite modulus and the martensite unload modulus. There are no plateaus or hysteresis loops, suggesting no phase change is occurring in each cycle. There is some evidence of cyclic hardening during the first 5 cycles, with increased stress levels for each cycle, after which the load-unload path is stable. The stability of the cycling modulus means that for material characterization, the results from the first cycle can be used when considering pulsatile fatigue resistance (as was seen for 0.4 % $\Delta\varepsilon$ cycling in compression).

3.4.5 Friction Effect Investigation

In all of the above uniaxial compression test results, the stress-strain curves show a vertical drop in stress when changing from loading to unloading. It was considered that this was not an effect of the material behaviour itself, but was likely a result of frictional forces in the wire holders. It was therefore decided to investigate the presence and magnitude of friction forces in the test set-up, with the aim of removing these forces from the results to obtain the true material response to compressive loading.

Initial testing was performed to verify the presence of friction by using the set-up shown in figure 3-2 and controlling the displacement to give a 10 second 'dwell' step every 1 % strain during loading and unloading. This was performed up to a maximum 6 % nominal strain. At zero load and at each subsequent 'dwell' position, attempt was made to

manually slide the stabilizing sheath (shown in figure 3-1) relative to the top and bottom holders. This test was repeated with and without lubricant ('Lubritech' Moly-paul 516 Extreme high temperature anti-seize compound) on three different samples. In every case, it was found that the sheath would glide freely over the holders at the zero load position, but for all subsequent strain positions the sheath could not be moved by hand. After full unloading, the stabilizing sheath could again glide freely over the holders. This behaviour was found whether lubricant was used between sheath and holders or not. In fact, even at 50 N applied compressive load (strain < 0.1 %), the sleeve could not be easily moved by hand. It is therefore considered that when the 1 mm nitinol wire is compressed using the set-up shown in figures 3-1 and 3-2, there is friction between the stabilizing sheath and the holder cylinders that will affect the load-deflection results (and the derived stress-strain results). Figure 3-21 shows a schematic diagram explaining the likely reason for these frictional forces: angular misalignment between the top and bottom holders.
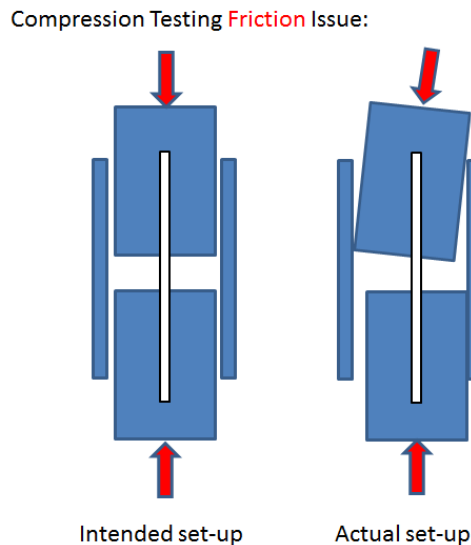
Figure 3-21: schematic diagrams showing intended set-up (left) with ideal alignment of compresive test rig and 'real world' set-up (right) with some degree of angular misalignment between top and bottom holders, which will cause friction between the holders and the stabilising sheath.

Having established the presence and likely cause of friction in the tests, the next step was to try and quantify the effects of friction on the compression results. Test sets 1, 4 and 7-10 from table 3-2 were repeated, with the exception that 10 second 'dwells' were used to hold the sample stationary at certain positions during loading and unloading. The purpose of this was to investigate whether the applied force would change when motion was stopped and re-started, and to quantify these force changes. The assumption was that when motion was stopped, the 'static' state of the test rig would allow measurement of the compressive stress of the material sample itself at that displacement position.

Figure 3-22 shows the stress-strain results from these tests performed at room temperature (17 C). For samples 1 to 3, dwells were used every 2 % nominal strain during loading and unloading, with maximum strain of 6 %. For sample 4, dwells were used every 2 % nominal strain during loading to 6 % and then every 1 % nominal strain during unloading.
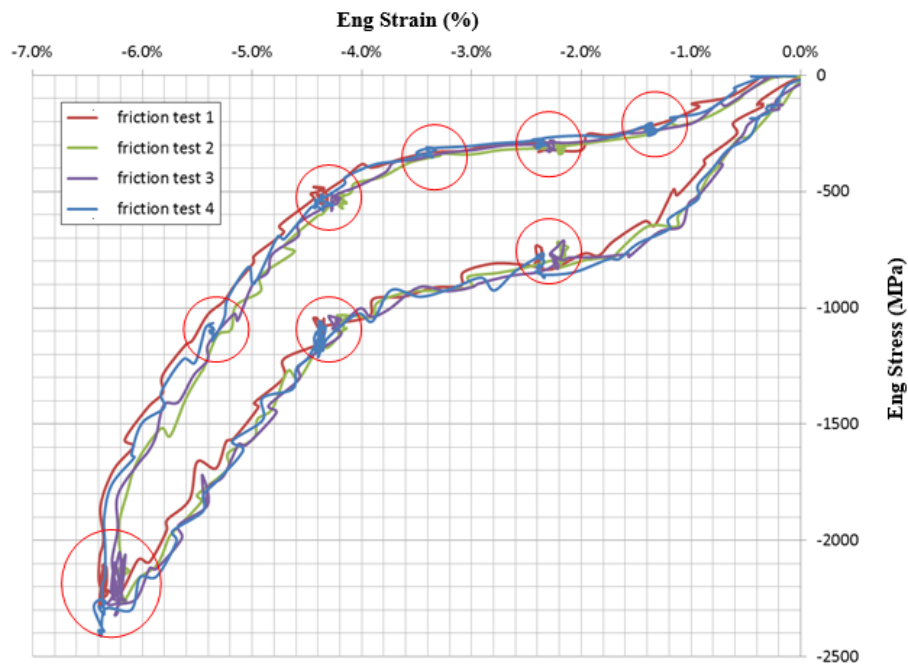
Figure 3-22: Compressive stress-strain curve for friction investigation: 1mm wire, single load-unload cycle to 6 % compressive strain with 'dwells', at 17 C (4 samples). Static 'dwell' points are circled.

Figure 3-23 shows the stress – strain results from friction investigation tests at 37 C to various strain excursions, with dwells used every 1 % nominal strain during loading and unloading.
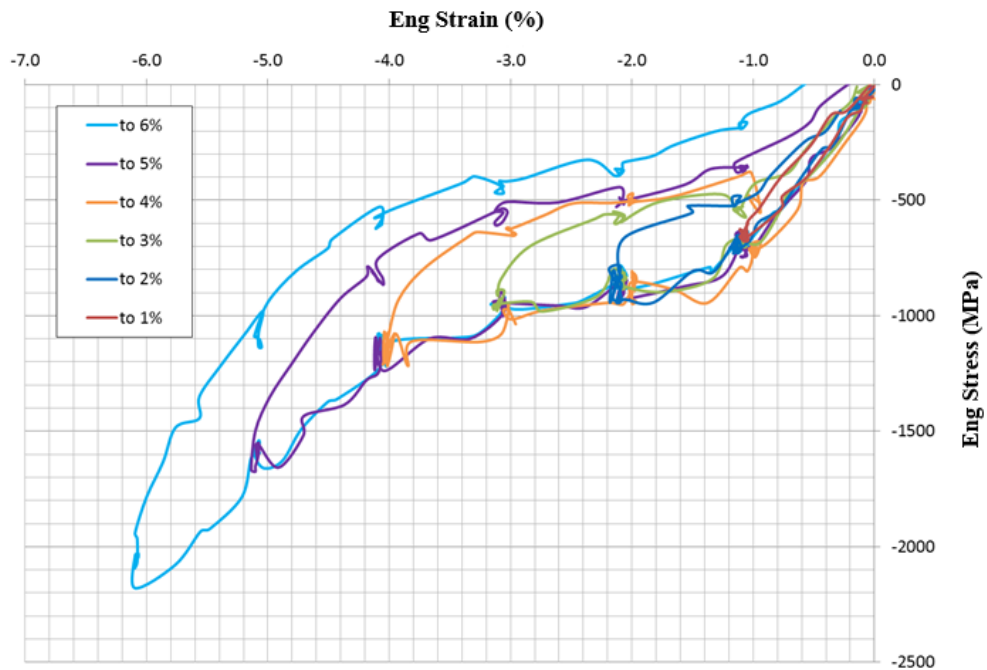
Figure 3-23: Compressive stress-strain results for friction investigation: 1 mm wire, single load-unload cyles to various compressive strains with 'dwells', at 37 C (6 samples, one sample for each maximum strain). Static 'dwell' points are seen by vertical stress changes on plot.

The friction investigation results of figures 3-22 and 3-23 show that during loading, the measured (applied) force drops when displacement is stopped. During unloading, the force increases when displacement is stopped. These force changes can be understood in terms of friction effects by considering the following conditions:

For Loading:

For compressive loading displacement to occur:

$$F_{applied} > F_{material} + F_{friction\ load}$$

It follows that if the friction force '$F_{\text{friction load}}$' is removed (i.e. displacement is stopped), it will take a lower applied force 'F_{applied}' to balance the force from the material's internal stresses 'F_{material}' and satisfy the following condition for static equilibrium:

$$F_{\text{applied}} = F_{\text{material}}$$

For unloading:

For compressive unloading displacement to occur:

$$F_{\text{material}} > F_{\text{applied}} + F_{\text{friction unload}}$$

It follows that if the friction force '$F_{\text{friction unload}}$' is removed (i.e. displacement is stopped), it will take a higher applied force 'F_{applied}' to balance the force from the material's internal stresses 'F_{material}' and satisfy the following condition for static equilibrium:

$$F_{\text{applied}} = F_{\text{material}}$$

Having gained some insight into the effects of friction in loading and unloading, it was decided to use the 'friction investigation' test results (figures 3-22 and 3-23) to quantify the test rig friction forces so that the previous compression testing results could be 'corrected' to give a better representation of the material properties. To determine the values to use for this 'result correction', the data presented in figures 3-22 and 3-23 was used to find the % stress change at each 'dwell' point. These values from all the different tests were then used to define a representative % stress change value for each nominal strain in loading and unloading. It was found that these values could be categorized according to strain range, corresponding to the 6 distinct 'stiffness' regions seen in the compressive stress-strain curves. Table 3-3 shows the resulting '% stress change' values against strain range region.

Strain Range	Loading / Unloading	% Stress Change
0 – 1.5 %	L	6.75 % ↓
1.5 – 3.8 %	L	10 % ↓
3.8 – 6.3 %	L	7.2 % ↓
6.3 – 3.6 %	U	8.6 % ↑
3.6 – 1.2 %	U	12.5 % ↑
1.2 – 0 %	U	6.75 % ↑

Table 3-3: '% stress change' correction values derived from friction investigation testing, for estimation of material compressive properties without the influence of test rig friction

These correction values were then used to modify the results data from the original tests listed in table 3-2, yielding 'corrected' stress-strain curves for test sets 1 to 13. Figure 3-24 shows 'corrected' results from test sets 2 and 3: compression testing at 17 C.
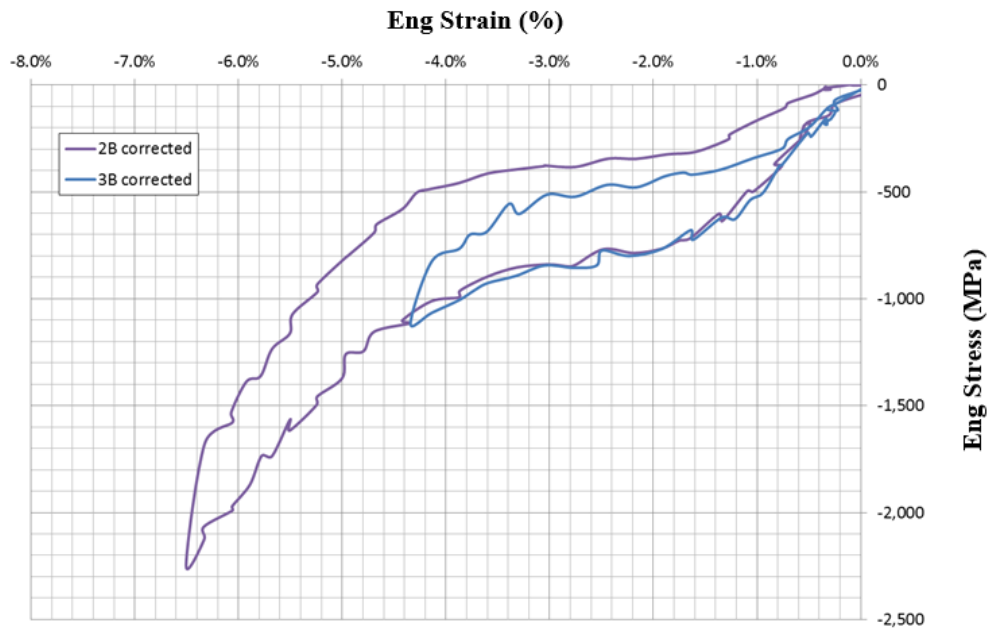
Figure 3-24: 'corrected' stress-strain results for test sets 2 and 3, from data modified to remove test rig friction forces: 1mm wire, compressive load-unload cycles, at 17 C

Comparing figure 3-24 (corrected) with figures 3-7 and 3-8 (original), removal of friction effects has decreased initial loading modulus, upper plateau level, 2nd loading modulus and 2nd unloading modulus, and has increased lower plateau levels and final unloading moduli.

Figure 3-25 shows 'corrected' results from test sets 4 and 6-10 of table 3-2: compression testing at 37 C.
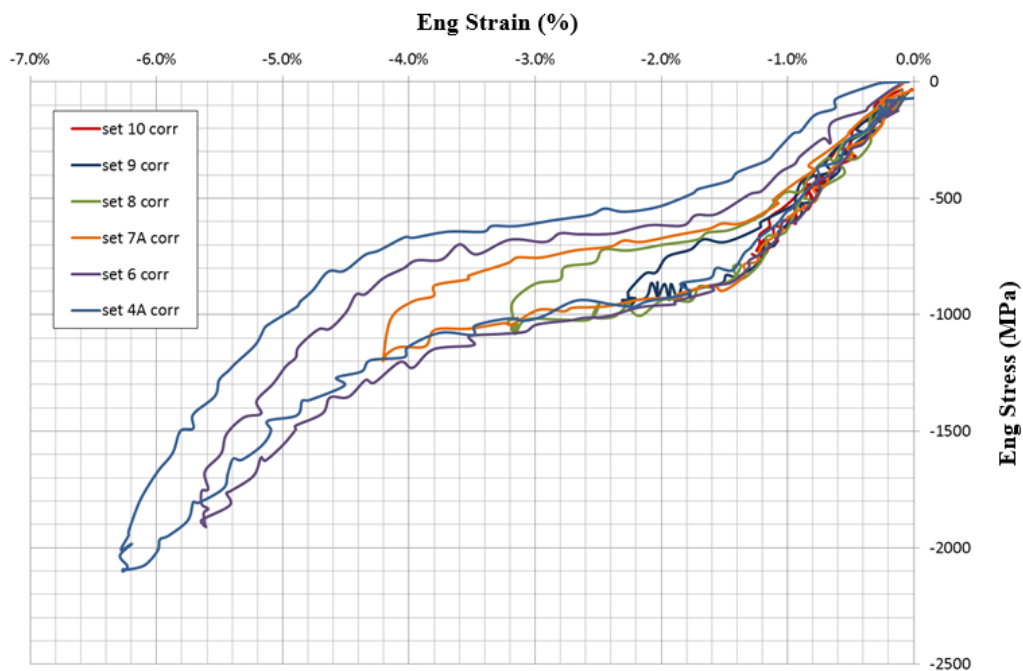
Figure 3-25: 'corrected' stress-strain results for test sets 4 and 6-10, from data modified to remove test rig friction forces: 1mm wire, compressive load-unload cycles, at 37 C

Comparing figure 3-25 (corrected) with figure 3-14 (original), removal of friction effects has again decreased initial loading modulus, upper plateau level, 2nd loading modulus and 2nd unloading modulus, and has increased lower plateau levels and final unloading moduli.

Figures 3-26 and 3-27 show 'corrected' results from test sets 12 and 13 of table 3-2, for 1.0 % and 0.4 % Δε cyclic testing 'from below' at 37 C. For clarity, only the 1st and 100th cycles are shown in each case. The main findings from these corrected plots are that stress plateaus and hysteresis are evident in compression for cyclic Δε levels > 0.5 % (seen in figure 3-26). For the 0.4 % Δε cycling (figure 3-27), the material path can be considered linear elastic, with stable cycles of modulus 55 GPa. These results suggest that at cyclic Δε levels < 0.5 % 'from below' in compression, phase transformation does not occur, with cyclic load-unload deformation being accommodated by austenite and martensite elasticity.
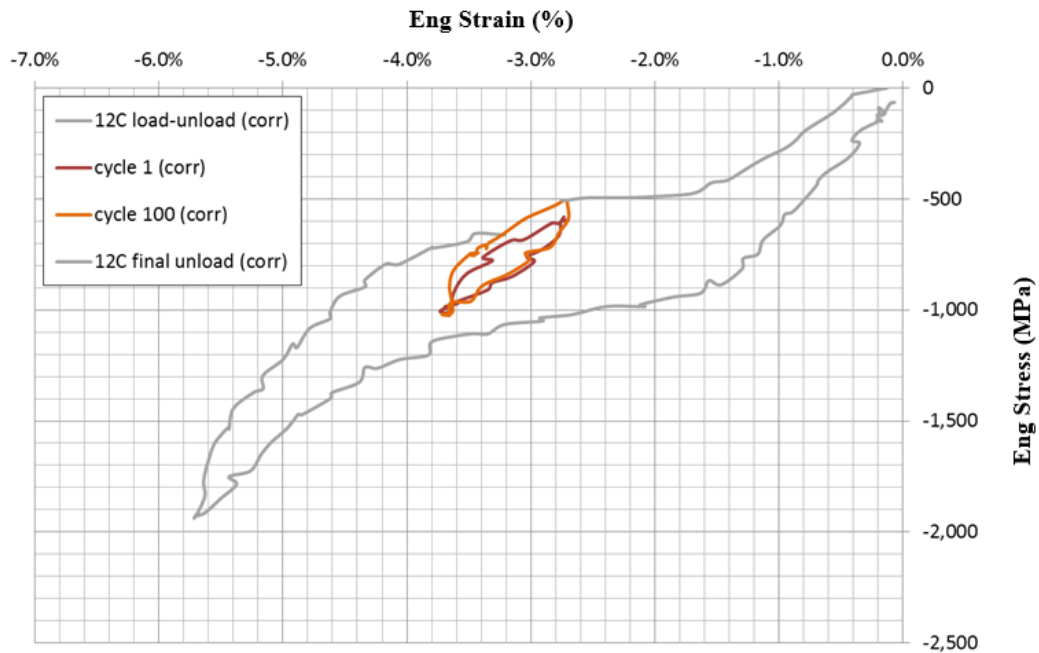
Figure 3-26: 'corrected' compressive stress-strain plot for 1 % peak-to-peak Δε cycling 'from below': 1 mm wire, at 37 C. The results are produced from data modified to remove test rig friction forces.
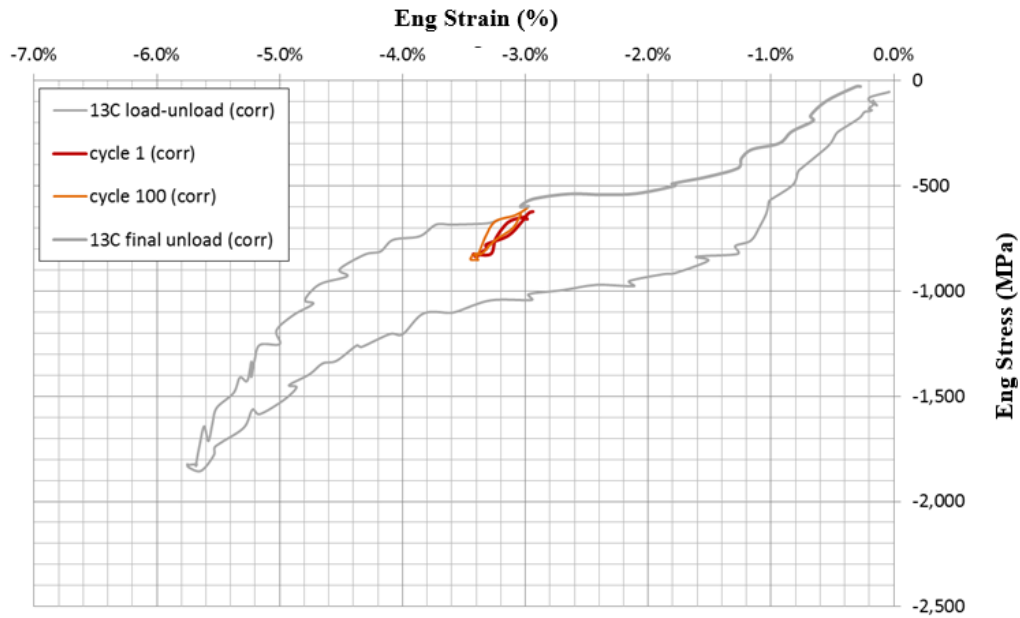
Figure 3-27: 'corrected' compressive stress-strain plot for 0.4% peak-to-peak Δε cycling 'from below': 1mm wire, at 37C. The results are produced from data modified to remove test rig friction forces

3.4.6 Compressive – Tensile Stress-Strain Plots

From the results presented in this chapter, it is useful to plot the compressive and tensile stress-strain results together, giving a clear representation of the tensile-compressive asymmetry. In order that these plots can provide relevant values for material modeling (as will be reported in Chapter 6), true stress and true strain values were calculated from the nominal data using the following equations:

$$\varepsilon_{true} = \ln (1 + \varepsilon_{nom})$$
$$\sigma_{true} = \sigma_{nom} * (1 + \varepsilon_{nom})$$

Figure 3-28 shows the (true) stress-strain results for the material in uniaxial tension and compression at 37 C.
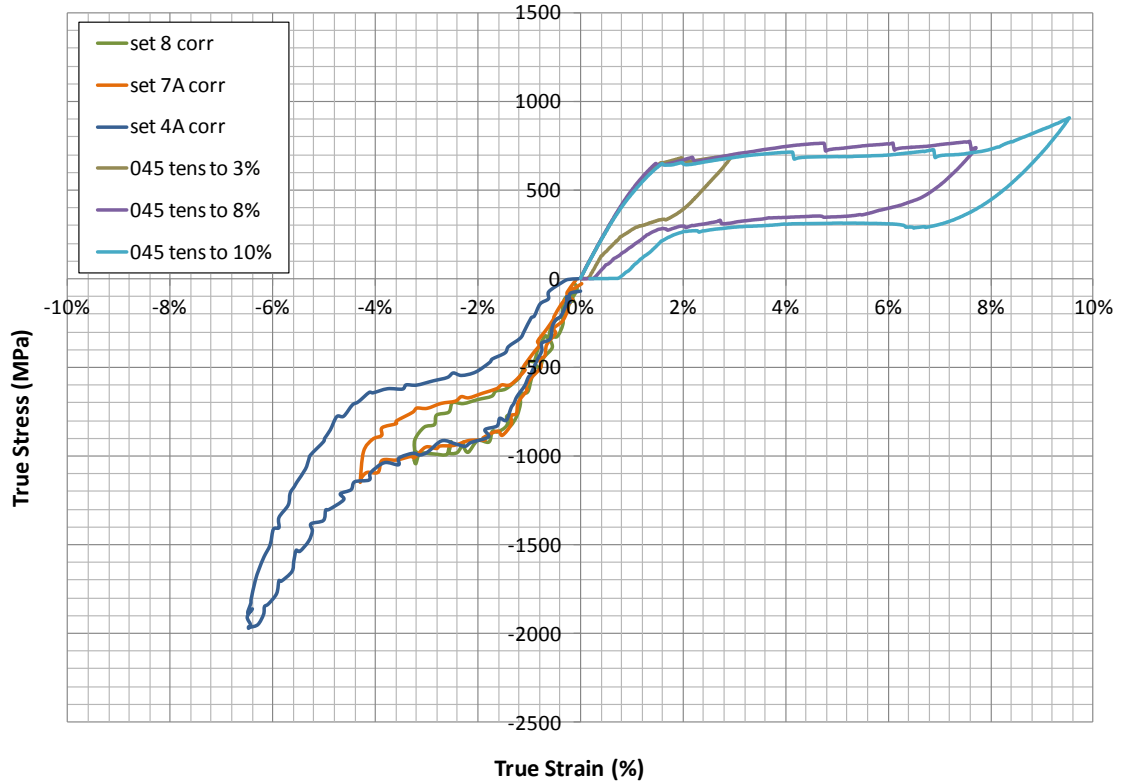
Figure 3-28: Uniaxial tensile and 'corrected' compressive true stress-strain results at 37 C: from tensile testing on 0.45mm wire and compressive testing on 1 mm wire. The plots show load-unload cycles to various maximum strains.

The high strain tensile plots from figure 3-28, from testing performed at Vascutek, were compared against data from Fort Wayne Metals' (FWM) Certificate of Conformance (CoC) for the material. The FWM testing involves loading the material to 8% nominal strain, unloading to zero and then loading until failure. Figure 3-29 shows the FWM plot up to 10 % strain overlaid with the high strain tensile plots from Vascutek's testing. The results show good agreement for initial elastic modulus and for stress plateau levels. However, the Vascutek results show greater residual strain after unloading from 8 %, and also show a lower '2nd loading modulus' beyond 8 % nominal strain than the FWM plot. These differences are attributed to slippage of the wire sample in the grips used by Vascutek at high tensile strains. For this reason, the FWM CoC data will be used to find

values for 2nd modulus and for residual strain after unloading from 8 %, for use in material modelling (as will be reported in chapter 6). The unload stress plateau values from Vascutek's high strain testing are still reliable, as these are not affected by sample slippage.
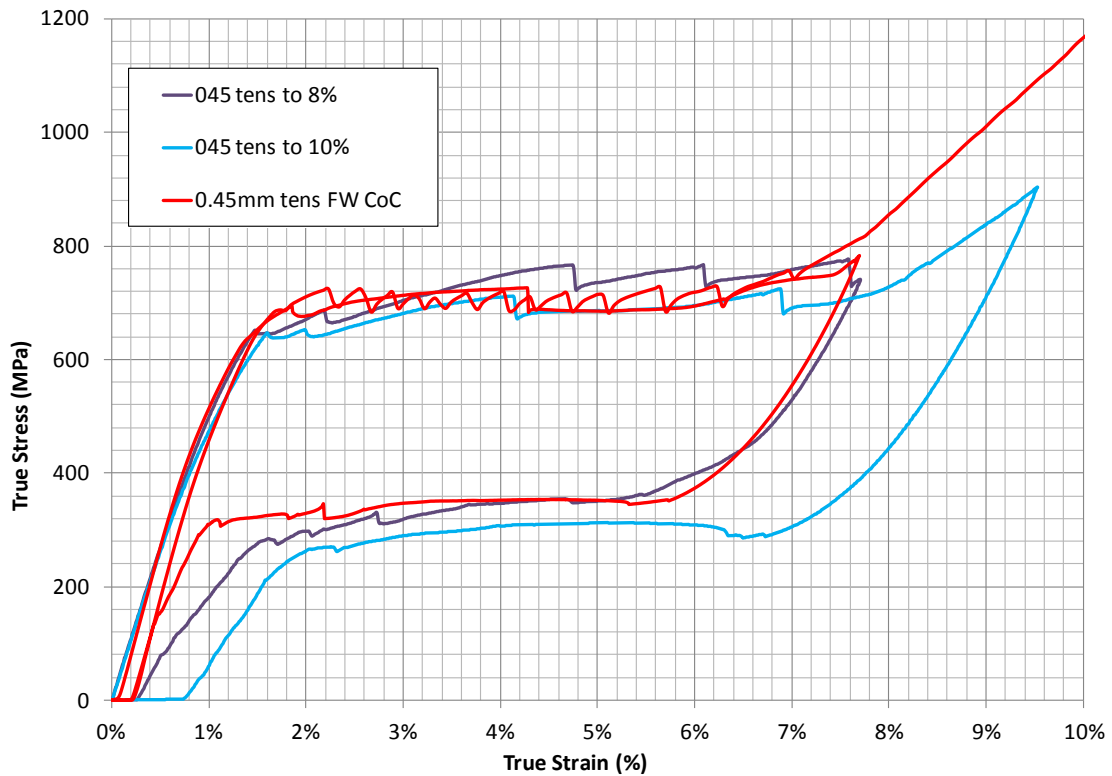
Figure 3-29: Uniaxial tensile stress-strain results at 37 C: from tensile testing on 0.45mm wire, performed at Vascutek (blue and purple plots) and at Fort Wayne Metals (red plot).

Figure 3-30 shows plots of uniaxial tensile and corrected compressive data from the Nitinol wire testing at Room Temperature (17 C for compression, 23 C for tension) reported here, with results converted to true stress and true strain.
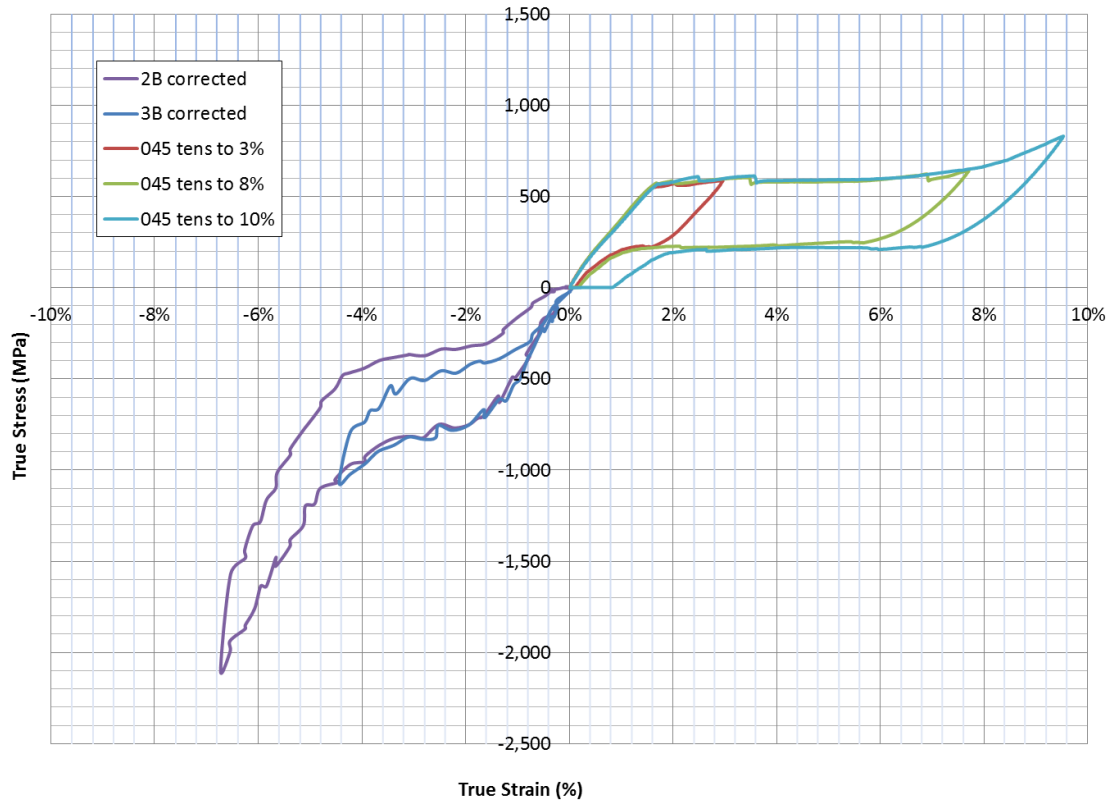
Figure 3-30: Uniaxial tensile and 'corrected' compressive true stress-strain results at Room Temperature: from tensile testing on 0.45 mm wire at 23 C and compressive testing on 1 mm wire at 17 C. The plots show load-unload cycles to various maximum strains.

3.5 Improved Compression Testing Approach: Initial Feasibility Testing and Results

It is clear that future compression testing on Nitinol wire should focus on elimination of the friction forces due to the test set-up reported in this chapter. To this end, an alternative testing approach was investigated, which eliminates the requirement for lateral support holders. Initial feasibility of this approach has been performed by the author at University of Strathclyde in collaboration with another PHD student.

The proposed improved compression test method uses a small diameter 'equivalent processing' compression test sample cut to a short length, giving a suitable L/d ratio to avoid buckling or shear. For feasibility testing, 1 mm diameter samples were successfully cut to lengths of 3 mm using EDM machining, giving ends perpendicular to the wire axis. In the feasibility test set-up, the miniature test sample was held (with tweezers) between the compression plates of the uniaxial Load-Deflection test machine (described below), and the plates were moved together until a small pre-load was applied to hold the sample in place. Lubricant was used between the sample ends and the plates, to allow lateral expansion of the ends during compression.

Essentially, this approach is a scaled-down version of the 'large diameter sample, bulk material' compressive testing approach used by previous investigators (e.g. (4), (19), (21)) as described in Chapter 2. However, the Literature Review found no previous reports of the proposed small diameter, short sample length compression testing. The avoidance of this approach in previous investigations may be due to two issues:

- Requirement for high resolution test equipment that would be capable of accurate position control and strain measurement for such small samples.
- Concerns over end-effects on the compressive results

On the first point, a review of the equipment available at University of Strathclyde was performed and two potential candidates were found to meet the required specification for superelastic compression testing of ø1 mm x 3 mm NiTi wire samples, as outlined in Table 3-4 below. On the second point, it was proposed that in-situ microscopy could be used during compression testing to capture the shape change of the sample, and to assess whether any 'barreling' or buckling deformation occurs. For this reason, it was decided to use the Deben Microtest 2000 equipment for the compression testing, as this allows for in-situ loading with Scattered Electron Microscopy (SEM).

Feature	Required Specification	Instron 5969 series (ref 64)	Deben Microtest 2000 (ref 65)
Stiff support frame	Electromechanical system (not hydraulic)	Electromechanical (180 kN/mm)	Electromechanical
Test type	(quasi) static	(quasi) static	(quasi) static. Require compression clamps option
Max force	> 1.5 kN	50 kN	2 kN
Position control	< 3µ (0.1% strain)	0.0268µ	unknown
Displacement measurement resolution	< 0.3µ (1% of 1% strain)	±10µ position measurement accuracy (*)	Resolution 3µ, accuracy 10µ
Minimum speed (for $10^{-4}s^{-1}$ strain rate)	0.018 mm/min	0.001 mm/min	0.033 mm/min
Operating temperature range	10 – 37C (10 – 60C preferred)	10 – 38C	-20 to +160C possible with Peltier heating
*Following further discussions with Instron, it was found that displacement measurement control can be improved by attachment of an LVDT accessory for compressive testing. Purchase of this accessory would allow the Instron 5969 machine to meet all the requirements of the specification.			

Table 3-4: Required specification of equipment for proposed 'small diameter, short sample' compression testing, and specification of equipment available in University of Strathclyde's Advanced Materials Research Lab (AMRL)

The Deben Microtest 2000 tension / compression test stage is shown in figure 3-31. To enable the short 3 mm sample to be tested, compression plates were made and attached to the test stage. These plates were heat-treated to have a hardened surface to avoid deformation of the plates themselves during testing. As no heater was available for this equipment in the AMRL, the feasibility testing was only performed at ambient room temperature of 23 C.
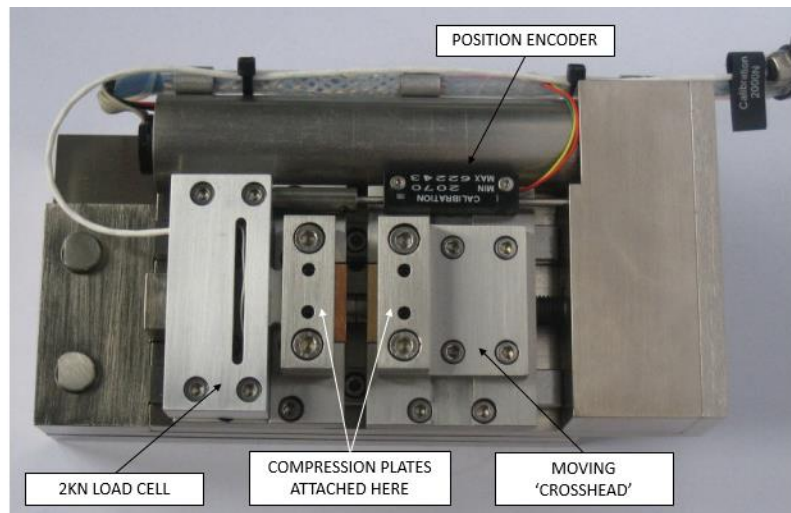
Figure 3-31: Deben Microtest 2000 tension / compression test stage

The test stage with the ø1 mm x 3 mm NiTi#1 compression sample was set up in the SEM equipment and displacement control was used to move the cross-head by 0.21 mm, to give a nominal compressive strain of 7 %. Figure 3-32 shows SEM images with measurements of the undeformed NiTi sample and of the compressively deformed sample after 0.21 mm crosshead displacement. These images and measurements provided two important results. Firstly, the compressed sample is uniform in width along its length, showing that the ends have been able to expand laterally, with no evidence of barreling or buckling of the sample. This provides confidence that the sample is undergoing pure compression, dealing with concerns over end effects in the results. Secondly, the sample length measurements show that the sample has only undergone 0.16 mm of compressive deformation, or 5.3 % engineering strain, for the 0.21 mm crosshead displacement. This shows that there is some compliance in the test stage / compression plates system, and means that crosshead displacement cannot be used to accurately calculate strain for the sample. Future development of this test would therefore need to implement a suitable method of sample strain measurement – for example, using Digital Image Correlation (DIC) of the SEM images.
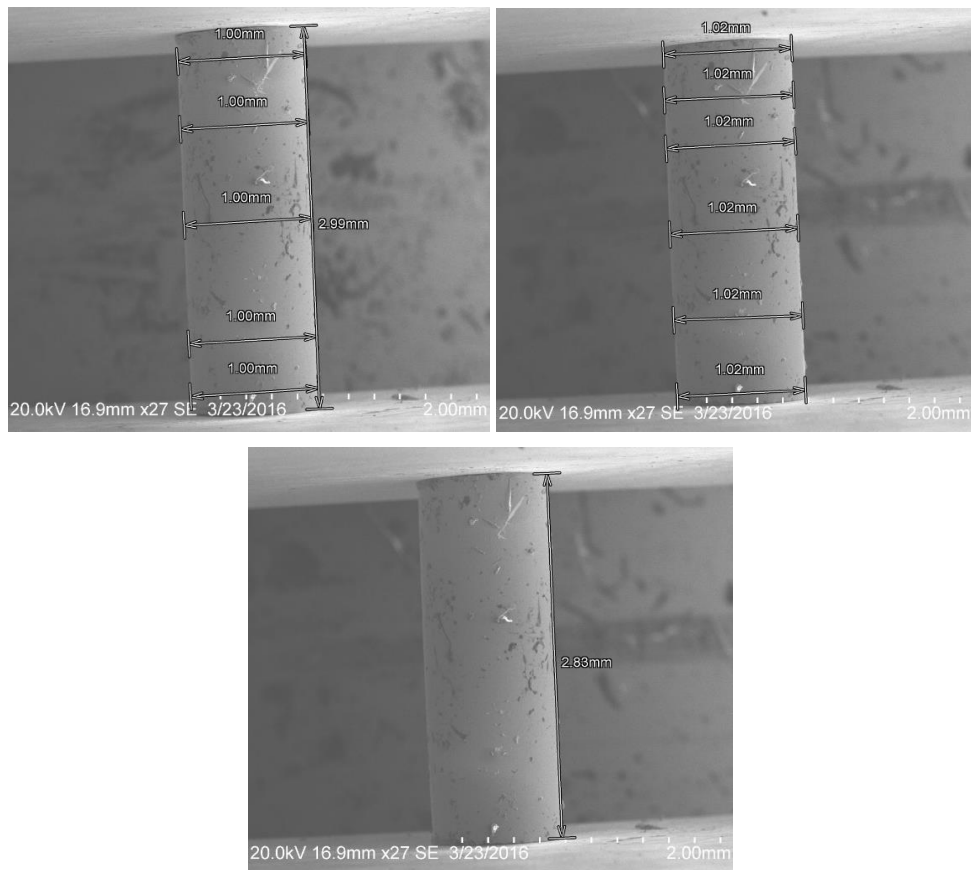
Figure 3-32: SEM images of NiTi#1 compressive test sample on Deben Microtest 2000 test stage. Undeformed sample with width and length measurements (top left); Deformed sample width measurements (top right); Deformed sample length measurement (bottom).

Despite the restriction on strain measurement, the compressive test could still be used to find the stress values at the transformation start and finish points for the superelastic material under compression, which would allow a level of validation of the 'corrected' stress values derived in the preceding section. Figure 3-33 shows the true stress plotted against the crosshead displacement for this test. Here, the compressive 'superelastic flag' shape can clearly be seen, showing the effects of forward and reverse phase transformations, with load-unload stress hysteresis.
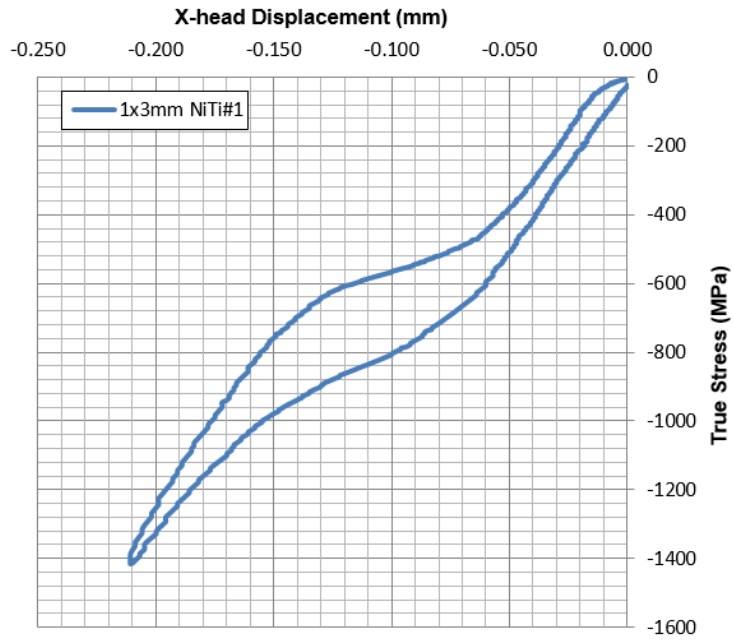
Figure 3-33: Uniaxial compressive stress-displacement results for 1 mm diameter x 3mm length wire sample, tested at 23 C using Deben Microtest 2000
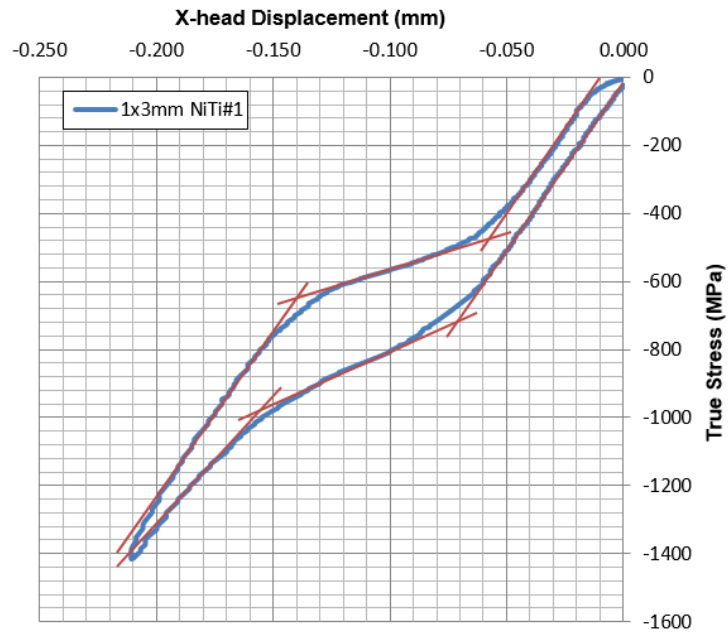
Figure 3-34: Compressive test results of figure 3-33 reproduced with lines overlaid to identify transformation stresses at line intersection points

In figure 3-34, lines have been overlaid on the graph, so that the line intersection points can be used to find the start and end transformation stresses in loading and unloading. This line-overlay approach is used later in chapter 6 to obtain key parameters from the 'corrected compressive' results reported in the preceding section (see chapter 6, figure 6-9 and table 6-3). The transformation stress results from both the 'corrected' results and the Deben Microtest results are shown below in table 3-5 for comparison. Note that in both tests, the 1mm diameter Nitinol material was identical, and it was only the specimen length that differed between the test methods.

NiTi#1 Compression Stress Result Parameter at Room Temp	From 'corrected' results of previous test method (MPa)	From new 'Microtest' method results (MPa)
Loading 'plateau' start stress	700	720
Loading 'plateau' finish stress	975	980
Unloading 'plateau' start stress	560	650
Unloading 'plateau' finish stress	350	480

Table 3-5: Transformation stress values found from 'Deben Microtest' compression testing, compared against values found from 'corrected' results of previous test method

Additional testing was performed using the Deben tester with dwells included during loading and unloading, to see if load drops (during loading) or rises (during unloading) would be observed with this test set-up. It was seen that no significant load changes were seen during the dwells, giving evidence that the load changes seen during dwells in the preceding testing could indeed be attributed to relief from test holder friction, and were not inherent to the specimen material behavior.

Referring to table 3-5, the forward transformation stress values (during loading) match closely, giving evidence that the corrected stress-strain results in loading give a good

representation of the true material behavior. For the reverse transformation, the new 'Microtest' method returns considerably higher values for the unloading stresses than the corrected results. This suggests that an even greater correction factor should have been used to account for friction and misalignment effects during unloading in the previous results (figures 3-24 and 3-30).

Despite these differences for the unloading results, for consistency the 'corrected' results of figures 3-28 and 3-30 will be used in chapter 6 to obtain inputs for FEA, due to the fact that the new testing has not been performed at 37C temperature, and due to the lack of an accurate strain measurement method for the new test. Clearly, though, future effort should be made to address these issues so that this promising new testing approach can be advanced.

3.6 Conclusions

The compressive tests reported here, together with relevant tensile test results, have allowed investigation of superelastic nitinol wire relevant to the in-service operation of stent graft components. The key findings of this investigation are summarized below.

1 mm diameter wire has been produced by Fort Wayne Metals with equivalent mechanical properties to thin nitinol wire (0.1 to 0.45 mm diameter) used in Vascutek's stent components. This 1mm wire was used for compressive testing to 6 % strain without buckling, using a 19.5 mm length in holders designed to prevent lateral movement.

In the particular test set-up used, any angular misalignment in the wire holders leads to friction forces affecting the measured load-deflection (and derived stress-strain) results. By investigating and accounting for these friction forces, results were obtained that better represent the material's compressive stress-strain response. Additional feasibility work using a new compression test method, with short material samples to avoid the problems associated with wire holder friction, helped to verify the data correction

method by showing that load changes during dwells in the previous method could indeed be attributed to friction (and not material stress relaxation). The new 'micro test' method also provided stress-displacement data for validation of the 'corrected' compression results obtained in this chapter Initial results from the new method show this to be a promising route for future compression test development.

The testing reported in this chapter has led to a greater understanding of the particular Nitinol material under study, yielding important knowledge for its use in stent design and development. Compressive-tensile asymmetry of the Nitinol material can clearly be seen from the results. In compression, the 'effective' initial modulus is higher than in tension at room and body temperatures, due to the presence and effects of R-phase. The material's forward phase transformation (austenite to martensite) is initiated at higher stress in compression than in tension, and the upper 'plateau' is not flat. The 'plateau' length (representing the total transformation strain) is shorter in compression, meaning that plastic deformation starts to occur at a lower strain (> 4 % in compression compared to > 8 % in tension). For unloading, the unload moduli are higher in compression than in tension, and the superelastic unload stress 'plateau' (again not flat in compression) is also higher in compression. The tensile-compressive asymmetry is important to consider for stress-strain analysis of bending nitinol components, as will be seen in chapter 5.

Compaction of stent ring components is anticipated to involve maximum compressive strains in excess of 4 % at certain regions of the wire, therefore causing permanent set in the material. This could have an effect on radial force, and it is therefore recommended that radial force or sealing verification testing is performed on components or devices that have undergone representative compaction strain history.

Worst case compaction history of 3 compactions at room temperature is anticipated to cause load-unload cycling up to 6 % maximum compressive strains for certain regions of stent components in service. Testing has shown that this large strain cycling at room

temperature will result in a low level of permanent set (< 0.6 %) and has no effect on the subsequent compressive stress-strain response in loading and unloading. Again, though, verification testing of components should include this 'worst-case' pre-processing.

The stress-strain response of the nitinol wire in compression is highly temperature dependent. In the range 17 C to 55 C, initial modulus increases by ~ 0.5 GPa/C and upper and lower stress plateaus increase by ~ 7.5 GPa/C. This means that stent components will have higher radial (sealing) force and resistance to pulsatile loading at body temperature than at room temperature, and therefore simulated use testing of devices should be performed at representative service temperature. At 55 C, there is increased permanent set following high strain loading (> 4 %) compared to results at 17 or 37 C, which is significant for sterilization of compacted nitinol components. In terms of design of devices, this means that relevant verification testing should be performed on components or devices that have undergone representative temperature and strain processing history to simulate the effects of sterilization on a compacted device prior to deployment.

Investigation of load-path dependency for the nitinol wire in compression shows that if the material is loaded up to any strain in the 'upper plateau' range (up to 4 % compressive strain), it will recover the strain along a common 'unload plateau' path as phase change is reversed. If the material is loaded to beyond 4 % compressive strain, further deformation occurs by martensite elasticity and plastic dislocation movement, resulting in permanent set. This plasticity has three effects on the stress-strain response during unloading: firstly, it causes an increase in the unloading modulus; secondly, it causes the material to unload along a lower 'unload plateau'; thirdly, it causes residual strain upon full unloading. Each of these unloading effects is increased with increasing maximum compression strain in the range 4 – 6 %.

In compression, the nitinol $\Delta\varepsilon$ cycling behaviour 'from below' (during unloading) follows a linear elastic stress-strain path with modulus between the initial austenite

loading modulus and the martensite unloading modulus, as long as $\Delta\varepsilon < 0.5$ %. At this low $\Delta\varepsilon$ level, deformation occurs without phase transformation, showing no hysteresis loop in the cycle path. Also, for these small $\Delta\varepsilon$ levels, the cycling is stable from the first cycle. This small deformation cycling is relevant to in-vivo pulsatile performance of stent components, where maximum compressive $\Delta\varepsilon$'s are anticipated to be < 0.2 %. The fact that deformation is linear elastic for these small cycles in compression is desirable for fatigue performance of the stent components.

As has been seen, the uniaxial testing of nitinol wire has resulted in a clear understanding of the tensile – compressive behaviours and stress-strain values pertinent to stent component performance.

Chapter 4: 3-Point Bend Load - Deflection Testing

4.1 Background

For endovascular stent graft devices, the service loads will primarily subject the nitinol components to bending deformations. It was therefore decided that experimental bend testing should be performed to gain a better understanding of the material's in-service behaviour. The bend test results will also be useful for validation of material models that will be created using the tensile and compressive stress-strain results reported in Chapter 3. The validation of these models for Finite Element Analysis (FEA) simulations will be reported in Chapter 6.

It was decided that symmetrical 3-point bend testing would be performed, as this would give a reasonable representation of how Nitinol wire is loaded and unloaded with large deformations in the case of Vascutek's stent ring components. In these ring components, the peaks and valleys of the rings undergo maximum local curvature changes during compaction and deployment, while in 3-point bend testing there is maximum curvature change at the central indenter position of the beam as it is deflected. 0.14 mm and 0.45 mm wire sizes were chosen for the bend testing, representative of smaller and larger wires in the diameter range used for Vascutek's nitinol components.

4.2 Objectives

The main objective of the 3-point bend testing is to characterize the bending behaviour of thin nitinol stent wire under service conditions, including relevant operating temperatures and cycling regimes.

In order to achieve this objective, the following sub-objectives were identified for 3-point bend testing of wire:

- At room temperature, characterize the Load-Deflection response up to large 'compaction' bend deflections, representing anticipated conditions during device compaction
- At room temperature, investigate the effect of additional load-unload cycles to large 'compaction' bend deflections, representing cycling due to multiple compactions
- Characterize the load-deflection response in bending at different 'in service' temperatures: room temperature (23 C) and body temperature (37 C).
- Characterize the cycling behaviour for small $\Delta\varepsilon$ load-unload cycling 'from below' (i.e. during unloading) at 37 C: this is useful for understanding the wire's bending response to in-vivo pulsatile loading.

An additional objective of this work is to obtain experimental Load-Deflection data for representative wire material that can be used for validation of constitutive material models for use in FEA simulations.

4.3 Equipment and Methods

4.3.1 Testing Machine and 3-Point Bend Attachments

3-point bend Load-deflection testing was performed using a Bose Electroforce 3200 machine. This bench-top machine uses an electromagnetic linear motor for high accuracy uniaxial displacement, and is capable of static or high frequency dynamic testing. For the present quasi-static 3-point bend testing of thin nitinol wires, this machine was chosen due to its suitability for low-force testing, with availability of load cells as small as 2.5 N, and for the ability to test at elevated temperatures using the water bath accessory.

For testing of 0.45 mm NiTi#1 wire, suitable 3-point bend pin attachments were available, supplied by Bose. The machine and attachments are shown in figure 4-1.
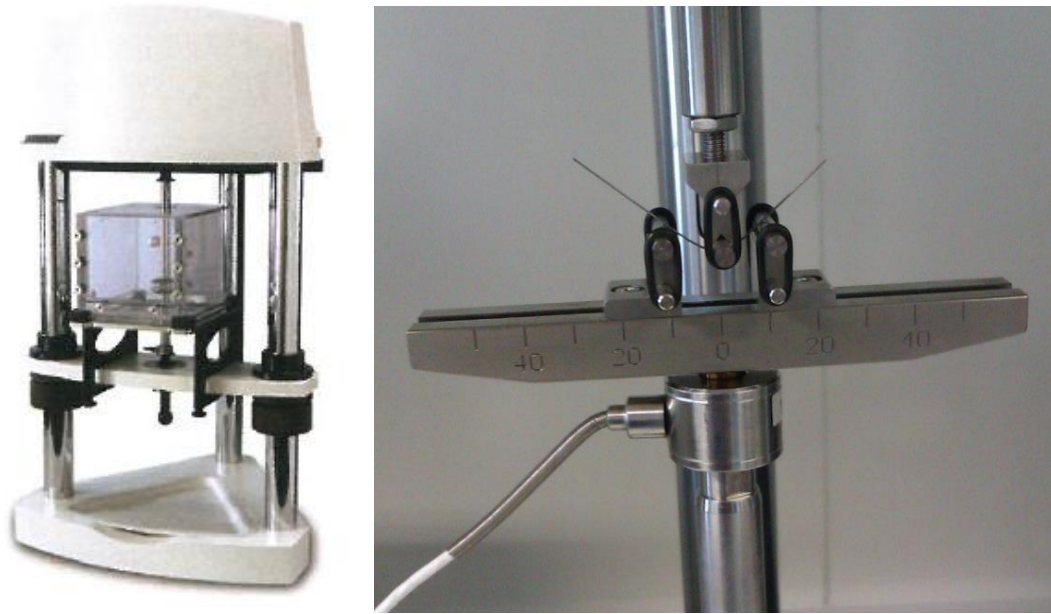
Figure 4-1: Bose Electroforce 3200 test machine with water bath (left) and adjustable 3-Point Bend attachments used for 0.45 mm wire testing (right). The photograph here shows a single strand of 0.45 mm NiTi#1 wire (Lot F5298520) in 3-point bending.

The pin configuration and deflection range used for 3-point bend testing of the 0.45 mm wire are shown schematically in figure 4-2. This set-up was designed to ensure the material would be subjected to large axial strains in bending, typical of compaction, while minimizing shear strains (due to a large 'span length : cross-sectional area' ratio).
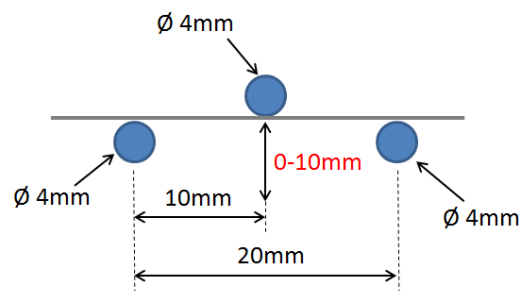
Figure 4-2: schematic diagram of 3-Point Bend set-up for testing of 0.45mm Nitinol wire, showing indenter pin displacement range of 0-10 mm for deflection of wire to large 'compaction' strains

For testing of thinner 0.14 mm wires, custom 3-point bend pins were designed and manufactured for attachment to the machine. These attachments are shown in figure 4-3. The pin configuration and deflection range are shown schematically in figure 4-4.
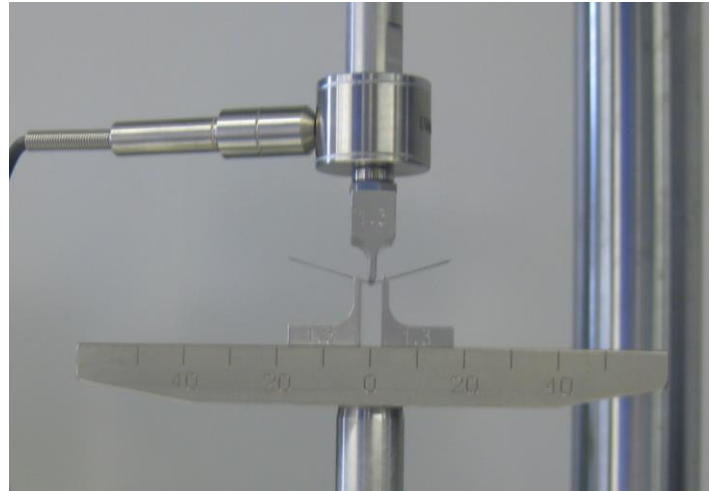
Figure 4-3: 3-Point Bend attachments for 0.14 mm wire testing. The photograph shows 10 strands of 0.14 mm NiTi#1 wire (Lot F5208630) in 3-point bending.
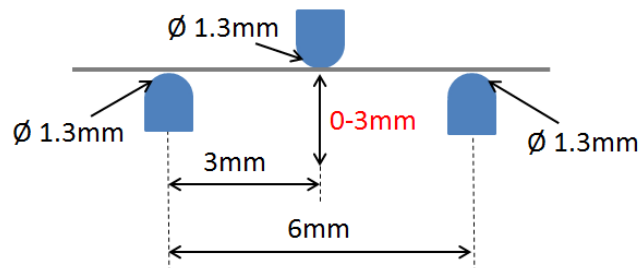
Figure 4-4: schematic diagram of 3-Point Bend set-up for testing of 0.14 mm Nitinol wire, showing indenter pin displacement range of 0-3 mm for deflection of wire to large 'compaction' strains. The surface radius of curvature of each pin is 0.65 mm.

4.3.2 Load Cell and Number of Wire strands

From initial testing using the Bose equipment, it was found that measurement of very small loads with the smallest 2.5 N load cell led to a large amount of noise in the results.

Therefore, it was found to be impractical to perform 3-point bend testing on a single strand of 0.14 mm wire. To solve this problem, testing was performed with multiple strands of the 0.14 mm wire side-by-side, giving Load-Deflection (L-D) results with minimal noise. The L-D response could then be derived for a single strand by dividing the load data by the number of wire strands. The optimal number of wire strands depended on the test temperature, with Nitinol wire having greater bend stiffness at higher temperatures. The number of wire strands used for each test is shown in table 4-1 of the 'Test Plan' section below.

For testing of 0.45 mm wire, good results could be obtained for a single strand of wire using a 10 N load cell.

4.3.3 Test Conditions

Bend testing was conducted both in air at 23 C and in water at 37 C. For testing in air, the temperature of the room was controlled by a thermostat. For testing in water, a water bath with temperature probe and software-controlled heater was used to maintain test temperature at 37 C. Although the temperature of the specimen itself was not measured during testing, the ambient test temperature (of air or water) was monitored and controlled to within ± 1 C.

The testing was performed using displacement control of the indenter head, with no preload. Before each test, the wire was set up on the support pins and then the indenter head moved under manual control to a position close to the wire surface without making contact. This was the test start position. Results were later corrected to position the Load-deflection curves start point at the origin (by removing the start position 'gap' from all deflection data).

Test speeds were chosen to be low enough to avoid adiabatic heating effects while giving a good representation of loading and unloading rates which may be seen in service during compaction, deployment and cycling. The chosen test speeds can be seen in table 4-1 in the 'Test Plan' section below.

4.3.4 Test Sample Material

0.45 mm sample wire (Lot F5298520) and 0.14 mm sample wire (Lot F5208630) were used for 3-point bend testing. Supplier (Fort Wayne Metals) Certificate of Conformance data for these batches can be seen in table 3-1 of Chapter 3. These wire sizes were chosen as they represent diameter sizes at the upper and lower ends of the range used by Vascutek for device components. All wires in this range have the same specification for uniaxial tensile stress-strain properties, and therefore these wires can be taken to represent all wires used in Vascutek's nitinol components.

4.3.5 Test Plan

Table 4-1 outlines the tests undertaken in order to meet the objectives for 3-point bend Load-Deflection testing, as stated in section 4.2. The maximum deflections used here were chosen based on initial testing of both wire sizes to find the deflections required for the wire to exhibit superelastic bending behaviour. This behaviour could clearly be seen from the Load-Deflection results plots, with the intial elastic stiffness followed by compliant deformation due to phase change, seen by the deflection proceeding with little or no load increase. From the previous chapters, it is known that this constant force phase transformation behaviour occurs at strains above 1.2% in tension and compression. For the 0.45 mm wire, it was found that 3-Point Bend deflections > 5 mm would allow this superelastic bending behaviour to be clearly observed, and deflections as high as 10 mm were used to investigate the effect of large bend deflections, representing the behaviour of a stent wire during compaction into a delivery sheath. For the 0.14 mm wire, the 3-Point Bend pin configuration and deflections were approximately linearly scaled down from the 0.45 mm wire set-up, as there is a linear

relationship between maximum strain and the wire diameter / bend radius, meaning that the two wire sizes would be strained to similar maximum levels in bending using these test parameters.

Test Set name	Temp (C)	Wire dia (mm)	Load Cell (N)	No. wire strands	Description	Displacement Steps	Speed (mm/s)
045_3pb1	23	0.45	10	1	Load to 10mm deflection, unload to 0 (1 cycle)	Load to 10mm in 10s	1
						Dwell for 5s	
						Unload to 0 in 10s	
045_3pb2	23	0.45	10	1	Load to 10mm deflection, unload to 0 (2 cycles)	Load to 10mm in 10s	1
						Dwell for 5s	
						Unload to 0 in 10s	
						Dwell for 5s	
						(x 2 cycles)	
045_3pb3	23	0.45	10	1	Load to 5mm deflection, unload to 0 (1 cycle)	Load to 5mm in 5s	1
						Dwell for 5s	
						Unload to 0 in 5s	
014_3pb1	23	0.14	2.5	10	Load to 3mm deflection, unload to 0 (3 cycles)	Load to 3mm in 6s	0.5
						Dwell for 1s	
						Unload to 0 in 6s	
						(x 3 cycles)	
014_3pb2	37	0.14	2.5	6	Load to 3mm deflection, unload to 0 (1 cycle).	Load to 3mm in 6s	0.5
						Dwell for 1s	
						Unload to 0 in 6s	
014_3pb3	37	0.14	2.5	6	Load to 3mm deflection, unload to 0 (2 cycles). On 2nd cycle during unloading, cycle between 1.0 – 1.1mm deflections (100 cycles)	Load to 3mm in 6s	0.5 (large cycles); 0.05 (small cycles)
						Dwell for 1s	
						Unload to 0 in 6s	
						Dwell for 1s	
						Load to 3mm in 6s	
						Dwell for 1s	
						Unload to 1.05mm in 4.5s	
						Load to 1.1mm in 1s	
						Unload to 1.0mm in 2s	
						Load to 1.1mm in 2s	
						(x100 cycles)	
						Unload to 0 in 1.5s	

Table 4-1: 3-point bending load-deflection test sets

4.4 Results and Discussion

4.4.1 Single Cycle 3-Point Bend L-D Curves

The following results show single cycle 3-point bend results for Vascutek's NiTi#1 wire, in order to understand the load-deflection behavior in bending and to provide useful empirical data that can be used for validation of FEA-based constitutive material models.

Figure 4-5 below shows results from test sets '045_3PB1' and '045_3PB3', giving load-deflection plots for 0.45 mm NiTi#1 wire at room temperature (23 C).
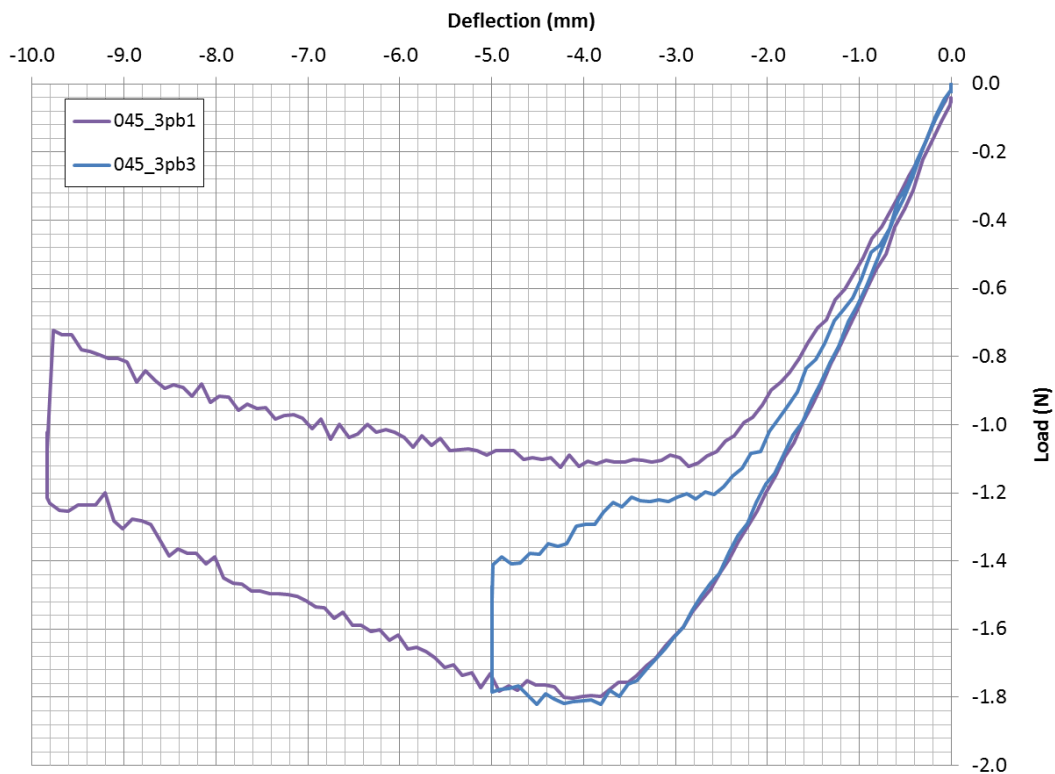
Figure 4-5: single load-unload cycle L-D results for 3-point bending of 0.45 mm NiTi#1 wire at 23 C to different maximum deflections (1 wire strand)

The L-D curves shown in figure 4-5 are useful in understanding the behaviour of superelastic nitinol wire in bending to large deformations. Note that the x-axis shows the

deflection of the central indenter pin, and the y-axis shows the applied force of this pin as recorded by the load cell.

Considering test '045_3pb1', the results in figure 4-5 show the following characteristics.

In loading

The L-D curve shows initial 'linear elastic' bending stiffness of 0.6 N/mm, where all material in the bending wire is in its austenite phase (the slight reduction in stiffness beyond 2.5 mm loading deflection is assumed to be due to the presence of R-phase).

At 3.6 mm deflection, a load plateau begins where the wire shows compliant bending behaviour as further deflection up to 5 mm occurs at a relatively constant force. Considering the material behaviour, this load plateau occurs as the material at the outer and inner bend surfaces of the wire's central bend 'apex' region (where applied moment and curvature are at a maximum) goes through Stress-Induced Martensite phase transformation at near-constant stress.

Beyond the load plateau region, from 5 mm deflection, the curve then shows negative stiffness up to the maximum 9.8 mm deflection. This characteristic of the L-D curve is considered to be due to two effects:

- sliding of the wire over the support pins beyond a certain wire bend angle, meaning that indenter pin deflection can increase with minimal additional bending of the wire
- increased moment arm length of the highly deformed wire, meaning a lower force is required to increase the applied moment on the wire within the support pin span

At the maximum deflection position (9.8 mm), the wire was held in position during a 5 second dwell period. During this 'dwell', the curve shows a vertical drop in the force.

Then, as unloading commences, there is an immediate further vertical force drop seen. These force drops are due to friction between the nitinol wire sample and the stainless steel support pins (despite the pins having a polished finish), as was seen during FEA simulations of 3-point bending (reported in chapter 6). If friction were eradicated between the wire and pins, the loading forces would be reduced while the unloading forces would be increased compared to the results of figure 4-5.

In unloading

From the maximum displacement down to 5 mm deflection, the effects of sliding and the long moment arms can again be seen as the force increases with decreasing pin deflection. However, the slope of this 'negative stiffness' path is different from that in loading between 5 mm and 9.8 mm deflection, showing evidence of load-unload hysteresis independent of the friction effects.

Below 5 mm deflection, there is an unloading plateau where bend deflection decreases at constant force. This behaviour is due to the reverse phase transformation of nitinol material that has reached its unload stress plateau following unloading with martensite elasticity. This unload force plateau extends down to 2.8 mm deflection, which is lower than the deflection where phase transformation at constant force was seen to occur in loading (at 3.6 mm). Therefore, the bending wire is fully austenite in loading between 2.8 mm and 3.6 mm, while in unloading for the same deflection range it contains some martensite phase. This behaviour will be explored further in chapter 5, where it is shown that the wire takes a different shape and therefore has different strain distribution in loading and unloading for the same 3-Point Bend deflection position.

When deflection reaches 2.8 mm in unloading, the wire begins to unload with linear stiffness, showing that all material has returned to its original austenite state. Final unloading then occurs with austenite elasticity.

At zero force, there is no residual deflection, meaning that the wire has returned to a straight shape with no residual bend deformation.

Test '045_3pb3' subjected the wire to a lower maximum bend deflection of 5 mm, and therefore avoided the 'negative bend stiffness' behaviour associated with large deflections and sliding. With reference to the results in figure 4-5, the L-D curve shows the same load path as '045_3pb1' up to 5 mm deflection, including initial austenite stiffness followed by the force plateau. During the 'dwell' and subsequent deflection direction change, the effects of friction can again be seen in the vertical force drop.

For unloading, the '045_3pb3' results show an interesting path that was not evident in the previous results. Between 5 mm and 3.6 mm deflection, the wire unloads with near-linear elastic stiffness, which can be understood by the elastic strain recovery of martensite material in the wire during initial unloading.

Below 3.6 mm deflection, there is an unload plateau as the wire straightens at constant force, showing that martensite material in the wire is undergoing reverse phase transformation to austenite, giving strain recovery at constant stress. As can be seen from figure 4-5, this unload plateau occurs at a higher force for '045_3pb3' than for '045_3pb1'. This gives evidence of load history dependence of the unload L-D path in bending for Nitinol.

Below 2.8 mm deflection, the wire unloads with a linear Load-Deflection relationship, showing that the wire material has fully returned to austenite at this unloading bend deflection.

For the purpose of FEA material model validation, it is useful to extract some key parameters from the results. Table 4-2 shows some useful results extracted from these 3-point bend tests on 0.45 mm NiTi#1 wire at 23 C.

Parameter	Value
Initial austenite bend stiffness	0.6 N/mm
Load plateau force	1.8 N
Load plateau start deflection	3.6 mm
Load drop due to friction (@ 5 mm deflection)	0.4 N
Load drop due to friction (@ 9.8 mm deflection)	0.5 N
Martensite unload bend stiffness (from 5 mm deflection)	0.15 N/mm
Unload plateau force (for 5 mm max load deflection)	1.2 N
Unload plateau force (for 9.8 mm max load deflection)	1.1 N
Unload plateau end deflection	2.8 mm

Table 4-2: parameters from 3 Point Bend test results for 0.45 mm NiTi#1 wire at 23 C

(as plotted in figure 4-5)

Figure 4-6 shows results from test set '014_3PB1' for Load-Deflection of 0.14 mm NiTi#1 wire in bending at room temperature (23 C). For clarity, only the first cycle is shown. The results in figure 4-6 for 0.14 mm wire show the same general bending behaviours seen in test set '045_3pb1' (figure 4-5):

- Initial linear stiffness due to austenite elasticity
- Loading plateau showing compliance in bending due to Stress-Induced Martensite phase change
- Negative stiffness due to sliding and large deformation issues
- Friction effects
- Unloading with reduced negative stiffness, as strain is recovered through martensite elasticity
- Unload plateau showing compliance in bending as material undergoes reverse phase change
- Final unloading with linear stiffness due to austenite elasticity
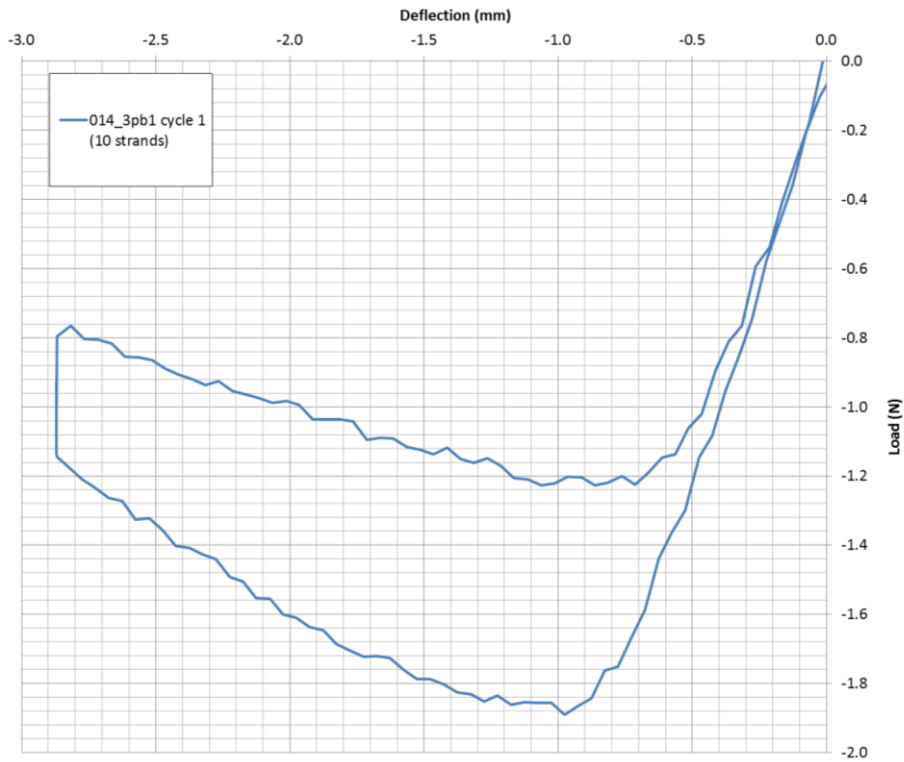
Figure 4-6: single load-unload cycle L-D results for 3-point bending of 0.14 mm NiTi#1 wire at 23 C (10 wire strands)

Table 4-3 gives key parameters from test '014_3pb1' results, showing values for 10 wire strands and then the derived values for 1 strand.

Parameter	Measured Value (10 strands)	Derived value (1 strand)
Initial austenite bend stiffness	2.6 N/mm	0.26 N/mm
Load plateau force	1.85 N	0.185 N
Load plateau start deflection	0.9 mm	0.9 mm
Load drop due to friction (@ 2.9 mm deflection)	0.36 N	0.036 N
Unload plateau force (for 2.9 mm max load deflection)	1.2 N	0.12 N
Unload plateau end deflection	0.6 mm	0.6 mm

Table 4-3: parameters from 3 Point Bend test results for 0.14 mm NiTi#1 wire at 23 C

(as plotted in figure 4-6)

Figure 4-7 shows results from test set '014_3pb2' for Load-Deflection of 0.14 mm NiTi#1 wire in bending at body temperature (37 C). Again, the results of figure 4-7 (test '014_3pb2') show the same general bending behaviours discussed previously, but at higher loads due to the elevated temperature, showing clearly the temperature sensitivity of Nitinol's superelastic bending behaviour. Note, however, that the unloading path at large deflections has almost exactly the same slope as in loading, unlike in the previous cases. This may be due to the effect of the test medium (water) on the sliding of the wire over the support pins at large deflections. The different friction properties due to test medium will also affect the amount of 'force drop' at the maximum deflection.
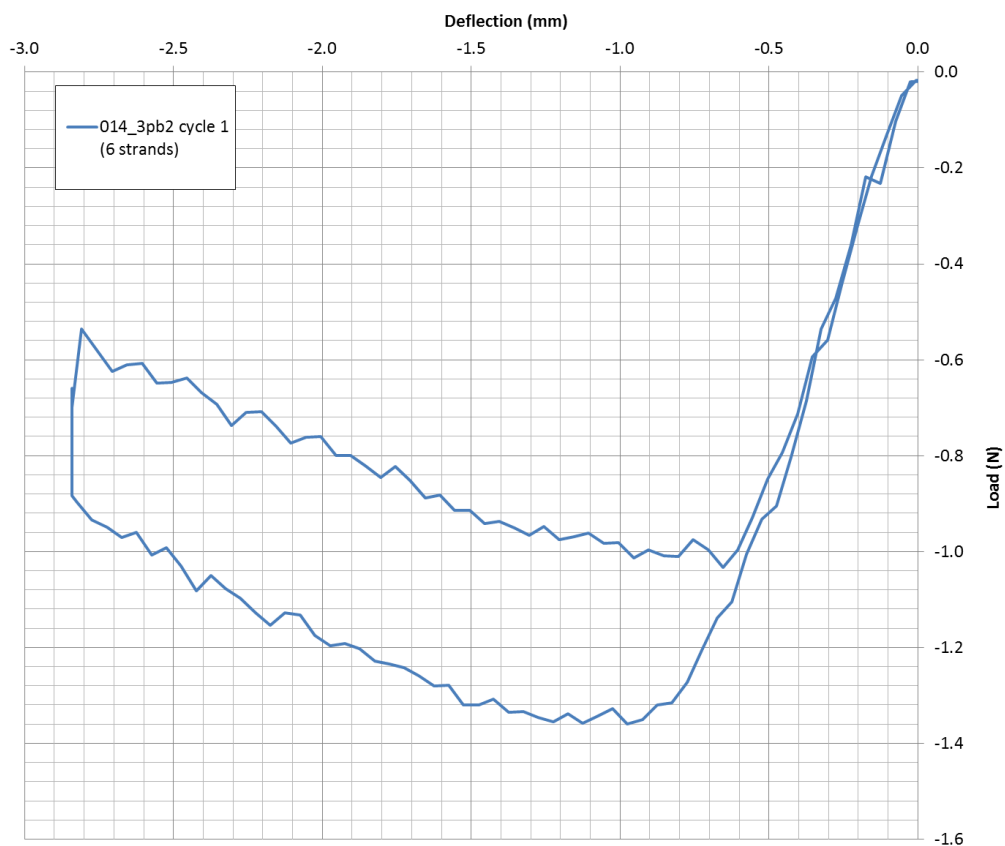
Figure 4-7: single load-unload cycle L-D results for 3-point bending of 0.14 mm NiTi#1 wire at 37 C (6 wire strands)

Table 4-4 gives key parameters from test '014_3pb2' results of figure 4-7, showing values for 6 wire strands and then the derived values for 1 strand.

Parameter	Measured Value (6 strands)	Derived value (1 strand)
Initial austenite bend stiffness	1.8 N/mm	0.3 N/mm
Load plateau force	1.36 N	0.227 N
Load plateau start deflection	0.9 mm	0.9 mm
Load drop due to friction (@ 2.85 mm deflection)	0.34 N	0.057 N
Unload plateau force (for 2.85 mm max load deflection)	1 N	0.167 N
Unload plateau end deflection	0.6 mm	0.6 mm

Table 4-4: parameters from 3 Point Bend test results for 0.14 mm NiTi#1 wire at 37 C

(as plotted in figure 4-7)

4.4.2 'Compaction Deflection' Cyclic Bend Testing

Figures 4-5 and 4-6 showed the Load-Deflection results for large 'compaction' bend deflections at room temperature, representing anticipated deformations that may be seen in device compaction. The characteristics of these curves have been discussed in the previous section. In order to investigate the effect of additional load-unload cycles to large 'compaction' bend deflections, representing cycling due to multiple compactions during assembly, test sets 045_3pb2 and 014_3pb1 were performed at room temperature (23 C). The results are shown in figures 4-8 and 4-9 respectively.

With reference to figure 4-8, the two cycles are nearly identical, suggesting that the material has been unaffected by the first large-deflection cycle. In figure 4-9, a slight drop in the load plateau values can be seen on consecutive cycles, which may be due to decreasing stress levels for Stress-Induced Martensite (see figure 2-28 of Literature Review, Chapter 2). The unload path is nearly identical for each cycle.
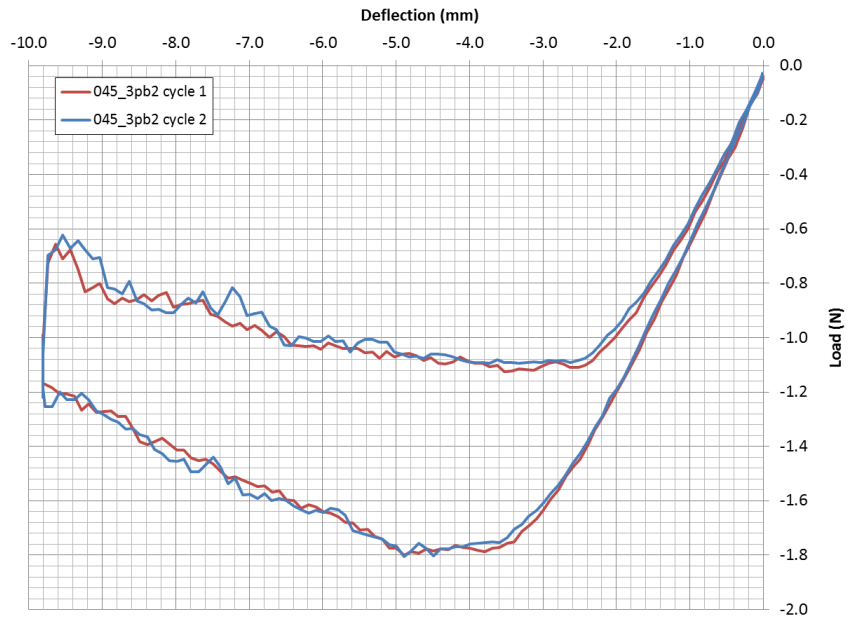
Figure 4-8: L-D results for 3-point bending of 0.45 mm NiTi#1 wire at 23 C, 2 load-unload cycles (1 wire strand). Results are from test set 045_3pb2.
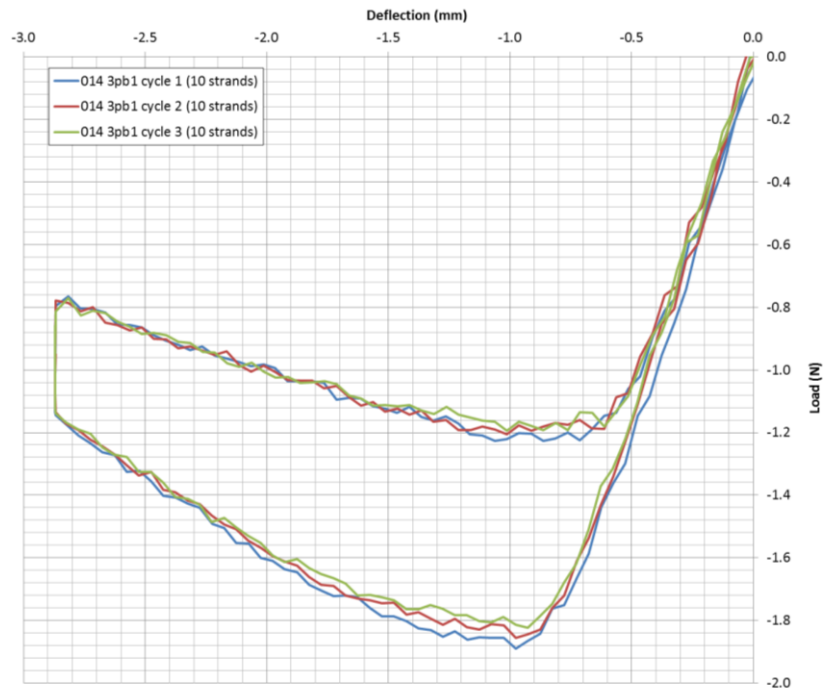
Figure 4-9: L-D results for 3-point bending of 0.14 mm NiTi#1 wire at 23 C, 3 load-unload cycles (10 wire strands)

The figure 4-8 and 4-9 results show that for this level of wire bending deformation, multiple load-unload cycles have little or no effect on the bending stiffness behaviour of the nitinol wire. There was no evidence of plastic deformation of the wires following unloading.

4.4.3 Temperature Dependence

To investigate the load-deflection response in bending at different 'in service' temperatures, test sets '014_3pb1' and '014_3pb2' were performed at 23 C and 37 C respectively. The test at 37 C had to be performed using 6 wire strands (instead of 10) to avoid exceeding the upper limit of the 2.5 N load cell. For comparison, these results were then used to derive the equivalent force for 10 strands at 37 C. The comparative results are plotted in figure 4-10, showing first cycle only for each test set for clarity.
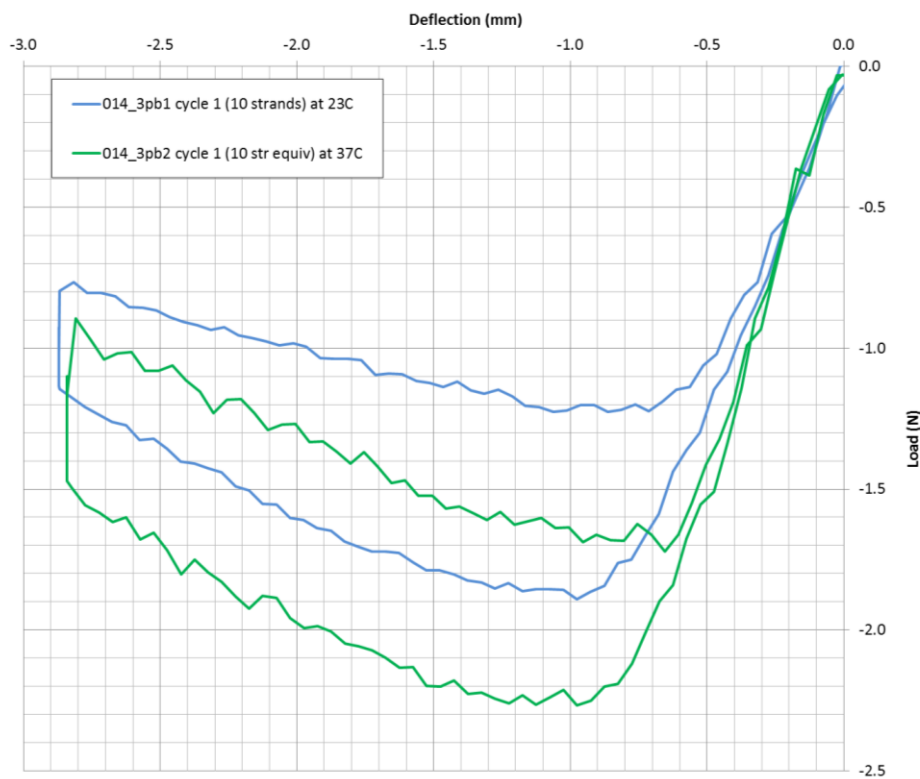
Figure 4-10: L-D results for 3-point bending of 0.14 mm NiTi#1 wire at 23 C (10 wire strands) and at 37 C (10 strand equivalent data derived from 6 wire strand test results). A single load-unload cycle is shown in each case.

Figure 4-10 clearly shows that increasing the test temperature from room temperature (23 C) to body temperature (37 C) has a significant effect on the Load-Deflection response of nitinol wire in bending. Increasing the temperature results in:

- Increased initial 'austenite' bending stiffness (~15 % increase from 23 C to 37 C)
- Increased upper load plateau level (~ 20 % increase from 23 C to 37 C)
- Increased unload plateau force level (~ 40 % increase from 23 C to 37 C)

In terms of stent performance, these results mean that radial force will be higher at body temperature than room temperature. This is beneficial in the product's life cycle as it will allow lower force compaction during production at room temperature, while providing higher Chronic Outward Force (COF) and Radial Resistive Force (RRF) for in-vivo sealing, anchoring, vessel damping and fatigue resistance. In terms of the design process, this temperature dependent behaviour means that verification and validation testing on nitinol components must be performed at the correct test temperatures to simulate the in-service conditions.

4.4.4 ΔD Cycling in Bending

To consider the bending behaviour of nitinol stent wire when it is cyclically loaded due to in-vivo pulsatile loading, the 3-Point Bend set-up was used to perform cyclic bending on the wire during unloading at 37 C, with small Δ deflection cycles. Based on the 3-point bend test results shown previously in this chapter, the mean deflection level for this cycling was chosen such that cycling would take place from the unloading 'plateau' region of the L-D curve following large deflection bending, representing a stent wire's bending deflection when deployed in an artery following compaction. Δ deflection cycles of 0.1 mm were used so that the wire material would be deformed elastically in each cycle without phase change, as is expected in-vivo. Figure 4-11 shows the results from test set '014_3pb3', with Δ deflection cycles 1-3 and 97-100 highlighted.
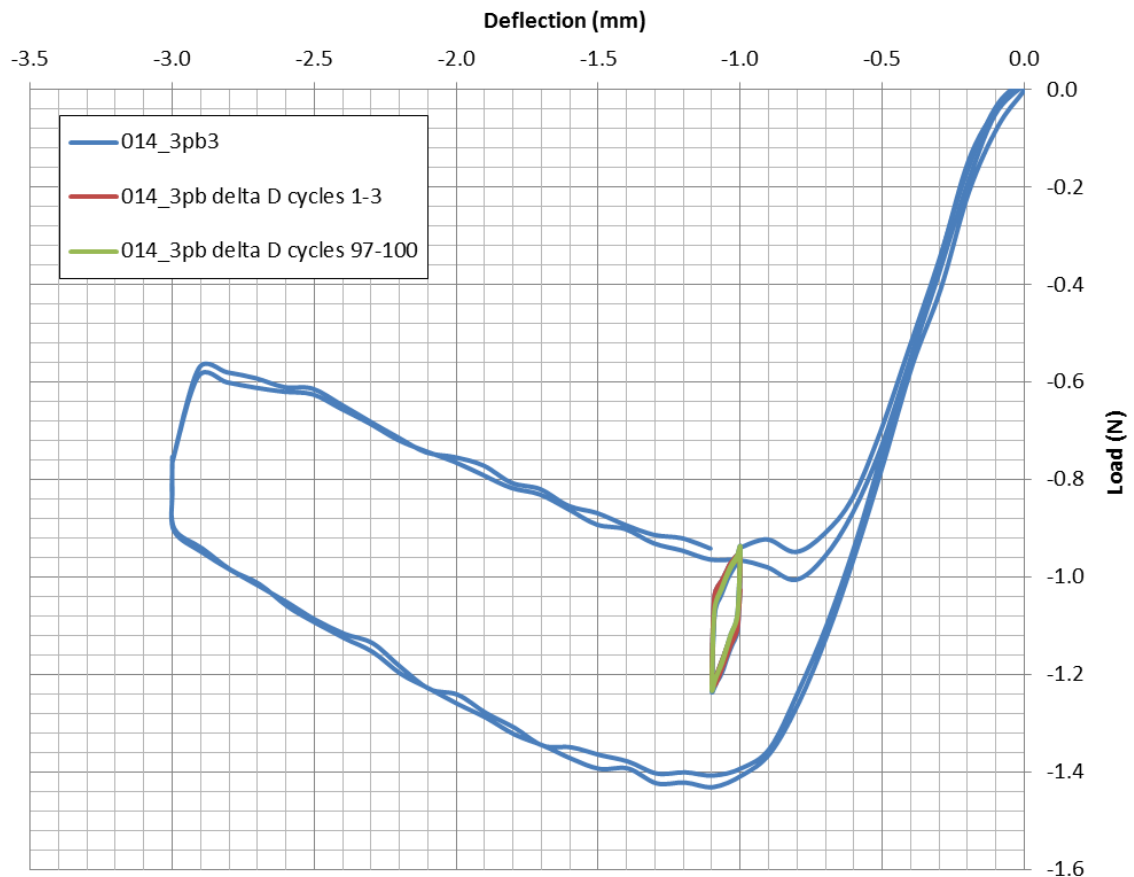
Figure 4-11: L-D results for 3-Point Bending of 0.14 mm NiTi#1 wire at 37 C (6 strands), 2 large deflection cycles with 100 Δ deflection cycles during unloading of 2nd large cycle. Delta D cycles 1-3 and 97-100 are highlighted to consider any changes due to cycling.

Considering the ΔD cycles shown in figure 4-11, there appears to be a hysteresis loop in each cycle. This can be fully attributed to friction effects as the force vertically increases at the start of each cycle and vertically drops at the end of each cycle. There is no phase transformation plateau seen in these ΔD cycles – the material is undergoing elastic deformation only. The plots show that when the wire is re-loaded from the lower force plateau, it has a bending stiffness that is a little lower than the initial austenite bending stiffness. This characteristic of the bending wire gives a nitinol stent its Radial Resistive Force when deployed in vessel under pulsatile loading conditions. In terms of cycling

stability, comparison of delta deflection cycles 1-3 with cycles 97-100 in figure 4-11 show no significant difference, meaning this small deformation cycling (representative of in-vivo pulsatile cycling) is stable from the 1st cycle.

4.5 Conclusions

Using Strathclyde University's Bose 3200 test equipment, it was possible to perform 3-Point Bend testing on thin superelastic nitinol wires to large deflections. The results from these tests will provide useful data for validation of material models to be used in FEA simulations of nitinol stent components.

The testing also provided useful information on the wire's bending response under the following conditions that will be seen in-service:

- Multiple large bend deflection cycles at 23 C: previous cycles had little or no effect on the load – deflection bending response of the wire, with no evidence of plastic deformation following unloading.

- Different temperatures: the wire has greater stiffness and 'plateau force' levels at 37 C compared to 23 C. In terms of device performance, this is beneficial as room temperature assembly will allow low-force compaction while body temperature deployment will give high chronic outward force (COF) and radial resistive force (RRF) for stents.

- Δ Deflection cycling during unloading of the wire in bending: the results showed an L-D path with slightly lower stiffness to that of initial austenite bending. For small Δ deflection levels (representing in-vivo bending behaviour), this cycling occurs without phase change in the material and the L-D path is stable from the first cycle. For device performance, these bending characteristics are desirable for long-term fatigue safety of the ring stent components.

Chapter 5: 3D Microscopic DIC Strain Measurement for Superelastic Nitinol Wire in Bending

5.1 Background and Introduction

The requirement to measure strains on thin superelastic wire in bending was identified in Chapter 2 (Literature Review) in order to experimentally investigate the findings of Van Zyl et al (33) regarding load path history effect on strain state during unloading for Nitinol in bending. Further to this, it is also desirable to acquire experimental bending strain data that can be used for validation of FEA material constitutive models.

As described in Chapter 2, Digital Image Correlation (DIC) was identified as a potentially feasible method, having been used by Reedlunn et al (34) for full-field strain measurement of thin nitinol wires (Ø0.762 mm) in uniaxial tension. However, no previous reports of DIC for measuring strains on thin superelastic wires in bending were found in the literature. The use of DIC for this application was therefore considered an exciting research opportunity, which would require development of a novel test method.

Following an initial feasibility study, 'microscopic 3D DIC' was identified as the most suitable technique to be used for this application. Equipment and technical support were then hired from LaVision UK.

This chapter describes the method developed to use microscopic 3D DIC to obtain strain measurements for thin Nitinol wire in superelastic bending, with appendix 3 expanding on certain details that may help future investigators to obtain useful results. The chapter then focuses on the investigation of strain history during 3-Point Bending using DIC strain measurement. Finally, the chapter includes description of an investigation using a specially designed 'freebend' test rig to obtain results for surface strains of thin Nitinol wire in bending.

The work described here formed the basis for a technical paper (66) presented by the author at the 'Shape Memory & Superelastic Technologies Conference 2013' (SMST 2013, Prague, Czech Republic).

5.2 Objectives

The initial objective of this work was to develop a suitable test method using microscopic 3D DIC that would allow measurement of strains around the surface of thin nitinol wire in bending to large deflections. This was successfully achieved and the method is described in detail in this chapter and in Appendix 3. Having developed a suitable test method, the following key objectives were set:

- Investigate the strain history of nitinol wire during loading and unloading in 3-Point bending
- Obtain experimental bending strain data for validation of FEA models

A further objective of the DIC strain measurement was to characterize the NiTi#1 wire by investigating its strain asymmetry at a given bend radius. This work was performed using a 'Free Bend' test rig and is described at the end of the chapter.

5.3 Equipment and Methods

5.3.1 3-D Microscopic Digital Image Correlation Introduction

Digital Image Correlation (DIC) is a technique that can be used to measure surface strains of a sample as it is deformed, by using digital images of the sample taken during deformation. The sample must have a surface pattern that can be tracked from an 'undeformed' image to a 'deformed' image, in order to measure the local displacements of points across the surface. The resulting deformation field can then be used to derive the surface strains for the deformed sample.

Digital Image Correlation is a highly scalable technique. Using two cameras mounted on a microscope for image capture, it is possible to use DIC to measure the surface strains for a thin round wire as it is deformed. In order to achieve this, a suitable surface pattern comprising very small random speckles must be applied. Also, a suitable method of deforming the sample must be used, ensuring that the region of interest on the sample remains in focus within the microscope's field of view (FOV).

In order to measure the strains for thin superelastic Nitinol wire in bending, 3D Microscopic Digital Image Correlation was used with the test method outlined below.

5.3.2 3-D Microscopic DIC Equipment

The following equipment was hired from LaVision UK:

- Stereo Microscope: Zeiss Lumar V12 (including beam splitter /camera mounting)
- 2 x CCD Cameras (Imager E-lite 5M)
- Positionable LED lights and power source (Stemmer Imaging, item CCS LDL2-80/16-SW)
- Strain Master Controller: with manual image capture trigger input and synchronization board (PTU9) input (LaVision).
- Synchronization Board PTU9 (LaVision)
- PC Laptop
- 2D and 3D Strain Software Modules
- Micro calibration plate and stage

2 days on-site technical support and training from LaVision UK was also purchased, to ensure correct equipment set-up and operation in order to obtain the desired strain results.

Figure 5-1 shows the equipment set-up in Vascutek's R&D laboratory, with the main components labelled.
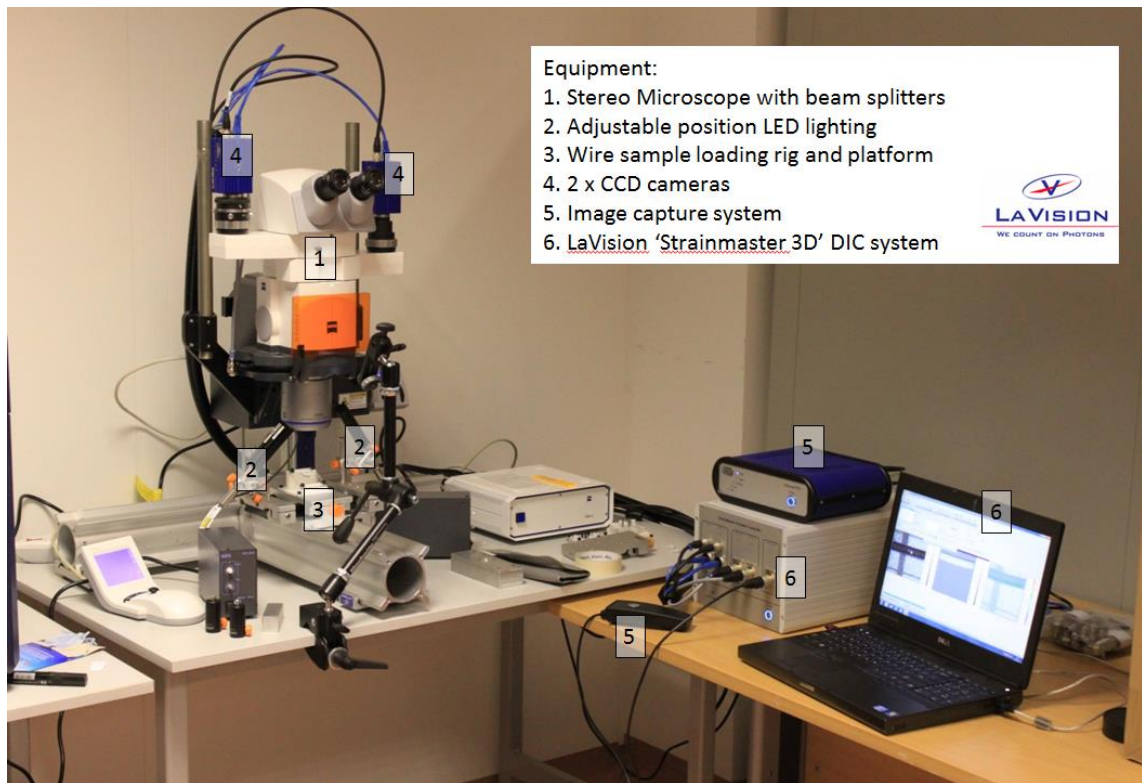
Figure 5-1: 3D Microscopic DIC Equipment Set-Up

5.3.3 Sample Material

0.45 mm sample wire (Lot F5298520) was used for bend testing with the DIC measurement equipment. Supplier Certificate of Conformance data for this batch can be seen in table 3-1 of Chapter 3. This is the same wire batch that was used for 3-Point Bend Load-Deflection testing (Chapter 4) and is representative of Vascutek's stent component wire, diameter range 0.1 to 0.45 mm with identical mechanical property specification across the size range.

In terms of feasibility for microscopic 3D DIC strain measurement, 0.45 mm wire was suitably large to meet the following criteria:

- Accommodate a sufficient number of speckles (applied by airbrush) across the surface for good spatial resolution of DIC strain field results. This is explained further in section 5.3.7 'Method Detail' below.

- Allow large microscope Field of View (FOV) so that the wire's bend apex will remain in the FOV even if rigid body translation occurs during deformation. (Note: this is important for the 'Free Bend' tests described in section 5.6).

5.3.4 3-Point Bend Rig Design

In order to measure strains of nitinol wire specimens in bending, it was necessary to design a suitable loading rig to apply bending deformations to the wire. The following design requirements were identified for the bending rig:

- Allow controlled bending deformation of the wire in small increments
- Allow load and unload bending of the wire
- Allow the shape or deflection of the wire to be recorded for measurement at each deformation increment
- Allow bending of the wire to maximum strains typical of those expected during stent ring compaction ($\geq$ 8% axial normal strain at outer surface)
- Maintain the apex of the bending wire in (approximately) the same position during loading and unloading to ensure that the area of interest (region of maximum bend curvature) will remain in the microscope's FOV
- Allow suitable lighting of the specimen for capture of images that can be DIC processed

It was considered that a 3-Point Bend Rig could be designed to meet these requirements. In addition, it was decided that the rig should have the same pin layout and deflection range as was previously used for 3-Point Bend Load-Deflection testing of 0.45 mm wire (reported in Chapter 4), shown schematically in figure 5-2. This would allow assessment of both the load and strain for a known 3-Point bend deflection, providing valuable data for material characterization and for FEA model validation.
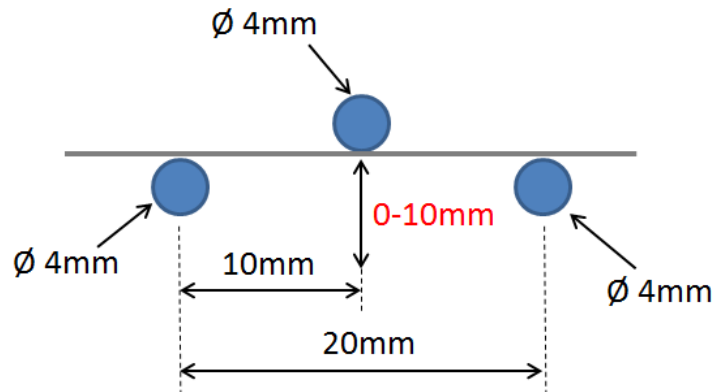
Figure 5-2: Schematic diagram of 3-Point Bend set-up for testing of 0.45 mm nitinol wire, showing pin layout and deflection range to match those used for 3-Point Bend Load-Deflection testing

The 3-Point Bend test rig for DIC testing, designed to meet the above specification, is shown in figure 5-3 as it is used to deform the 0.45 mm wire. (Note that the steel pins have been painted black ('Golden Airbrush Carbon Black (#8040)') to reduce reflection and improve lighting for digital image capture. This will give different friction properties from the stainless steel pins used for 3-Point Bend Load-Deflection testing. While this will affect the forces to bend the wire, it is considered that the effect on strain distribution along the wire length in bending will be negligible.)
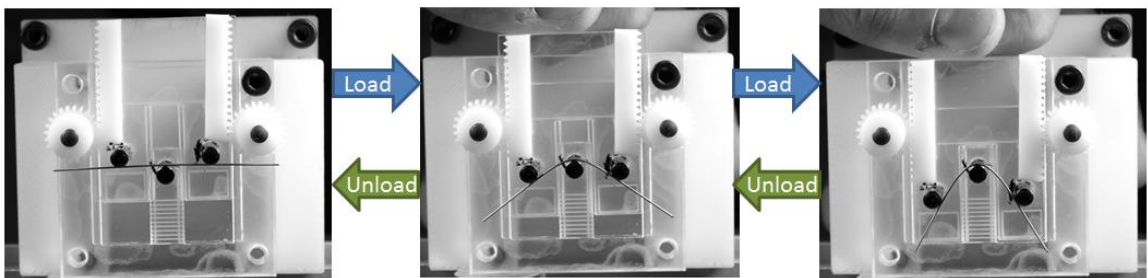
Figure 5-3: 3-Point Bend Rig used to deform a 0.45 mm NiTi#1 wire in bending

A limitation of the 3-Point Bend rig for DIC testing is that the central pin obstructs the view of the inner bend surface of the wire, preventing direct measurement of the maximum compressive strains during bending. For this reason, a second bending rig was designed to allow measurement of the full strain range across the wire. This 'Free Bend' rig and its use are described in section 5.6.

5.3.5 Mounting Platform Design

For round wires, 3D Digital Image Correlation cannot measure the surface deformations (and strains) at the edges of the wire, which are vertical in the view of the DIC cameras. Therefore, when the 3-Point Bend rig is mounted flat on the microscope stage, the deformations at the outer and inner bend surfaces cannot be measured. This would be a major limitation of the technique, as it would then be impossible to directly measure the maximum tensile strain of the wire in bending.

In order to overcome this problem, angled and vertical mounting platforms were designed for the 3-Point Bend rig that could be attached to the microscope stage, allowing the rig to be positioned at an angle under the microscope for viewing of different regions around the wire surface. Figure 5-4 shows CAD images of the flat and 30° mounting platforms, which were manufactured using FDM Rapid Prototyping. As well as mounting to the microscope stage, these platforms could also be mounted to a vertical clamp to allow 60° and 90° viewing of the wire's outer bend surface. The schematic diagram in figure 5-5 shows how these various mounting configurations allow viewing of different regions of the wire in bending for strain measurement.
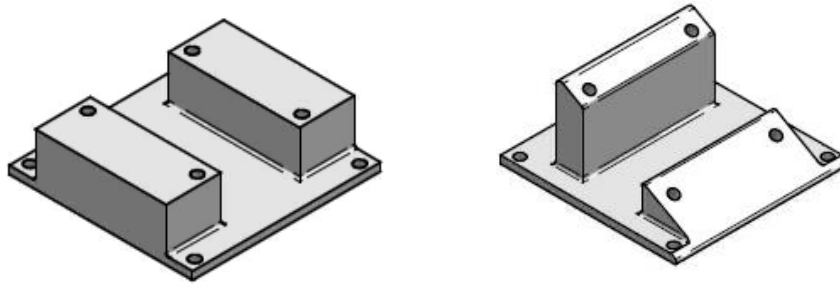
Figure 5-4: CAD images of Flat (left) and 30° Angled (right) platforms for mounting the wire bend rigs on the microscope stage
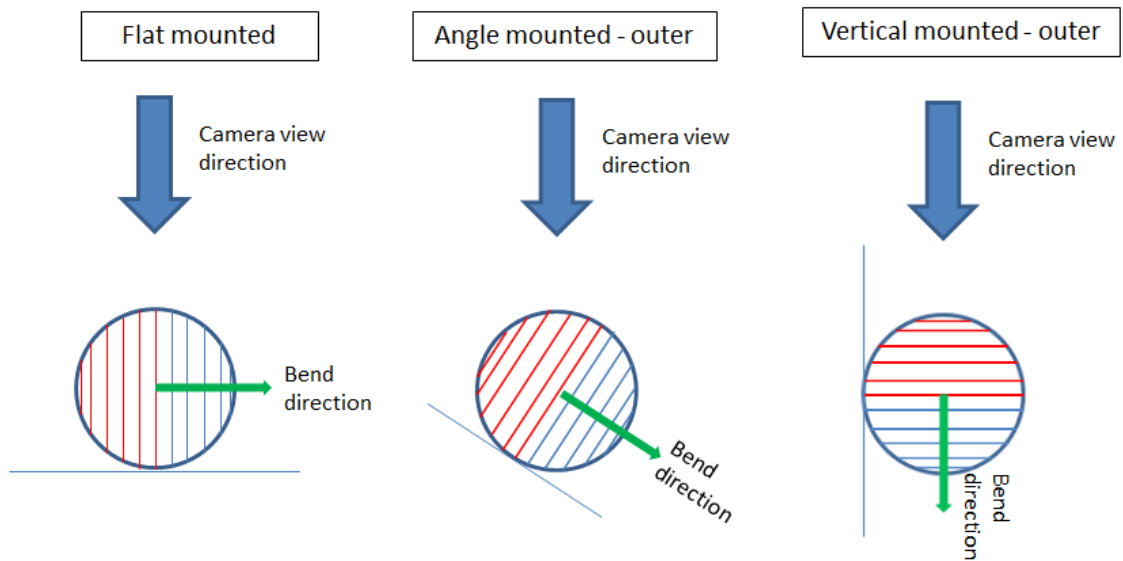
Figure 5-5: schematic diagrams showing the viewing angle relative to the bend direction for different bend rig mounting platforms. The red and blue lines represent the outer tensile and inner compressive regions respectively of the wire section in bending

5.3.6 Method Overview: Flowchart

Flowchart 5-1 below gives an overview of the approach used with the 3-Point Bend set-up and microscopic 3D DIC processing to obtain useful results to meet the objectives. The flow chart has been split into 5 main steps:

- Calibration
- Sample preparation and set-up
- Wire bending and image capture
- DIC processing using 'DaVis' software
- Results extraction and plotting

Section 5.3.7 (together with Appendix 3) then give a detailed description of each step in this approach, to allow a good understanding of the DIC method and to allow this strain investigation work to be extended in future.

Note that step 5 of the flowchart includes use of the 'Exx' strain and the strain gradient 'k'. 'Exx' strain refers to the normal strain in the 'x' direction after removal of local rigid body translation and rotation, where the 'x' direction is the axial direction of the undeformed straight wire. Strain gradient 'k' is the gradient of Exx strain across the wire's diameter during bending, from intrados to extrados. This value 'k' is found from the linear trend line formula for the plot of Exx vs wire width – an example from the DIC results analysis is shown in figure 5-24. The 'Exx' strain component and strain gradient 'k' are explained further in section 5.3.7.

Step 1: Calibration

Calibrate stereo microscope set-up → Calibration model

Step 2: Sample preparation and set-up

```
┌─────────────────────┐
│  Prepare sample with │
│   surface speckle    │
│      pattern         │
└─────────────────────┘
          │
          ▼
┌─────────────────────┐
│   Set up sample on   │
│   3PB Bending Rig    │
│ (flat, angle or vertical │
│      mounted)        │
└─────────────────────┘
          │
          ▼
┌─────────────────────┐
│  Adjust microscope   │
│  head position and   │
│ lighting for optimal │
│   focused image      │
└─────────────────────┘
```

Step 3: Wire bending and image capture

```
┌─────────────────────┐
│ Capture undeformed   │ ──→   Camera 1 ref image
│  reference images    │
└─────────────────────┘       Camera 2 ref image
          │
          ▼
┌─────────────────────┐
│     Bend wire        │
│ incrementally using  │
│   3PB bending rig    │
└─────────────────────┘
          │
          ▼
┌─────────────────────┐
│ Capture deformed     │ ──→   Camera 1 bend image
│   wire images        │
└─────────────────────┘       Camera 2 bend image
┌─────────────────────┐
│ Capture 3PB rig pin  │ ──→   'Macro' 3PB bend
│  deflection image    │        image
└─────────────────────┘
```

Repeat for all load and unload steps

Flowchart 5-1: Microscopic 3D DIC Method Overview

5.3.7 Method Detail

5.3.7.1 3D Calibration (Flowchart step 1)

The first step in using 3D microscopic DIC is to set up the calibration model for the particular microscopic focus (zoom) and for the position of the two cameras. Once the calibration process was completed, the microscopic focus and the camera positions were left unaltered for all tests.

The calibration process involved the following steps:

- Mount the '200 μm' calibration plate and stage under the microscope lens. The calibration plate has a grid of equally spaced (200 μm centre-to-centre) black dots across its surface. The microscope stage can be moved vertically relative to the microscope lens, in steps as small as 350 nm using the fine controls, allowing the calibration plate's 'z' position to be precisely adjusted.

- Input the dot spacing (from drop-down menu) and z (height in μm relative to start) position into the software. Capture the image of the dots in this position – in fact, this captures 2 images for this position, one with camera 1 and another with camera 2.

- Repeat the previous step for 10 different 'z' positions, adjusting the relative vertical distance of the calibration plate to the microscope lens each time by 50 μm. This gives an overall calibrated volume with height 0.5 mm

- The software can then use all this input information to create a calibration model for the set-up, consisting of mapping functions that have been calculated to transform the (x_1, y_1) and (x_2, y_2) co-ordinates for the dots from cameras 1 and 2 to (x, y, z) global position coordinates for the dots.

The calibration model can then be used by the software to calculate the (x, y, z) global coordinates for points on the surface of the wire specimen within the Field of View, using the (x, y) coordinates from the 2-camera images. Note that this is only valid as long as the specimen surface remains within the calibrated depth of focus (0 ± 0.25 mm).

5.3.7.2 Sample Preparation (Flowchart step 2)

DIC surface strain measurement requires a random speckle pattern on the specimen surface that can be used to calculate local surface displacements. For Vascutek's etched wire, there is no naturally occurring surface pattern that can be used for this purpose. Therefore, it was necessary to apply a suitable surface pattern for microscopic DIC.

Reedlunn et al (34) describe a technique for applying a very fine random speckle pattern to the surface of a thin nitinol wire for DIC testing using an airbrush. The same apparatus was purchased and the same technique applied for preparation of our ⌀0.45 mm nitinol wires. The equipment is outlined below:

- Iwata Custom Micron-B Airbrush with 0.18 mm nozzle
- Golden Airbrush Titanium White paint (#8380) - for background coat
- Golden Airbrush Carbon Black paint (#8040) – for speckle coat
- Studio Series Power Jet Lite compressor

As described by Reedlunn (34), these airbrush paints are opaque, give strong contrast and have good adhesion, even under superelastic strains. Therefore, they are suitable for DIC testing of nitinol wires in large deformation bending. In order to apply the smallest possible speckles, the nozzle was opened and the compressor set at a high pressure (50 PSI), producing a fine mist of paint from the airbrush. This gave speckles on the surface of approximately 0.035 mm diameter.

5.3.7.3 Sample Set-Up (Flowchart step 2)

The 3-Point Bend rig is mounted on the appropriate platform – flat, angled or vertical – depending on the region of the bending wire that is to be studied. The speckled wire sample is then mounted between the pins of the 3-Point Bend rig, and the rig is set up under the microscopic lens. The key points to consider here are:

- Ensure the surface pattern is in focus. The microscope zoom MUST NOT be adjusted, as the calibration model is only valid for the calibrated zoom position.

Instead, focus is adjusted by adjusting the 'z' position of the sample (i.e. moving the microscope stage relative to the microscope lens).

- Ensure the lighting is suitable: the speckle pattern should be clearly visible with clear contrast between dark and light areas, and there should be no bright reflection points or dark shadow regions. The image quality can be checked by capturing test images using the software and interrogating the gray-scale intensity values of the wire surface.

- Ensure that in its initial 'undeformed' position, the straight wire sample longitudinal axis lies in the 'global x-axis direction' (i.e. Parallel to the x-axis of the microscope stage). (Note: captured image sets can be corrected by rotation if necessary prior to DIC processing).

Figure 5-6 shows an example of a suitable wire image following set up (image taken from the 'Freebend' test set-up described in section 5.6).
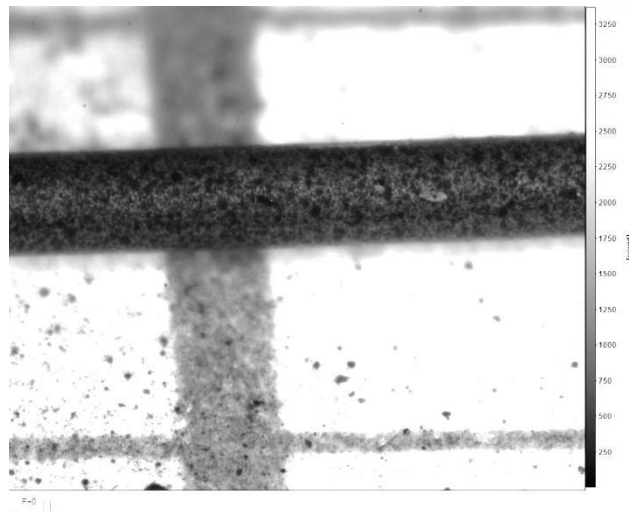
Figure 5-6: wire image captured during DIC process (from 'Freebend' test set-up). The image shows suitable focus and intensity contrast for subsequent DIC processing.

5.3.7.4 Wire Bending and Image Capture (Flowchart step 3)

With the wire specimen set up under the microscope, bend deformation and image capture can be performed.

Initial 'undeformed' images (cameras 1 & 2) of the straight wire are captured by pressing the manual trigger. These images provide the reference for DIC processing and calculation of strains for all subsequent images. These reference 'undeformed' images from the two cameras are also used by the software to calculate the initial height profile of the surface.

The wire sample is then incrementally deformed in bending using the 3-Point Bend or the freebend loading rig, with manual image capture (using the trigger) at each stage of deformation. This provides an image from each camera's perspective of the bending wire apex in the FOV at every deformation increment. Figure 5-7 shows a deformed wire image from camera 1 (image taken from the 'Freebend' test set-up).
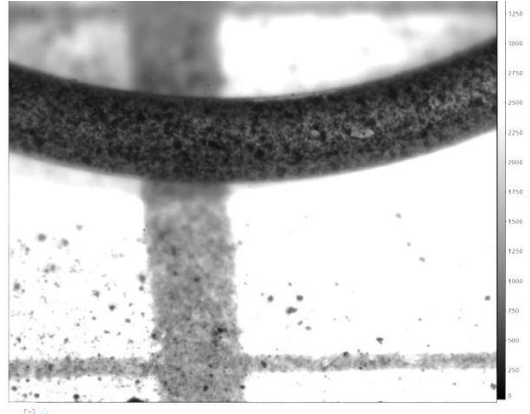
Figure 5-7: deformed wire image captured by camera 1 during DIC process (from 'Freebend' test set-up).

For every bending step, a 'macro view' image of the wire shape was also captured as described below.

For 'flat-mounted' test set-ups, this wire shape was captured by zooming out in the microscopic view to give a much larger Field of View (12 mm x 12 mm), and then using the manual trigger. The microscope's lens was then moved back to the original, calibrated zoom position (2.5 mm x 2.5 mm FOV). This movement between zoom positions was made possible by the microscope's control system, allowing zoom positions to be stored and chosen using a touch-screen interface.

For angled platform or vertical test set-ups, the 'macro view' wire shape was captured using a digital camera (Canon 500D with macro lens) mounted on an adjustable stand in order to position the lens's line of sight perpendicular to the mounting platform.

Figures 5-8 and 5-9 show examples of each of the 'macro view' wire shape images described.
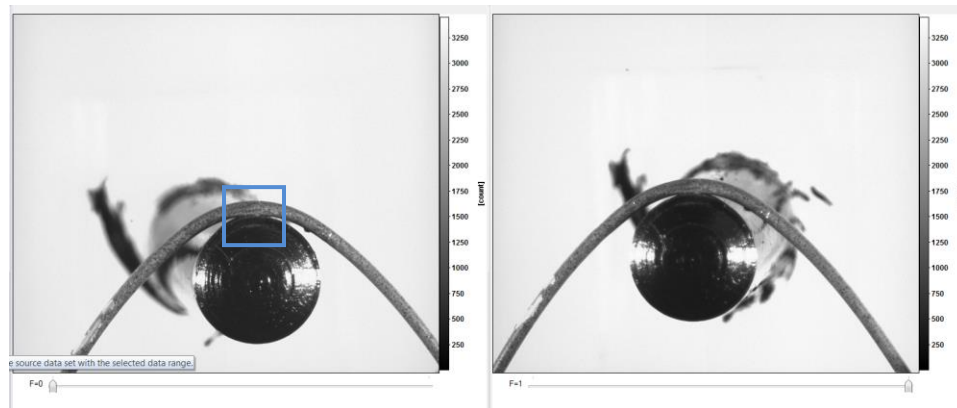
Figure 5-8: 'zoomed-out' images (from cameras 1 & 2) of the NiTi wire at its maximum bend position on the flat-mounted 3-Point Bend rig. The blue box in the left hand image represents the 2.5 mm x 2.5 mm field of view used for microscopic 3-D DIC image capture.
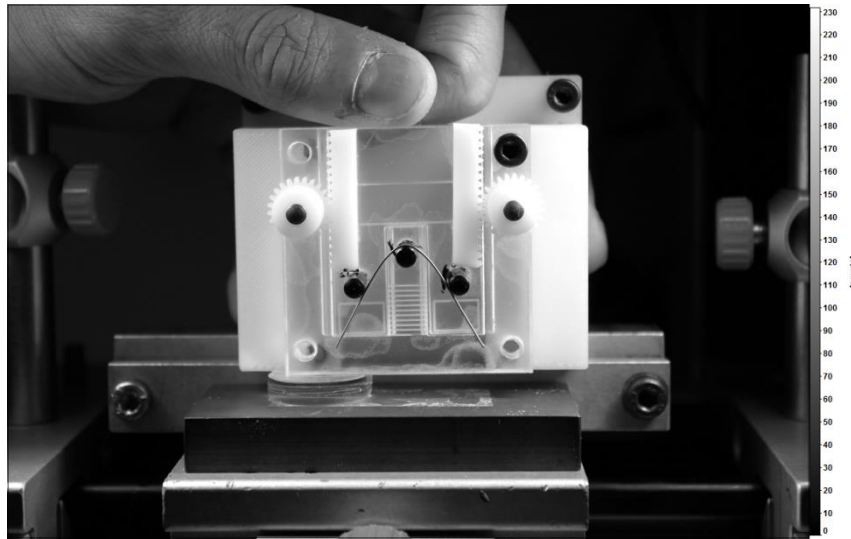
Figure 5-9: 'Macro' image of bending wire on 3-Point Bend rig with vertical mounting, taken using Canon 500D digital camera on adjustable stand

5.3.7.5 DIC processing using 'DaVis' software (Flowchart step 4)

The captured microscopic images of the bending wire during loading and unloading were used as inputs for 3-D DIC processing, to find the deformation field and surface height results for each bend deformation position. The DIC processing steps are outlined below.

1. The undeformed 'reference' image is selected and 'masked' to select the region of interest for DIC processing. For this testing, the reference image was always the 'image 1, camera 1' image of the straight wire with longitudinal axis in the x-direction (for example, Figure 5-6).

2. Subset seeding point selection: for DIC, the surface region for each image must be discretized into 'subsets', each of which contains a unique gray-scale intensity pattern (from the random speckle pattern). These subsets are used for Digital Image Correlation to calculate local displacements, as will be explained below. An initial 'seed' subset is used as a starting point for DIC calculations by the software, and must be selected by the operator. This 'seed' subset position was chosen to be in a central region on the wire that would see little local

displacement during bending. Figure 5-10 shows an example of masking and subset seed positioning for an undeformed wire image.
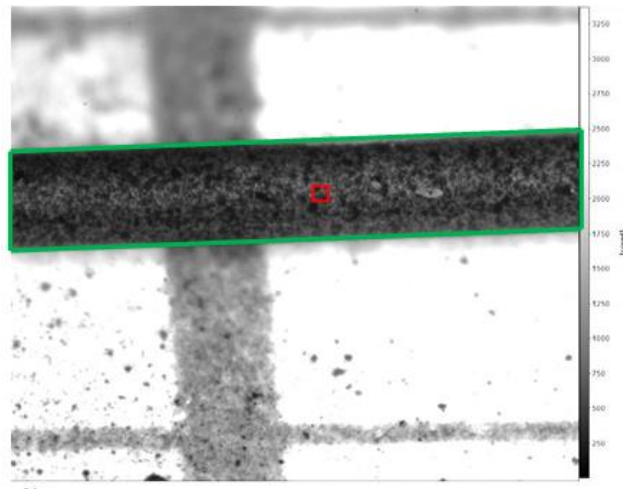
Figure 5-10: Masking and Subset seeding of reference image 1

3. Subset size and Step size selection: The subset size must be large enough to contain 3 - 6 distinct pattern features (speckles), as seen in figure 5-10 above. The 'Step size' determines the extent of overlap between one subset and its neighbors – as illustrated in figure 5-11. For this testing, it was recommended by LaVision that 63x63 pixel subset size with 15 pixel step size be used to optimize spatial resolution and accuracy of results. This Subset / Step size gives an overlap between subsets of approximately 75%.
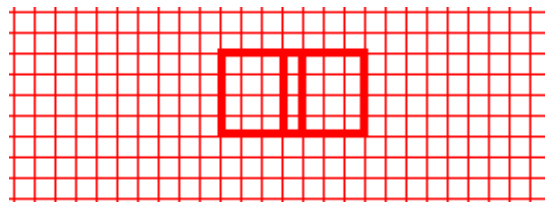
Figure 5-11: The thick-lined boxes represent subsets, offset by a distance equal to the Step size. The thin-lined grid represents the total number of subsets, determining the spatial resolution of results.

4. 2-D Displacement Vector Processing: The Digital Image Correlation software performs cross-correlation between the subsets in the 'deformed' image and the reference subsets in the 'undeformed' reference image to calculate the displacement vector for each subset in the deformed image. This is outlined in the figure 5-12 process flow below.
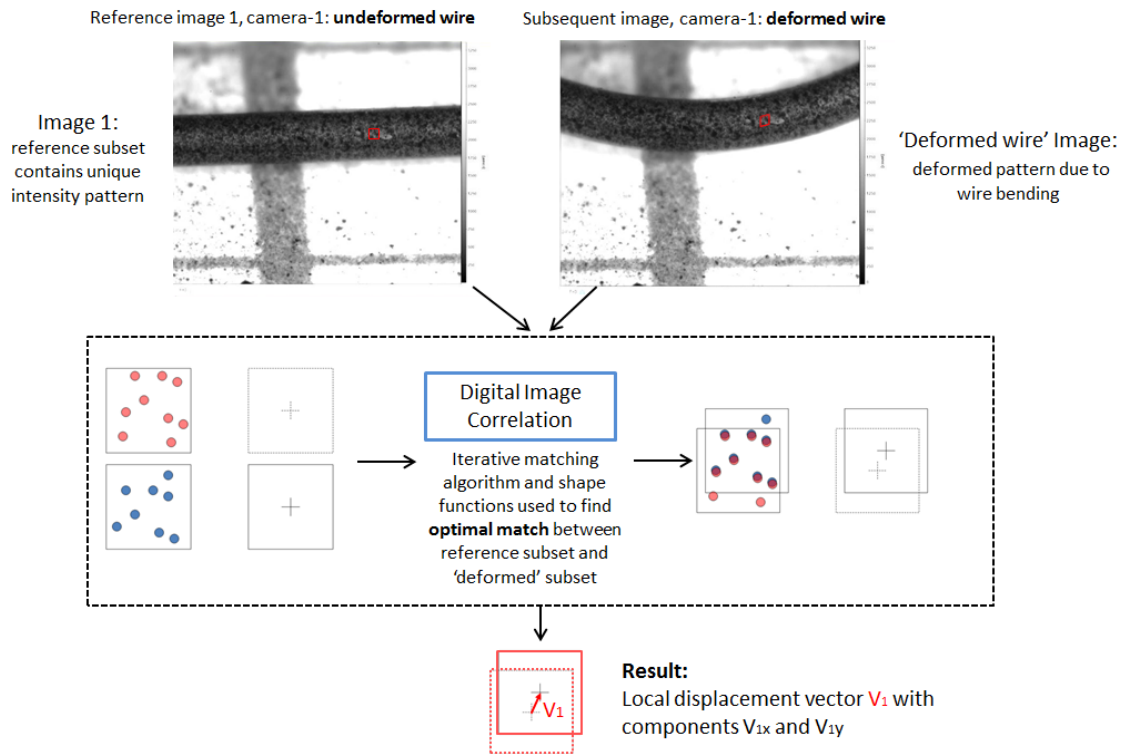
Figure 5-12: Process for DIC 2-D Displacement Vector Processing. This process is performed for every subset of every 'deformed' image to find the deformation field for each wire bend deflection during loading and unloading.

5. 3-D Displacement Vector Processing: Using the 2-D Displacement Vectors calculated from the camera 1 image set and the camera 2 image set (see figure 5-12), together with the calibration model, the DIC software calculates the 3-D Displacement Vectors for the deformed surface to give the 3-D Deformation Field. This process is described in figure 5-13.
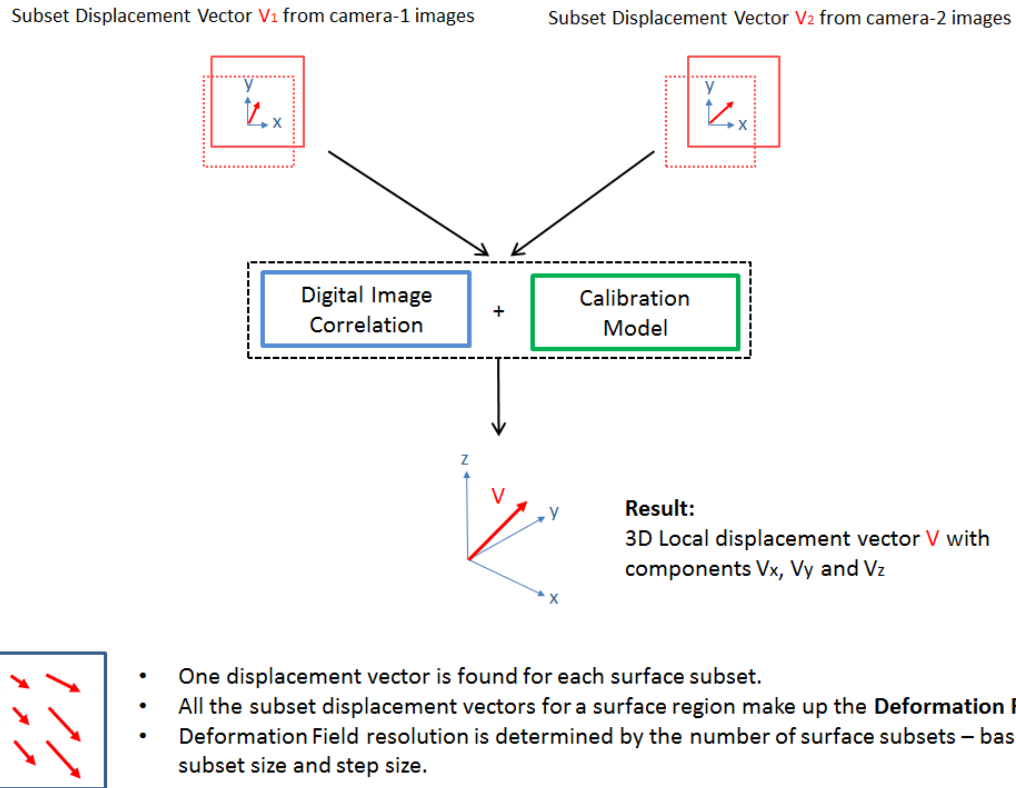
Figure 5-13: Description of 3D-DIC process to calculate the 3-D deformation field from the stereo camera 2-D displacement vectors

6. DIC Surface Height Processing: Using the camera 1 and camera 2 'undeformed' reference images, a reference 'Surface Height Profile' is calculated by the software for the straight wire. This reference profile is then used together with the z-components of the 3-D displacement vectors to calculate the surface height profiles for all subsequent 'deformed' wire positions. Figure 5-14 gives details of the process flow for reference Surface Height processing.
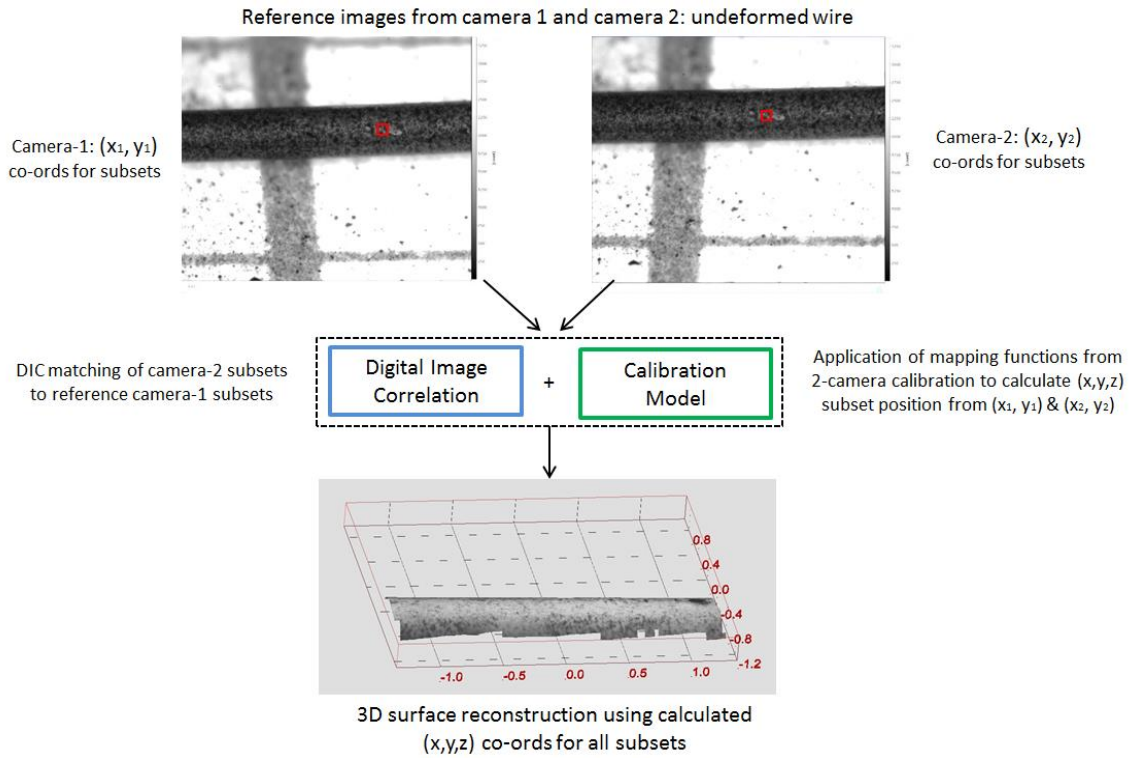
Figure 5-14: Process used by 3-D DIC software to calculate the reference Surface Height Profile for the wire

Surface Strain Calculation

The deformation field results from 3D DIC are then used by the 'DaVis' software to derive the surface strains for the deformed wire. This process is described below:

1. The local strain field for each surface region of the wire is calculated using 5 'neighbor' displacement vectors. A local deformation field is illustrated by the 5 red 'displacement vector' arrows in figure 5-15.
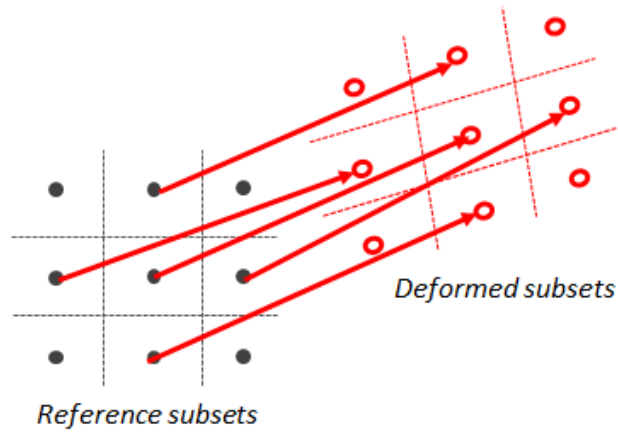
Figure 5-15: Local deformation field described by 5 subset displacement vectors (red arrows)

2. Local Rigid Body Motions are removed. This involves subtraction of rigid body translations (average vector lengths) and rigid body rotations (average vector angles) to obtain a new set of 'shape change' displacement vectors, as shown in figure 5-16 below:
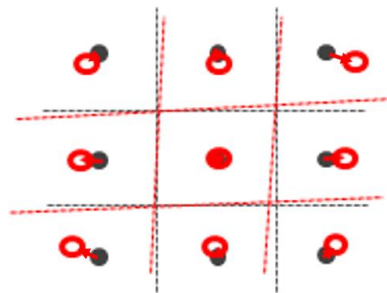
Figure 5-16: 'Shape Change' displacement vectors (short red arrows) after Rigid Body Motion removal

3. The components of the new 'shape change' displacement vectors (V_x, V_y, V_z) are used to calculate the local 3D strain field components:

$$E_{xx}, E_{xy}, E_{xz}$$
$$E_{yx}, E_{yy}, E_{yz}$$
$$E_{zx}, E_{zy}, E_{zz}$$

Each strain component E_{ij} can be defined as the gradient of 'shape change' vector components V_i in the direction of the j-axis. This is explained below with the aid of figure 5-17, showing initial lengths dx and dy of a surface region, together with the deformed shape of that region following bending illustrated by the red lines. The change in shape, or strain, can be described with reference to the initial lengths dx and dy and the displacement vectors V1, V2, V3 and V4.
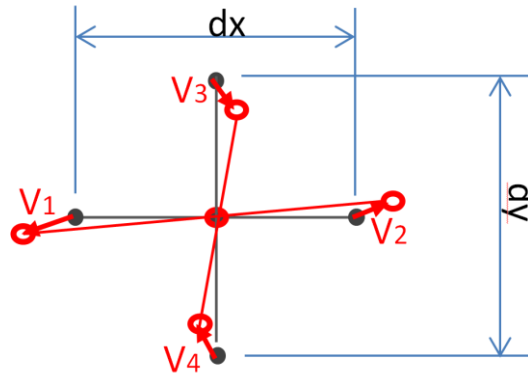
Figure 5-17: initial 'undeformed' surface region illustrated by lengths dx and dy, together with deformed shape following bending illustrated by the red lines

From figure 5-17, it can be seen that the normal strain in the x-direction, E_{xx}, is equal to the change in length of V_x components of V1 and V2 over distance dx in the x-axis direction:

$$E_{xx} = \Delta V_x / dx$$

Likewise, the transverse shear strain, Eyx, is equal to the change in length of Vy components of V1 and V2 over distance dx in the x-axis direction:

$$E_{yx} = \Delta V_y / dx$$

In the same way, all other strain components can be understood by taking 5 local 'shape change' displacement vectors and considering the change in length of the vector components in a given direction.

For output and analysis of the present testing, the Exx strain component results were chosen for the following reasons:

- The main interest is in understanding the bend test results with reference to the uniaxial tensile and compressive results obtained for Vascutek's NiTi#1 wire (see chapter 3), meaning the tensile and compressive axial strain results were most relevant.

- with the 2-dimensional bend set-up (3-Point Bending) with large moment-arm length (support pin span = 20mm) used here, it is assumed that bending will predominantly result in axial strains, with minimal transverse shear.

Figure 5-18 shows an example Exx strain field result for the wire in 3-Point Bending obtained from DIC processing:
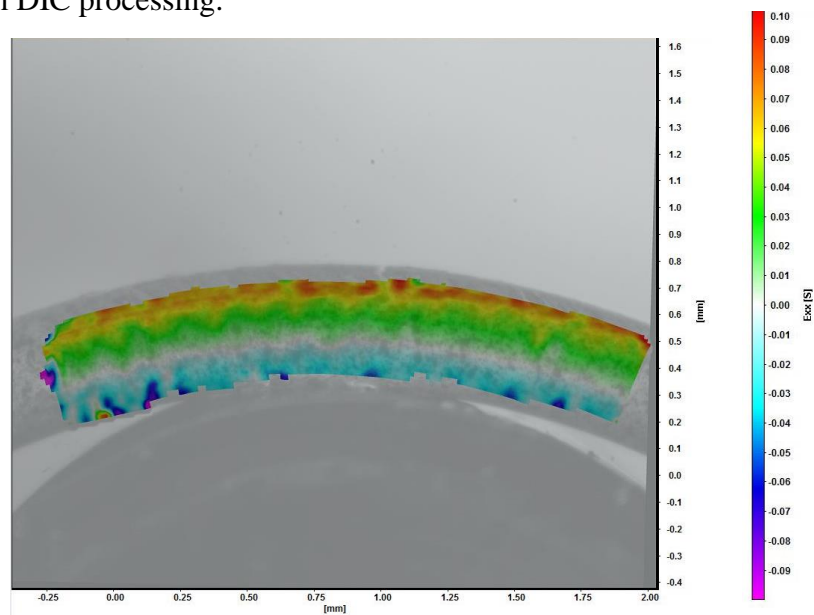
Figure 5-18: DIC result for the NiTi wire on the 3-point bend rig (flat-mounted) at 10mm pin deflection. The image shows the 'Exx' strain field for the wire apex region within the field of view, overlaid on the captured digital photo of the deformed wire.

Error Estimation

LaVision's reference document '*A error estimation of vector components and strain values*' explains that when the components of the strain tensor E_{ij} are derived from the deformation field components, the achievable precision (and the error) depend on the error of the vectors used and the vector spacing (i.e. the grid resolution). The document derives estimated errors for vectors and for strain components based on the vector type and spatial resolution. Relevant error estimates from the document are given below.

Vector Error:

For good quality images (high intensity contrast within a subset, large dynamic range), the precision of 3D vectors is calculated to be **0.025 pixels** for 64x64 pixel subset size.

Exx Error:

For subset size 64x64 pixels with 75% overlap (step size = 16 pixels), the absolute error for E_{xx} strain component derived from 2D vectors is calculated to be 440 µs (0.044%). For strain components derived from 3D vectors, the calculated absolute error doubles, giving a value of 880 µs (0.088%).

For the DIC processing used in the present testing, the subset size was 63 x 63 pixels with step size of 15 pixels, and 3D displacement vectors were used. Therefore the estimated *absolute* error in our Exx results is **900 µs (0.09%).** For superelastic wire in bending, we are mainly interested in strains ranging from 1 to 10%. For this range, the estimated *relative* error in Exx results is 9% for Exx strain result of 1% and 0.9% for Exx result of 10%. The Exx results calculated by DIC are therefore increasingly accurate at higher strains, meaning the method is well suited to measuring superelastic strains of Nitinol wire in bending.

Additional Precision Assessment

In order to assess the baseline precision of the DIC results, the software was used to perform correlation on 2 images where the wire had not moved (i.e. where the trigger had been pressed twice without changing the wire shape). This should give zero values for displacement and strain. In reality, though, the results will not be zero and the erroneous values allow an assessment of the baseline precision of the DIC set-up. This approach was used for 3 sets of identical images – figure 5-19 shows the Exx strain plot for one of these cases.
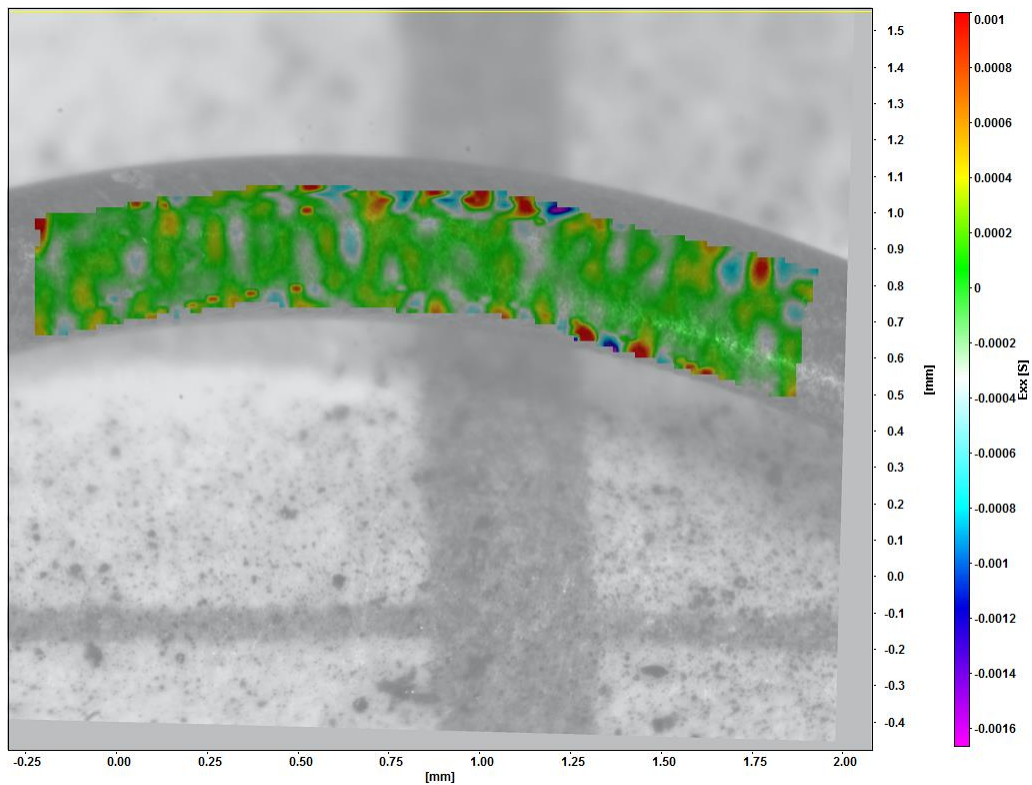
Figure 5-19: DIC strain plot derived from 2 images where no wire deformation has occurred between the 2 images, used to assess the baseline precision of the DIC system

The results from these correlations are given in Table 5-1.

'no deformation' image set	Max strains in centre region (S)	Max strains at edge regions (S)
1 (images 7-8)	± 0.0002	+ 0.0016 / - 0.0017
2 (images 23 – 24)	± 0.00015	+ 0.0012 / - 0.0024
3 (images 35 – 36)	± 0.0002	+ 0.001 / - 0.0016

Table 5-1: strains calculated using DIC for images with no relative deformation, giving baseline precision assessment for the DIC system

The results show that there is some error level in the Exx strain results calculated using the DIC system, and that this error is greater at the edges of the strain field, with relatively high precision in the centre of the strain field. Given these 'baseline error level' results, it was seen that care needed to be taken when analyzing the Exx strain results from the DIC testing, with particular attention to results at the strain field edges.

5.3.7.6 Identification of 'in-focus' bending apex region (Flowchart step 4)

For the tests performed with angled or vertical mounting, the bending direction was out-of-plane relative to the x-y plane of the microscope's platform. A limitation of the 'DaVis' DIC software used was that axial strains could only be correctly calculated from displacement vectors parallel to the x-y plane.It was therefore necessary to identify the bend region where the wire surface had remained axially parallel to the original x-y platform plane (here named the 'in-focus' bend region for simplicity). It is only in this region that the calculated Exx strain field describes the normal axial strain of the wire (after rigid body motion removal). For the 'out-of-focus' bend regions (axial direction not parallel to x-y plane), the Vx components of the displacement vectors (following rigid body motion removal) are not in the normal axial direction of the bending wire, meaning that Exx calculated from these local V_x components will not correctly describe the wire's axial strain. Figure 5-20 helps to describe this limitation of the software in

calculating Exx strain results for a length of wire with out-of-plane bend direction relative to the microscope x-y platform plane:

- V_1 is the 3D displacement vector for a subset in a bend region that remains axially parallel to the x-y plane. Following rigid body motion removal, the V_x component of V_1 is parallel to the x-y plane and so describes the axial displacement of the wire surface at this point. Therefore Exx (= $\Delta Vx / dx$) describes the normal axial strain of the wire in this region.

- V_2 is the 3D displacement vector for a subset in an 'out-of-focus' bend region, which is not axially parallel to the x-y plane. Following rigid body motion removal, the V_x component of V_2 is not parallel to the x-y plane and so does not describe the axial displacement of the wire surface. Therefore Exx (= $\Delta Vx / dx$) does not describe the normal axial strain of the wire in this region.
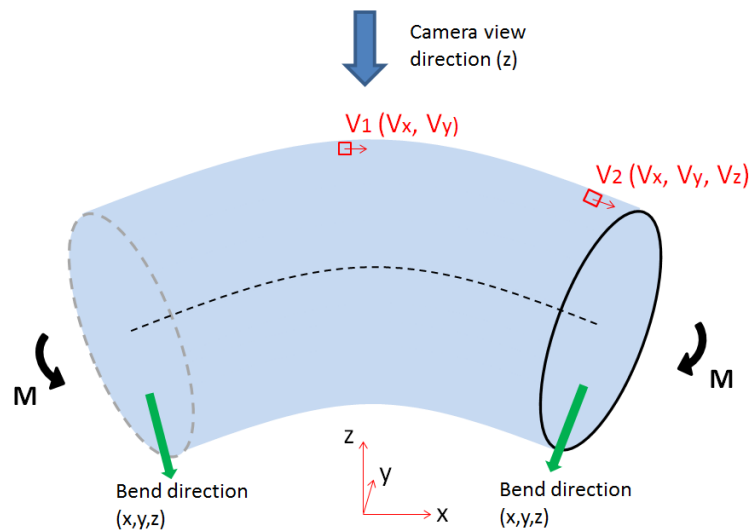
Figure 5-20: Schematic diagram of bending wire with DIC testing using the 'tilt' platform, causing 'out-of-plane' bending of the wire. The diagram shows displacement vector V₁ for the 'in-focus' bend region, described by x and y components, and also vector V₂ for an 'out-of-focus' bend region, described by x, y and z components. For the in-focus region, calculated E_{xx} (= $\Delta V_x / dx$) describes the normal axial strain. For the out-of-focus region, E_{xx} calculation will give an incorrect result for normal axial strain and so cannot be used.

Note that for surface regions that move vertically within the depth of focus during bending but remain axially parallel to the original x-y plane, Exx is still a valid measure of the normal axial strain. The vertical 'z' displacements are accounted for by the Rigid Body Movement subtraction in the Exx calculation.

Appendix 3 provides the detailed steps (with example screenshots) that were followed to identify the 'in-focus' bending apex region for results from 'tilt' and 'vertical' test set-ups.

'In-focus' bending region identification was not performed for results from 'flat' mounted wire tests, where the bending takes place in the x-y plane, as it was assumed in these cases that the wire surface had remained axially parallel to the x-y plane throughout bending deformations.

5.3.7.7 Results Extraction and Plotting (Flowchart step 5)

The Exx strain results and wire 'height profile' results were extracted for the bend apex region (for 'tilt' and 'vertical' test set-up results, this is the 'in-focus' region identified in the previous step). This allowed accurate location of the axial strains on the wire surface, with distance 'y' from the wire's cross-section centerline used for surface location. Appendix 3 includes details of the steps used to achieve this. Figure 5-21 shows an example plot of 'Exx' axial strain against surface location at wire width 'y' from the centreline, from the maximum deformation position during a 30º angle-mounted 3-Point Bend test.
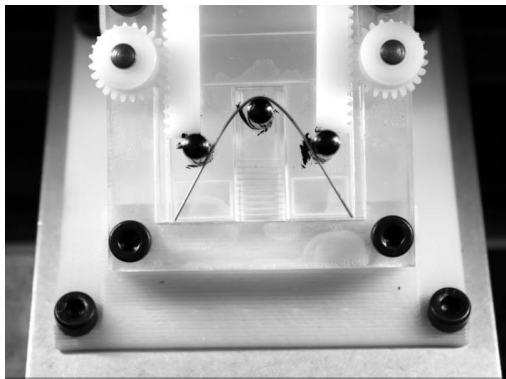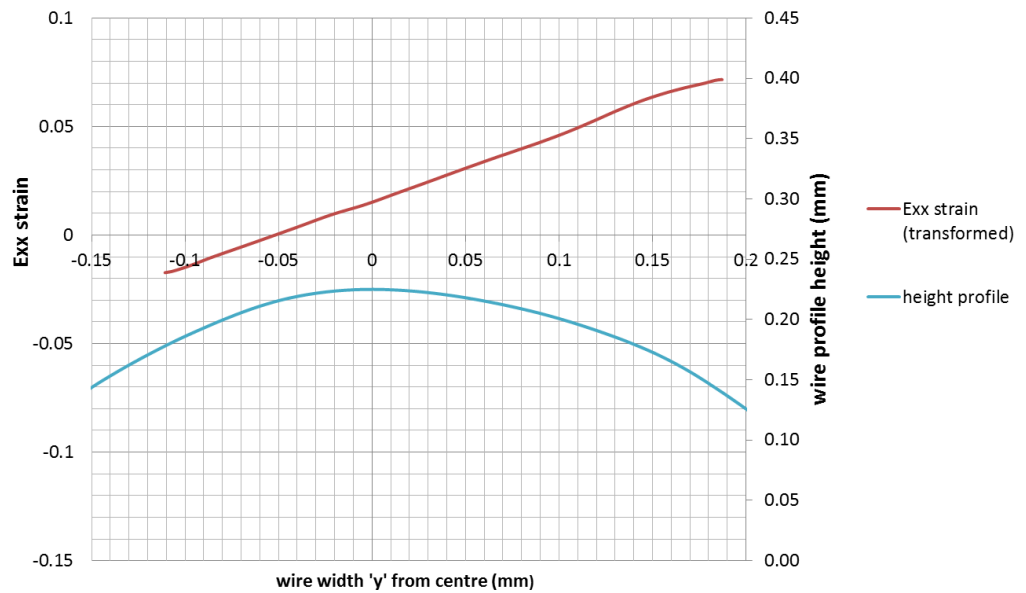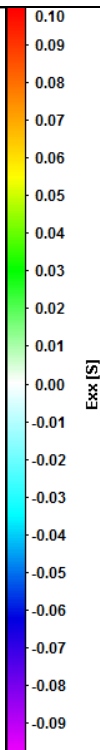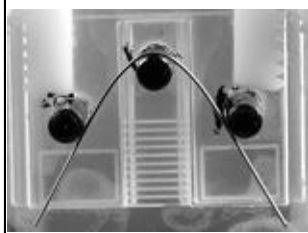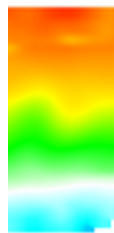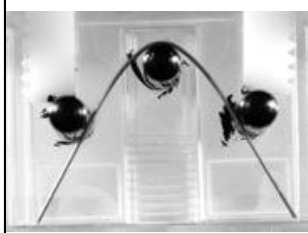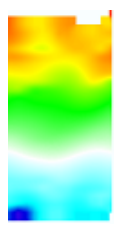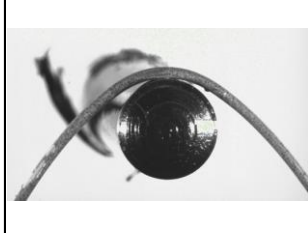
Figure 5-21:(top) Exx strain and Height profile vs wire width (y) for angle-mounted 3-Point Bend test: 0.45 mm wire in 3-Point Bending, 30° angle mounting, 10 mm deflection; (bottom) 'macro view' image of 3-PB pin deflection and wire bend deformation taken with digital camera

Exx Strain Overlay Plots

Using the extracted and transformed Exx strain results, it was also interesting to overlay plots from tests performed on different angle mounting platforms for the same pin deflection. Table 5-2 shows extracted Exx strain field results for the bend apex region of the wire in 3-Point Bending at 10mm deflection, for three different mounting angles. Here, the 'gage length' (width of extracted strain field) is 0.15mm. Figure 5-22 then

shows the Exx profile overlay plot of the results from the three mounting angles for this bend deflection. The Exx values used in this plot are average values across the gauge length of the extracted strain field. It can be seen that the strain profile of figure 5-22 extends to the extrados (0.225 mm from geometric centre) but does not extend to the intrados. This is due to the central 'indenter' pin, which blocks the view of this apex intrados for 3-Point Bend tests.

Exx scale	Test set name	Mounting orientation	Extracted Exx strain field	Wire bend Macro view
	3PB vert 1	vertical - outer		
	3PB 30deg tilt	30 degree angle mounted - outer		
	3PB flat 1	flat mounted		

Table 5-2: extracted strain field results for bend apex of 0.45mm wire at 3-Point Bend deflection of 10mm, from three different mounting angles
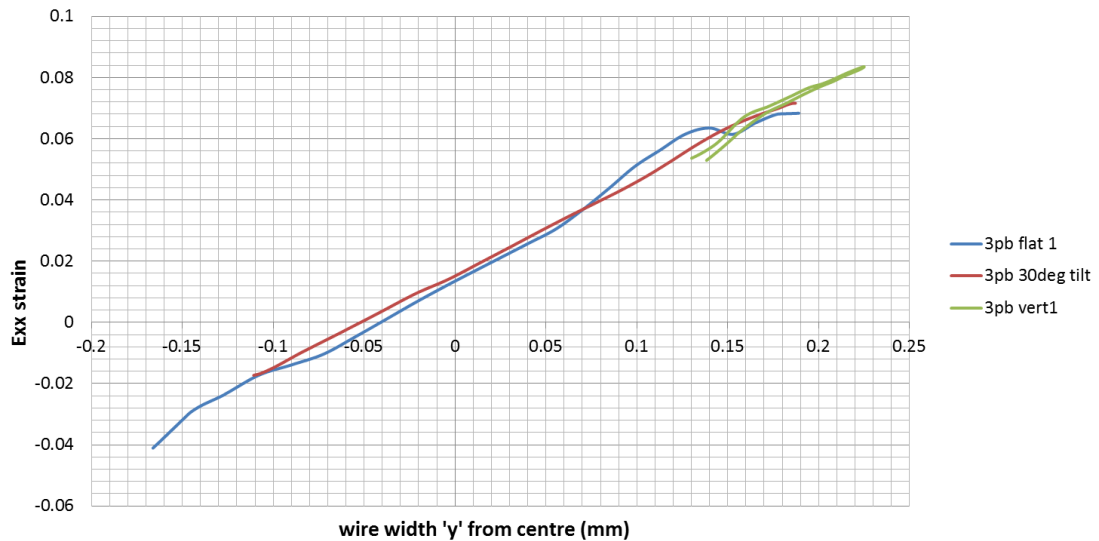
Figure 5-22: Exx strain' overlay plot from 3 Point Bend tests with various mount angles, showing strain distribution across the wire bend apex for pin deflection of 10 mm

From the above 'overlay' plot, it can be seen that the axial strain decreases almost linearly from the outer bend surface towards the inner bend surface, showing that the transverse planes are planar for this large bend deformation. The following parameters can be taken from the linear trendline (not shown in fig 5-22) of this plot, which are useful for validation of FEA simulation:

- Strain gradient across wire width (ie. Curvature) 'k' = **0.31**
- Neutral axis position = 0.048 mm (10.66 % of wire diameter) towards intrados
- Maximum tensile Exx strain = 8.4 % at extrados (at wire width y = 0.225)

Wire deflection measurement from 'macro view' digital images

For every bending deformation step, a 'macro view' image of the wire shape on its test rig was captured (see section 5.3.7.4). These images could then be used to obtain a measure of bending deformation, which was necessary for analyzing the material behavior and as an input for FEA validation simulations. Details of how the wire deflection measurements were performed are given in Appendix 3.

Final Results Plotting

In order to investigate the strain history behavior of Nitinol wire in bending, and to obtain useful experimental data for FEA material model validation, the 'Exx' strain results and wire deflection values from the corresponding 'macro' images were used to plot the following graphs:

- Maximum Exx strain vs Deflection
- Strain gradient 'k' vs Deflection

These plots are shown in Section 5.4 'Results', with detailed analysis and discussion relating to the strain history behavior of Superelastic Nitinol in bending in Section 5.5 'Discussion'.

5.3.8 Test Conditions

The DIC bend testing was conducted in air at room temperature (approximately 23 C). Temperature control and monitoring were not used, and it was assumed that small changes in ambient room temperature would have negligible effect on the strain of the nitinol wire during bend testing. However, it is recommended in future testing that a thermocouple adjacent to the wire sample surface be used to monitor temperature. This bend testing was performed under static conditions, as the wire was deformed incrementally and then held static for DIC image capture at each deflection position.

5.3.9 Test Plan
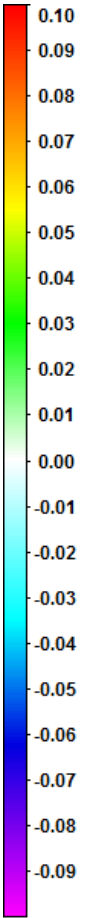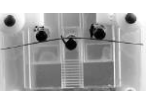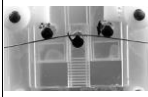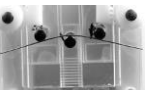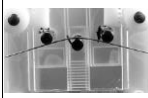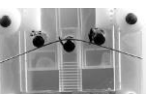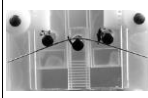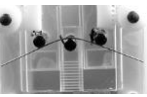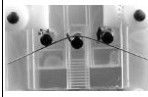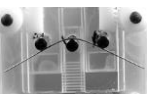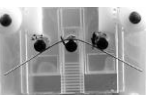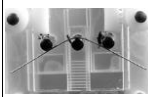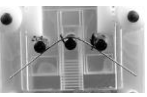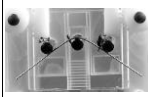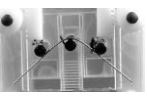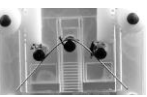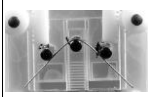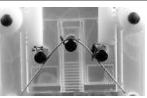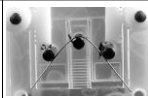
Table 5-3 outlines the tests undertaken on the 0.45 mm NiTi wire samples in order to meet the objectives set for 3PB DIC testing, allowing investigation of strain history effects of nitinol wire in bending.

Test No.	Test Set Name	Mounting Orientation (see figure 5-5 above)	Pin Deflection Description (with deflection increments of approximately 0.3 mm)	Required Measurements
1	3PB vert1	Vertical	Load to 10mm pin deflection, unload to 0mm	Max 'Exx' strain
				Pin deflection (mm)
2	3PB vert2	Vertical	Load to 10mm pin deflection, unload to 0mm	Max 'Exx' strain
				Pin deflection (mm)
3	3PB vert3	Vertical	Load to 8mm pin deflection, unload to 4mm, cycle* with ΔD = 1 mm	Max 'Exx' strain
				Pin deflection (mm)
4	3PB flat1	Flat	Load to 10 mm pin deflection, unload to 4 mm, cycle* with ΔD = 1 mm	Strain gradient 'k'
				Pin deflection (mm)
5	3PB flat2	Flat	Load to 8 mm pin deflection, unload to 4 mm, cycle* with ΔD = 1 mm	Strain gradient 'k'
				Pin deflection (mm)
6	3PB 30tilt1	30^0 angled outer	Load to 10 mm pin deflection, unload to 0 mm	Strain gradient 'k'
				Pin deflection (mm)
7	3PB 30tilt2	30^0 angled outer	Load to 7 mm pin deflection, unload to 0 mm	Strain gradient 'k'
				Pin deflection (mm)
• ΔD cyclic deflections were not successfully executed in DIC testing. Strain results were analysed to the lowest unload deflection recorded.				

Table 5-3: 3-Point Bend DIC test sets

5.4 Results

The testing described above allowed full-field surface strain measurement of the Nitinol wire in bending. A key outcome from this was the ability to measure the maximum strains at the bend apex extrados. Table 5-4 below shows results from the '3PB vert1' test set for the apex region at bend deflections during loading and unloading.

Exx scale	Loading				Unloading			
	deflection (mm)	max Exx strain*	Extracted Exx strain field	Wire bend Macro view	deflection (mm)	max Exx strain*	Extracted Exx strain field	Wire bend Macro view
	1	0.6%			1	0.6%		
	2	1.2%			2	1.3%		
	2.5	1.5%			2.5	3.5%		
	3	2.2%			3	5.8%		
	3.6	5.4%			3.6	6.2%		
	4	6.6%			4	6.4%		
	5	7.5%			5	6.7%		
	6	7.8%			6	7.0%		
	7	8.1%			7	7.3%		
	8	8.2%			8	7.7%		
	9	8.3%			9	8.0%		
	10	8.4%						

* maximum from extracted data for 'av Exx' across gage length (0.15mm)

Table 5-4: 3-Point Bend DIC test results from '3PB vert1' test set, showing maximum extrados strains at the bend apex during loading and unloading deflections

The strain field images in Table 5-4 clearly show the evolution of the strain during loading from 1mm deflection (with apex extrados strain of 0.6%) to 10mm (with extrados strain of 8.4%). By showing the load and unload results for given 3-Point Bend deflections alongside each other, the table also clearly shows evidence of load-unload strain hysteresis for the superelastic wire in bending.

To further investigate the strain history effects in bending, which was a key objective of the DIC work, it was necessary to plot the data in a relevant manner. It was found that two plots in particular were useful for investigating this behaviour:
- Maximum Exx Strain vs Deflection
- Exx Strain Gradient 'k' vs deflection

These results are plotted and described in this section, and are then used for a detailed consideration of the strain history effects in Section 5.5 'Discussion'.

5.4.1 Maximum Tensile Strain vs Deflection for Nitinol Wire in 3-Point Bending

Figure 5-23 shows results from test sets '3PB vert1', '3PB vert 2' and '3PB vert 3', plotting maximum tensile Exx strain (at the bend apex extrados) against 3-Point Bend pin deflection during loading and unloading.

From figure 5-23, the same general behaviour can be seen in all tests, with the strain history following the same pattern during loading and unloading in bending for each test set. The consistency of this experimentally observed behaviour is important, meaning it is predictable and can be used as a basis for validating FEA simulation models. This behaviour will be described and discussed in depth in Section 5.5 'Discussion', but the main pattern followed during each test is outlined below the figure.
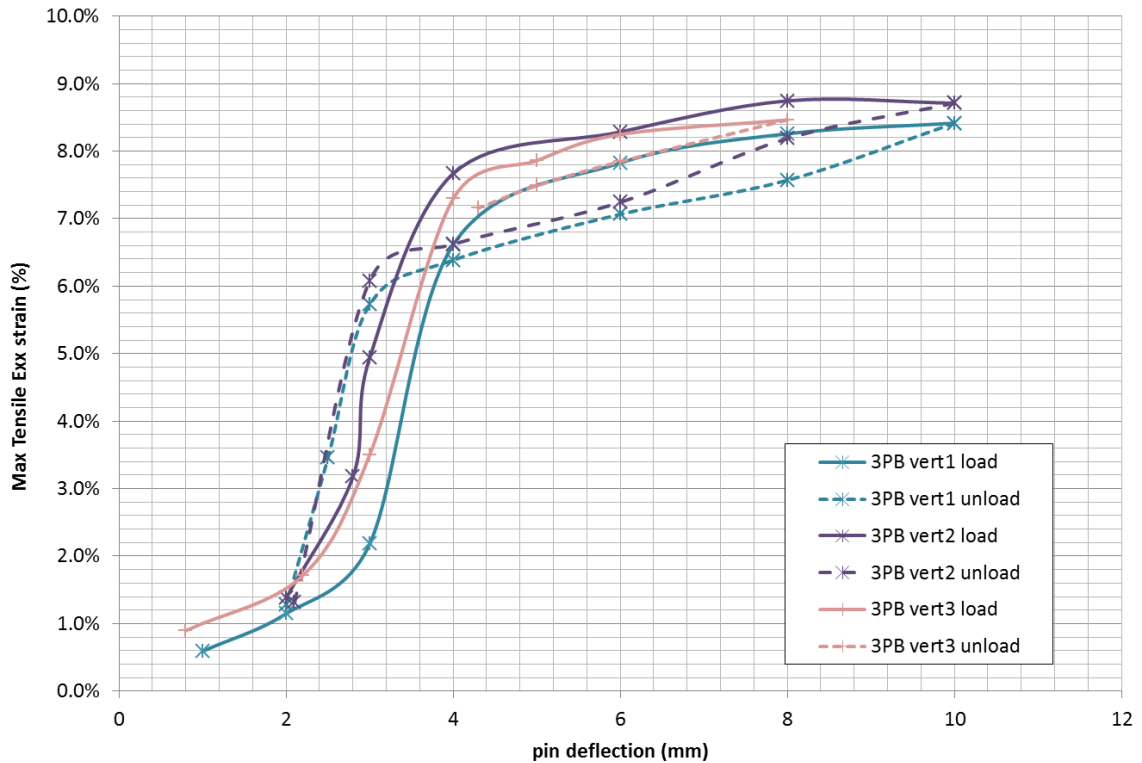
Figure 5-23: Maximum tensile Exx strain vs indenter pin deflection for 0.45 mm NiTi#1 wire in 3-Point Bending during loading and unloading

Max strain – Deflection behaviour in loading:

1. Initial 'linear' Max Strain – Deflection increase
2. Steep increase in Max Strain for a small Deflection increase
3. Max Strain 'plateau' with minimal strain increase for a large deflection increase

Max strain – Deflection behaviour in unloading:

1. Gradual decrease in Max Strain for a large unloading deflection
2. Steep decrease in Max Strain for a small deflection decrease, occurring at a lower deflection range than for the loading step (2) above.
3. The strain results at lower unloading pin displacements (<2 mm) were not plotted, but the 1mm and 2mm max strain values in table 5-4 show that the

strain-deflection behaviour in this 0-2 mm deflection region is the same in unloading as in loading.

It is important to note that between maximum deflection and approximately 2 mm deflection, the unloading strain path is different from the loading strain path. This hysteresis between loading and unloading is related to the strain history dependence effects observed by van Zyl et al (33) as described in chapter 2 'Literature Review', and will be discussed in detail in the Section 5.5 'Discussion'.

5.4.2 Strain Gradient vs Deflection for Nitinol Wire in 3-Point Bending

Figure 5-24 shows a plot of the 0.45 mm wire's 'Exx' surface strain against the distance 'y' from the wire's centre, for the bend apex section. This plot shows the strains across the wire width when the wire is at a 3-Point Bend deflection of 10mm (for corresponding strain field image, see '3PB 30 deg tilt' row in table 5-2). A linear trend-line has been fitted to this plot and its equation displayed. The strain gradient 'k' was taken from this trend-line – in this case k = 0.3091 – and could then be used for analysis of the bend apex curvature, as described below.
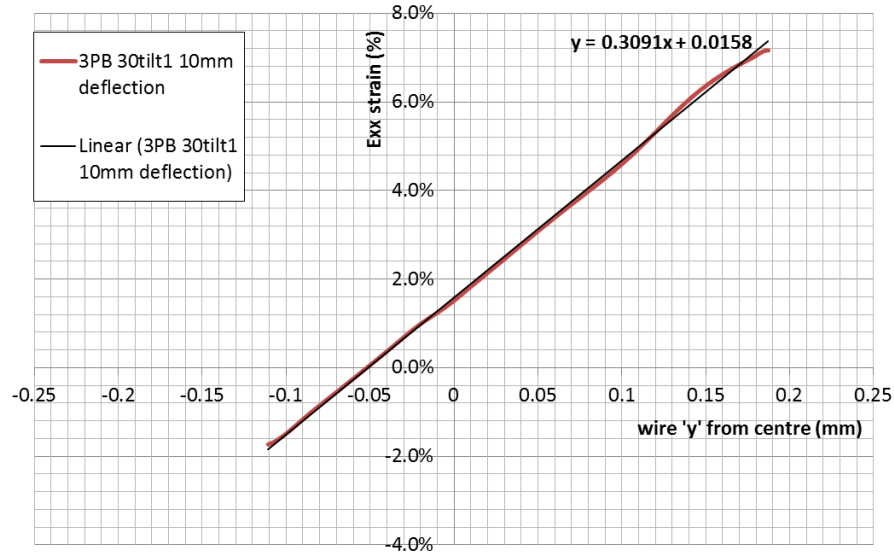
Figure 5-24: Example of how Exx strain gradient 'k' is found from the plot of Exx against wire width position, using the linear trend-line equation. In this case, for 10 mm bend deflection, the 0.45 mm wire bend apex has strain gradient 'k' of 0.3091

Figure 5-25 shows results from test sets '3PB flat1', '3PB flat2', 3PB 30tilt1' and '3PB 30tilt2', plotting strain gradient 'k' against 3-Point Bend pin deflection during loading and unloading. From beam bending theory, it is known that the axial strain gradient 'k' is inversely proportional to the Radius of Curvature for a section in bending. Therefore, the plots of figure 5-25 give a clear indication of the change in apex bend curvature with deflection of the wire. [Note that for the 3PB flat1 and 3PB flat 2 data, the unload curves stop at or above 4 mm deflection. As noted in Table 5-3, this was due to failure to execute ΔD cycling from these unloading deflections using the current equipment and method, and so strain results were analysed to the lowest unload deflection recorded for these cases.]
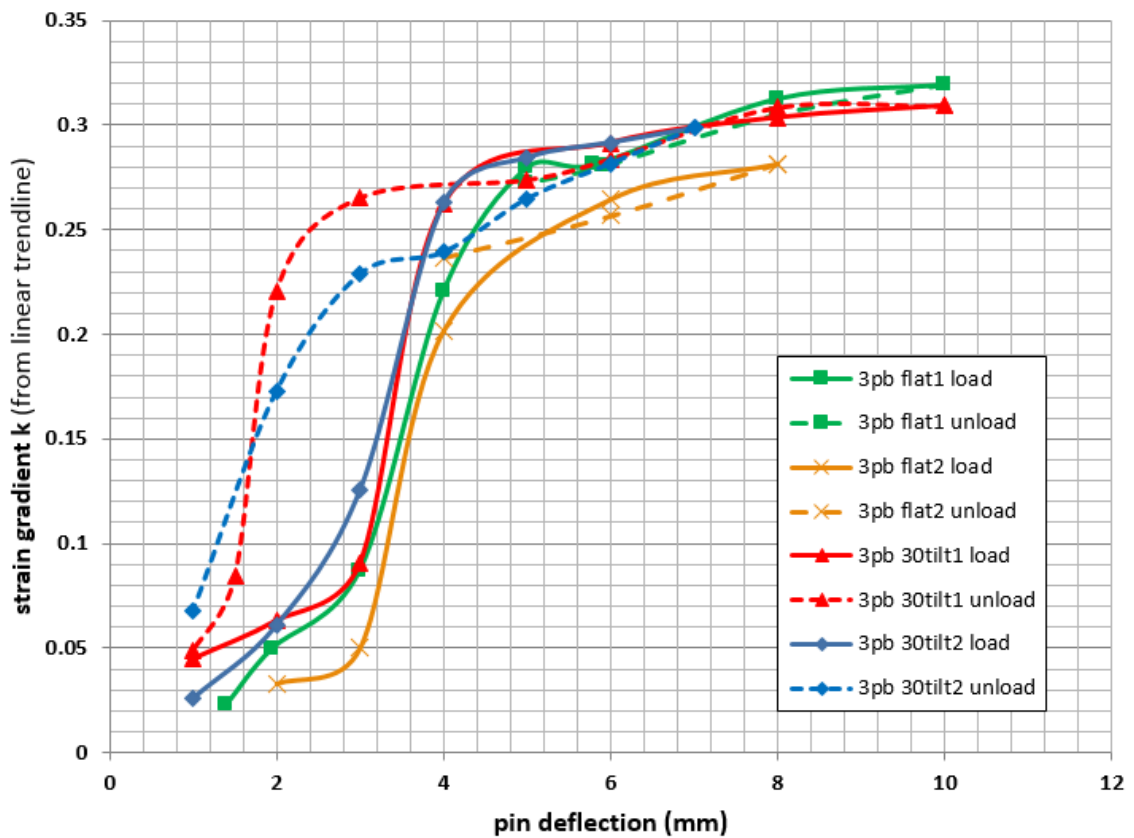
Figure 5-25: Exx strain gradient 'k' vs indenter pin deflection for 0.45 mm NiTi#1 wire in 3-Point Bending during loading and unloading.

Although there is some scatter in the results seen in figure 5-25 (thought to be due to slight differences in mounting angle of the wire on the test rig and due to error in the pin deflection measurements, particularly for the 'flat-mounted' tests), the general behaviour is again consistent across the test sets and is useful for understanding strain history effects for nitinol in bending. By considering the link between strain gradient and bend curvature, the general pattern is described below.

In loading:

1. Initial gradual increase in bend curvature with bend deflection

2. Steep increase in curvature for a small deflection increase – suggesting localized bending at the apex region

3. Strain gradient 'plateau' with minimal curvature increase for a large deflection increase – suggesting the global wire deflection is being accommodated by bending of the wire at different axial locations away from the central 'apex' region

In unloading:

1. Gradual decrease in curvature for a large unloading deflection – suggesting that unloading deflection is mainly being accommodated by straightening of the wire at different axial locations away from the central 'apex' region

2. Curvature remains high during unloading for deflections where it was much lower in loading, meaning that the bend apex has a different shape in this deflection range depending on whether it is loading or unloading. In fact, this can be seen in figure 5-26, showing a different 'macro view' wire bend shape at 3.5 mm pin position in loading and in unloading following 3-Point bending to 10 mm max deflection.

3. Steep decrease in curvature for a small deflection decrease – suggesting localized straightening at the apex region. This can be seen in figure 5-27, showing a large change in the 'apex' bend shape for a small change in global unloading deflection for the wire from 3.5 mm to 2.5 mm deflection.

4. For small deflections near zero, the curvature will be the same in unloading as in loading. Evidence for this is given in figure 5-28, showing the same wire bend shape in loading and unloading at 2 mm deflection for a flat-mounted 3-point bend test.
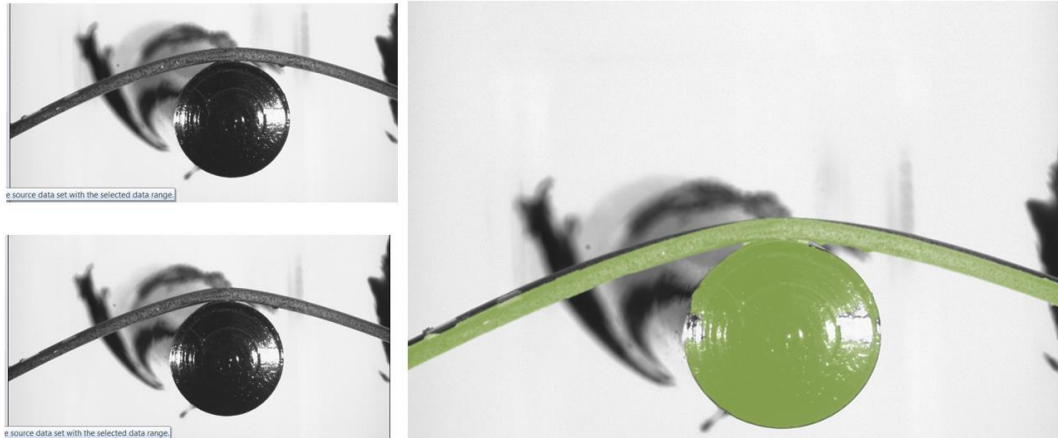
Figure 5-26: left: 'macro view' wire bend shape images from 3-Point Bending, during loading (top) and unloading (bottom) at the same pin deflection position of 3.5 mm. Right: overlay of the pin and wire from the 'unload' image (in yellow) with the 'loading' image, showing more localized apex bend curvature in unloading.
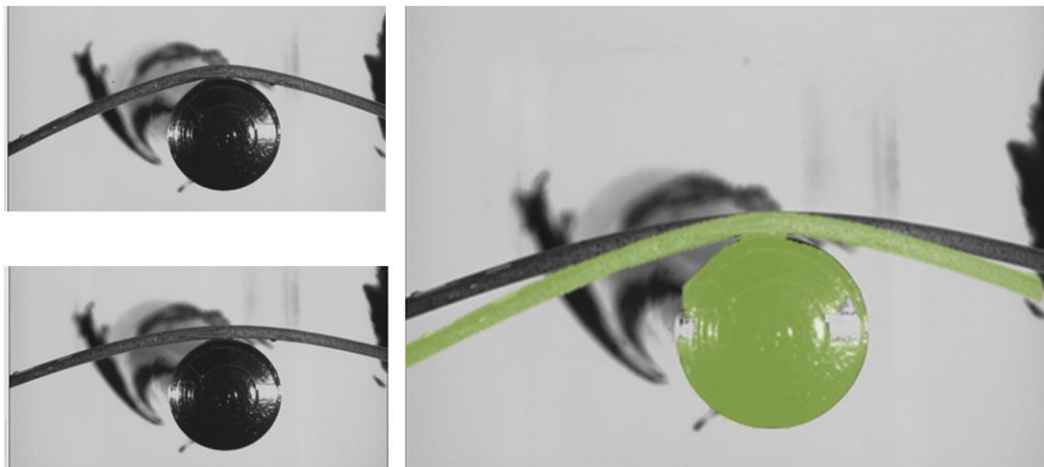
Figure 5-27: left: 'macro view' 3PB wire bend images during unloading at 3.5mm pin deflection (top) and 2.5mm deflection (bottom). Right: the 3.5mm deflection image (yellow) overlayed with the 2.5mm deflection image, showing a large local change in curvature at the bend apex region for this small change in global bend deflection.
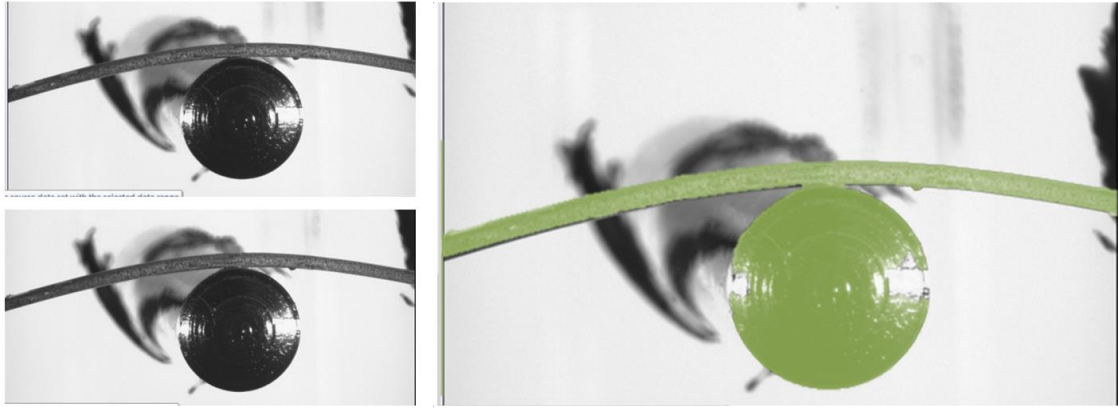
Figure 5-28: left: 'macro view' 3PB wire bend images, during loading (top) and unloading (bottom) at the same pin deflection of 2mm. Right: the unloading image (yellow) overlayed with the loading image to demonstrate the similarity in shapes, showing that for small pin deflections (0-2mm), the loading and unloading shapes and strain paths are the same.

Experimental Error

With reference to the results presented here in section 5.4, and in particular to figures 5-23 and 5-25, there is clearly a level of variability between tests evident in these results. Considering the 'error estimation' and 'baseline precision' values found in section 5.3.7.5, the DIC processing itself could only account for a small part of this variability (equal to a maximum of 0.11% strain from the absolute error in Exx calculation plus the maximum baseline error). It is thought that the variability is largely due to the following aspects of the experimental method: the set-up of the wire on the 3PB test rig, where the wire may shift and therefore slightly alter its bending plane during the test; the manual method used to incrementally load and unload the wire in bending on the 3PB rig, which could lead to small differences in the pin positioning and therefore the wire shape for a given deflection; the deflection measurement methods, which could lead to error of up to 0.3mm in the measured deflection taken from the 'macro view' images (as outlined in Appendix 3). Beyond this, there actually may be variations between wire test specimens

in the local bend apex strains for a given 3PB deflection – particularly in the phase transition region from 1.2% to 7.5% strain, as noted by Reedlunn et al (18).

Clearly, future development of this test method should focus on reducing experimental variability by improving the design and control of the 3PB test rig and deflection measurement method. The 3-D microscopic DIC system itself is capable of good accuracy for this application. Despite the variability between tests, the results of figures 5-23 and 5-25 have consistently shown clear features that are very useful for understanding the behaviour of superelastic nitinol wire in bending, as will be discussed further below.

5.5 Discussion

Before considering the bending behaviour of nitinol wire to large deflections, it is useful to consider the basic principles of beam bending theory in terms of bending moments and distributions of stress and strain. These basic principles can then be used to help understand the more complex nitinol bending behaviour.

5.5.1 Beam Bending Theory *(ref 26)*

For a beam in bending, the applied transverse loads produce bending moments. For a particular cross-section along the length of the beam, the bending moment acts about the neutral axis and attempts to rotate that section. This is illustrated in figure 5-29 below, for a beam in symmetrical 3-point bending. The units of moment are Nm, as the moment acting on a section is a product of the applied force and its distance from the section.
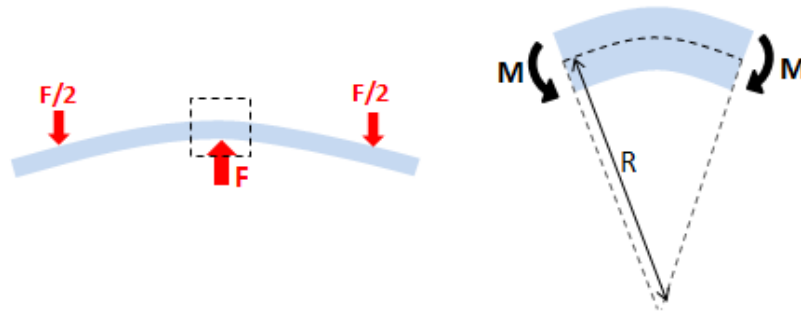
Figure 5-29: Free Body Diagram of symmetrical 3-point bending (left), with detail (right) showing the applied moments acting about the neutral axis at a central region, bending the region into a curve where the neutral axis has radius of curvature R

In order to achieve static equilibrium at a given bend radius, the applied moment about the neutral axis of a given section must be balanced by an internal moment. This internal moment is produced by the axial tensile and compressive stresses generated in the section, as shown in figure 5-30a below. The internal moment is given by the summation of the force x the distance from the neutral axis for all the internal elements within the section, where force = stress x area of element. This is illustrated in fig 5-30b below.
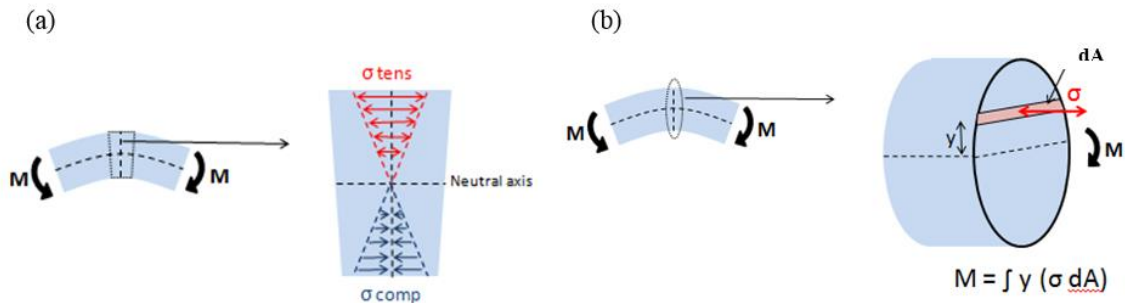
Figure 5-30: (a) shows the tensile and compressive stresses generated in a section due to applied moments; (b) shows how an internal moment is produced by the stresses acting on elements at distances 'y' from the neutral axis

The bending moment produces axial strains at that section in the beam, with a gradient 'k' across the width of the beam (see figure 5-31 below). 'k' is inversely proportional to the radius of curvature of the neutral axis 'R'.
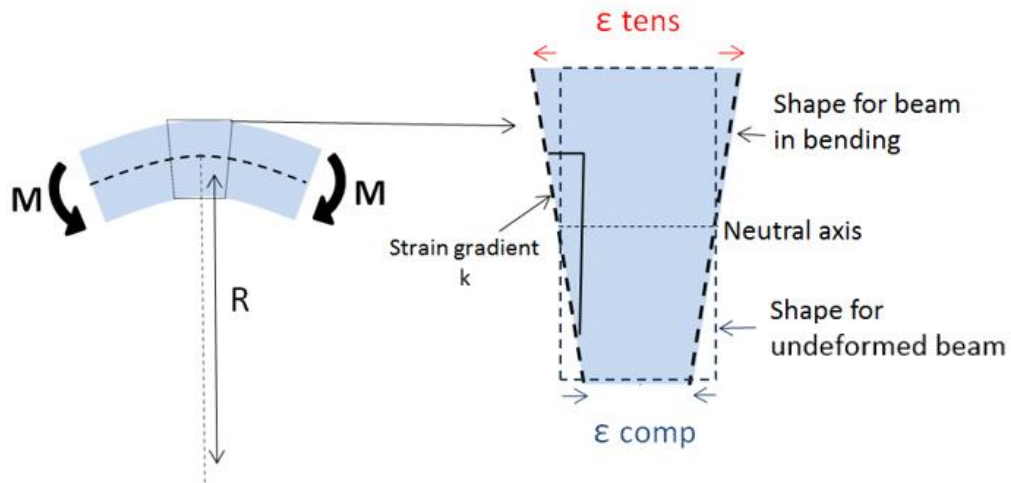
Figure 5-31: diagrams show how strain changes linearly across the width of a beam in bending, with strain gradient k. The deformed section has maximum compressive strain at the intrados and maximum tensile strain at the extrados

5.5.1.1 Neutral Axis Position in Beam Bending

To achieve static equilibrium in beam bending, the forces above the neutral axis must be balanced by the forces below the neutral axis for a given section along the beam's length. Therefore, the sum of the tensile forces on one side of the neutral axis must be equal and opposite to the sum of the compressive forces on the other side, giving the equation:

$$\int \sigma_{tensile} \, dA = \int \sigma_{compressive} \, dA$$

This is illustrated in figure 5-32 below for a material having a higher modulus in compression than in tension, so that the neutral axis is shifted towards the compressive side to achieve equilibrium. The figure also shows how this neutral axis shift causes

strain asymmetry across the wire, in this case giving a higher value for maximum tensile strain (at the extrados) than for maximum compressive strain (at the intrados).
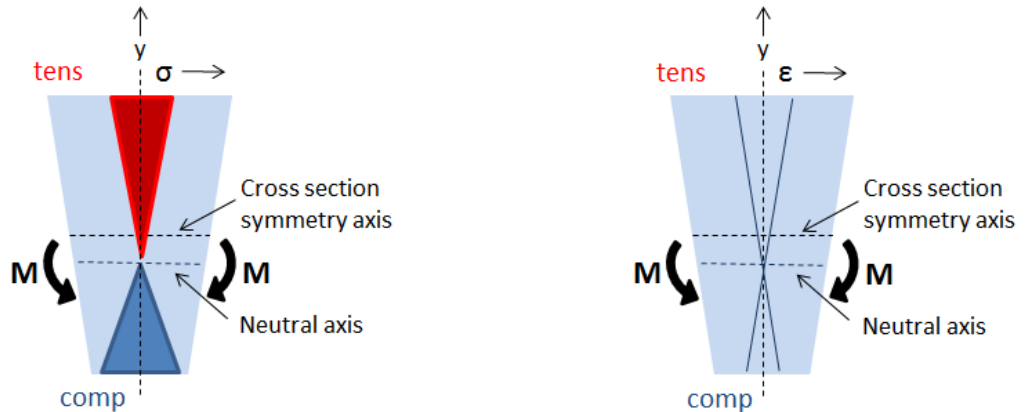
For static equilibrium:

$$\int \sigma_{tens} \, dA = \int \sigma_{comp} \, dA$$

Figure 5-32: tensile – compressive stress asymmetry causes a shift in the neutral axis position (left), which causes asymmetric strains in tension and compression (right)

5.5.1.2 Plastic Deformation during Beam Bending

Ref (26) gives a good explanation of what happens when a beam is deformed in bending to beyond the material's elastic limit. This explanation is quoted in summary below:

"Consider a material exhibiting elastic – perfectly plastic behaviour, as shown below: (figure 5-33, reproduced from ref 26):
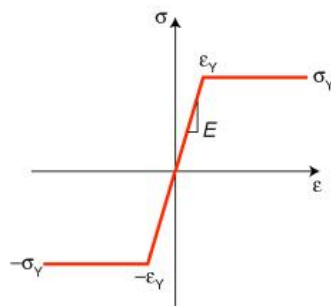
Figure 5-33: Stress-strain curve for an elastic – perfectly plastic material (reproduced from ref 26)

Stress and strain distributions when applying a moment sufficient to cause plastic deformation are shown below (figure 5-34, reproduced from ref 26). In the outer regions of the beam, the stress will be capped at σ_y, although the strain will continue to increase linearly with distance from the neutral axis, as in the elastic case. The curvature (strain gradient), k, induced by a given moment, M, will now be greater, since this increase will be required in order to bring the internal moment back up to the level of the applied moment – i.e. Bending will increase."
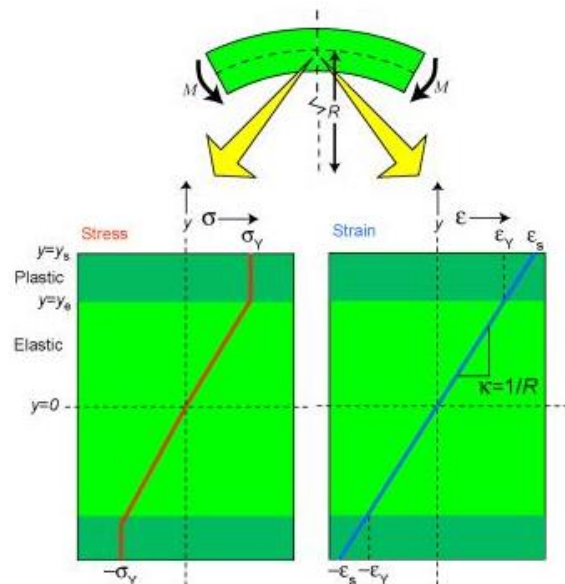
Figure 5-34: distributions of stress and strain within a beam due to application of a moment sufficiently large to cause plastic deformation (reproduced from ref 26)

This explanation of plastic beam bending behaviour gives a key insight to understanding the behaviour of superelastic nitinol in bending: when the stress 'plateaus' at the outer bend regions, the bend curvature must increase by a greater amount for a given change in applied moment in order to achieve equilibrium.

5.5.2 Analysis of Strain History of Nitinol Wire in Bending

The beam bending theory outlined above can be used to help in understanding the behaviour seen in the figure 5-23 and 5-25 results. In order to investigate this, a single data set from each graph is again plotted below (figures 5-35 and 5-36), with the key regions of the plots numbered for description and analysis.
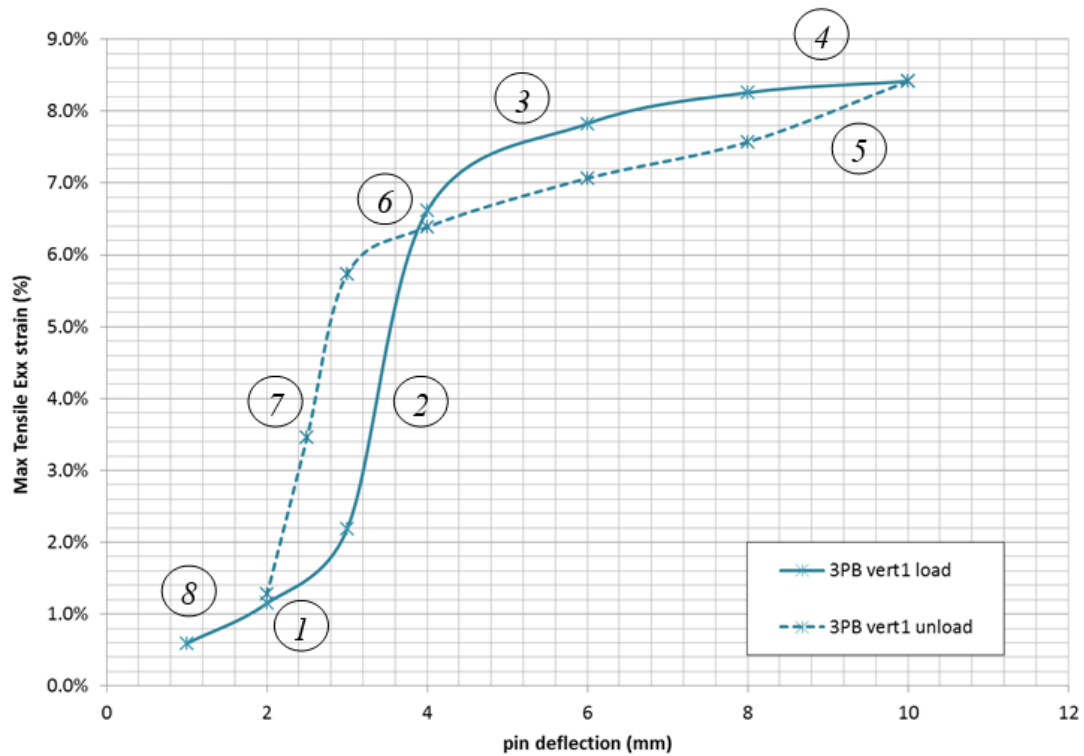
Figure 5-35: Max Tensile 'Exx' Strain (at extrados) vs Deflection plot from DIC testing, test set '3PB vert1', with the different regions of the load and unload curves numbered for analysis

208
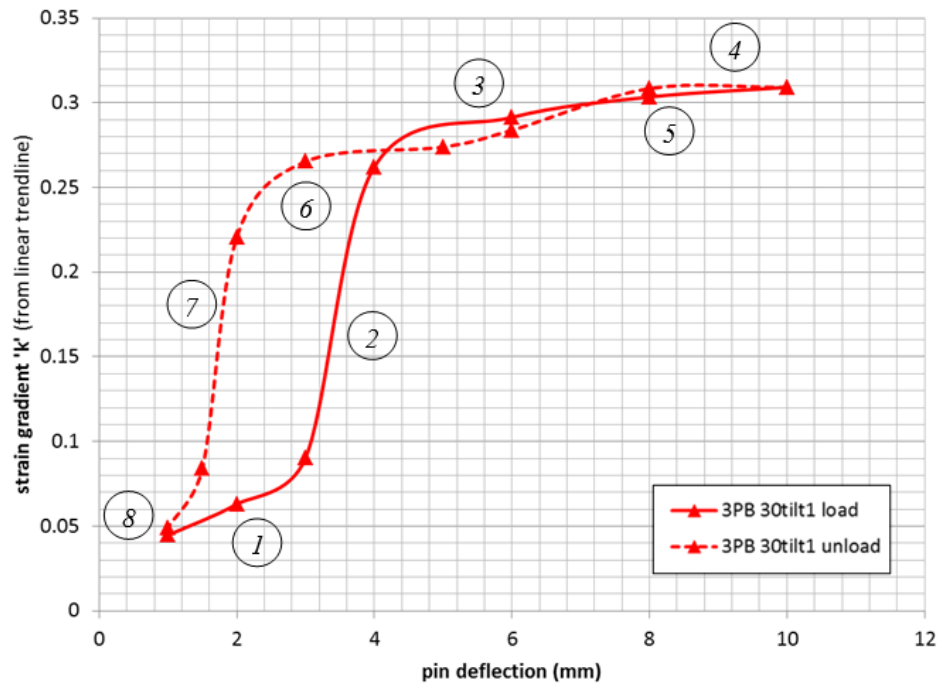
Figure 5-36: Exx Strain Gradient 'k' vs Deflection plot from DIC testing, test set '3PB 30tilt1', with the different regions of the load and unload curves numbered for analysis

Each of the numbered regions in figures 5-35 and 5-36 will be described and analysed below. For each region, diagrams will be shown to represent the stress distribution and strain distribution across the width of the bend apex region that satisfy the equilibrium conditions for applied moment vs internal moment and for Σ tensile forces vs Σ compressive forces (according to beam bending theory). DIC result images from flat-mounted 3-Point Bend testing will also be shown to give experimental evidence for the theoretical explanation, in particular showing how the strain field evolves axially along the bending wire during loading and unloading. Reference will also be made to the maximum strain values from table 5-4, as these values are from direct DIC measurement of the bend apex extrados during vertical mounted testing and correspond with the strain values plotted in figure 5-35.

Loading:

Region (1) Up to an indenter pin deflection of approximately 2.6 mm, the wire bends according to Euler-Bernoulli beam theory (for small deflection bending of linear elastic material beams) up to a strain of approximately 1.5 %. The stress and strain distributions across the bend apex section are represented in figure 5-37.

The key equations for Euler-Bernoulli beam theory as it applies to symmetrical 3-point bending are given below figure 5-37.
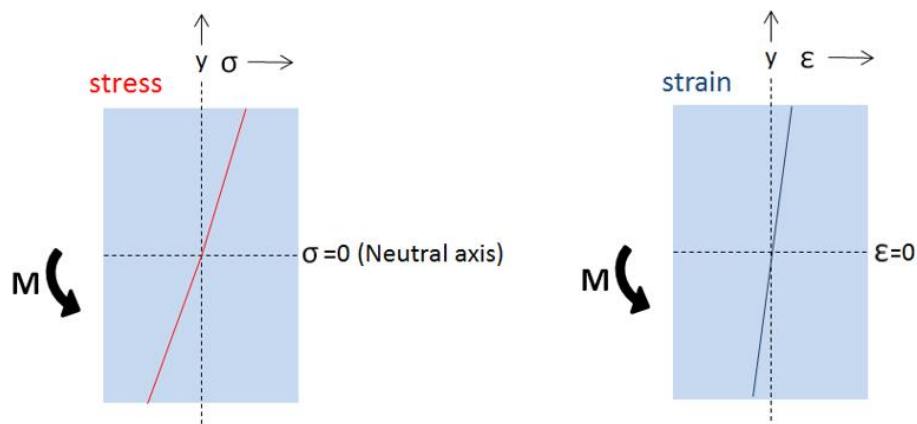
Figure 5-37: schematic diagrams of distributions of stress and strain within the bend apex section during loading region (1)

Applied moment **M = Fx / 2**, where F = applied load, x = distance along beam from support pin

The maximum moment is at the centre of the bending beam, where x=L/2, and is given by **M = FL / 4**

σ = M y / I, where σ is the stress in the section at a given distance 'y' from the neutral axis. I is the second moment of area which depends on the cross-sectional shape of the beam. For the wire tested here, the cross-section is circular and **I = Πr⁴ / 4**

Axial strain Ɛ at a given distance from the neutral axis is given by $Ɛ = σ / E$, where E is the young's modulus of the linear elastic material. Note that for our Nitinol material, the modulus E is slightly higher in compression than in tension for the initial 'linear' part of the stress-strain graph, meaning that there is stress and strain asymmetry even at small bending deflections, with the neutral axis shifted slightly towards the compressive bend side.

Axial strain Ɛ at a distance 'y' from the neutral axis is also given by $Ɛ = ky$, where k is the strain gradient across the wire. For small deflections of the round wire where the neutral axis is approximately the same as the geometric axis, the maximum tensile and compressive strains can be well approximated by $Ɛ = r / R$ (using y = wire radius 'r' and k = 1 / R, where R is the bend radius of the neutral (and in this case, geometric) axis).

Deflection at a given position 'x' along the overall span 'L' of the symmetrical 3-Point Bend beam is found using the following equations:

$$w(x) = \begin{cases} -\frac{Px(4x^2-3L^2)}{48EI}, & \text{for } 0 \le x \le \frac{L}{2} \\ \frac{P(x-L)(L^2-8Lx+4x^2)}{48EI}, & \text{for } \frac{L}{2} < x \le L \end{cases}$$
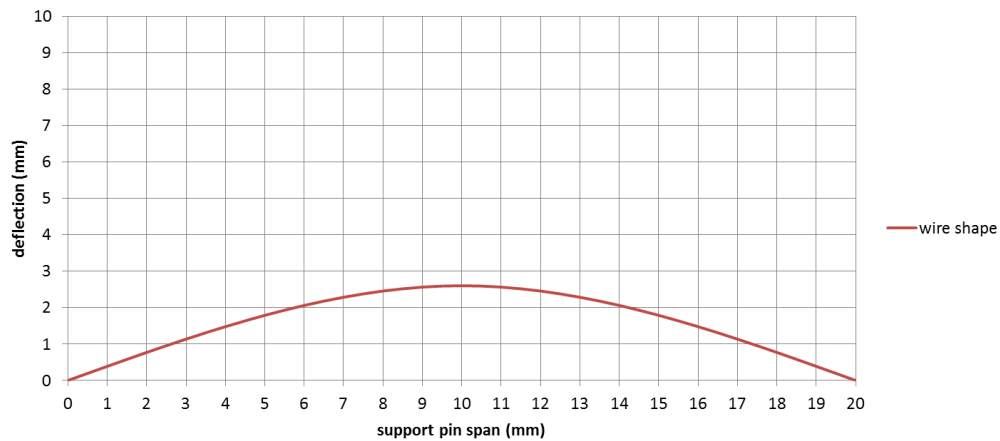
Figure 5-38: theoretical wire shape between the support pins for 2.6mm indenter pin deflection, plotted using Euler-Bernoulli beam theory for symmetrical 3-Point Bending to calculate deflection at a given distance 'x' along the beam

In terms of distribution of curvature along the wire between the support pins, the curvature will increase linearly from zero (straight wire) at one support pin to a maximum at the central indenter pin (bend apex) – see figure 2-21 of 'Ch 2: Literature Review'. To further illustrate this, the curve in figure 5-38 above has been plotted using Euler Bernoulli beam theory for deflection to show the theoretical wire shape (distribution of deflection) for the present 3-Point Bend set-up with indenter pin deflection of 2.6 mm.

Flat-mounted DIC Result Images for Region 1

Figures 5-39 and 5-40 below show images from the DIC testing using the flat-mounted 3PB rig, with Exx strain field results overlaid on the digital photo of the deformed wire at 2mm and 2.6mm deflections during loading. Alongside this is the 'macro view' to give a wider view of the deformed wire shape.

From these images, it can be seen that the strain is distributed along the length of wire in the microscopic view (approx. 2mm x 2mm FOV) of each figure, and that the tensile and compressive strains are similar either side of the central neutral area. These features, together with the 'macro view' wire shapes, show typical small-deformation, elastic bending behavior. From table 5-4, the maximum extrados strain (averaged across the DIC gage length) at 2.5mm is 1.5%. From uniaxial testing (see figure 5-42 below) this is close to the upper limit for austenite elastic loading before onset of Stress-Induced Martensite (SIM) phase transformation.
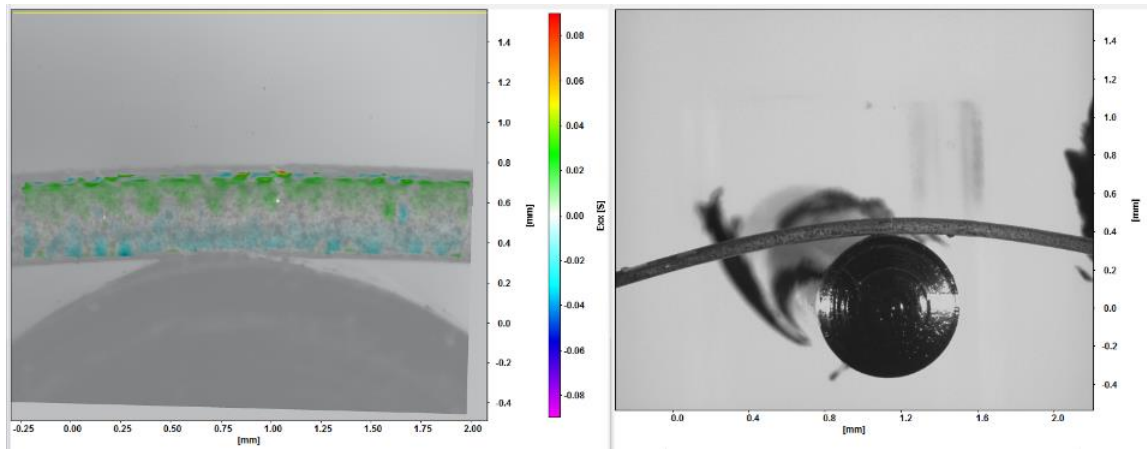
Figure 5-39: (Left) DIC microscopic image of wire and 3PB indenter pin with overlaid Exx strain field on the wire (flat-mounted) at 2 mm deflection during loading. (Right) Macro view.
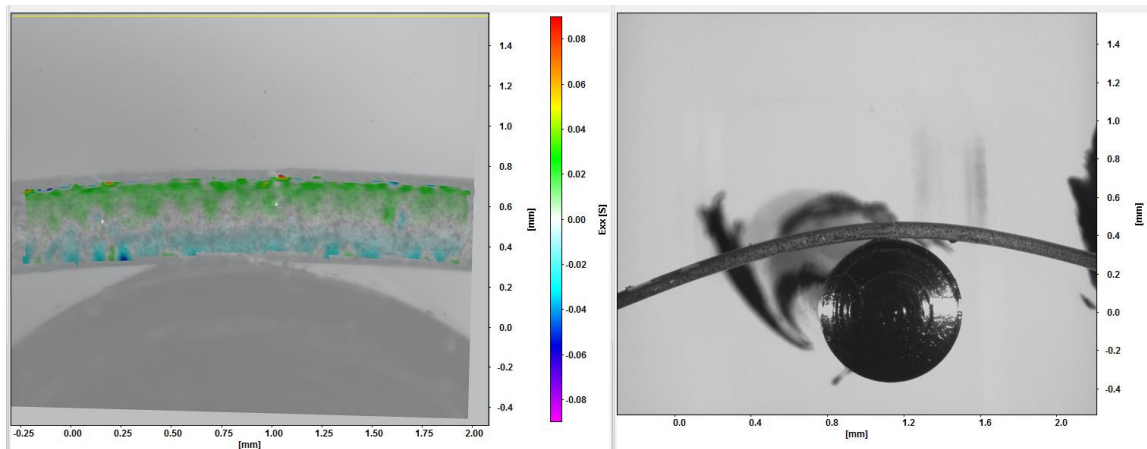
Figure 5-40: (Left) DIC microscopic image of wire with overlaid Exx strain field at 2.6mm deflection during loading. (Right) Macro view.

Region (2)   There is a steep increase in the 'max Exx' strain and the apex bend curvature as the indenter pin is further deflected between 3 and 4 mm. This can be understood with reference to figure 5-41, illustrating stress and strain distributions across the bend apex section.

Figure 5-41: schematic diagrams of distributions of stress and strain within the bend apex section during loading region (2)

Beyond approximately 1.5 % strain, Stress Induced Martensite (SIM) phase transformation occurs both in tension and compression (though at a higher stress in compression), which causes the stresses to plateau at the outer regions. This is comparable to the situation described previously for plastic deformation during beam bending (ref 26). For any further increase in the applied moment, the only way to sufficiently increase the internal stresses to balance that moment is to rapidly increase the strain gradient (curvature) – as can be seen in figure 5-36 above. This mechanism can be described as a 'hinge' that causes a large increase in the strains at the bend apex for a small change in pin deflection. In this way, localized bending occurs in sections where the outer bend regions are in the SIM transformation strain range.

For loading region (2), the neutral axis shifts towards the intrados as the compressive plateau stresses are considerably higher than the tensile plateau stresses, as seen in figure 5-42 below. Therefore, the maximum tensile strain (at the extrados) is higher than the maximum compressive strain (at the intrados). The neutral axis eccentricity can clearly be seen in the plot of figure 5-24, where the Exx strain plot crosses the x-axis at

-0.05 mm (11.1% of the wire diameter) from the centre (i.e. the neutral axis, where strain = 0, is located 0.05 mm from the wire's geometric centerline towards the intrados at this bend deflection).
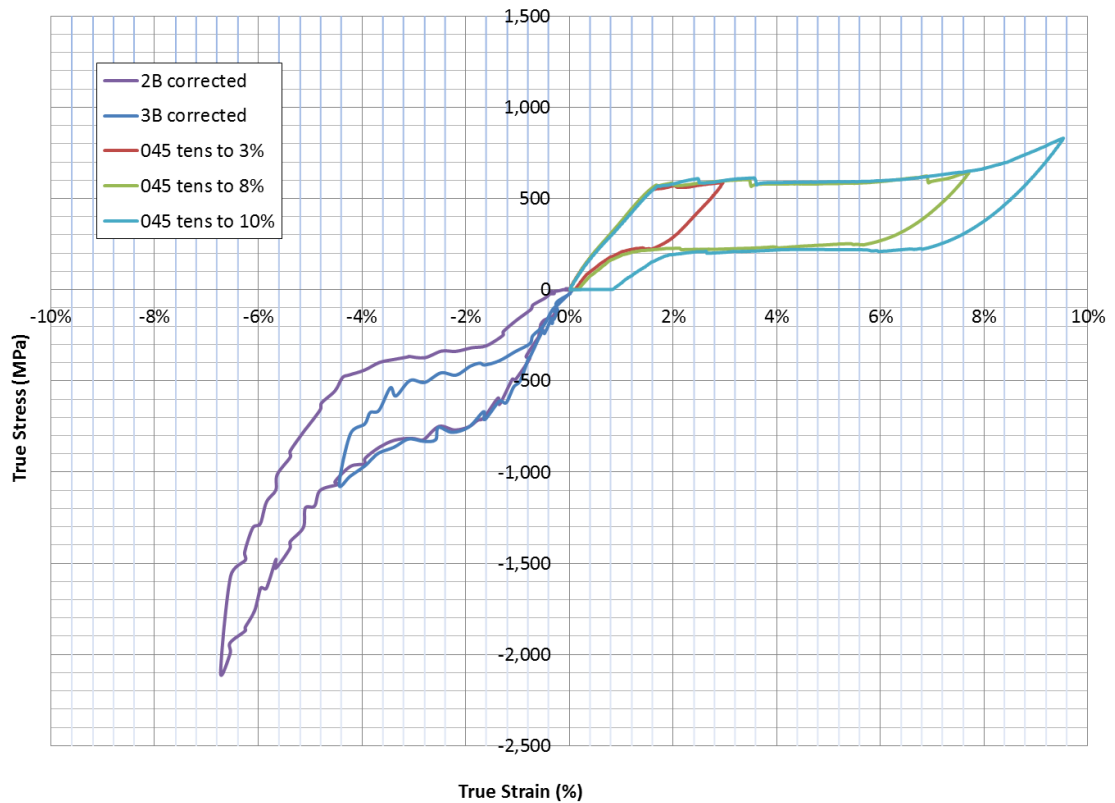
Figure 5-42: uniaxial compressive and tensile stress-strain plots for NiTi#1 wire at room temperature, taken from figure 3-30 in Chapter 3. These curves are useful for considering tensile-compressive asymmetry, which leads to neutral axis eccentricity during bending of Nitinol.

Flat-mounted DIC Result Images for Region 2

Figures 5-43 to 5-45 above show the Exx strain field results for the central wire region at 3mm, 3.5mm and 4mm deflections during loading.

Figure 5-43: (Left) DIC microscopic image of wire with overlaid Exx strain field at 3mm deflection during loading. (Right) Macro view.

Figure 5-44: (Left) DIC microscopic image of wire with overlaid Exx strain field at 3.5 mm deflection during loading. (Right) Macro view.

Figure 5-45: (Left) DIC microscopic image of wire with overlaid Exx strain field at 4mm deflection during loading. (Right) Macro view.

These DIC images show the transition from distributed deformation along the wire to localized deformation with concentrated high strains at the bend apex extrados as the wire undergoes 'hinging' due to SIM phase transformation. From table 5-4, the maximum extrados strains (averaged across the DIC gage length) for these bend deflections are 2.2%, 5.4% and 6.6% respectively. In figures 5-54 local higher strain spots can be seen in the apex extrados region, where material has locally undergone full phase transformation from austenite to martensite. In figure 5-55, localization is again evident where small spots of low strain material remain in the midst of the predominantly high strain apex outer bend material.

Region (3)   Beyond 4 mm pin displacement, maximum strain and strain gradient of the bend apex begin to plateau, so that the maximum tensile strain (from table 5-4) only increases from 6.6% to 8.2% between 4 and 8 mm pin deflections. Figure 5-46 helps to explain this behaviour.
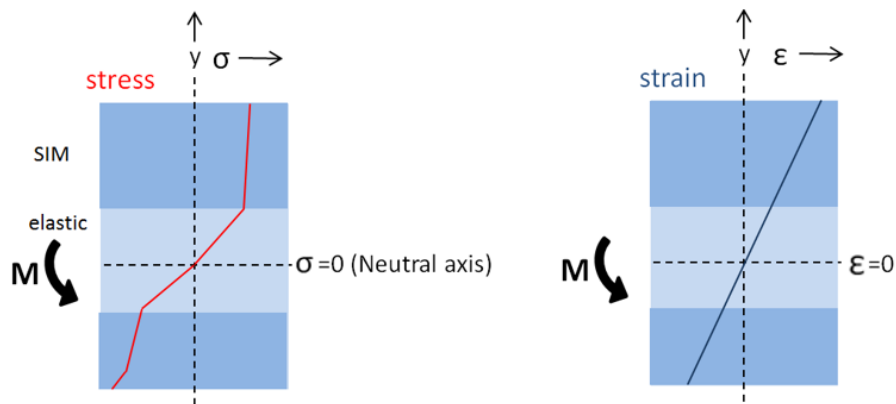
Figure 5-46: schematic diagrams of distributions of stress and strain within the bend apex section during loading region (3)

Localised tensile and compressive materials at the extrados and intrados have transformed from austenite to martensite and so have reached the end of their stress 'plateau's (at strains of 7.8 % and 4 % respectively - see figure 5-42), and in this stage the small increase in 'averaged' maximum strain is due to the small areas of remaining localised austenite material in the apex outer bend region transforming as deflection

increases, while most of the global defection is accommodated by the high strain region spreading along from the apex region (see 'Region 4' description below for more detail). The neutral axis is now located towards the compressive side due to the tensile-compressive stress and strain asymmetry. At the end of this stage, the material at both the intrados and extrados of the apex is at a stress on the '2nd modulus' beyond the loading plateau (see tensile loading region beyond 8 % strain and compressive loading region beyond 4 % in figure 5-42). In bending, this '2nd modulus' of the nitinol material prevents the wire from kinking following hinging, as will be explained for region (4).

Flat-mounted DIC Result Images for Region 3

Figures 5-47 to 5-49 show flat-mounted Exx strain field results for the central wire region at 5 mm, 6 mm and 7 mm deflections during loading. The DIC results here show the high strain region spreading from the apex along the wire axially, as well as remaining localized austenite regions at the outer bend being transformed to martensite (going from low to high strain) between 5 and 7mm deflections. This localized material transformation is believed to be behind the small increase in 'averaged' maximum extrados strain and in apex curvature seen in figures 5-35 and 5-36 for this region '3' of the graphs..

The neutral axis eccentricity – towards the compressive inner bend side – can also be seen from the DIC strain field results in the figures.
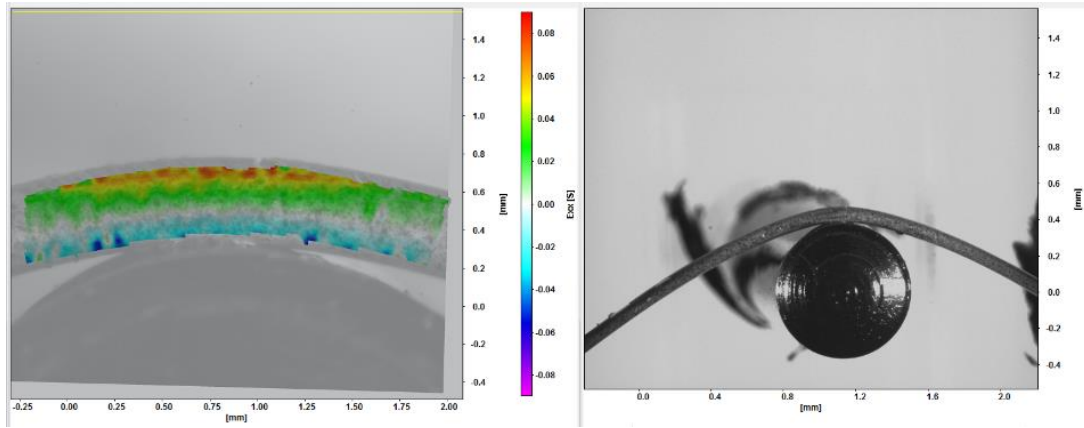
Figure 5-47: (Left) DIC microscopic image of wire with overlaid Exx strain field at 5mm deflection during loading. (Right) Macro view.
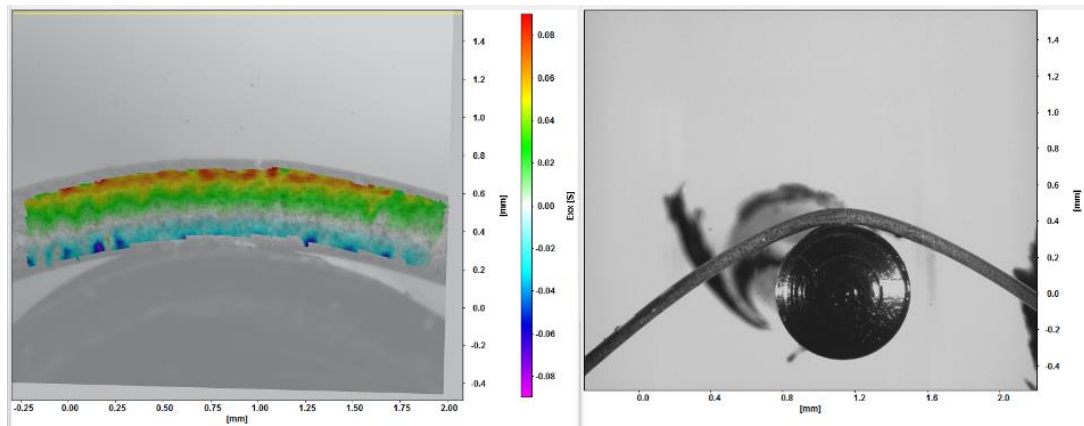
Figure 5-48: (Left) DIC microscopic image of wire with overlaid Exx strain field at 6mm deflection during loading. (Right) Macro view.
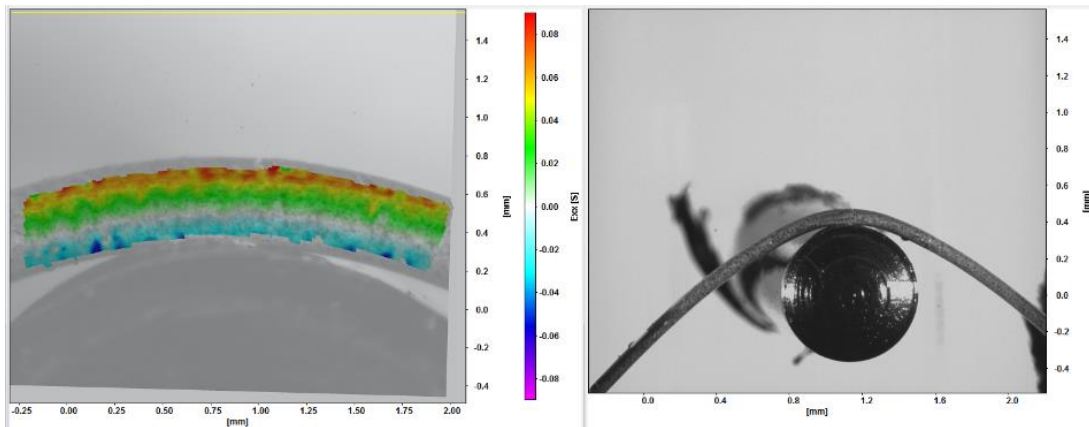
Figure 5-49: (Left) DIC microscopic image of wire with overlaid Exx strain field at 7mm deflection during loading. (Right) Macro view.

Region (4)   Beyond 8 mm pin deflection, there is almost no change in the maximum strain or strain gradient for the bend apex section. The maximum tensile strain plateaus close to 8.4 %. Figures 5-50 and 5-51 illustrate what happens during this stage.
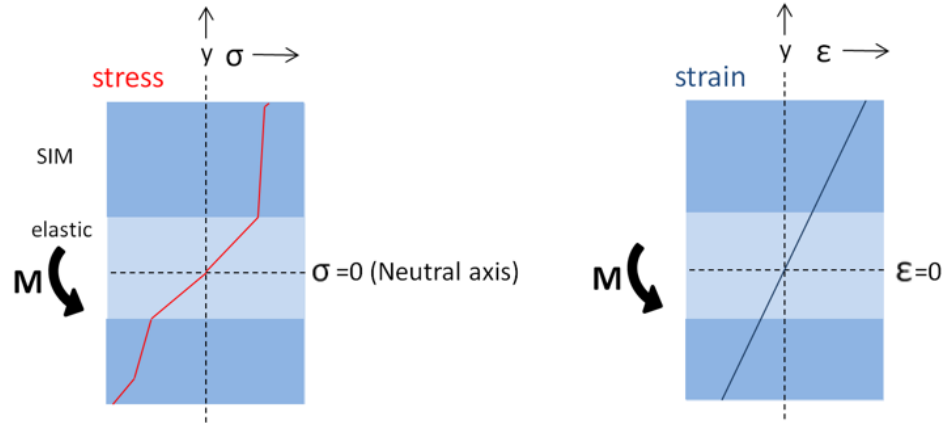
Figure 5-50: schematic diagrams of distributions of stress and strain within the bend apex section during loading region (4)
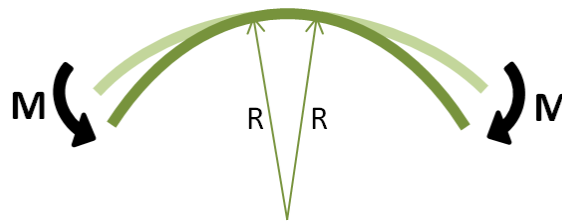
Figure 5-51: schematic diagram illustrating change in distribution of curvature along wire during loading region (4)

The material at the apex intrados and extrados is now beyond its tensile and compressive stress plateaus, with well-distributed (non-localized) maximum strains. The outer surface is at 8.4 % tensile strain, while the inner surface will be at approximately 5.5 % strain (from extrapolation of the plot in figure 5-24). At these strains, the material is fully transformed to martensite and further loading must occur by a combination of martensite elasticity and plasticity. Beyond these strains, the stresses for both tension and

compression loading will rise rapidly (see figure 5-42). It therefore becomes very difficult to increase the curvature of this section of the wire, which is essentially 'locked'. In contrast, sections along the beam away from the apex are still at a lower stress state on the loading plateau, and so can easily increase their curvature with increased applied moment by pin deflection. In this way, localized bending moves outwards from the central region, where the intrados and extrados material is fully transformed, to surrounding sections where it is yet to undergo phase change. As illustrated in figure 5-51, the effect is that the central apex region remains at a constant curvature 'R', while increasing bend deflection is accommodated by regions along the wire, until they too reach a curvature 'R'. In this way, a region of constant curvature develops with maximum surface strains evenly distributed along its length. This behaviour is the reason for the excellent kink resistance of Superelastic nitinol wire.

The neutral axis position in the apex section will not change during this stage of loading as the section maintains a constant stress state.

Flat-mounted DIC Result Images for Region 4

Figures 5-52 to 5-53 show flat-mounted Exx strain field results for the central wire region at 8.3 mm deflection during loading and at 10 mm maximum deflection. The strains in the central microscopic view (left images) do not change between these deflections, with the central region being essentially 'locked'. The global deflection increase is instead accommodated by bending deformations along the wire to either side of the central region. This can be appreciated by comparison of the 'macro view' images on the right of the two figures, where the central region can be seen to stay at a constant curvature, while bending occurs further along the wire on each side.
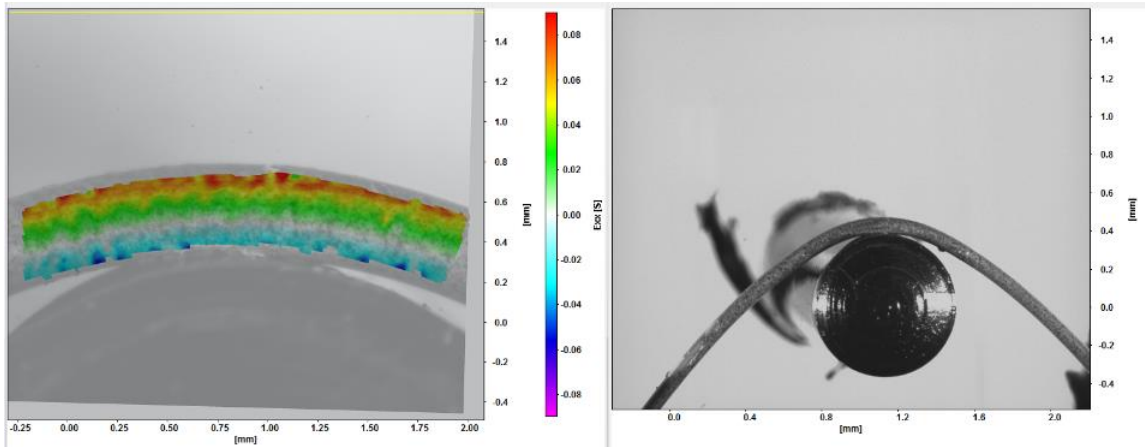
Figure 5-52: (Left) DIC microscopic image of wire with overlaid Exx strain field at 8.3mm deflection during loading. (Right) Macro view.
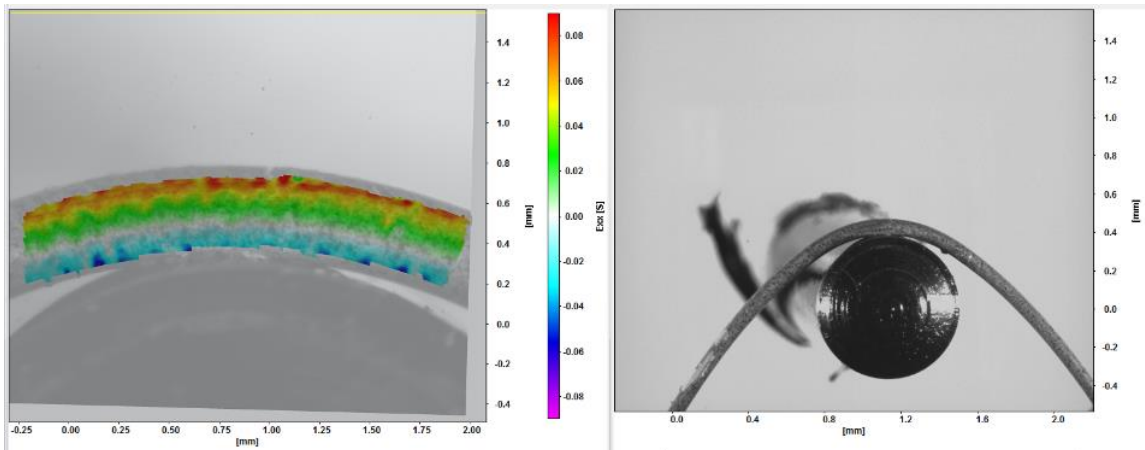
Figure 5-53: (Left) DIC microscopic image of wire with overlaid Exx strain field at 10mm deflection. (Right) Macro view.

Unloading

During unloading from large deflections, Nitinol material follows a different stress-strain path from that which it took in loading. This stress hysteresis for the material under both tension and compression can be seen in figure 5-42. Consideration of this load – unload stress hysteresis is key to understanding the strain history effects for nitinol wire in bending.

Region (5)   The indenter pin is now moved back down from its maximum deflection position, and the wire material begins to unload. With reference to figure 5-35, the apex outer surface strain initially decreases linearly from 10 - 8 mm pin deflections. This gives a lower strain in unloading than in loading for this range of pin positions (also clearly seen in table 5-4). Figures 5-54 and 5-55 illustrate what is happening during this stage.
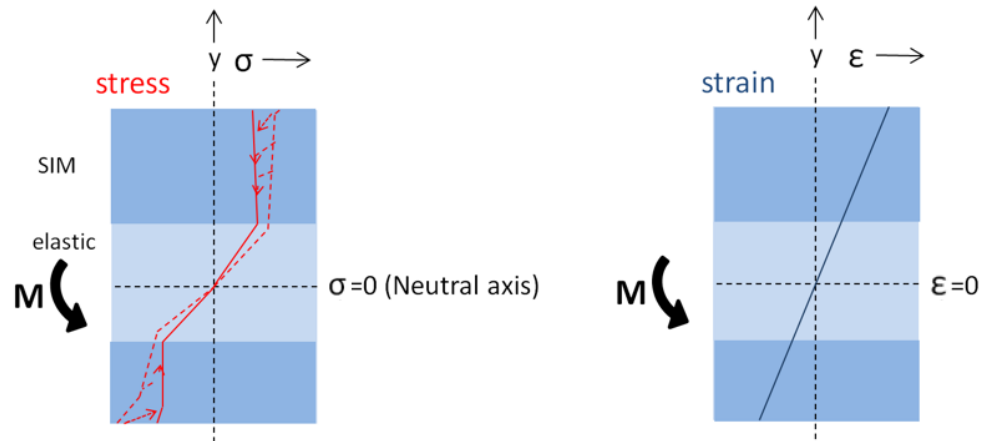
Figure 5-54: schematic diagram of distributions of stress and strain within the bend apex section during unloading region (5)
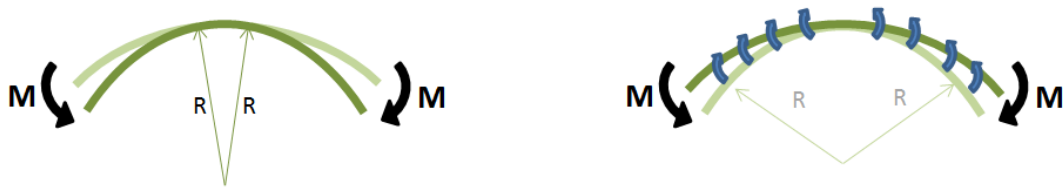
Figure 5-55: schematic diagram illustrating change in distribution of curvature along wire during loading region (4) (left) and start of unloading region (5) (right)

During initial unloading, all the material in the wire unloads elastically. This is illustrated for the bend apex section in figure 5-54. The modulus of this elastic unloading depends on the strain the material has reached (see figure 2-25 in Chapter 2), and therefore depends on its position in the cross-section. For the bend apex region, this initial elastic unloading causes a rapid reduction in stress and means the applied moment

change can be balanced by internal moment change with a small reduction in curvature. This change in curvature during unloading is different from the case in loading, where the apex section was essentially 'locked' (see region (4) explanation above). Figure 5-55 illustrates this, showing how the central region remained at curvature 'R' while surrounding regions accommodated the bending deflections with localized bending in loading (left-hand diagram), while in unloading there is distributed deformation as the central region reduces its curvature to < R at the same time as surrounding regions (right-hand diagram).

This 'distributed deformation' of the wire in unloading (due to elastic deformation of the material), in contrast to the 'localized' bend deformations that occurred in loading (due to 'SIM' deformation of the material) means that the wire bend shape is slightly different in unloading than in loading. This explains why the maximum tensile strain of the apex is lower in unloading than in loading between 10 and 8 mm (table 5-4 and figure 5-35).

Considering the neutral axis position during this stage, the investigation of Reedlunn et al (18) on Nitinol in bending would suggest that it will remain fairly constant during this initial elastic unloading stage (shown by neutral axis position plot of figure 2-23 in Chapter 2).

Flat-mounted DIC Result Images for Region 5

The DIC result from 10 mm (maximum) deflection is again shown in figure 5-56 for easy comparison with figure 5-57, which shows flat-mounted Exx strain field results for the central wire region at 8 mm during unloading. Comparing the 2 figures, there is little change in the strain distribution along the wire, as the bend deformation is recovered in a distributed manner. It can be seen that some of the deep red regions from figure 5-56 are a lighter red or orange colour in figure 5-57, showing a local drop of ~ 0.7 % strain (seen more clearly in the extrados strain fields of table 5-4). Also, a few additional green low strain spots are seen amongst the high strain material in figure 5-57, showing that some localized martensite to austenite phase change has occurred in the region.
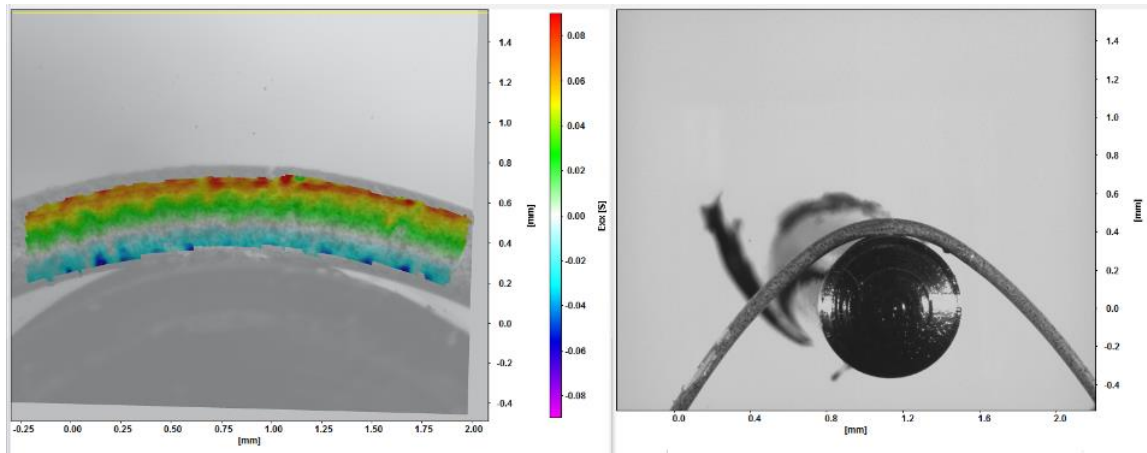
Figure 5-56: (Left) DIC microscopic image of wire with overlaid Exx strain field at 10mm deflection. (Right) Macro view.
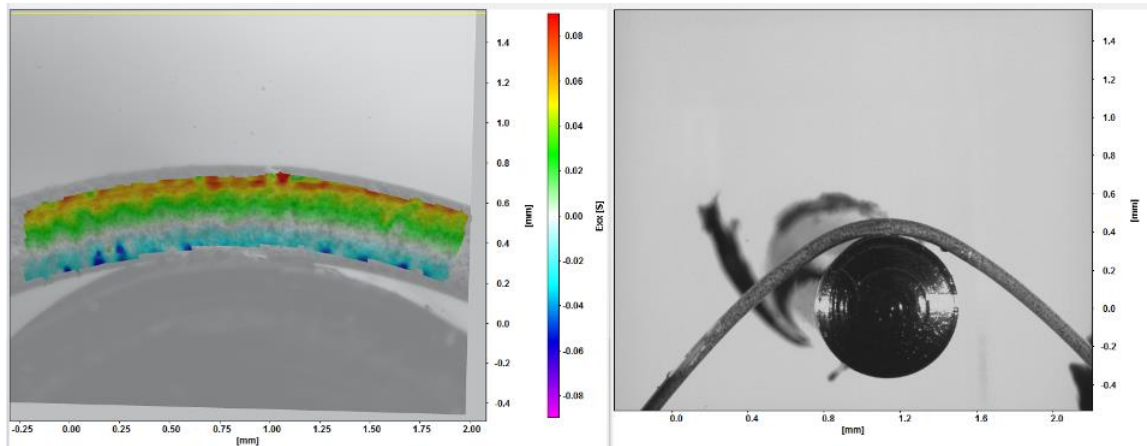
Figure 5-57: (Left) DIC microscopic image of wire with overlaid Exx strain field at 8mm deflection during unloading. (Right) Macro view.

Region (6)   Below 8 mm deflection, there is relatively little reduction in the apex extrados strain or curvature down to 3 mm pin deflection. This can again be attributed to bending localization. During unloading, a critical curvature will be reached where the section material reaches its unload stress plateau and begins to rapidly reduce its curvature to accommodate the reducing applied moment. This will occur for all other regions along the wire before it occurs for the bend apex. Therefore, the large global unloading deflection from 8 to 3 mm is accommodated by localized bend recovery of

other regions along the wire length while the central apex region remains at curvatures greater than the critical curvature for local bend recovery (or 'unhinging'). Figure 5-58 below illustrates this.
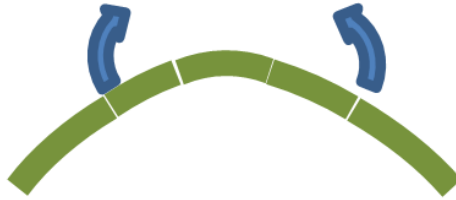
Figure 5-58: diagram of nitinol wire during bend unloading, showing localized deformation recovery of regions along from the central apex region, while the apex remains at a high curvature. This gives the appearance of a slight kink. See also figure 5-27 (left top image).

Referring to figures 5-35 and 5-36, of particular interest is the unloading region below 3.8 mm deflection, where the apex extrados strain and curvature are higher in unloading than for loading. This behaviour is key to understanding the strain history effects seen by van Zyl in his FEA study (33). In loading, the apex section was the first to have extrados material reach the upper stress plateau and therefore undergo localized 'hinge' deformation (between 3 and 4 mm pin deflections). Localized bending then occurred at locations along the wire from the apex as global bend deflection increased. In unloading, localized deformation occured at wire locations in reverse order from that in loading. Therefore in unloading, the central apex section (which has the highest applied moment for a given pin deflection) will be the last to undergo localized bend recovery.

In terms of internal stress state of the apex section, figure 5-59 below illustrates a comparison of the state in loading (left) and in unloading (right) at pin deflection of 3.5 mm. In loading, the outer material is at a stress on the upper plateau (ie. undergoing phase change at constant stress) and so the apex section is 'hinging' as it rapidly

increases curvature to increase its internal moment. In unloading, the material in the section is still unloading elastically and has not yet reached the unloading stress plateau. There is little reduction in curvature as global bend deflection decreases, and so the apex region remains at a high curvature with high extrados strain. This is the reason for the wire shape difference that was seen in figure 5-26.
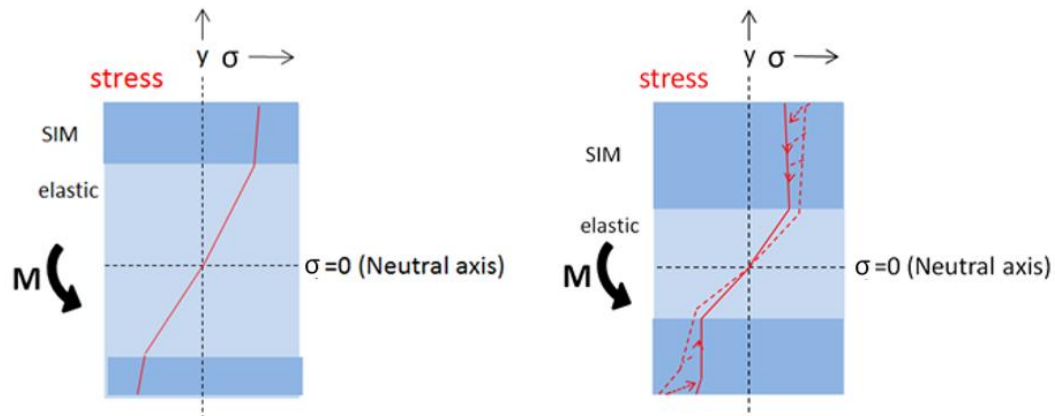
Figure 5-59: schematic diagrams of stress distributions across apex section at 3.5 mm pin deflection for loading (left) and unloading (right). The darker blue regions represent phase transformation material.

Clearly, then, the results of table 5-4 and figure 5-35 give evidence of the strain history effects proposed by van Zyl (ref 33), as a different strain is found at the apex extrados in loading than in unloading for the same global bend deflection (pin deflection in the range 2.5 to 3.6 mm). This will be examined further in Section 5.5.3 '*Discussion of Strain History Effects*'.

Again, in terms of neutral axis position, this would be expected to remain constant for the apex section during unloading stage (6), as the apex material is still unloading elastically (as seen in figure 2-23 of Chapter 2).

Flat-mounted DIC Result Images for Region 6

Figures 5-60 to 5-62 show the Exx strain field results for the central wire region at 7, 5 and 3.5 mm deflections during unloading.
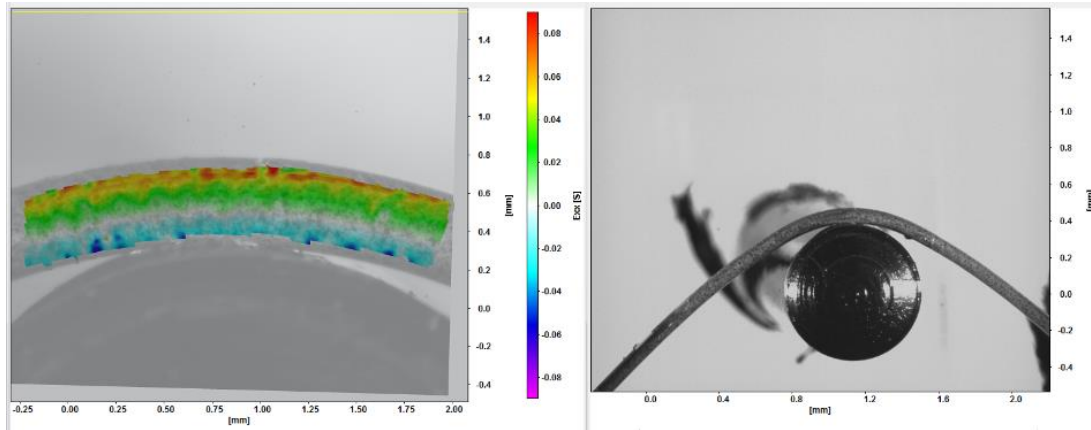
Figure 5-60: (Left) DIC microscopic image of wire with overlaid Exx strain field at 7mm deflection during unloading. (Right) Macro view.
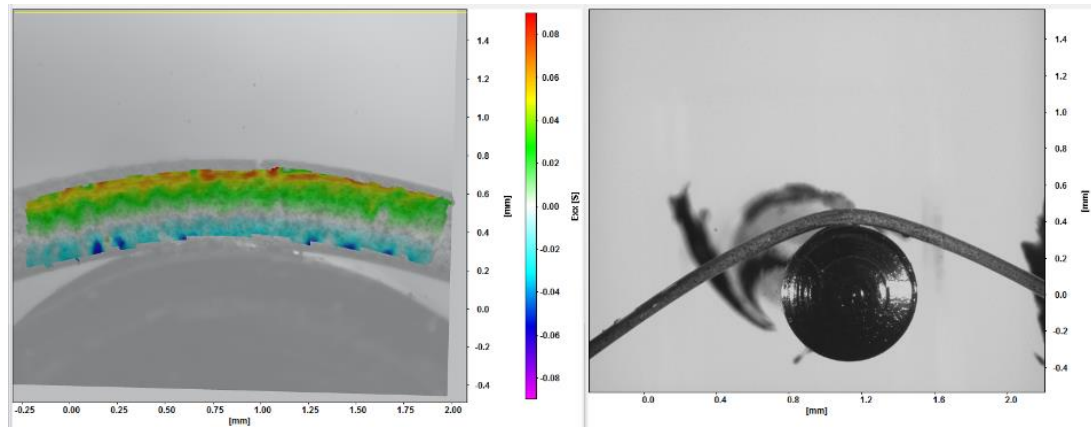
Figure 5-61: (Left) DIC microscopic image of wire with overlaid Exx strain field at 5mm deflection during unloading. (Right) Macro view.
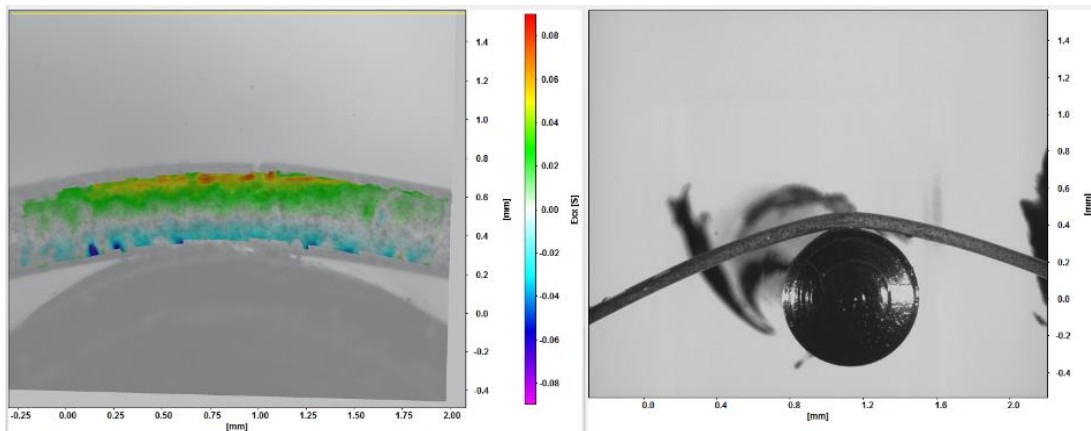
Figure 5-62: (Left) DIC microscopic image of wire with overlaid Exx strain field at 3.5mm deflection during unloading. (Right) Macro view.

The progression in the strain field results from figure 5-60 to 5-62 shows that the strain recovery is occurring at regions either side of the apex, with material at the outer curve away from the apex undergoing reverse transformation (martensite to austenite, from high to low strain), while the apex region remains at high strain (figure 5-62). Comparison with figure 5-44 shows that for the same pin deflection (3.5 mm), there is considerably more high strain material during unloading than there was during loading, where there were only a few localized spots of martensite material present. Table 5-4 shows a similar load-unload difference for a bend deflection of 3.6mm.

Region (7)   Between 3mm and 2mm pin deflections in unloading, the apex extrados strain rapidly decreases from approximately 6% to 1.3% (see table 5-4 and figure 5-35). Figure 5-36 also shows the strain gradient (bend curvature) rapidly decreasing for region (7). Figure 5-63 below helps to explain this with respect to the internal stress and strain state.
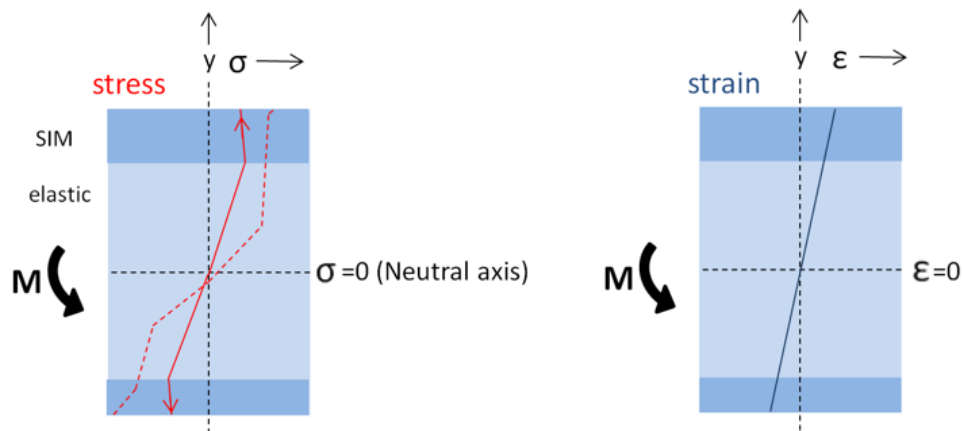
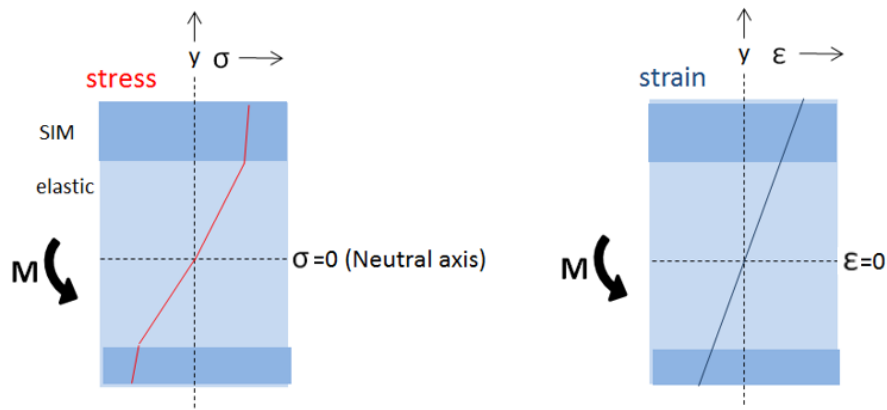*Figure 5-63: schematic diagrams of distributions of stress and strain within the bend apex section during unloading region (7)*

At around 3 mm unloading pin position, the internal stresses in the apex section have decreased to a level where all the material in the transformation regions (tensile and

compressive) is on the unloading plateau – i.e. each element across the width of the region is at the stress where martensite to austenite transformation occurs as strain is reduced. As the applied moment continues to decrease (by the 3-Point bend pin deflection being reduced), the only way the section can now sufficiently reduce its internal stress state to achieve equilibrium is by rapidly reducing its curvature. Localized bend recovery occurs at the apex region, causing the 'unhinging' effect seen in the results of figures 5-35 and 5-36, region (7). This large localized deformation recovery for a small global bend deflection is visible in the 'macro view' wire shape photographs of figure 5-27.

As bend curvature rapidly reduces due to phase transformation, the neutral axis position remains in approximately the same position (towards the compressive side) as both the compressive and tensile stresses are unloading along a plateau (see figure 5-42), with the compressive unload plateau being higher than the tensile one. Evidence of this can be seen in chapter 2 (figure 2-23) from the results of Reedlunn et al (18).

Flat-mounted DIC Result Images for Region 7

Figures 5-64 and 5-65 show flat-mounted Exx strain field results for the central wire region at 3.5 mm and 2.5 mm deflections during unloading. It can be seen that for this small change in deflection, the apex region sees a large drop in the maximum strain (a drop in averaged max extrados strain from 6.2% to 3.5% with reference to table 5-4). As explained above, this is accompanied by a large reduction in the apex curvature, which is evident in the 'Macro view' photographs. Figure 5-64 shows localized high strain around the apex and neutral axis eccentric towards the inner compressive side, while figure 5-65 shows lower strains more evenly distributed along the length in the FOV, with central neutral region.
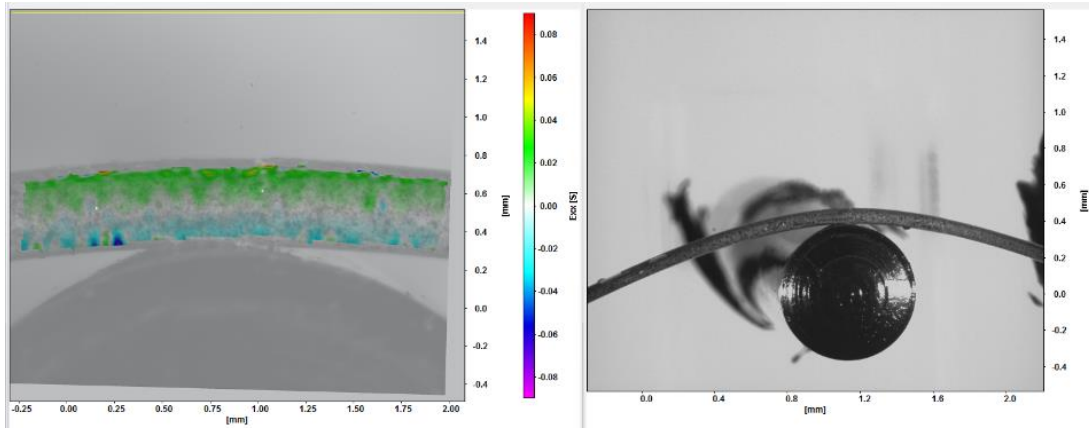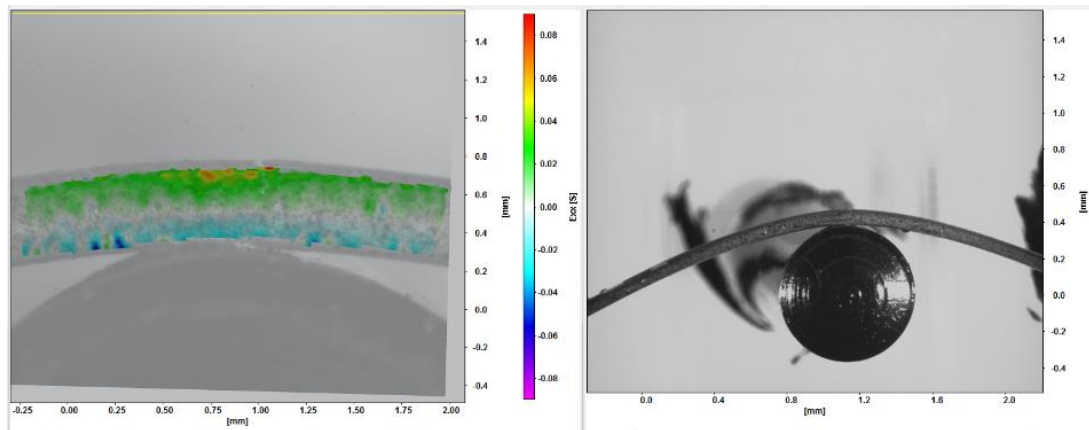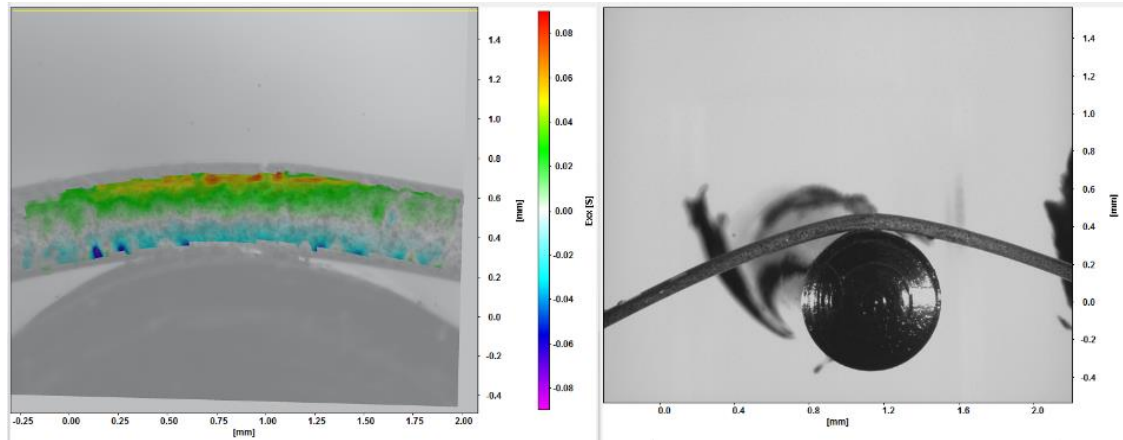
Figure 5-64: (Left) DIC microscopic image of wire with overlaid Exx strain field at 3.5mm deflection during unloading. (Right) Macro view.
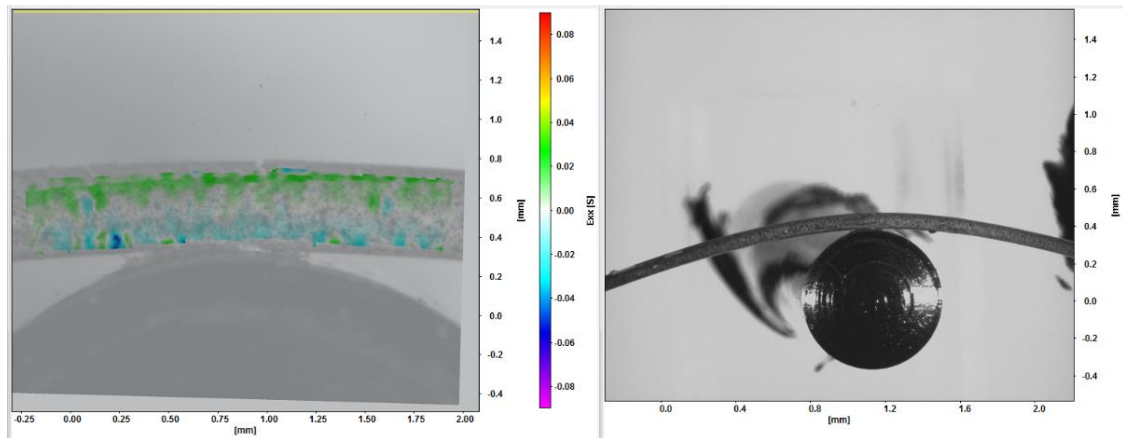
Figure 5-65: (Left) DIC microscopic image of wire with overlaid Exx strain field at 2.5mm deflection during unloading. (Right) Macro view.

Region (8) As discussed previously, the results of table 5-4 show that at low deflections of 2mm and below the same strain-deflection path is followed in unloading as for loading, with linear elastic behaviour. Figure 5-66 represents the stress and strain states of the apex section at these small deflections. The wire unloads elastically according to Euler-Bernoulli beam theory, from apex extrados strain of approximately 1.3%. Note that this strain is lower than the 'hinge' start strain during loading (approximately 1.5 %). With reference to figure 5-42, this can be explained by the lower

strain values for the end of the unload plateaus compared to those at the start of the loading plateaus for Nitinol tensile and compressive stress-strain curves.

The neutral axis location will move back towards the centroid axis during this stage (evidenced by the plot in figure 2-23 and the figure 5-65 DIC results).
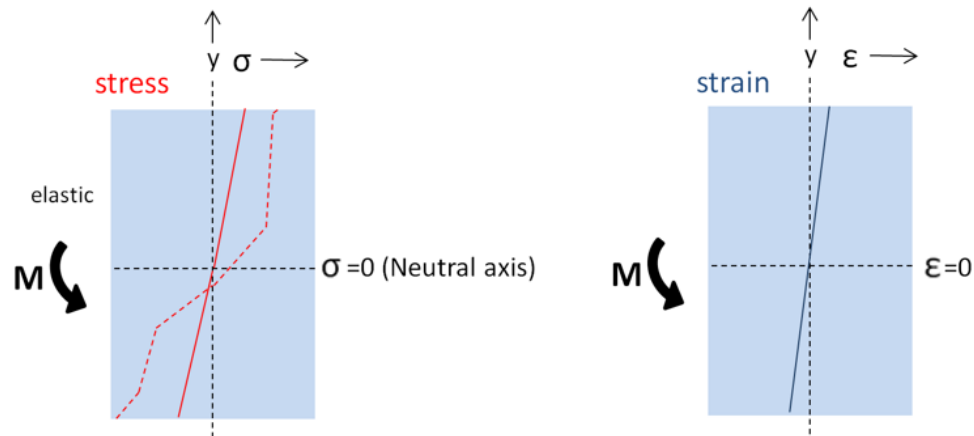
Figure 5-66: schematic diagrams of distributions of stress and strain within the bend apex section during unloading region (8)
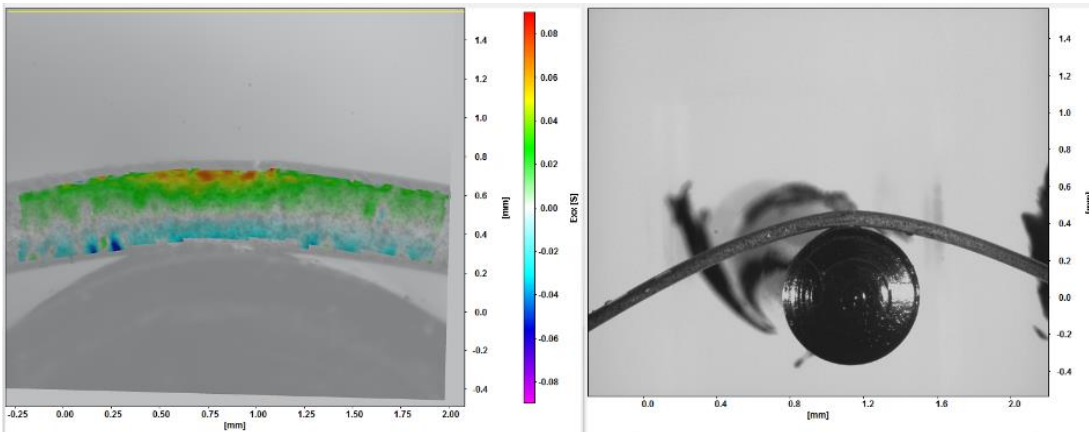
Flat-mounted DIC Result Image for Region 8
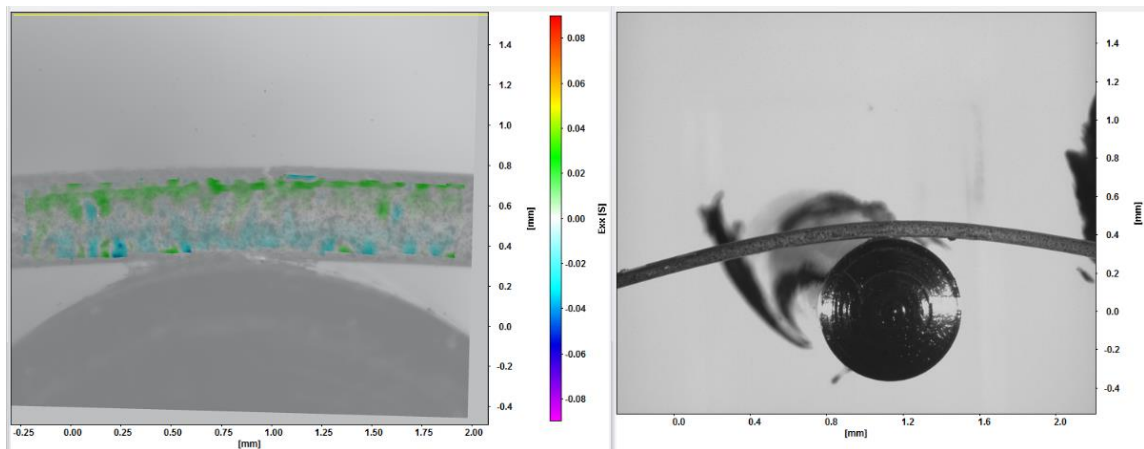
Figure 5-67: (Left) DIC microscopic image of wire with overlaid Exx strain field at 2mm deflection during unloading. (Right) Macro view.

Figure 5-67 shows flat-mounted Exx strain field results for the central wire region at 2 mm deflection during unloading. Comparison with figure 5-39 (2mm deflection during loading) shows that the results and macro view shape are nearly identical (also seen in table 5-4), demonstrating that the wire follows the same strain-deflection path for loading and unloading below 2 mm deflection.

[Note: the 3-Point Bend tests performed in this work using DIC did not plastically deform the wires, evidenced by the wires being straight when unloaded to zero deflection. If plastic deformation had occurred, material near the extrados and intrados would not undergo full elastic recovery, resulting in residual stresses and strains in the material upon full unloading.]

5.5.3 Discussion of Strain History Effects

As seen in Chapter 2 (Literature Review), Van Zyl et al (33) used FEA simulations to demonstrate that in bending the final strain state of a nitinol beam during unloading is dependent on its load-path history. However, no experimental studies could be found to back up this theory, and it was a stated aim of the present DIC work to provide experimental evidence of these strain history effects.

The experimental DIC testing reported here has demonstrated that there is strain hysteresis in bending of superelastic Nitinol wire, as seen from the different loading and unloading paths in figure 5-35 (plotting maximum tensile 'Exx' strain against pin deflection) and from the DIC results (table 5-4). This experimentally observed strain hysteresis behaviour will now be used to explain the FEA results of van Zyl et al (33).

Figure 5-68, taken from ref (33), shows the FEA nitinol beam in cantilever bending, with a brief explanation of the study performed.
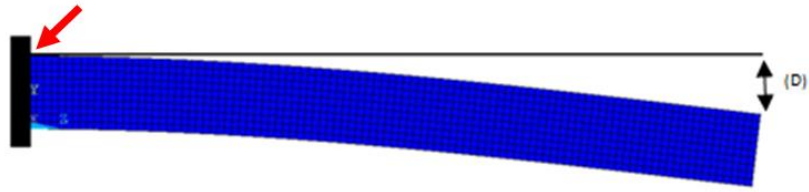
Figure 5-68: FEA model of Nitinol beam in bending, from ref (33). The FEA study involved loading to deflection 'D', then through an extra deflection ΔD, and then unloading back to D. Different values of ΔD were used in order to study the effect of loading history on the final stress-strain state of a 'maximum strain' element (at the root location, outer fiber – identified in the image by the red arrow)

Figure 5-69, also taken from ref (33), shows the essential 'strain history effect' result from Van Zyl's FEA study (also shown in Chapter 2: 'Literature Review', figure 2-27).
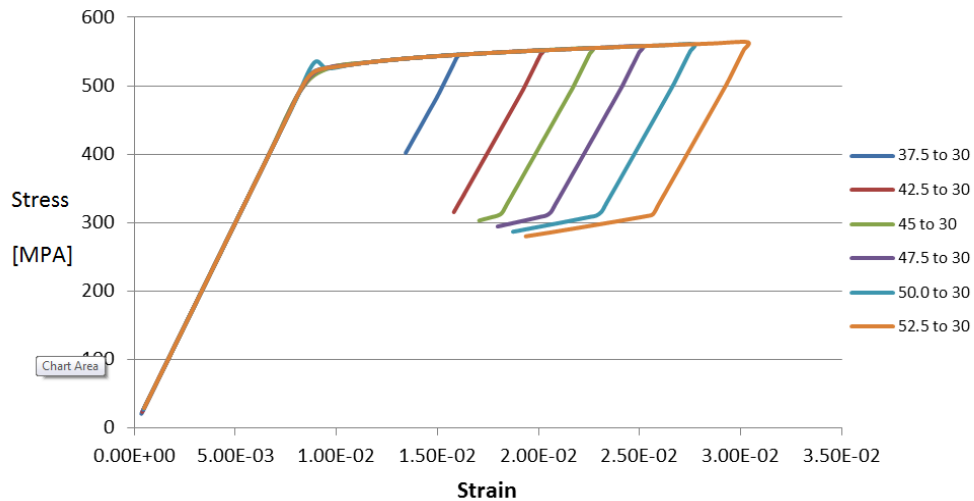
Figure 5-69: From Ref (33) Nitinol cantilever beam study. Stress-strain measurements for maximum first principal stress and total mechanical strain at the root location of the beam (outer fiber), for different loading histories. A single element was chosen and used throughout computational work.

The interesting finding from this FEA study was that for a given final beam deflection 'D', the final strain of the 'maximum strain' element depends on the maximum deflection reached during the beam's loading history (i.e. the 'ΔD' value used).

By considering the load-unload strain hysteresis seen in the experimental 3-Point Bend DIC results, this same behaviour can be demonstrated. Figure 5-70 shows the Max Tensile 'Exx' strain – Deflection results for test set '3PB vert1' with overlay of different load-unload paths to reach a final global bend deflection 'D' of 2.5 mm. Unfortunately, testing was not performed to obtain these overlay paths – they are the 'expected' results based on understanding of the material behaviour of nitinol in bending, as will be described below. It would be a useful area of future experimental work to perform further DIC testing that would validate these 'expected' results.

The overlaid 'expected' paths were derived by considering the stress distribution for the bend apex section at different global bend deflections. Firstly, the load-unload strain hysteresis is considered in terms of the internal stress state. Figure 5-71 shows schematic diagrams of the stress distribution for deflection 'D' during loading, maximum deflection 'D + ΔD' and deflection 'D' during unloading. The light blue and dark blue regions show the austenite material and transformation (SIM) material regions respectively. Where there is a greater area of transformation material (darker blue regions), the section is at a greater bend curvature with higher maximum strains.
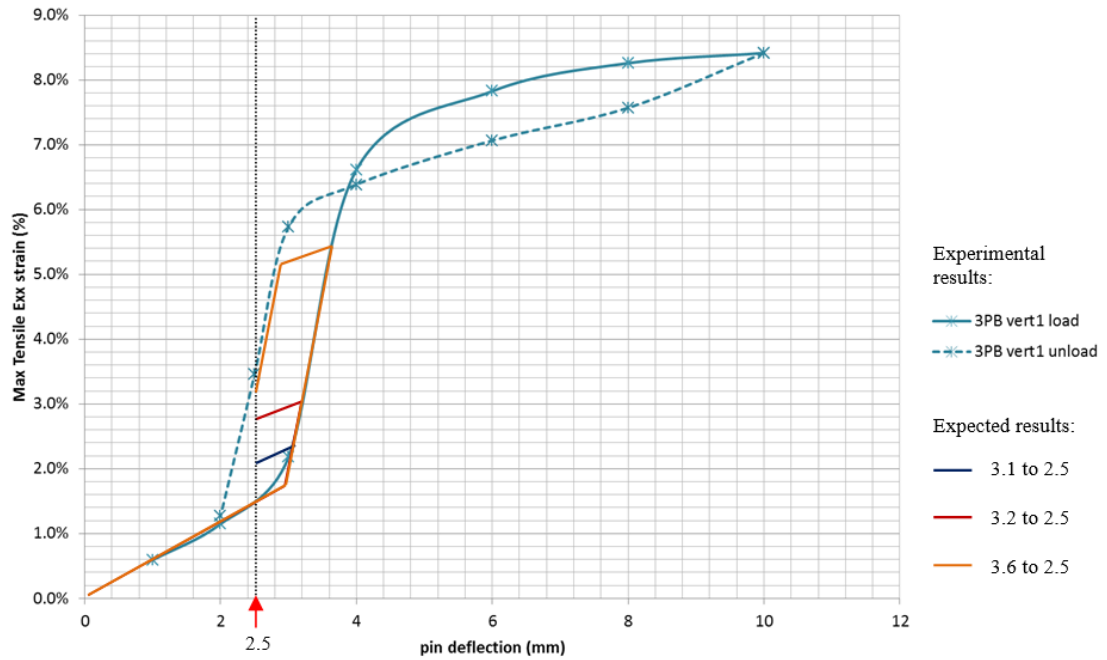
Figure 5-70: Experimental Results for Max Tensile 'Exx' Strain - Deflection from DIC testing, test set '3PB vert1', with overlaid 'expected' results for different strain history paths to reach 2.5 mm final deflection.
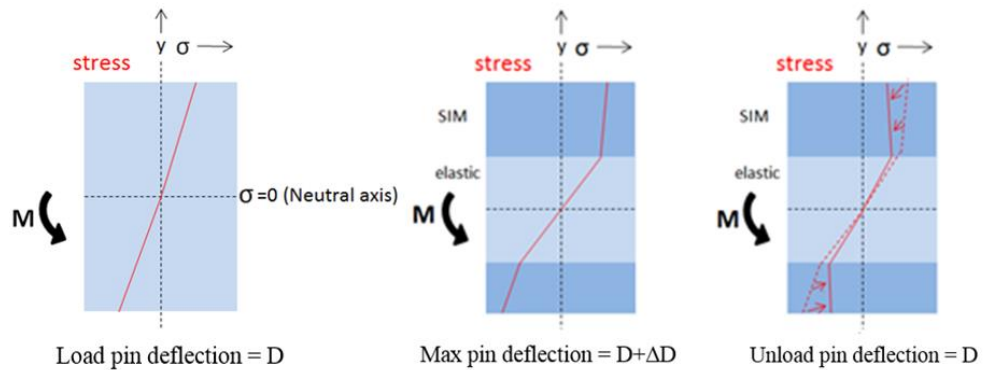
Figure 5-71: schematic diagrams of stress distributions across bend apex section for global bend deflection'D' in loading (left), 'D + ΔD' (centre) and 'D' during unloading (right).

With reference to the 'expected behaviours proposed in figure 5-70, 'D' can be taken to be 2.5 mm. During loading at 2.5 mm pin deflection, the apex bend curvature is small enough that the material is still fully austenite and is deforming with linear elasticity (figure 5-71, left). During additional deflection, for example to 3.2 mm (see red path in figure 5-70), the extrados and intrados material of the apex section reaches a critical stress where SIM phase transformation occurs (fig 5-71, centre). As explained previously, this results in the local wire region rapidly increasing its bend curvature to balance any additional applied moment. At the maximum deflection 'D+ΔD' (eg. 3.2 mm), the apex section extrados is therefore at a relatively high strain (3 % in the example) due to the localized bending or 'hinging' that has occurred. When the wire is then unloaded back to deflection 'D' (2.5 mm in figure 5-70), the phase-transformed material does not unload along the same 'upper stress plateau' path but instead unloads elastically (fig 5-71, right). The apex section can therefore reduce its internal stress state to match the applied moment without localized bending (as global deflection is accomodated by distributed bending reduction along the wire), and so the curvature and extrados strain remain high. The final strain state (max strain = 2.8 %) is thus considerably different to the loading strain state (max strain = 1.5 %) for the same deflection, demonstartating strain hysteresis in bending due to the stress hysteresis of the Nitinol material.

Having considered the load-unload strain hysteresis for bending, the loading history dependence of the final strain state can now be understood with reference to the different 'expected' load-unload paths in figure 5-70. The dark blue path reaches a lower 'D+ΔD' value (3.1 mm) and therefore the apex undergoes less localized bending and has a considerably lower maximum strain (2.3 %). During unloading to D = 2.5 mm, the material unloads elastically rather than by phase transformation and so the curvature and strain reduce little from the maximum values (final max strain = 2.1 %). As the maximum curvature and strain were considerably less for the blue loading path than for

the red path in figure 5-70, the final strains are therefore considerably different (2.1 % and 2.8 % respectively).

For the orange path in figure 5-70, the 'D+ΔD' value is 3.6 mm. The apex experiences a large amount of localized bending in loading, reaching a maximum strain of 5.4 %. On unloading, the apex initially has a small decrease in curvature and strain as the phase-transformed material unloads elastically (figure 5-71, right). However, in this case the apex curvature reduces to a point where the phase-transformed material reaches its unload plateau stress. Beyond this point, the material deforms with little change in stress and so the internal moment must be reduced by localised 'unhinging' at the apex. The extrados strain rapidly reduces to a final strain of 3.2 % at d = 2.5 mm. As was seen in Van Zyl's study (figure 5-69), the differences in final strain become less pronounced at higher 'D+ΔD' values, where 'unhinging' occurs during unloading.

In this way, the experimental 3-Point Bend DIC test results have been analyzed to demonstrate how the final strain state of a bending nitinol beam during unloading is dependent on its load-path history. Van Zyl (33) has demonstrated that this behavior is evident in FEA simulations that use a constitutive model for Nitinol (Aurrichio-Taylor model). Therefore, FEA could be a useful tool for further study of this effect and the underlying stress-strain state of the material.

5.6 'Free Bend' Testing with DIC Measurement

A limitation of the 3-Point Bend test rig is that the central indenter pin obstructs the camera view of the wire's inner bend surface, preventing direct DIC measurement of the maximum compressive strains in this region. One solution was to try a 4-Point Bend set-up, but initial feasibility testing showed that this would not work for the following reasons:

- the central region of interest of the bending wire moved out of the microscope's field of view (FOV) for large deflections and so subsequent DIC processing could not be performed
- lighting was a problem for capturing good images for DIC, due to shadows cast on the wire surface by the central pins.

For these reasons, it was desirable to design a loading rig that would allow the wire to be deformed in bending in such a way that the central 'apex' region could be viewed around its surface from outer to inner bend surfaces, and so that this region would remain in the field of view of the microscope (2.5 x 2.5 mm) with minimal rigid body translation during bending.

Such a rig could then be used, together with the different angled mounting platforms, to study the full strain distribution across the surface of the wire apex section using microscopic DIC. The main objective of this additional DIC testing was to obtain experimental results for strain distribution across thin NiTi#1 wire for a given bend curvature, allowing capture of the following key parameters for a given bend curvature:

- Maximum tensile strain
- Maximum compressive strain
- Strain gradient across section
- Neutral axis position

These parameters have two main uses:
- Quantitative characterization of the tensile – compressive strain asymmetry in bending
- Validation of FEA material models used for simulation of wire bending

Particular focus was given to obtaining results at large bending deformations, in order to provide useful information for understanding the strain state of the wire during compaction of stent components.

5.6.1 'Free Bend' Test Rig Design

Figure 5-72 shows the free-bend rig, which was manufactured using laser cutting of acrylic sheet in the 'Design, Manufacture and Engineering Management' (DMEM) centre at University of Strathclyde.
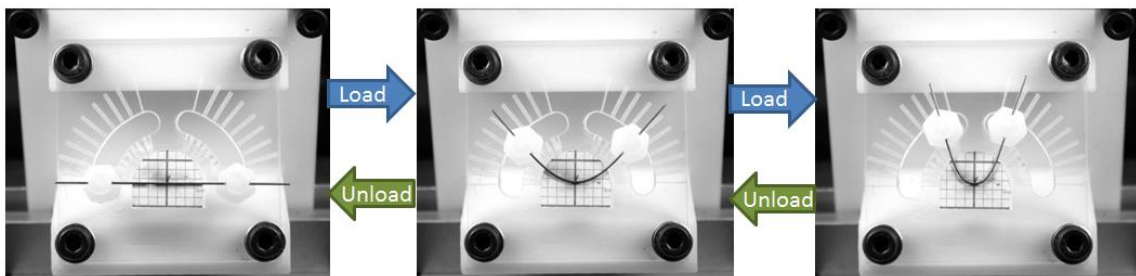
Figure 5-72: Free-Bend Rig used to deform a 0.45 mm NiTi#1 wire in bending

This rig allows the ends of the 0.45 mm wire (with airbrushed speckle surface) to be fixed within upright posts (using Loctite 406 adhesive) which are moved round pre-defined arc-shaped tracks in order to bend the wire. The shape of the tracks was designed so that the bend apex would remain in approximately the same position for large deflection loading and unloading – as seen in figure 5-72 above. This rig has the advantage of allowing unobstructed viewing around the wire surface at the bend apex, allowing measurement of the full strain distribution from extrados to intrados.

5.6.2 Equipment and Test Method

Using the test rig shown in figure 5-72, the same DIC equipment and method was used as described in Section 5.3, up to and including the 'Exx Strain Overlay Plots' section in 5.3.7.7. The only difference was that in mounting the rig on the microscope stage,

additional mounting angles were used to allow viewing of the inner (compressive) bend surface. The different mounting angles used for 'free bend' testing are illustrated in figure 5-73 below.
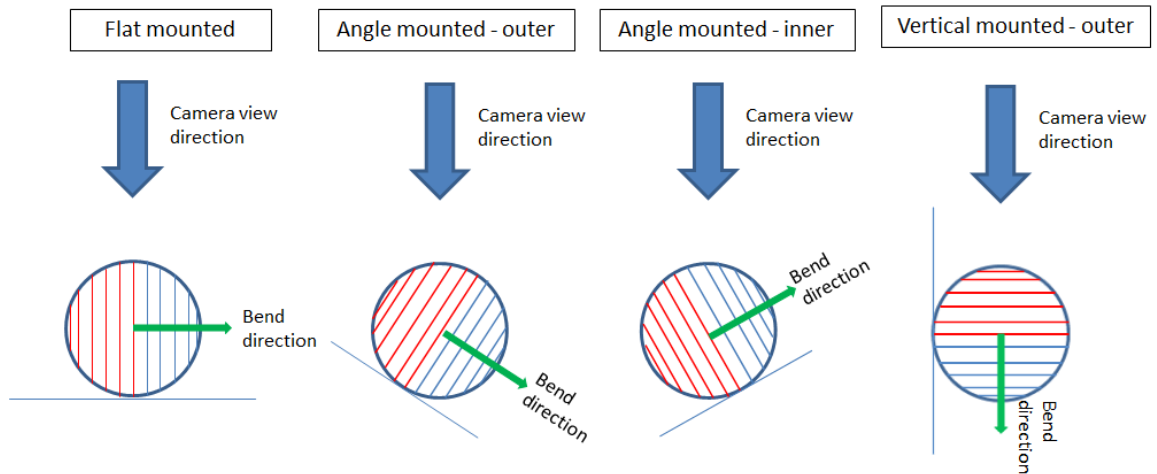
Figure 5-73: schematic diagrams showing the viewing angle relative to the bend direction for different 'free bend' rig mounting platforms. The red lines represent the outer tensile region of the wire section in bending; the blue lines represent the inner compressive region of the wire section in bending

5.6.2.1 Wire deformation measurement from 'macro view' digital images

As with the 3-Point Bend tests, a 'macro view' image of the wire shape on the 'Free bend' test rig was captured for every bending deformation step. These images could then be used to obtain a measure of bending deformation, which was necessary for material behavior characterization and as an input for FEA validation simulations.

In order to meet the main 'Free bend' test objective of obtaining strain values across the wire at large bend deformations, it was determined that the most useful way to measure deformation was to measure the wire apex region bend shape, rather than the displacement of the constraining clamps. The radius of curvature of the wire apex region

was measured, as illustrated in figure 5-74. (Recall from the discussion in section 5.5.2 that at large bend deformations the bend 'apex' region would be expected to have a constant radius of curvature (from 'Region (4)' analysis including figures 5-51 to 5-53)).
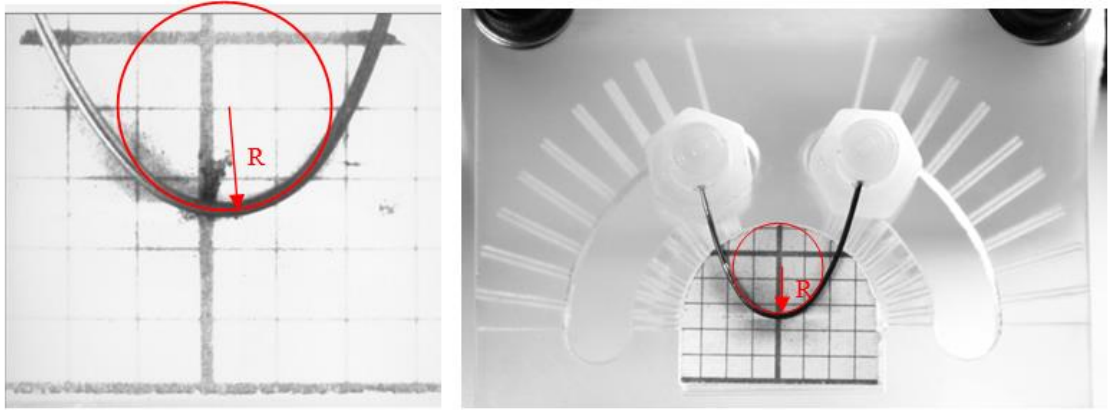
Figure 5-74: 'Macro view' wire bend deformation images from (left) flat mounted test and (right) 30º angle mounted test, with radius of curvature measurement of the bend apex region in each case. In both these images, bend apex radius of curvature was measured to be 3.4 mm.

Using the digital 'macro view' images, the following method was used to measure apex radius of curvature for all 'Free bend' tests:

1. Save the image as a bitmap, ensuring no loss of quality due to compression.
2. Import the image into SolidEdge CAD software's 'draft' environment.
3. Using the grid paper boxes for a reference dimension, scale the image down so that the grid spacing is 2 mm per box, giving 1:1 scaling of the image.
4. Verify the following dimensions for the scaled 1:1 image: grid box width = 2 mm; grid box height = 2 mm; wire width = 0.45 mm.
5. Mark points along the centerline of the wire apex region.
6. Position a circular arc and resize until the best fit through these centerline points is found.
7. Measure the radius of curvature of the 'best-fit' arc – this is taken to be the radius of curvature of the wire apex.

The detailed dimensional verification step 4 ensured that the dimensioning of the curvature was correct within the CAD software, and the ability to zoom in on the apex region when fitting the circular arc allowed an accurate measurement of the curvature.

5.6.3 Results

In order to investigate the strain distribution for a given bend radius, DIC measured 'Exx' strain results were compiled from different mounting angle tests. Table 5-5 shows extracted Exx strain field results for the 'freebend' wire with central bend radius of 3.4mm, for five different mounting angles. Here, the 'gage length' (width of extracted strain field in central bend region) is 0.15mm.

Exx scale	Test set name	Mounting orientation	Extracted Exx strain field	Wire bend Macro view
	fb 60tilt comp	60 degree angle mounted - inner		
	fb 30tilt comp	30 degree angle mounted - inner		
	fb flat	flat mounted		
	fb 30tilt tens	30 degree angle mounted - outer		
	fb 60tilt tens	60 degree angle mounted - outer		

Table 5-5: extracted strain field results from 'Freebend' testing of 0.45mm wire with bend radius of 3.4mm, from five different mounting angles

Figure 5-75 shows an overlay plot, compiled from the Exx strain results for the five different mounting orientations, of Exx strain distribution across the wire for this bend radius of 3.4 mm.
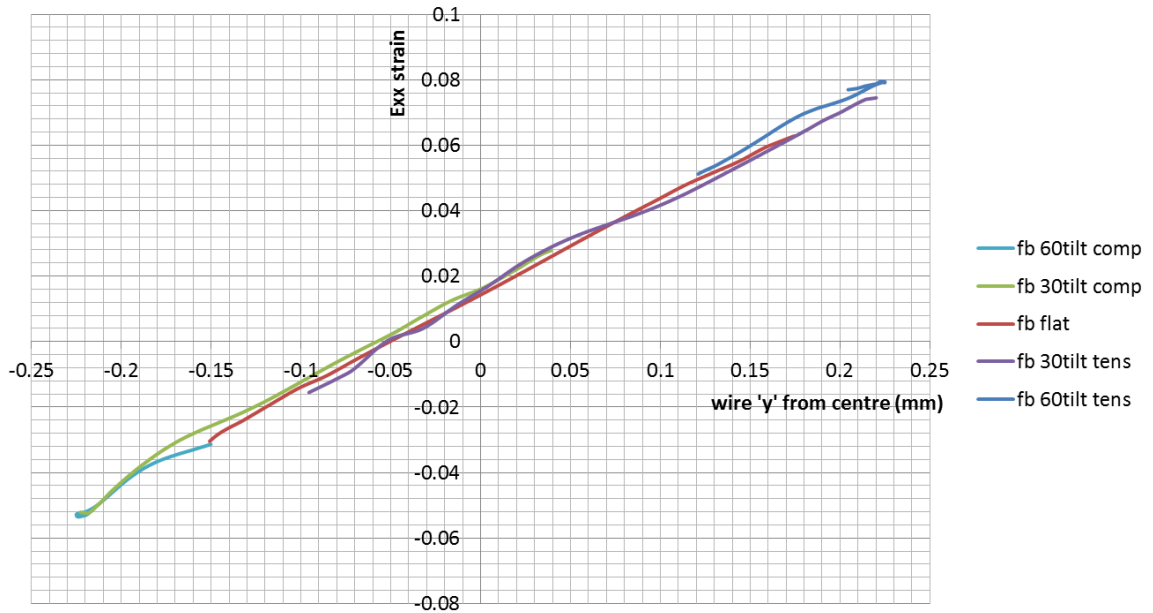
Figure 5-75: DIC measured 'Exx strain' overlay plot from 'Free bend' tests with various mounting angles, showing strain distribution across the 0.45 mm wire width for a bend radius of 3.4 mm

From the figure 5-75 graph, the following parameters were found for 0.45 mm diameter NiTi#1 wire at a bend radius of 3.4 mm:

- Maximum tensile strain = 8 % at the outer bend surface
- Maximum compressive strain = 5.3 % at the inner bend surface
- Strain gradient 'k' = 0.295 (from best-fit linear trend-line between maximum and minimum Exx values)
- Neutral axis position = 0.048 mm (10.66 % of wire diameter) towards inner bend surface

These results clearly show the tensile – compressive strain asymmetry of the Nitinol wire at a large bending deformation. The parameters above will be useful for validation of an FEA constitutive model of the material, by comparison with results of an FEA bend simulation using R = 3.4 mm.

5.6.4 Application of results to compaction strain estimation tool

When designing stents (for example Vascutek's 'Anaconda' ring stents), a common method for estimating maximum compaction strain of nitinol wires is to measure the centroid radius of curvature of a compacted wire and then use the following equation:

$$\varepsilon max = r / R$$

where r is the wire radius and R is the measured compacted bend radius. In order to measure the centroid radius of curvature of compacted wire, Vascutek have developed a method using micro-CT scans with CAD measurement, as described in ref (67). As reported in (67), the accuracy of this method is high, with intra-operator repeatability being the main error source (giving overall S.D of 2.95% for r/R values).

The r/R equation uses the relationship k = 1/R for the strain gradient. Comparing with the results parameters above, this relationship gives a good estimation of the wire's strain gradient at R = 3.4 mm:

$$k = 1 / 3.4 = 0.294$$

However, the r/R equation assumes that the neutral axis is central, with symmetric tensile and compressive strains. This is clearly not the case for Nitinol wire, as seen from the asymmetric strain results above. It is therefore useful to apply the DIC results for large deformation bending to obtain a better approximation of maximum strains in compaction.

The results above show neutral axis position to be approximately 10.5% of the wire diameter, or 0.21r, towards the compressive bend surface. From figure 2-23 in Chapter 2 (reproduced from Ref 18) it can be seen that this neutral axis position will be nearly

constant for large bending deformations in loading. Therefore, it is assumed that this value of 0.21r can be applied to find neutral axis position for other high bend curvatures.

Using this neutral axis position calculation, the maximum tensile and compressive strains can then be estimated using the following adjusted calculations:

$$\varepsilon\text{tensile max} = (1+0.21)r \,/\, R = 1.21r \,/\, R$$

$$\varepsilon\text{compressive max} = (1-0.21)r \,/\, R = 0.79r \,/\, R$$

Using these calculations for the case of a 0.45 mm diameter wire at bend radius 3.4 mm and assuming operator measurement error of $\pm$ 2.95% for the r/R measurement (from ref 67) gives:

$$\varepsilon\text{tens max} = 8.01 \pm 0.24\%$$

$$\varepsilon\text{comp max} = 5.23 \pm 0.15\%$$

In this way, by accounting for the strain asymmetry, a better estimation of the maximum strains for large deformation bending can be achieved. These 'adjusted calculations' above could be used for estimating compaction strains when wire diameter and bend radius are known (for example from micro-CT measurement).

5.7 Conclusions

3D Microscopic DIC has been successfully applied to measure surface strains of thin superelastic Nitinol wire (diameter = 0.45 mm) in large deformation bending, using specially developed loading rigs and mounting platforms. The accuracy of the DIC system was suitable for measuring superelastic strains, with estimated absolute error in 'Exx' strain of 900µs (0.09%).

Using this method with a 3-Point Bend loading rig, the load-unload strain hysteresis for superelastic Nitinol in bending was clearly demonstrated using Strain-Deflection results, and these were also used to explain the load history dependence of strain state at a given bend deflection. Elastic and plastic beam bending theories were used to analyse the Strain-Deflection behaviour, which was understood by considering the following characteristics of Nitinol:

- Stress plateaus in tension and compression, where strain increases or decreases are accommodated at near-constant stress by phase transformation, lead to localized bending effects ('hinging' and 'unhinging')
- Load-unload stress hysteresis in tension and compression lead to load-unload strain hysteresis in bending, with local curvatures (and global bend shape) being different for a given global deflection in loading and in unloading
- Dependence of the stress-strain path during unloading in tension and compression on the maximum strain history means that for 3-point bending, local curvatures (and global bend shape) at a given bend deflection during unloading are dependent on the maximum deflection reached during loading.

As well as being useful for understanding the bending behaviour of wires, the Strain-Deflection plots obtained by DIC testing will also provide useful results for validation of 3-Point Bend FEA simulations that use a constitutive model to represent Nitinol .

Using both the 3-Point Bend rig and a 'Free bend' rig, useful test result parameters were obtained for known bend deformations:

- Maximum Tensile Exx strain
- Maximum Compressive Exx strain
- Neutral axis position (as % of wire diameter)
- Strain gradient across wire

These results will be useful for validation of the FEA model, particularly in validating the strain asymmetry in bending.

The DIC testing clearly demonstrated the strain asymmetry of nitinol wire in bending, with the neutral axis observed to shift from the centroid towards the intrados during bending. This behaviour was understood by considering the compressive – tensile stress-strain asymmetry of Nitinol.

Chapter 6: Calibration and Validation of FE-Based Nitinol Material Models Using Experimental Results

6.1 Background and Introduction

Compressive, tensile and bend tests have been performed on superelastic wire used for stent graft devices in order to characterize the mechanical response of the material to relevant loading conditions. Results and analysis from this testing are detailed in chapters 3 to 5. As well as providing better understanding of the material's in-service behaviour, an important aim of the experimental work was to provide sufficient data for parameter input to a constitutive model of the Nitinol material for use in Finite Element Analysis (FEA). The experimental results from chapters 4 and 5 then provide useful data for validation of the material model by comparison against FEA bending simulations. In this way, the experimental results will allow an assessment of the FEA material model's suitability for use in simulations of stent graft components. The following chapter reports the use of the experimental data for Vascutek's NiTi#1 stent wire in compression, tension and bending to calibrate and validate representative material models using the Abaqus FEA software.

Other collaborative projects between University of Strathclyde and Vascutek have focused on FEA modelling of Vascutek's stent components. Consideration of the optimal modelling approach has led to the Abaqus software (implicit solver) being chosen, with its built-in 'ABQ_SUPER_ELASTIC' UMAT material model for Nitinol. This software and constitutive model were therefore chosen for the current investigation. The 'ABQ_SUPER_ELASTIC' UMAT uses the constitutive model developed by Aurrichio and Taylor (42), which is widely used in the medical device industry for FEA simulations of superelastic Nitinol components. Section 2.2.3 in Chapter 2 gave an introduction to this constitutive model, its development and its capabilities.

6.2 Objectives

The main aim of the present work is to assess the validity of a representative Nitinol material model in Abaqus FEA software using experimental data for parameter input and for validation of the simulation outputs, in order to provide a suitable material model for performing simulations of stent graft components. To achieve this, the following objectives have been set:

- Calibrate a representative UMAT 'room temperature' material model using uniaxial tensile and compressive data inputs derived from Chapter 3.
- Calibrate a representative UMAT 'body temperature' material model using uniaxial tensile and compressive data inputs derived from Chapter 3.
- Validate each UMAT model using the 3-Point Bend Load-Deflection test results from chapter 4.
- Validate the 'room temperature' UMAT model using the experimental strain results for the NiTi#1 wire in bending from chapter 5.

Having calibrated and validated a suitable FE-based material model, it is intended to use this to meet the following additional objective:

- Use FEA simulations to investigate strain history paths, load history paths and cycling behavior for the Nitinol wire in bending.

6.3 Methods

Abaqus version 6.11-2 software was used for all modeling and simulations, with the implicit solver. This software includes the built-in user material model (UMAT) for superelastic Nitinol, based on the constitutive model developed by Aurrichio and Taylor (42), which is a phenomenological model that is calibrated for a specific material using parameters obtained from uniaxial test results. In the present work, the appropriate parameters were obtained from the uniaxial compressive and tensile stress-strain data presented in Chapter 3.

For validation, 3-Point Bend simulation models were set-up within Abaqus. (Note: this FEA modelling built on parallel collaborative work between University of Strathclyde and Vascutek on FEA modelling of stent components.) The 3-Point Bend models were based on the experimental set-ups used in Chapters 4 and 5, shown in the schematic diagrams of figures 4-2 and 4-4 of Chapter 4. Figure 6-1 below shows the 3-Point Bend FEA model for the 0.45 mm wire in its initial undeformed position and at its maximum deformation position (indenter pin deflection = 9.837 mm).
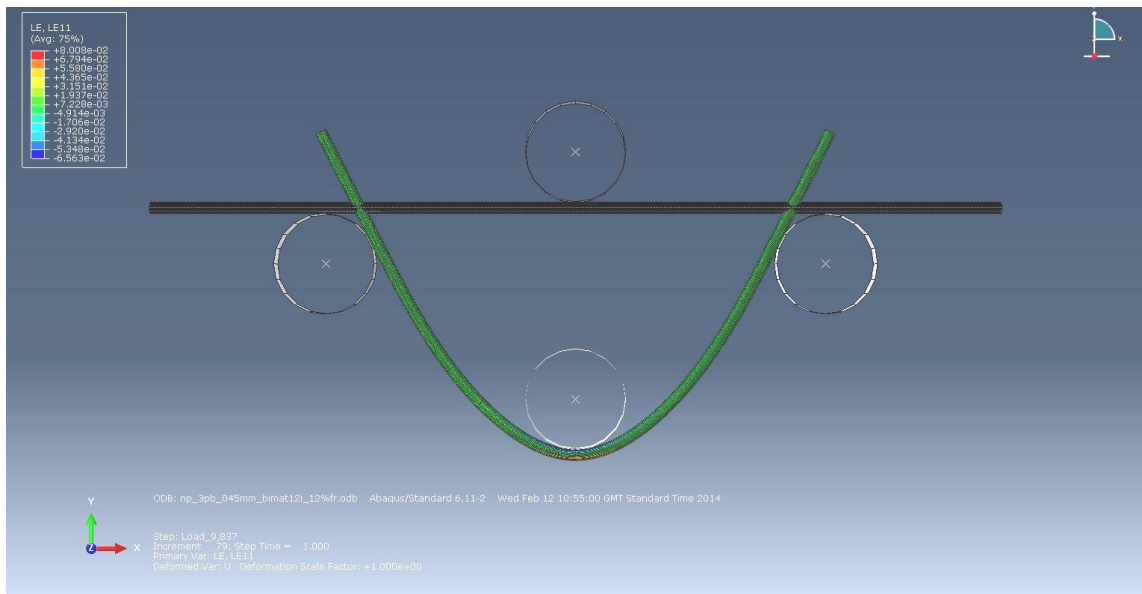
Figure 6-1: 3-Point Bend FEA model for 0.45 mm nitinol wire. Pin diameter, spacing and deflection range are identical to the experimental set-up used in Chapters 4 and 5

The 3-Point Bend Test simulations were modelled using 'analytical rigid surface' elements (ref 68) for the pins and C3D8I type elements (8 node linear brick, 3D stress, with incompatible mode) (ref 69) for the wire.

Rigid surface contact elements could be used for the pins as they can be assumed to be rigid (non-deformable) when used to impart bending deflections on the thin superelastic wire. The 'analytical rigid surface' contact elements were of the 3-D cylindrical surface

type, using circular curved segments to model the pin's surface. This modelling method has two main advantages in contact modelling over defining element based rigid surfaces: firstly, decreased computational cost; secondly, the curved segments give a smooth surface and therefore a better approximation of the physical contact between round pin and wire with less contact noise than would be achieved with a rigid surface formed by element faces. Analytical surface elements are associated with a reference node, in this case at the centre of the cylindrical surface, used to govern the motion of the surface.

The 8-node first-order (linear) hexahedral (brick) continuum element type with incompatible mode was chosen for the wire as this element type can provide good accuracy and computational efficiency for non-linear analyses involving contact. The 'incompatible mode' option enhances the element's degrees of freedom and enables simulation of bending with increased accuracy at minimal additional computational cost compared to C3D8 elements. Suitability for bending simulations was also ensured by keeping the element length suitably small compared to the wire diameter. The suitability of element type and mesh density (see figure 6-6) for the wire modelling was established from a mesh convergance study that had been performed previously in the University of Strathclyde / Vascutek FEA collaboration work, where a high density mesh of C3D20 elements was used as a datum, as reported in ref 70.

For constraints, the reference nodes for the outer (support) pin surfaces were fixed and the reference node for the central (indenter) pin was displacement driven for loading and unloading of the wire. Additionally, the centerline of the wire was constrained to prevent lateral motion relative to the pins.

For the contact interaction between the wire surface and the pin surfaces, the standard isotropic Coulomb friction model was used with the 'penalty' method to define elastic slip (ref 71). The Coulomb friction model operates on the basis that no relative motion

(i.e. 'sticking') will occur between the contacting surfaces if the frictional shear stress across the interface is less than the critical shear stress, at which the surfaces will start sliding relative to each other. The critical shear stress is defined in the model as a fraction of the contact pressure between the surfaces, with the fraction 'μ' being the coefficient of friction. In our model, the coefficient of friction 'μ' was set (after a series of trial and error simulations, as described below) to be 15 %, meaning that sliding would occur when the equivalent shear stress at the contact between the wire and pin surfaces was ≥ 0.15 * contact pressure. It should be noted that for the 3-Point Bend test, the frictional (shear) stresses are very low for small bend deflections as the wire ends essentially rotate around the support pins on either side as bending occurs in between. Therefore, the frictional model plays little part in the accuracy of the simulation for small deflections. At larger deflections, though, the contact shear stresses become more significant relative to the contact normal stress (pressure), and so it is important that the friction model can accurately describe the resistance to sliding of the physical contact surfaces. In the present work, the effect of friction in 3-Point Bending could be clearly seen in the experimental results (Chapter 4) by the vertical load drop between loading and unloading at the maximum deflection, as the frictional (shear) forces resisting tangential motion at the contact surfaces changed direction. Figure 4-5 in Chapter 4 clearly demonstrates this for two different maximum deflections of the 0.45 mm NiTi wire. In order to model this friction behavior using FEA, a trial and error approach was used where the 3-Point Bend simulations were run with different 'μ' values until the load drop at maximum deflection closely matched the values seen in figure 4-5, using μ = 15 % (see figure 6-15 in section 6.4 'Results'). The same friction value was found to work for the 0.14 mm 3-Point Bend simulations, as seen in figure 6-2 below where the simulated results with μ = 0.15 (blue curve) have a similar load drop at maximum deflection as the experimental results (green curve). For comparison, the red curve gives the results of a simulation with zero friction, where there is no load drop at maximum deflection – although load-unload hysteresis is still clearly evident.
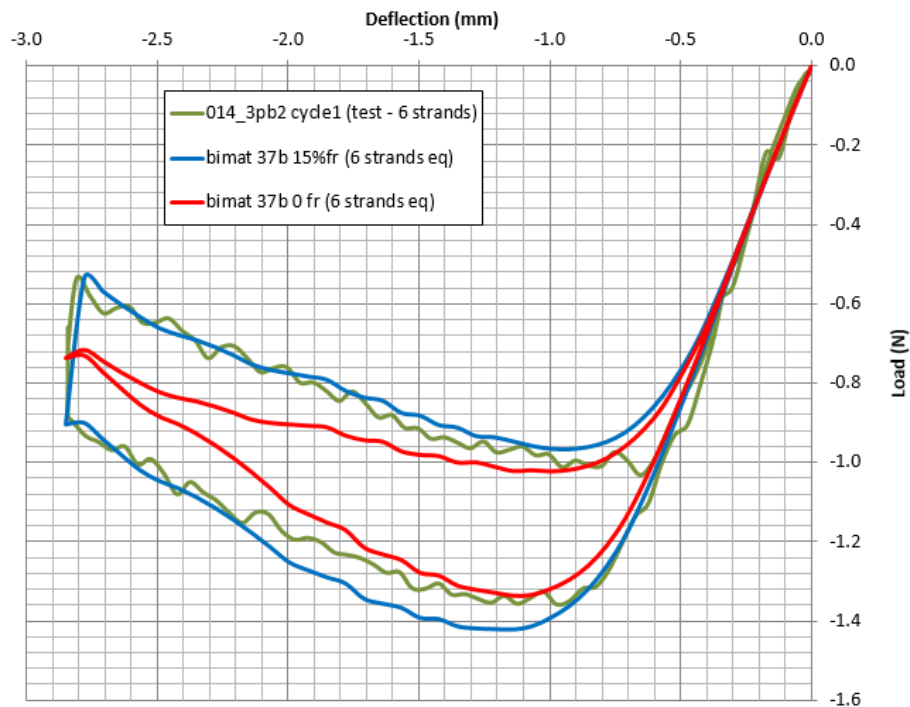
Figure 6-2: Load-deflection results from 0.14 mm wire 3-Point Bend simulations using friction coefficients of 0.15 (blue curve) and 0 (red curve), overlaid with experimental results at 37 C from chapter 4.

In order to model the Nitinol material for the wire, the 'ABQ_SUPER_ELASTIC' UMAT model was used. This is the built-in constitutive model described in Chapter 2, based on the work of Aurrichio and Taylor (42), which includes the following features:

- Ability to define different elastic properties (Young's modulus and Poisson's ratio) for austenite and martensite phases.

- Ability to include tension – compression asymmetry, whereby different stress-induced martensite start stresses are defined in tension and compression. Increasing the compressive stress parameter relative to the tensile one results in increased asymmetry, with higher forward transformation stresses, a steeper, shorter 'upper plateau' and slightly higher reverse transformation stresses in compression. The tension-compression asymmetry can be increased further by

using the 'volumetric transformation strain' parameter to shorten the compressive stress 'plateaus'.

- Definition of the uniaxial tensile stress-strain curve using 4 stress break points (representing the start and finish transformation stresses for loading and unloading) and transformation strain. For compression, only 2 parameters can be specified (SIM start stress and volumetric transformation strain), which are used to calculate the other features of the compressive stress-strain curve based on scaling of the tensile curve.

- Temperature–dependent stress-strain response, by definition of the rate of change of transformation plateaus with temperature

- Simulation of shape-set annealing (used for simulating stent material processing) whereby material stress-strain state can be re-set to zero at a chosen step in the analysis
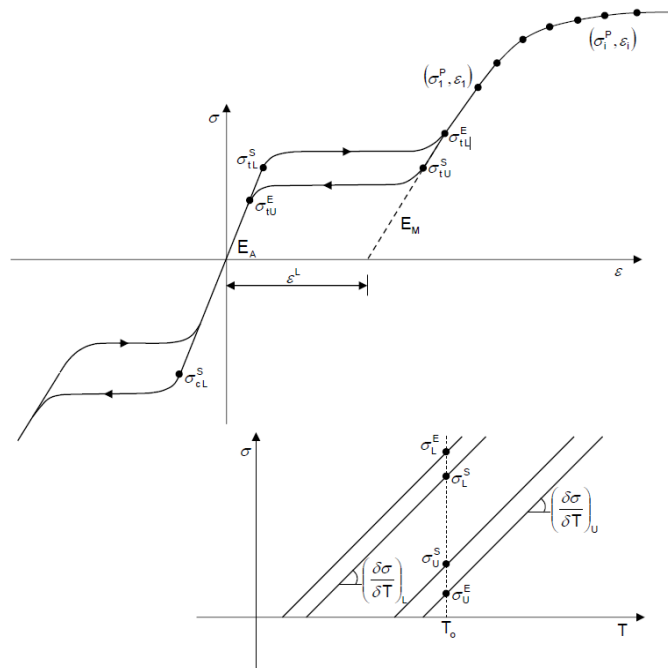
Figure 6-3: Input parameters for Nitinol UMAT model, as they relate to the uniaxial stress-strain curves (top) and stress-temperature curves (bottom) for Nitinol's superelastic-plastic behaviour. Taken from Dassault Systemes' 'UMAT for Superelasticity Elastic-Plastic Model' information sheet

The Abaqus material model is calibrated by the user for the specific nitinol material to be modelled by input of 15 parameters derived from uniaxial stress-strain test results for the material. Beyond the 15 parameters, further points can also be added to characterize the plastic stress-strain behavior beyond the loading plateau in tension, but this option was not used here as plasticity in bending is beyond the scope of the present work. Figure 6-3 above (taken from Dassault Systemes' 'UMAT for Superelasticity Elastic-Plastic Model' information sheet) shows how various input parameters relate to the uniaxial stress-strain curves and stress-temperature curves for Nitinol.

6.3.1 'Unimat' vs 'BiMat' Material Modelling

With reference to figure 6-3 (top), the tensile behaviour of Nitinol is well represented in the Abaqus UMAT constitutive model, with 7 input parameters used to describe the superelastic tensile stress-strain response at a given temperature. For compressive behaviour, however, there are only two parameters: the 'start of transformation stress' (σ^s_{cL}) and the 'volumetric transformation strain' (ε_v^L). Based on these two input parameters, together with scaling equations using the tensile parameters, the model gives an approximate representation of the compressive stress-strain response. Due to the lack of parameters to describe the compressive side, this representation is not as accurate as the tensile side, which leads to difficulties in accurately simulating bending behaviour of nitinol components.

This can be demonstrated using the 'unimat 37a' model parameters currently used by Vascutek engineers for performing Nitinol stent simulations with Abaqus. The model parameters are given in Table 6-1. Figure 6-4 then shows results from uniaxial tensile and compressive simulations performed with this model, overlaid with the 'corrected' experimental stress-strain results for NiTi#1 at 37 C from Chapter 3 (figure 3-28). Figure 6-4 clearly demonstrates that the 'unimat' model is more accurate for describing the material response in tension than in compression. These uniaxial simulation results could be improved by using a different value for 'volumetric transformation strain' (ε_v^L)

to reduce the compressive transformation strain. However, it was found that the material model was then unsuitable for bending simulations, which would fail to converge on a solution. Therefore, the parameter values given in Table 6-1 are used as a compromise to represent the material's uniaxial stress-strain response for application to stent simulations, which rely heavily on bending behaviour.

UMAT Parameter				37a Unimat Value
No	Symbol	Description	Units	
1	E_A	*Austenite Elasticity*	**MPa**	**61000**
2	ν_A	*Austenite Poisson's Ratio*		**0.45**
3	E_M	*Martensite Elasticity*	**MPa**	**32500**
4	ν_M	*Martensite Poisson's Ratio*		**0.45**
5	ε^L	*Transformation Strain*		**0.05**
6	$\dfrac{\delta\sigma}{\delta T}$	*Rate of change of plateau σ with T (Upper/Loading)*	**MPa/ °C**	**7.1**
7	σ_L^S	*Start of transformation loading*	**MPa**	**680**
8	σ_L^E	*End of transformation loading*	**MPa**	**710**
9	T_0	*Reference Temperature*	**°C**	**0**
10	$\left(\dfrac{\delta\sigma}{\delta T}\right)_U$	*Rate of change of plateau σ with T (Lower/Unload)*	**MPA/ °C**	**7.1**
11	σ_U^S	*Start of transformation unloading*	**MPa**	**380**
12	σ_U^E	*End of transformation unloading*	**MPa**	**350**
13	σ_{CL}^S	*0 for symmetry model*	**MPa**	**965**
14	ε_V^L	*Volumetric transformation strain*		**0.05**
15	N_A	*Number of anneals to be performed during analysis*		**0**

Table 6-1: 'unimat 37a' UMAT input parameters for NiTi#1 material at 37 C
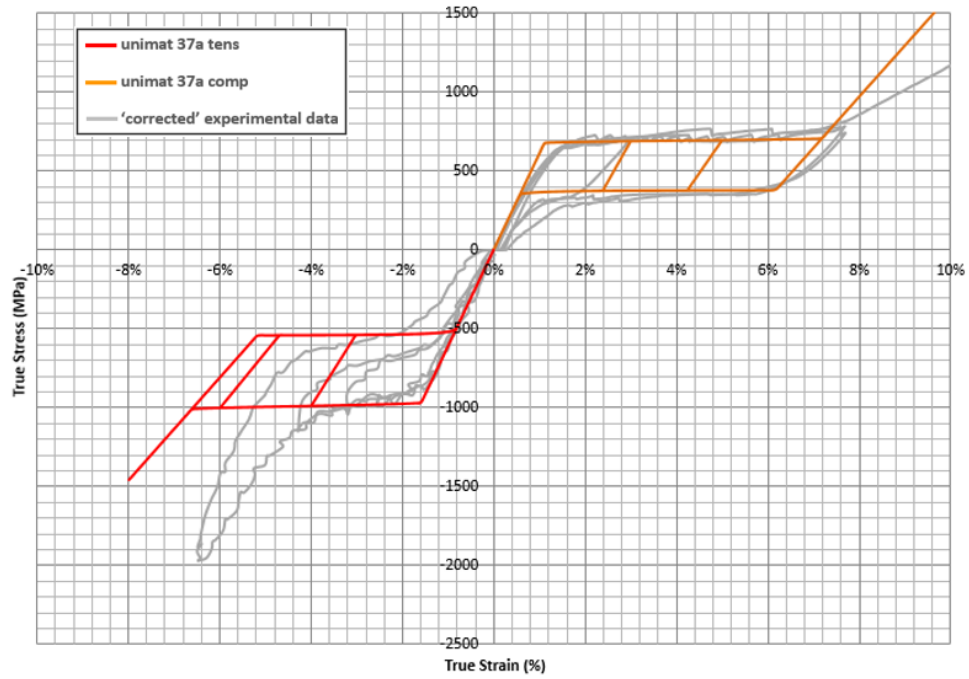
Figure 6-4: uniaxial tensile and compressive stress-strain results from simulations using 'unimat 37a' UMAT material model, overlaid with 'corrected' experimental results from testing of NiTi#1 wire material at 37 C (from figure 3-28).
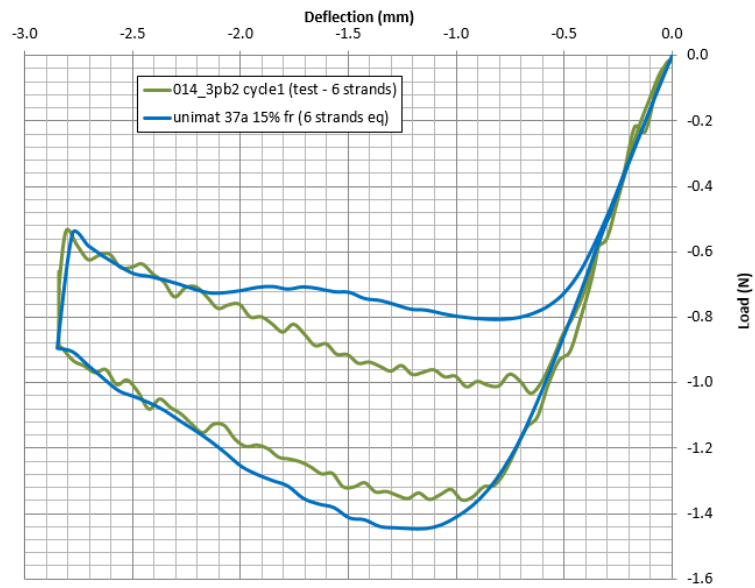
Figure 6-5: Load-deflection results from 0.14mm wire 3-Point Bend simulation using 'unimat 37a' model, overlaid with experimental results at 37 C from chapter 4.

Figure 6-5 shows results from a 3-Point Bend simulation using the 'unimat 37a' model, overlaid with experimental Load-Deflection results. Clearly there is considerable discrepancy between the simulation and the experimental results, particularly during unloading between 2 and 0.5 mm pin deflections. This discrepancy is not surprising, given the inaccuracy of the uniaxial simulation's compressive unloading curve seen in figure 6-4.

In order to overcome the limitations of the asymmetric UMAT model for representing the compressive material behaviour, an approach was developed through the University of Strathclyde / Vascutek FEA collaboration to more accurately represent the Nitinol material behaviour for bending simulations (initially for in-plane bending cases) (ref 72). This modelling approach is here referred to as the 'bimat' approach, where a different symmetric UMAT model is used for each of the tensile and compressive regions of a bending component (as opposed to the 'unimat' approach, which uses a single asymmetric UMAT model for all elements.)

Using the 'bimat' approach, the FEA wire part model is set up using the steps below:

1. Partition the model with a plane a distance 'x' from the geometric centre line, towards the compressive bend surface – see figure 6-6 below. 'x' was determined from iterative FEA studies to find the neutral axis position in the cross-section of the bend apex for maximum 3-Point Bending deflection. For the 0.45 mm wire model, x = 0.0376 mm. For the 0.14mm wire model, x = 0.0117 mm. In each case, 'x' is 8.35 % of the wire diameter. Note that the partition does not have to exactly coincide with the neutral axis, but must be located within the elastic regions of the tensile and compressive models throughout the simulation (see further explanation below).

2. Mesh the wire cross section by element size, using the 'x' value for the element size (see figure 6-6 below). This gives a good even distribution of elements throughout the cross-section. For meshing along the wire, the element length can

be greater than the 'x' value but the number of elements along the wire length must be even, ensuring that there are nodes coincident with the central cross-section of the wire for obtaining stress-strain results at the bend apex.
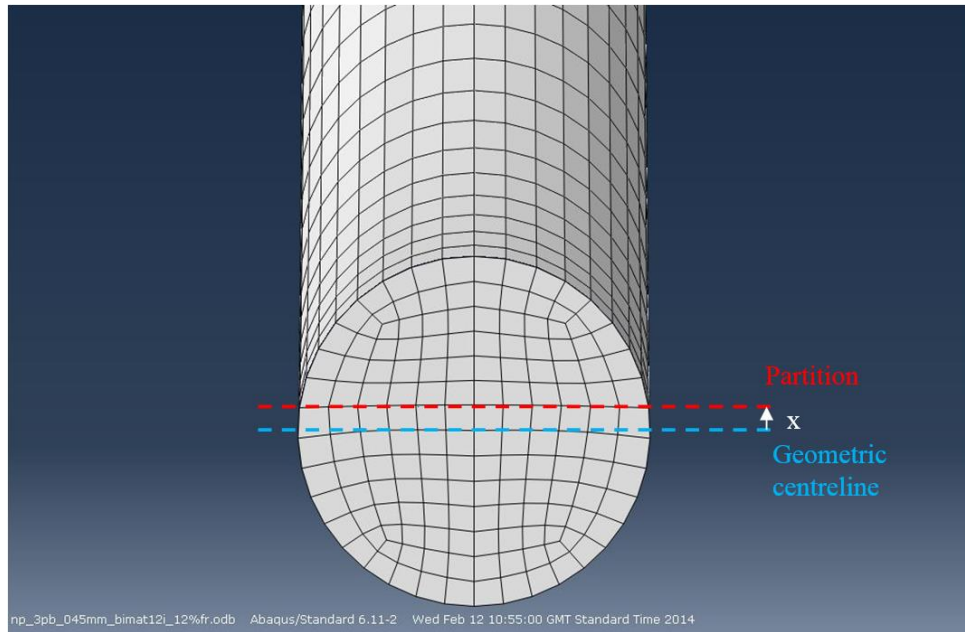
Figure 6-6: Apex cross section showing geometric centreline, partition line for 'bimat' modelling and mesh

3. Create two separate 'UMAT' material models, each of which is symmetric. One model is the 'tensile' material model, and will be applied to the tensile part of the wire model – below the partition line in figure 6-6 above. The other model is the 'compressive' material model, and will be applied to the compressive part of the wire – above the partition line in figure 6-6 above. An explanation of the different parameters for these two models is given in Table 6-4. It is essential that both models have the same austenite modulus E_A to ensure continuity in properties between the tensile and compressive parts (around the partition region) in bending simulations.

4. Apply each model to the appropriate region above or below the partition, as described in the previous step.

Once the 3-Point Bend model (including 'bimat' wire model) and study steps are fully defined, the FEA simulation can be run. During the analysis steps, the neutral axis can move from the central position to an eccentric position, providing useful simulation output data for neutral axis eccentricity at a given bend deflection. While the Neutral axis can move in this way, it is important that the elements surrounding the partition are at strains within the initial elastic limit throughout the analysis. As the E_A values are the same for both the tensile and compressive symmetric UMAT models, this ensures that there is continuity in the results from the compressive to the tensile side of the partition. This can be seen in figure 6-7 for the wire at its maximum 3-point bend deflection, where strains beyond the elastic limits are shown in grey. The coloured region represents elastically strained material. As can be seen, in this case there is continuity in results across the partition line, which approximately coincides with the neutral axis for this apex bend deformation.
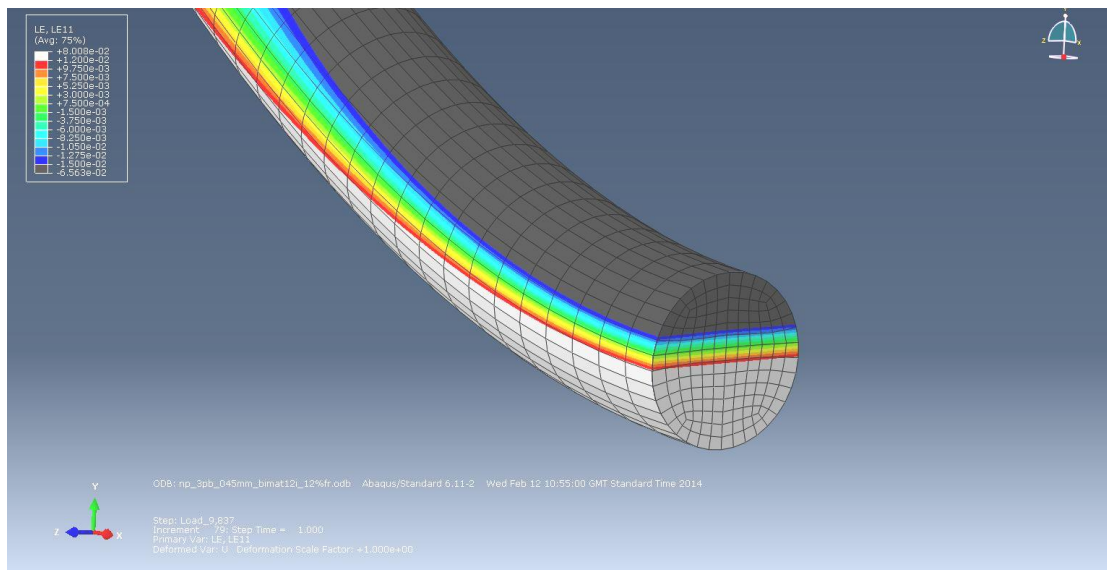
Figure 6-7: elastic strains (in colour) show continuity in results across the partition region. Grey regions represent material at transformation strains beyond the elastic limit (light grey: tensile; dark grey: compressive).

6.3.2 Material Parameters Derived from Uniaxial Test Data

The uniaxial stress-strain results from Chapter 3 were used to determine key parameters to describe the material behavior under tensile and compressive loading. The true stress-true strain results of figure 3-28 (results at 37ºC) and figure 3-30 (results at room temperature) were used for this purpose. Relevant parameters could then be used to derive input parameters for FEA material models, as will be described in section 6.3.3. It should be noted that the material behavior parameters determined here include some description of the material's plastic deformation behavior, while plasticity was not included in the FEA material modelling described in this chapter.

Figure 6-8 shows the uniaxial stress-strain plots at 37ºC, with overlaid lines to show how values were determined for key material characterization parameters. The key parameters for uniaxial tensile and compressive behavior of NiTi#1 wire at 37C are then set out in Table 6-2.
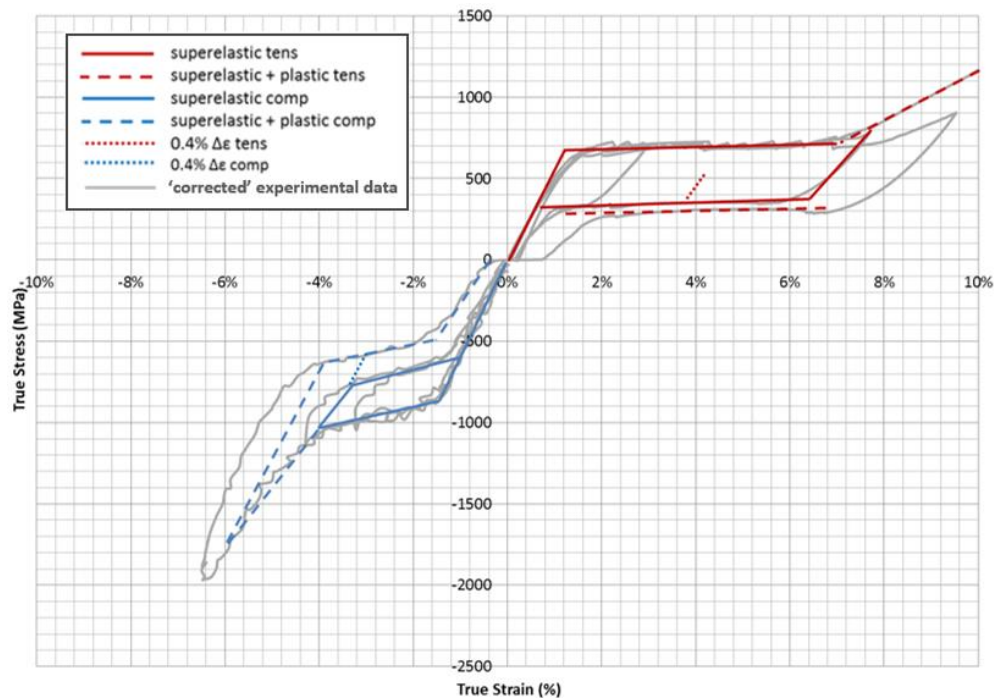
Figure 6-8: Uniaxial tensile and corrected compressive true stress-strain results for Vascutek NiTi#1 wire at 37C, with lines overlaid to show how material characterization parameters were determined

NiTi#1 Result Parameter @ 37C	Tension	Compression
Initial Load / Unload Modulus (found using MS Excel 'slope' function for initial raw data up to 400 MPa stress)	56 GPa	60 GPa
Loading plateau start strain	1.2 %	1.45 %
Loading plateau start stress	680 MPa	880 MPa
Loading plateau finish strain	7 %	4 %
Loading plateau finish stress	710 MPa	1030 MPa
Effect of unloading from different strains within the 'load plateau' region	Slightly decreased unload modulus for increased 'max' strain, down to common unload plateau from all strains	Slightly decreased unload modulus for increased 'max' strain, down to common unload plateau from all strains
(Minimum) Unload modulus from end of load plateau	32.5 GPa (from 7.8 % ε)	36.25 GPa (from 4 % ε)
- 'Common' unload plateau strain range	6.4 % - 0.6 %	3.3 % - 1 %
- 'Common' unload plateau stress range	380 – 310 MPa	780 – 600 MPa
Martensite Load Modulus (2nd Modulus beyond load plateau)	15 GPa (from 7.8-10 % ε)	36 GPa (from 4-6 % ε)
Effect of unloading from strains beyond the 'load plateau' region	Unload modulus increases slightly. Unload plateau decreases with increased max strain	Unload modulus increases up to value similar to initial modulus at 6 % max strain. Unload plateau decreases with increased max strain
Martensite Unload Modulus from max measured strain	Not clear from results due to slipping in grips	55 GPa (unloading from 6 % ε)
Unload plateau strain range from max measured strain	Not clear from results due to slipping in grips	3.9 % - 1.5 % (unloading from 6 % ε)
Unload plateau stress range from max measured strain	310 – 280 MPa (unloading from 10 % ε)	630 – 500 MPa (unloading from 6 % ε)
Residual strain for samples loaded to max strain	0.4 % (unloading from 9.6 % ε) (from previous test results, not shown)	0.4 % (unloading from 6 % ε)
Cycling modulus for 0.4% $\Delta\varepsilon$ load-unload from lower plateau	40 GPa (for 0.4 % $\Delta\varepsilon$, 4 % mean ε during unload from 8% max ε) (from previous test results, not shown)	55 GPa (for 0.4 % $\Delta\varepsilon$, 3.2 % mean ε during unload from 6 % max ε)

Table 6-2: Summary of key parameters for NiTi#1 wire at 37C, taken from uniaxial tensile and corrected compressive stress-strain results.

Figure 6-9 shows the uniaxial stress-strain plots at room temperature (compression at 17 C; tension at 23 C) from figure 3-30 in Chapter 3, with overlaid lines to show how values were determined for key material characterization parameters. The key parameters for uniaxial tensile and compressive behavior of NiTi#1 wire at room temperature are then set out in Table 6-3.
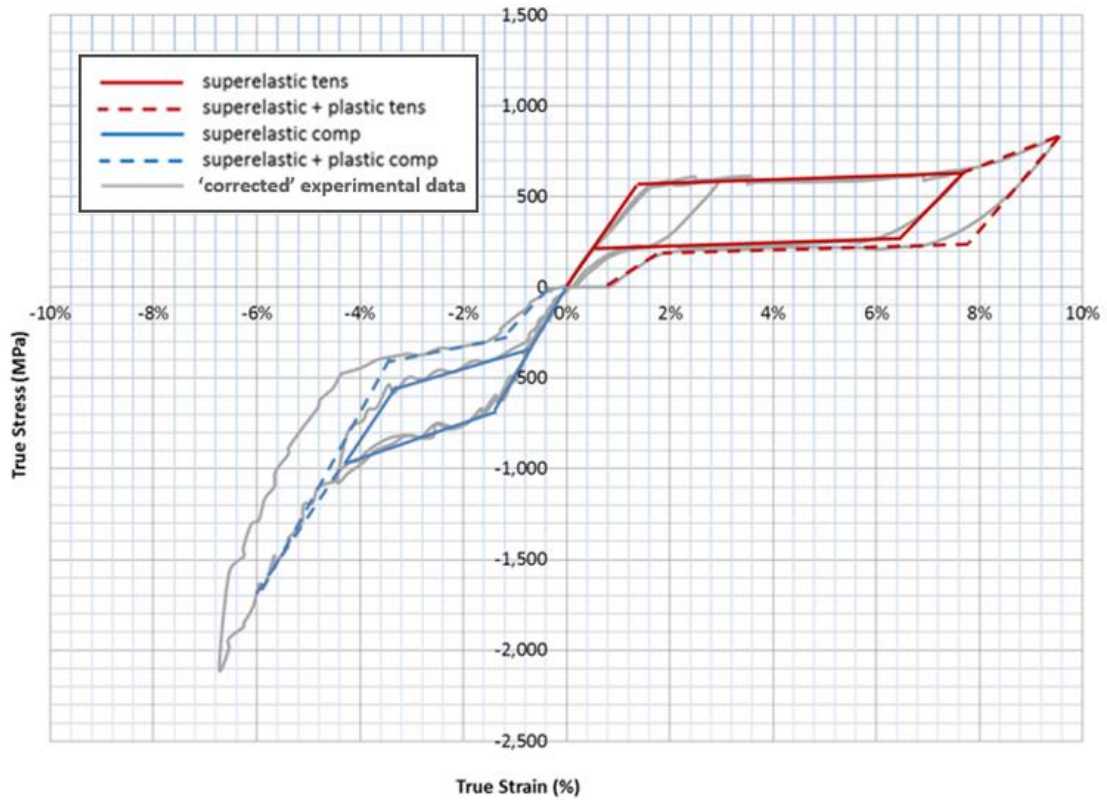
Figure 6-9: Uniaxial tensile and corrected compressive true stress-strain results for Vascutek NiTi#1 wire at room temperature, with lines overlaid to show how material characterization parameters were determined

NiTi#1 Result Parameter @ Room Temp	Tension	Compression
Initial Load / Unload Modulus (found using MS Excel 'slope' function for initial raw data up to 400 MPa stress)	41 GPa	50 GPa
Loading plateau start strain	1.4 %	1.4 %
Loading plateau start stress	560 MPa	700 MPa
Loading plateau finish strain	7.7 %	4.3 %
Loading plateau finish stress	620 MPa	975 MPa
Effect of unloading from different strains within the 'load plateau' region	Slightly decreased unload modulus for increased 'max' strain, down to common unload plateau from all strains.	Slightly decreased unload modulus for increased 'max' strain, down to common unld plateau from all strains
(Minimum) Unload modulus from end of load plateau	30 GPa (from 8 % ε)	42.5 GPa (from 4 % Ɛ)
- 'Common' unload plateau strain range	6.5 % - 0.6 %	3.3 % - 0.7 %
- 'Common' unload plateau stress range	280 – 210 MPa	560 – 350 MPa
Martensite Load Modulus (2nd Modulus beyond load plateau)	11 GPa (from 7.7 - 9.6 % ε)	42.5 GPa (from 4.3 - 6 % Ɛ)
Effect of unloading from strains beyond the 'load plateau' region	Unload modulus increases. Unload plateau decreases with increased max strain	Unload modulus increases. Unload plateau decreases with increased max strain
Martensite Unload Modulus from max measured strain	35 GPa (unloading from 9.6 % ε)	51.5 GPa (unloading from 6 % Ɛ)
Unload plateau strain range from max measured strain	7.8 % - 1.8 % (unloading from 10 % ε) (may include some slip of sample in grips)	3.5 % - 1.1 % (unloading from 6 % ε)
Unload plateau stress range from max measured strain	220 – 190 MPa (unloading from 10 % ε)	400 – 290 MPa (unloading from 6 % ε)
Residual strain for samples loaded to max strain	0.8 % (unloading from 10 % Ɛ) (may include some slip of sample in grips)	0.4 % (unloading from 6 % Ɛ)

Table 6-3: Summary of key parameters for NiTi#1 wire at room temperature, taken from uniaxial tensile and corrected compressive stress-strain results.

6.3.3 UMAT Parameter Values for 'Bimat' Modelling

In order to create the 'tensile' and 'compressive' UMAT material models for 'bimat' modelling, input values were required for the 15 material parameters in each case. Table 6-4 describes each parameter and shows the source for each parameter value used in the present work. These inputs largely relied on the values determined in section 6.3.2.

UMAT Parameter			Detail / Source	
			Tensile UMAT	**Compressive UMAT**
No.	**Symbol**	**Description**		
1	E_A	*Austenite Elasticity*	For bimat model, E_A in tension must be the same as E_A in compression. Values were found from a compromise of the initial modulus values in tension and compression (tables 6-2 / 6-3).	
2	ν_A	*Austenite Poisson's Ratio*	0.45 value taken from ref (18) Reedlunn et al	
3	E_M	*Martensite Elasticity*	compromise of the martensite load and unload modulus values from end of loading plateau (tables 6-2 / 6-3)	compromise of the martensite load modulus from 4 % strain and unload modulus from 6% (tables 6-2 / 6-3)
4	ν_M	*Martensite Poisson's Ratio*	0.45 value taken from ref (18) Reedlunn et al	
5	ε^L	*Transformation Strain*	found by tracing the E_M gradient from the end of the loading plateau down to the x-axis (using figures 6-8 or 6-9)	found by tracing the E_M gradient from 6 % maximum strain down to the x-axis (using figures 6-8 or 6-9)
6	$\dfrac{\delta\sigma}{\delta T}$	*Rate of change of plateau σ with T (Upper/ Loading)*	from results in Chapter 3, section 3.4.2 'Temperature Dependence'	from results in Chapter 3, section 3.4.2 'Temperature Dependence'
7	σ_L^S	*Start of transformation loading*	tensile stress level at start of loading plateau (tables 6-2, 6-3)	compressive stress level at start of loading plateau (tables 6-2, 6-3)
8	σ_L^E	*End of transformation loading*	tensile stress level at end of loading plateau (tables 6-2, 6-3)	compressive stress level at end of loading plateau (tables 6-2, 6-3)

UMAT Parameter			Detail / Source	
			Tensile UMAT	**Compressive UMAT**
No.	**Symbol**	**Description**		
9	T_0	*Reference Temperature*	for isothermal simulations, set to 0 – this means that parameter no.s 6 and 10 are not used	
10	$\left(\dfrac{\delta\sigma}{\delta T}\right)_U$	*Rate of change of plateau σ with T (Lower/ Unloading)*	from results in Chapter 3, section 3.4.2 'Temperature Dependence'	from results in Chapter 3, section 3.4.2 'Temperature Dependence'
11	σ_U^S	*Start of transformation unloading*	For bimats RTa and 37a, stress levels from 'common unload plateau stress range' are used (tables 6-2, 6-3). For bimats RTb and 37b, stress values were chosen so that the unload plateau passes through the 'slope change' points in unloading results of figures 6-8 / 6-9 – see examples in figures 6-10 and 6-11. These higher unload plateaus were found to give better results for the 3-Point Bend Load-Deflection validation in unloading.	
12	σ_U^E	*End of transformation unloading*		
13	σ_{CL}^S	*Start of transformation stress during loading in compression.*	Note: in Abaqus UMAT, if zero is stated then the symmetrical model is used. Set to 0. For bimat model, two symmetrical UMAT models must be used: one for tensile material, one for compressive material. These must be symmetrical so that the compressive material properties can be defined with the same detail as the tensile properties (using 7 parameters instead of 2 parameters for the asymmetric 'unimat' compressive model).	
14	ε_V^L	*Volumetric transformation strain*	Set the same as ε_L. This value is not used for symmetrical models**.**	
15	N_A	*Number of anneals to be performed during analysis*	Set to 0. No annealing simulations need to be performed.	

Table 6-4: description of parameters for 'tensile' and 'compressive' UMAT models used for 'bimat' modelling, together with explanation of method used for obtaining parameter values

Table 6-5 shows the parameter values used for two different 'Bimat' models (each consisting of a 'tensile' and a 'compressive' UMAT model) for Nitinol wire at 37 C. These different 'Bimat' models are summarized below:

- **Bimat 37a**: Body Temperature (37 C) model based on uniaxial loading and unloading values from Table 6-2.
- **Bimat 37b**: Body Temperature (37 C) model based on uniaxial loading values from Table 6-2, with unload plateau values modified to give improved validation results for 3-Point Bend Load-Deflection. The choice of modified tensile and compressive unload plateau values are explained by figures 6-10 and 6-11 respectively with accompanying explanation below.

				bimat 37a		bimat 37b	
UMAT Parameter				tens	comp	tens	Comp
No	**Symbol**	**Description**	**Units**				
1	E_A	*Austenite Elasticity*	**MPa**	61000	61000	61000	61000
2	ν_A	*Austenite Poisson's Ratio*		0.45	0.45	0.45	0.45
3	E_M	*Martensite Elasticity*	**MPa**	23000	45000	23000	45000
4	ν_M	*Martensite Poisson's Ratio*		0.45	0.45	0.45	0.45
5	ε^L	*Transformation Strain*		0.046	0.022	0.046	0.022
6	$\dfrac{\delta\sigma}{\delta T}$	*Rate of change of plateau σ with T (Upper/Load)*	**MPa/ °C**	7.1	7.5	7.1	7.5
7	σ_L^S	*Start of transformation loading*	**MPa**	680	880	680	880
8	σ_L^E	*End of transformation loading*	**MPa**	710	1050	710	1050

				bimat 37a		bimat 37b	
UMAT Parameter				**tens**	**comp**	**tens**	**Comp**
No	**Symbol**	**Description**	**Units**				
9	T_0	*Reference Temperature*	**°C**	**0**	**0**	**0**	**0**
10	$\left(\dfrac{\delta\sigma}{\delta T}\right)_U$	*Rate of change of plateau σ with T (Lower/Unload)*	**MPA/ °C**	**7.1**	**7.5**	**7.1**	**7.5**
11	σ_U^S	*Start of transformation unloading*	**MPa**	**380**	**780**	**445**	**880**
12	σ_U^E	*End of transformation unloading*	**MPa**	**310**	**600**	**390**	**760**
13	σ_{CL}^S	*0 for symmetry model*	**MPa**	**0**	**0**	**0**	**0**
14	ε_V^L	*Volumetric transformation strain*		**0.046**	**0.022**	**0.046**	**0.022**
15	N_A	*Number of anneals to be performed during analysis*		**0**	**0**	**0**	**0**

Table 6-5: Parameter values for the two different 37 C 'bimat' models (each consisting of a 'tensile' and a 'compressive' UMAT model).

Figures 6-10 and 6-11 show unloading of Nitinol wire from different maximum strains at 37 C in tension and compression respectively. It can be seen that during unloading in each case, there is an initial steeper linear section followed by a lower modulus slope before reaching the unload plateau. In each figure, a red dashed line has been drawn through the transition points between the initial steeper unloading slope and the lower modulus region of each plot. These red lines were used to find the modified tensile and compressive unload plateau stress values for bimat 37b in table 6-5.
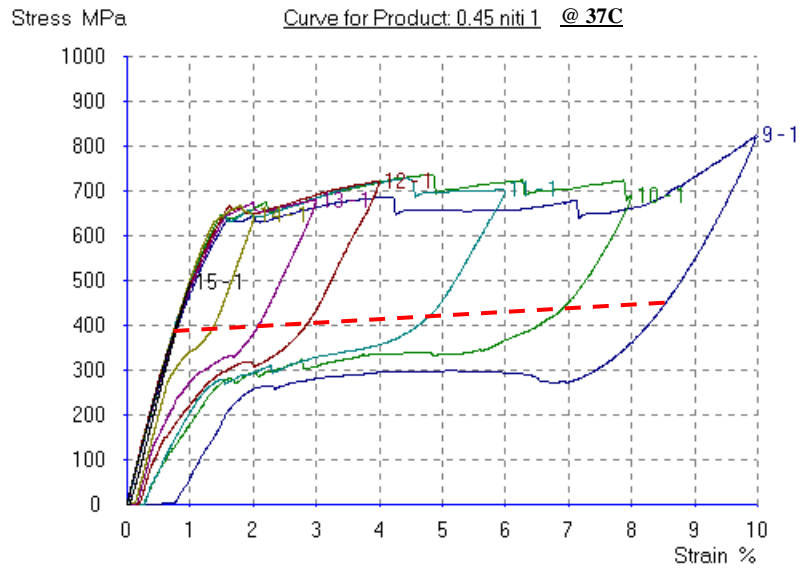
Figure 6-10: Tensile stress-strain plots (from fig 3-15) showing unloading of 0.45 mm Nitinol wire from different maximum strains at 37 C. The red dashed line depicts the modified tensile unload plateau stress level used for bimat 37b.
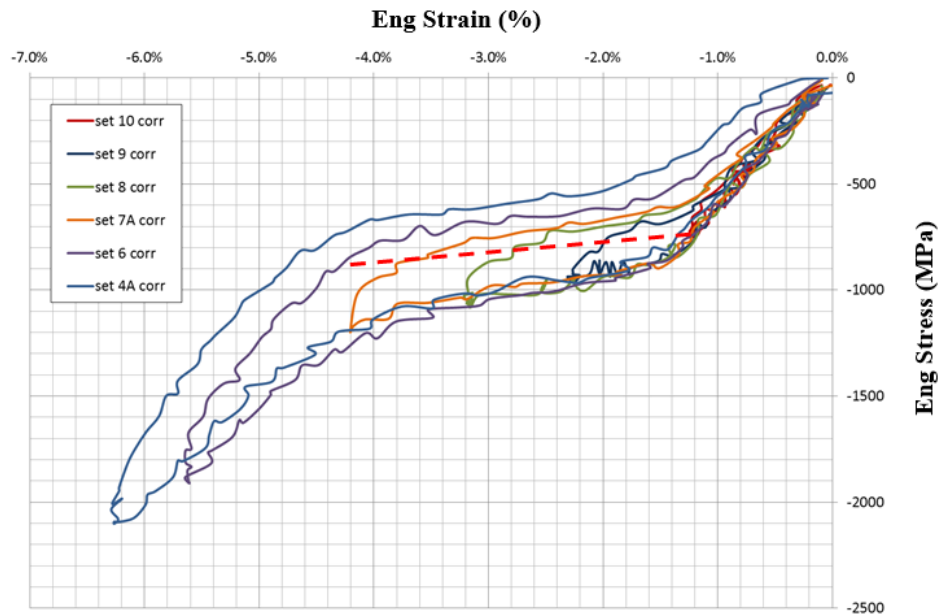
Figure 6-11: Compressive ('corrected') stress-strain plots (from fig 3-25) showing unloading of 1 mm Nitinol wire from different maximum strains at 37 C. The red dashed line depicts the modified compressive unload plateau stress level used for bimat 37b.

Table 6-6 shows the parameter values used for two different 'bimat' models (each consisting of a 'tensile' and a 'compressive' UMAT model) for Nitinol wire at room temperature. These different 'bimat' models are summarized below:

- **Bimat RTa**: Room Temperature material model based on uniaxial loading and unloading values from Table 6-3.
- **Bimat RTb**: Room Temperature material model based on uniaxial loading values from Table 6-3, with unload plateau values modified to give improved validation results for 3-Point Bend Load-Deflection. Modified unload plateau values were found using the same method described for figures 6-10 and 6-11.

				bimat RTa		bimat RTb	
UMAT Parameter				**Tens**	**Comp**	**tens**	**Comp**
No	**Symbol**	**Description**	**Units**				
1	E_A	*Austenite Elasticity*	**MPa**	47000	47000	47000	47000
2	ν_A	*Austenite Poisson's Ratio*		0.45	0.45	0.45	0.45
3	E_M	*Martensite Elasticity*	**MPa**	25000	42500	25000	42500
4	ν_M	*Martensite Poisson's Ratio*		0.45	0.45	0.45	0.45
5	ε^L	*Transformation Strain*		0.054	0.025	0.054	0.025
6	$\dfrac{\delta\sigma}{\delta T}$	*Rate of change of plateau σ with T (Upper/Loading)*	**MPa/ ºC**	7.1	7.5	7.1	7.5
7	σ_L^S	*Start of transformation loading*	**MPa**	570	700	570	700
8	σ_L^E	*End of transformation loading*	**MPa**	620	975	620	975
9	T_0	*Reference Temperature*	**ºC**	0	0	0	0

No	Symbol	Description	Units	bimat RTa		bimat RTb	
				Tens	Comp	tens	Comp
10	$\left(\frac{\delta\sigma}{\delta T}\right)_U$	Rate of change of plateau σ with T (Lower/Unload)	MPA/°C	7.1	7.5	7.1	7.5
11	σ_U^S	Start of transformation unloading	MPa	280	560	310	750
12	σ_U^E	End of transformation unloading	MPa	210	350	290	600
13	σ_{CL}^S	0 for symmetry model	MPa	0	0	0	0
14	ε_V^L	Volumetric transformation strain		0.054	0.025	0.054	0.025
15	N_A	Number of anneals to be performed during analysis		0	0	0	0

Table 6-6: Parameter values for the two different Room Temperature 'bimat' models (each consisting of a 'tensile' and a 'compressive' UMAT).

6.4 Results and Discussion

6.4.1 Comparison of Uniaxial Stress-Strain Curves: Bimat Model Simulations vs Experimental Results

The 'Tensile' and 'Compressive' UMAT models for each bimat model were used for uniaxial tensile and compressive simulations, with a single cube element (20-node quadratic brick type C3D20) model of dimensions 1mm x 1mm x 1mm. [Note: equivalence of C3D20 and C3D8I elements for these single element uniaxial simulations was checked by running tensile and compressive simulations for each element type with the 'bimat 37a' material model. The stress-strain results were found to be identical.] The stress-strain results of these uniaxial simulations could then be compared against the

experimental uniaxial results from chapter 3 in order to investigate the capabilities and limitations of the UMAT models, prior to use in bending simulations.

6.4.1.1 Comparison of Room Temperature Experimental Results with Bimat Models RTa and RTb

Figure 6-12 shows the uniaxial stress-strain simulation results for Bimats RTa and RTb, overlaid with the 'room temperature' experimental results from figure 3-30 in chapter 3.
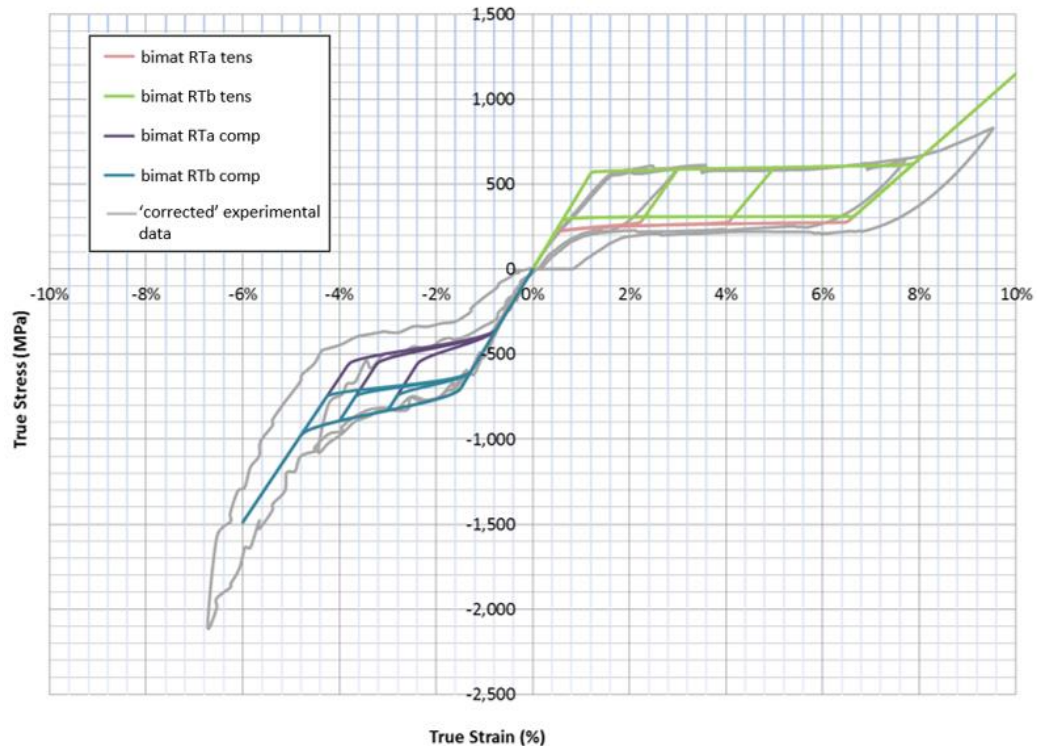
Figure 6-12: uniaxial tensile and compressive stress-strain results from simulations using bimat RTa and bimat RTb 'tens' and 'comp' UMAT material models, overlaid with 'corrected' experimental results from room temperature testing of NiTi#1 wire material (from figure 3-30). For simulation results, strain is found from 'E22', tensile stress is 'max principal stress' and compressive stress is 'min principal stress'.

With reference to figure 6-12, a number of interesting observations can be made about the ability of the UMAT material model to represent the loading stress-strain behaviours of the material.

For initial tensile loading, the experimental data shows effects of R-phase, with reduced modulus beyond 0.4 % strain, while the UMAT simulations show a constant modulus (straight line) up to the start of the upper stress plateau. This means that the UMAT models overestimate the tensile stress for strains between 0.4 % and 1.6 %. For initial compressive loading, there is a very good match between the experimental results and the UMAT simulations, as both show a linear response with similar moduli.

For the tensile loading plateau, the simulation results show a close match to the experimental results between 1.6 % and 7.6 % strain in loading. The UMAT models have a slightly longer plateau (1.2 % to 7.8 % strain) and do not show the 'sawtooth' effect seen in the experimental results (attributed to nucleation of new phase change fronts in the material), but give a good simplified representation of the stress-strain behavior here. For the compressive loading plateau, there is a good match between simulation and experimental results up to 4 % strain. Beyond this, the experimental results show increased stress with martensite elasticity, while the model continues on its plateau up to 4.8 % strain. This stress-strain path for the model was chosen to allow a good compromise in representing the loading and unloading material behaviours using the 'Elasticity' UMAT model in Abaqus. The result is that the model has lower compressive stress values in loading beyond 4 % strain than the experimental material.

The 2nd (martensite) tensile loading modulus of the UMAT models shows a higher modulus in loading than the experimental results, meaning that the simulation model will have higher stresses beyond 8 % strain than the experimental material. This simulation modulus comes from the 'E_M' input parameter, which is required to represent both the loading and unloading paths beyond the upper plateau for the 'Elasticity' UMAT model. The E_M value was therefore chosen as a compromise between loading and unloading values. This compromise could have been avoided by using the 'Plasticity' UMAT model (implemented by specifying additional parameters in the

Abaqus UMAT), which allows the loading path beyond the plateau to be modeled separately from the E_M value used for unload modulus (see figure 6-3 above). While this approach would improve the match with experimental results at high strains (> 8 %), the unloading path at lower strains would actually become less accurate with a higher E_M value. For this reason, as well as the additional complexity and computational expense, it was decided that the 'Elasticity' UMAT model was the best choice.

The 2nd (martensite) compressive loading modulus was defined by the 'E_M' parameter, and this closely matches the slope of the experimental results beyond the end of the compressive loading plateau. Due to the longer plateau for the model, the simulated compressive stresses between 4 % and 6 % strain in loading are lower than those seen experimentally.

Unlike the loading behavior, the unloading behavior of superelastic nitinol is load-path dependent due to stress-strain hysteresis and plasticity. The uniaxial simulations were therefore unloaded from different maximum strains in order to investigate the load-path dependence capabilities and limitations of the UMAT models. With reference to figure 6-12, the unloading results are discussed below.

For the various tensile unloading paths, the simulation results show that the unloading modulus is path dependent, with lower unloading modulus towards a limit of E_M as maximum loading strain increases. This is a good qualitative representation of the general experimental behavior (see figure 6-10 above for a clear example), and is based on the constitutive model calculating the unload modulus from the percentage of austenite and martensite present at a given strain (with martensite increasing from 0 to 100 % along the loading plateau). In terms of unload modulus values, the simulation under-predicts the initial modulus from the end of the upper plateau (due to the compromise E_M value chosen to represent both load and unload martensite modulus), but over-predicts the unload modulus from 3 % strain. This over-prediction at lower strains

is considered to be due to the presence of R-phase in the experimental material at room temperature and at lower strains, which reduces the unload modulus for these conditions.

The UMAT model is also limited in its ability to represent the non-linearity of the unload moduli seen in the experimental results. Experimentally, it can be seen that the material unloads with an initial modulus which then reduces before reaching the unload plateau. The UMAT model, which unloads with a single linear modulus down to the unload plateau, will therefore under-predict the stress for a given strain. For this reason, bimats RTb and 37b were adjusted to maintain higher stresses in unloading (see figures 6-10 and 6-11 with explanation).

For strains beyond the end of the upper plateau, nitinol's unload modulus is increased (see figure 2-25 of Chapter 2). This leads to load-unload hysteresis even at strains beyond the load plateau, as can be seen in the experimental results of figure 6-12. However, for the simulation results, loading and unloading occurs without hysteresis and with modulus 'E_M' from all strains > 8%. It should be noted that the 'high strain hysteresis' behavior could have been captured using the 'Plasticity' UMAT model to give a different path for loading and unloading. However, a representative unloading 'E_M' value would have led to even greater over-prediction of unload modulus from 3% strain. It was therefore decided that the 'Elasticity' UMAT model was the best choice.

For compressive unloading, the simulations give a good representation of modulus values seen experimentally for unloading from within the load plateau region, with decreasing modulus relative to increasing transformation strain. Again, the experimental results showed non-linearity of unload modulus, which could not be represented by the UMAT model. This leads to under-prediction of the stress for a given strain, which was addressed by designing bimats RTb and 37b to maintain higher stresses in unloading.

As in tension, the compressive unload modulus of Nitinol is increased for strains beyond the end of the upper plateau, leading to load-unload hysteresis even at these high strains (where the material is fully martensite). Again, the 'elasticity' UMAT model does not capture this, with loading and unloading occurring without hysteresis and with modulus 'E_M' from all compressive strains > 4.8 %. This results in over-prediction of stress during unloading from high strains (> 4.8 %) using the UMAT.

For the tensile unload plateau, the experimental results show a common unload plateau for all unload paths starting on the upper plateau. However, for maximum strains beyond the upper plateau (> 7.8 %), the unload plateau is lower due to plasticity effects. This behavior is not captured by the UMAT models, which have a common unload plateau level regardless of the maximum loading strain. Note that this is also true when using the 'Plasticity' function of the built-in UMAT model, with unloading limited to a single unload plateau path, regardless of maximum strain.

For the compressive unload plateau, the UMAT effectively represents the common unload plateau for strains within the transformation region, but again cannot capture the reduced unload plateau behavior due to plasticity for unloading from higher strains (as seen experimentally for unloading from strains > 4 %).

In terms of the different unload plateau levels for the two different bimat models, bimat RTa was designed to closely match the experimental unload plateau values, while bimat RTb was given higher unload stresses in order to improve bending results (as will be seen later in this chapter).

For final tensile unload modulus, the experimental results show that the final unload modulus (following transformation strain loading) is lower than the initial austenite loading modulus. The UMAT models do not show this behavior, simply unloading with modulus 'E_A' from approximately 0.6 % strain. As a result, the UMAT model will have

higher stresses in this unloading strain range than the experimental material. In compression, again, the final unload modulus of the UMAT is identical to the initial loading modulus (defined by parameter 'E$_A$'), while the experimental results show a lower final unload modulus. The UMAT models therefore give higher compressive stresses for unloading strains < 1.2 %.

Both in tension and compression experimental results, there is some residual strain due to plasticity for material unloading from beyond the upper plateau. The 'Elasticity' UMAT simulations, however, show full strain recovery for all unload paths. The use of the 'Plasticity' UMAT model would give permanent set in the high strain history results, but this was not used for reasons stated above.

6.4.1.2 Comparison of 37⁰C Experimental Results with Bimat Models 37a and 37b

Figure 6-13 shows the uniaxial stress-strain simulation results for bimats 37a and 37b, overlaid with the '37 C' experimental results from figure 3-28 in chapter 3. The previous analysis of capabilities and limitations of the 'room temperature' UMAT models (with reference to figure 6-12) largely applies to the 37 C material results seen in figure 6-13. Again, the same key limitations of the UMAT are seen:

- Inability to represent non-linear 'elastic' loading and unloading paths, including R-phase effects
- Inability to represent unload path effects from strains beyond the upper plateau (increased unload moduli, reduced unload plateaus)

For the '37C body temperature' case, there are however some small differences to the previous analysis worth noting.

In terms of initial loading tensile response, there is a good match between the models and the experimental results up to 0.8 % strain. Beyond this, the experimental path again shows non-linearity as it approaches the upper stress plateau.

For the compressive loading plateau, the UMAT results have a shorter plateau region (up to 4.4 % strain) than for the room temperature models (up to 4.8 % strain). This is because, when interpreting the 37ºC experimental results, the shorter upper plateau length provided a good compromise position for the 2nd (martensite) modulus (used to define loading and unloading paths at high strains for the 'Elasticity' UMAT model).

Figure 6-13 also clearly shows the differences between bimats 37a and 37b, with the latter having higher unload plateau values designed to maintain higher unload stresses in order to improve unload bending results (shown later).
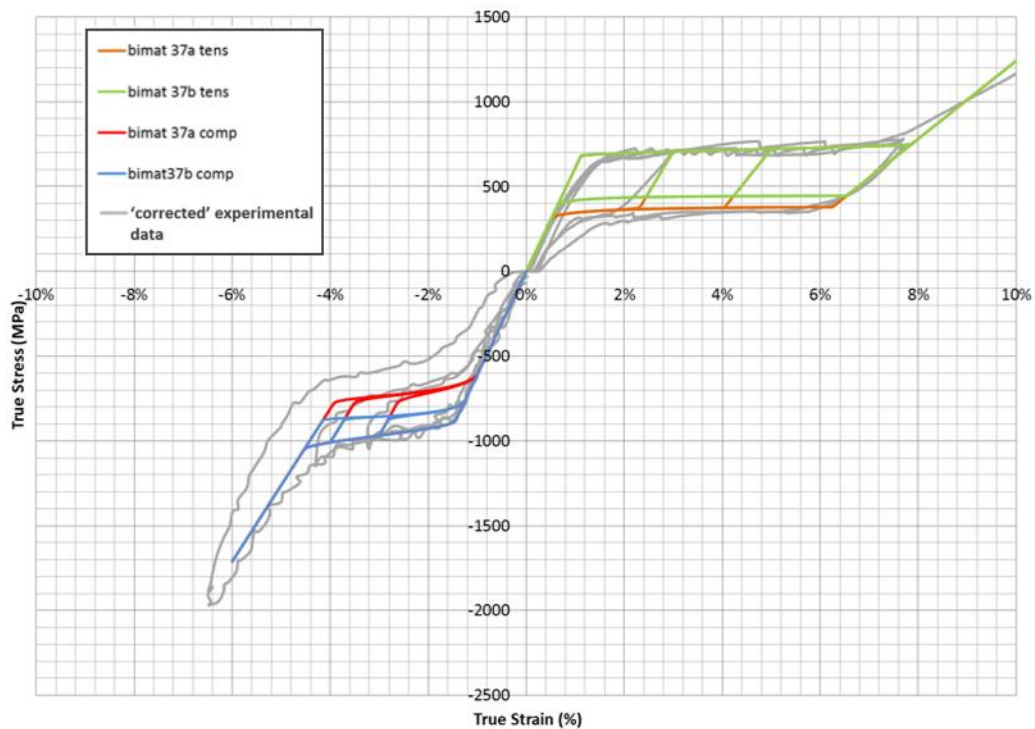
Figure 6-13: uniaxial tensile and compressive stress-strain results from simulations using bimat 37a and bimat 37b 'tens' and 'comp' UMAT material models, overlaid with 'corrected' experimental results from 37 C testing of NiTi#1 wire material (from figure 3-28). For simulation results, strain is found from 'E22', tensile stress is 'max principal stress' and compressive stress is 'min principal stress'.

6.4.1.3 Simulation of Uniaxial Δε Cycling During Unloading with Bimat 37a

A further uniaxial study was performed using the '37a' bimat model, in order to investigate the ability to represent small Δε cycling behavior during unloading. Figure 6-14 shows the UMAT results overlaid with the experimental stress-strain plots from figure 3-28.
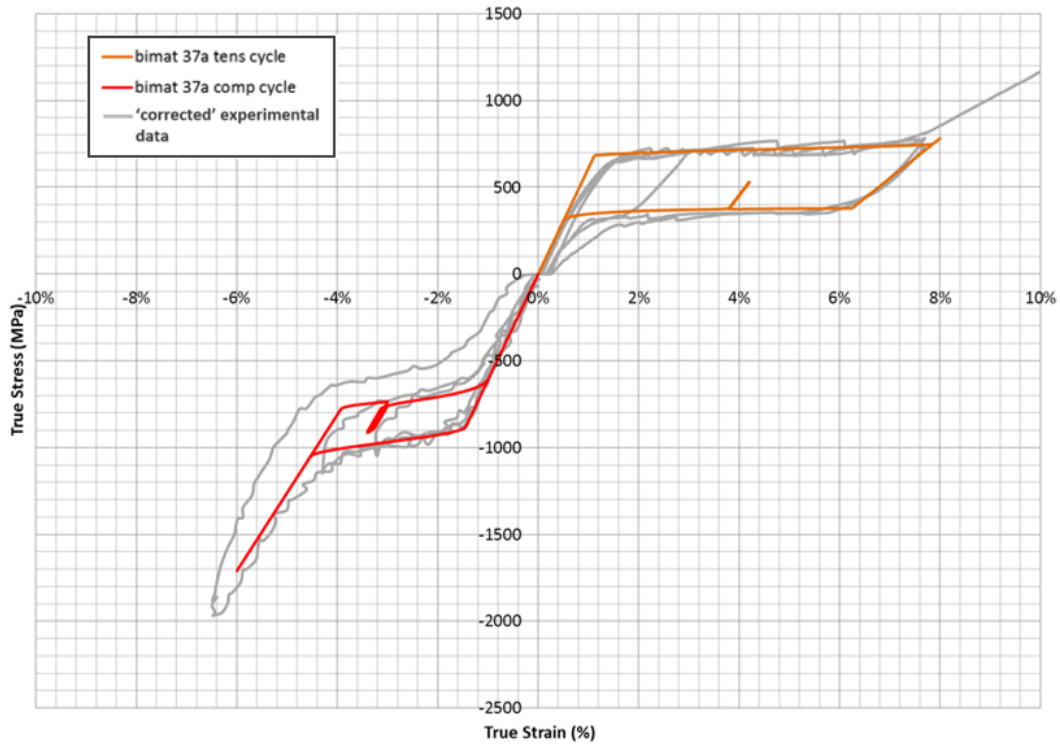
Figure 6-14: uniaxial tensile and compressive stress-strain results from simulations using bimat 37a 'tens' and 'comp' UMAT material models, with simulation of 0.4 % ΔΕ cycling (no. of cycles = 3) during unloading ('from below'). The simulation results are overlaid with the 'corrected' experimental results from 37 C testing of NiTi#1 wire material (from figure 3-28)

The 'cycling modulus' is an important characteristic for material performance as it relates to the in-vivo pulsatile loading behaviour of a stent component. The simulation results give the following values for tensile and compressive modulus using the bimat 37a UMAT models:

- Tensile cycling modulus = 37.8 GPa
- Compressive cycling modulus = 50 GPa

As expected, these values are between the austenite modulus 'E_A' and martensite modulus 'E_M' parameter values for each case.

The following experimental values were reported in Table 6-2 for uniaxial $\Delta\varepsilon$ cycling at 37 C:

NiTi#1 Result Parameter @ 37 C (experimental)	Tension	Compression
Cycling modulus for 0.4% $\Delta\varepsilon$ load-unload from lower plateau	40 GPa (for 0.4 % $\Delta\varepsilon$, 4 % mean ε during unload from 8 % max ε)	55 GPa (for 0.4 % $\Delta\varepsilon$, 3.2 % mean ε during unload from 6 % max ε)

Comparison of the simulation moduli with the experimental values from table 6-2 show a good match, with the simulation results being slightly lower (approximately 5.5% and 10% lower modulus for tension and compression respectively) and therefore conservative if the models were applied to in-vivo device simulations for fatigue analysis). In terms of cycling modulus, then, the UMAT models represent the material well. It should be noted, though, that the compressive simulation is cycling between higher stress levels than would occur experimentally, where the material unload plateau from 6% strain is at a lower stress level.

Qualitatively, it is interesting to see that the simulated compressive cycling shows a very small hysteresis loop, which was also seen in the experimental results (see chapter 3, figure 3-27). (Note: in the simulation result of figure 6-14, the upper plateau of this small hysteresis loop is seen to start at the same stress as specified for the 'start of transformation loading' parameter.) The tensile simulation, meanwhile, shows only

linear elastic behavior for 0.4 % $\Delta \varepsilon$, as would be expected from results in chapters 2 and 3. These results show that the bimat 37a UMAT models can give a good representation of the $\Delta \varepsilon$ cycling stiffness that is important for in-vivo nitinol stent performance.

The bimat 37b UMAT models would also be expected to capture this cycling modulus behavior, as they use the same E_A and E_M parameter values as bimat 37a. However, the 37b model will cycle between higher stress levels and will be limited to smaller cyclic $\Delta \varepsilon$ levels before exhibiting hysteresis, due to the smaller load-unload tensile and compressive hysteresis loops for bimat 37b (see figure 6-13). The limited $\Delta \varepsilon$ levels should not be a problem for modeling ring stent components, where maximum $\Delta \varepsilon$ levels are expected to be $\leq 0.2\%$.

6.4.2 Validation of 'Bimat' Material Models: Bending Simulations vs Experimental Results

Having determined suitable input parameters for the 'bimat' material models from uniaxial data, it was then important to assess the validity of these models (which are based on the Aurrichio-Taylor constitutive model for Nitinol implemented in Abaqus) to represent NiTi#1 stent wire material under loading conditions relevant to its in-service use. This assessment was focused on the following criteria:

- Ability of material models to represent Load-Deflection behavior in bending
- Ability of material models to represent strains in bending (particularly for large deflections and during unloading)

These criteria are important indicators of a material model's ability to represent radial force and strain state for fatigue analysis in stent simulations.

Load-deflection and Strain-deflection results were therefore obtained from the 3-Point Bending simulations (using both 0.45mm and 0.14mm wire 3PB set-ups), and were compared against relevant experimental results from chapters 4 and 5. 'Free Bend' strain

distributions were also compared. The plots in this section show the overlaid simulation and experimental results for validation comparisons.

6.4.2.1 Room Temperature Material Models Validation

6.4.2.1.1 Load-Deflection Results Comparison for Room Temperature Material

Figure 6-15 shows the 0.45mm wire 3-Point Bend simulation load-deflection results for bimat RTa and bimat RTb (using the model set-up shown in figure 6-1), overlaid with 'room temperature' (23 C) experimental results from chapter 4 (figure 4-5). Table 6-7 then shows key parameters extracted from the results in figure 6-15, for comparison of the bimat models with the experimental material.
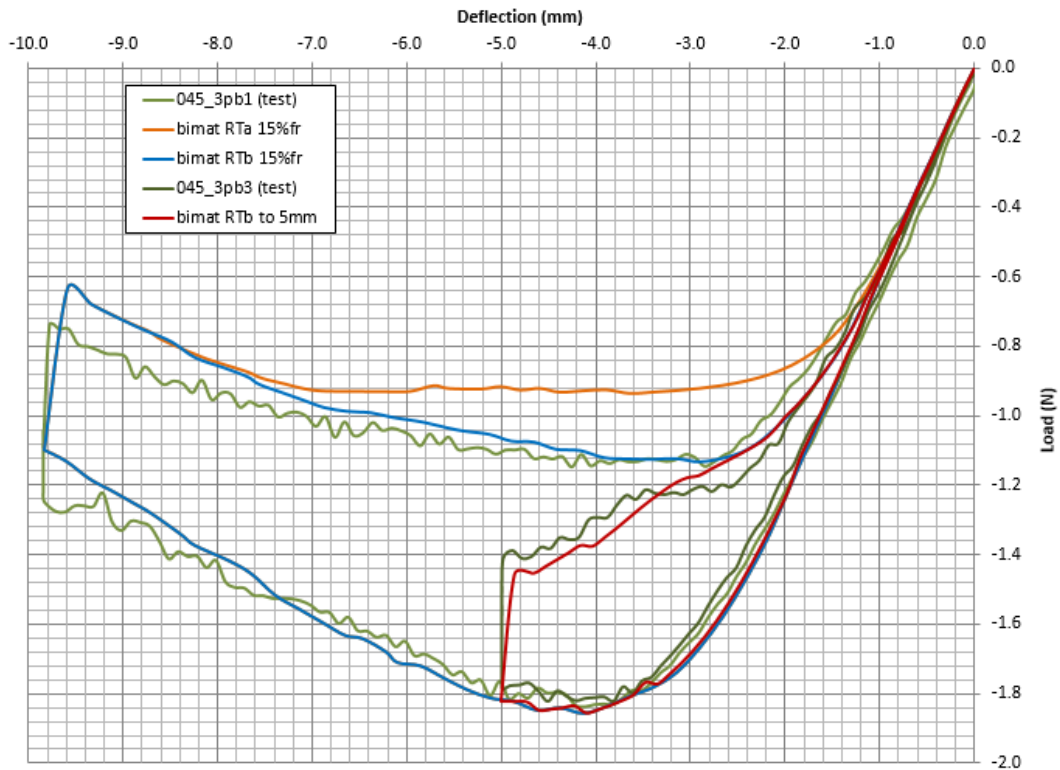
Figure 6-15: Load-deflection results from 0.45 mm wire 3-Point Bend simulations using bimats RTa and RTb, overlaid with experimental results from chapter 4.

Parameter	Experimental value	Bimat RTa value	Bimat RTb value
Initial 'austenite' bend stiffness (N/mm)	0.6	0.6	0.6
Load plateau force (N)	1.8	1.84	1.84
Load plateau start deflection (mm)	3.8	4	4
Load drop due to friction @ 5mm deflection (mm)	0.4	-	0.38
Load drop due to friction @ 9.8mm deflection (mm)	0.5	0.48	0.48
Unload bend stiffness (from 5mm deflection) (N/mm)	0.133	-	0.113
Unload plateau force (from 5mm max deflection) (N)	1.22	-	No clear plateau
Unload plateau force (from 9.8mm max deflection) (N)	1.12	0.92	1.12
Unload plateau end deflection (mm)	2.8	2.6	2.6

Table 6-7: Parameters from experimental and simulated 'room temperature' 3-Point Bend Load-deflection test results for 0.45mm NiTi wire

It should be noted that the Load-deflection (L-d) validation results shown in figure 6-15 are for Nitinol material at room temperature, which is most relevant to compaction of a stent device (where the material is in loading). In-service deployment (involving unloading and cyclic reloading of the material) will be performed at body temperature (37 C), and L-d validation of 'body temperature' material models will be reported later in this chapter. However, it is still worthwhile considering the unloading response validation for the room temperature materials, as the same general capabilities and limitations in modeling the material's bending behavior will apply for both temperature cases.

From the results above, it can be seen that bimats RTa and RTb have identical behavior in loading, and give a good representation of the experimental material in bending when

loaded. Of particular importance to stent simulation is the good match for initial 'austenite' bend stiffness, as much of the material in a stent ring will act in-service at small bend deflections like these.

Between loading and unloading, the similarity in force drop for experimental and simulated results (both at 5 mm and 10 mm deflections) shows that the '15 % friction coefficient' 3-Point Bend model is effectively capturing the effects of friction on Load-deflection results.

During unloading from 9.8 mm deflection, it can be seen that bimats RTa and RTb initially follow the same L-D unload path (between 9.8 mm and 8 mm deflection). In this range, all material in the wire is unloading with martensite elasticity 'E_M', which is the same for both bimat models. At lower deflections, though, the unload L-d paths for the two models diverge. Bimat RTb, with its raised unload plateau stresses (see figure 6-12), follows a very similar L-D path to the experimental material, with identical unload plateau force of 1.12 N. Bimat RTa, however, plateaus earlier at a lower force, under-predicting the unload plateau force by approximately 18 %. This result shows that the limitations of the UMAT constitutive model in representing Nitinol's unload behavior (particularly the non-linear initial unload path of Nitinol – see figures 6-10 and 6-11) lead to under-estimation of forces exerted by the material during bend unloading. By increasing the lower plateau of the model in order to maintain higher stresses during unloading, this limitation has been compensated for with bimat RTb.

Simulation of unloading from 5 mm deflection was also performed using bimat RTb, to investigate whether it would also produce good validation results for a different loading history. As can be seen from figure 6-15 above, the 'bimat RTb to 5mm' curve compares well against the '045_3pb3' experimental curve, showing similar unloading stiffness (slope of initial unload curve). The simulated result does not exhibit the clear unload plateau seen in the experimental result between 3.5 mm and 2.6 mm deflections, but the

unloading forces are very similar at all deflections. In both the experimental and simulated results, load-history dependence of unloading force can be seen (for example, compare red vs blue unloading plots and dark green vs light green unloading plots at 3.5 mm deflection in figure 6-15). This load-history dependence could have important implications in terms of recommended procedure for stent grafts, where in-situ loading (collapse) and unloading (re-opening) of stent rings could provide increased radial force compared to initial force after unsheathing.

The bimat RTa and RTb material models were also applied to simulations of 0.14mm wire in 3-Point Bending, based on the set-up used in Chapter 4 (see figure 4-4). For the simulations, a single wire strand was used for 3-Point Bending, and then the Force results were multiplied by 10 to get the '10 strand equivalent' results for validation comparisons. Figure 6-16 shows the simulation results overlaid with the 'room temperature' (23 C) 0.14 mm wire experimental results from chapter 4 (figure 4-6). Table 6-8 then shows key parameters extracted from the figure 6-16 plots, for comparison of the Bimat models with the experimental material.

As with the previous results, the 0.14mm 3PB simulation results show identical behaviour in loading when using bimats RTa and RTb, with good representation of the experimental bending behaviour, including a close match in the initial 'austenite' stiffness. In unloading, excellent validation results are obtained for the 'bimat RTb' material, which closely follows the experimental results unload curve and again gives identical unload plateau force to the test material. The bimat RTa model again under-predicts the unloading force for intermediate pin deflections, by approximately 17 %.

From these results, the 'bimat RTb' model again shows the best comparison against experimental data in terms of Force vs. bend deflection. This material model compensates for limitations in the constitutive model by using raised unload plateau stress values.
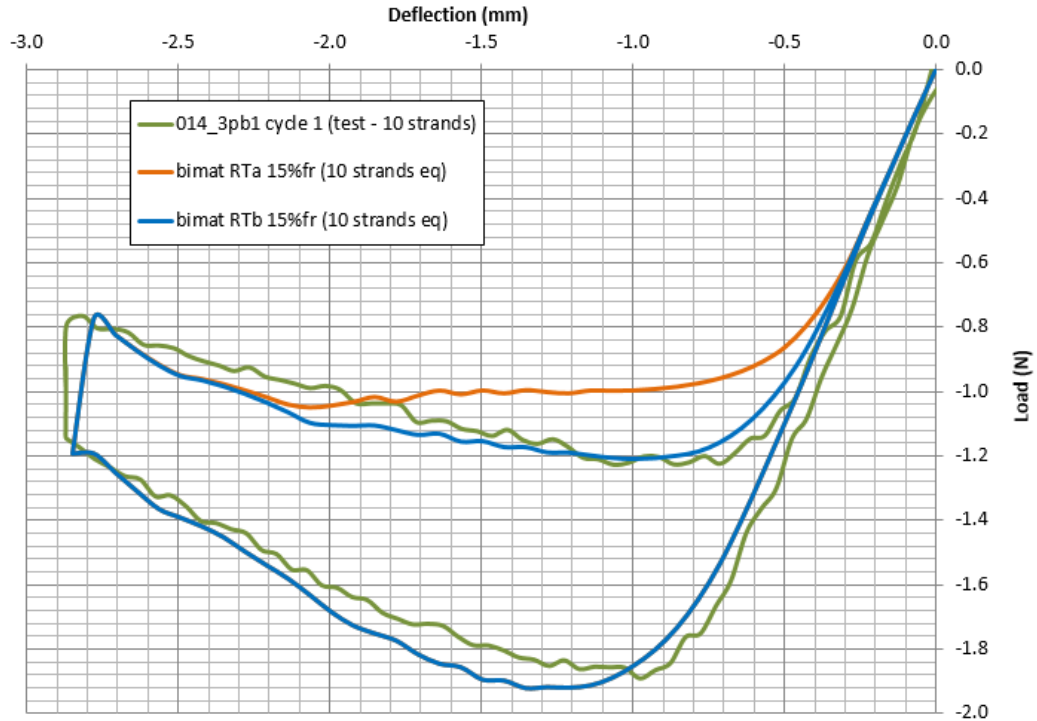
Figure 6-16: Load-deflection results from 0.14 mm wire 3-Point Bend simulations using bimats RTa and RTb, overlaid with experimental results at room temp from chapter 4.

Parameter	Experimental value (10 strands)	Bimat RTa value (10 strands eq)	Bimat RTb value (10 strands eq)
Initial 'austenite' bend stiffness (N/mm)	2.4	2.25	2.25
Load plateau force (N)	1.85	1.92	1.92
Load plateau start deflection (mm)	0.9	1.1	1.1
Load drop due to friction @ 2.9 mm deflection (mm)	0.36	0.4	0.4
Unload plateau force (from 2.9 mm max deflection) (N)	1.2	1.0	1.2
Unload plateau end deflection (mm)	0.7	0.9	0.8

Table 6-8: Parameters from experimental and simulated 'room temperature' 3-Point Bend Load-deflection test results for 0.14mm NiTi wire

6.4.2.1.2 Strain Results Comparison for Room Temperature Material

The results from chapter 5 allowed further validation of the 'room temperature' material models using Strain-deflection criteria. Figure 6-17 shows the 0.45 mm wire 3-Point Bend simulation Max Tensile Strain vs. deflection results for bimats RTa and RTb, overlaid with the 'room temperature' experimental DIC results from chapter 5 (figure 5-35).
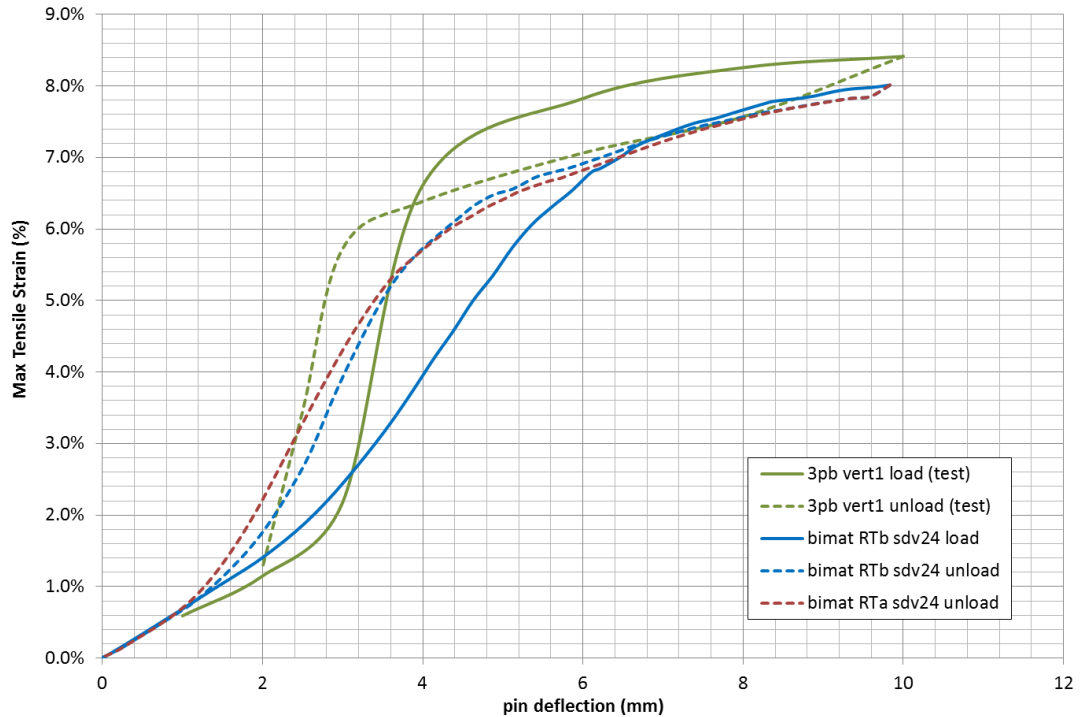
Figure 6-17: Max tensile strain vs deflection for 3-Point Bending of 0.45 mm NiTi wire during loading and unloading at room temperature. 'Bimat RTa' and 'bimat RTb' simulation results are overlaid with experimental results from chapter 5 (green plots).

In figure 6-17 above, the maximum values from the 'SDV24' output are plotted for the 'bimat' results. This output from the UMAT is defined as 'Equivalent uniaxial tensile total strain'. For the 3-Point Bend simulations performed here, this was found to be equivalent to 'E_{11}' (normal strain in the direction of the wire axis) for the apex cross-

section, which is the same definition as for 'E$_{xx}$' found from DIC testing. Therefore, SDV24 and E$_{11}$ results are used interchangeably in this chapter when reporting apex cross-section strain results from bending simulations.

With reference to the loading curves in figure 6-17 (solid lines), the simulations initially show a linear increase in strain with deflection up to 2.4 mm, as does the experimental result but with slightly lower gradient. Beyond this initial region, though, considerable differences emerge as bend deflections increase. The experimental material (green line) is seen to 'hinge' with significant local strain increase for a small bend deflection between 3 and 4 mm. For the simulation model (blue line), there is also an increase in strain-deflection slope beyond 3 mm deflection, but this is much less pronounced. This shows that the model does not represent the highly localized bending at the apex that occurred in the experiments, with the simulation instead distributing the deformation more evenly along the wire length throughout bending.

Figure 6-18 also demonstrates this, representing the change in apex curvature with bend deflection. For the simulation results plots in figure 6-18, apex strain gradient 'k' was found from measuring the maximum tensile and compressive strains on the wire surface at the apex cross-section and then calculating strain gradient using:

$$k = (\varepsilon_{tens\ max} - \varepsilon_{comp\ max}) / \text{wire diameter}$$

The experimental DIC results in figure 6-18 are taken from chapter 5 (selected results from figure 5-25). The experimental results show a sharp increase in apex curvature during loading between 3 and 4 mm deflection, while the simulation results show more gradual curvature increase.
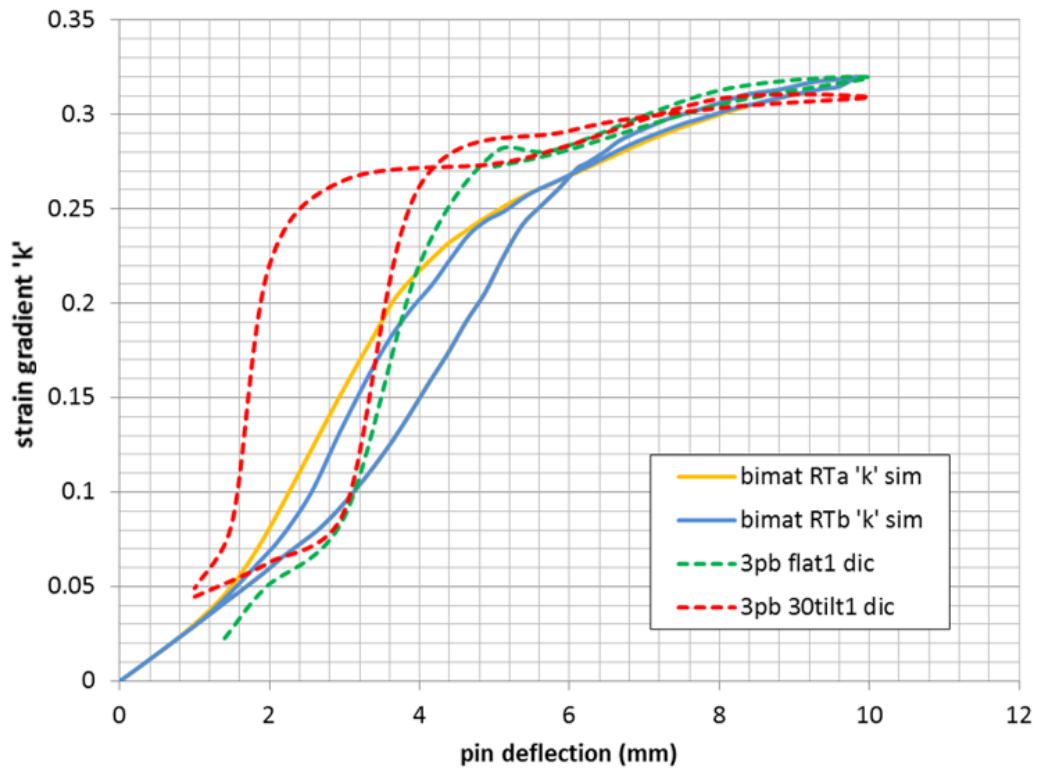
Figure 6-18: Plot of apex cross-sectional strain gradient 'k' vs 3-Point bend deflection for 0.45 mm NiTi wire at room temperature, showing the change of curvature of the wire bend apex during loading and unloading. The dotted lines show results from DIC testing, the solid lines show simulated results using bimats RTa and RTb.

Numerous unsuccessful attempts were made with different 'bimat' material parameters and different contact friction conditions to reproduce this highly localized bend behavior of the experimental nitinol wire. This inability to accurately represent the localized bending behavior of nitinol is considered to be a limitation of the 'UMAT' Auricchio-Taylor constitutive model built in to Abaqus. This can result in large underestimations of the maximum tensile strain during loading (for example, from figure 6-17 there is a difference of 2.6 % strain at 4 mm deflection during loading between simulation and test result).

With reference to figure 6-17, the maximum tensile strain at 9.8 mm deflection is 8 % for the simulations, with the experimental result giving 8.4 %. The bimat models

therefore give a reasonable approximation of the maximum strain at high 3PB deflections (beyond 8 mm), with error (underestimation) of around 5 %. Validation of the maximum strain at high bend deformations is important for use of material models in device compaction strain simulations.

For unloading, the Max tensile strain vs. deflection paths of the 'bimat' models in figure 6-17 actually match very closely to the experimental unload path from 9.8 mm down to 5 mm deflection, and below this give a closer comparison than in loading, despite the limitations in representing localized bending. The maximum difference in strain between the 'bimat RTa' simulation model and the experimental material during unloading is 1.6 % (at 3 mm deflection). This improved match in unloading is important for validation, as it is the strains during unloading of a stent component that will be relevant to determining mean strains for fatigue safety assessment. (Note that this validation is for room temperature material while in-vivo unloading of a stent will occur at 37 C. While the strain state of Nitinol wire is not thought to be highly temperature dependent, it would still be useful in future to obtain DIC strain history results for wire at 37 C for further validation. The 'room temperature' strain validation can, however, provide useful information regarding under- or over- prediction of strains using the Auricchio-Taylor constitutive UMAT material model in Abaqus.)

An important feature of the figure 6-17 plots is that the simulation models demonstrate load-unload hysteresis for strain at 'intermediate' bend deflections. This phenomenon is seen between deflections of 2 mm and 6 mm for the 'bimat' models, and between 2 mm and 3.8 mm for the experimental material, where the strain during unloading is higher than that during loading for a given deflection. This means that the wire is taking a different shape during loading and unloading for the same global deflection (seen also in figure 6-18, showing different apex curvatures for loading and unloading). This demonstrates that the simulation models can simulate the load-history effect on final strain state for Nitinol material in bending, which was discussed extensively in chapter 5.

Indeed, the bimat RTb model will be used later in this chapter to investigate different strain history paths, giving further evidence for the theories laid out in chapter 5.

Having considered 3-Point Bend strain history, a further useful validation is to consider the cross-sectional strain distribution for the wire at a given deflection. This is useful to validate the model's effectiveness in representing strain asymmetry of the material in bending. Figure 6-19 shows the simulated 'LE11' (logarithmic) strain distribution across the bend apex cross-section for the 0.45 mm wire at maximum deflection, using bimat RTb.
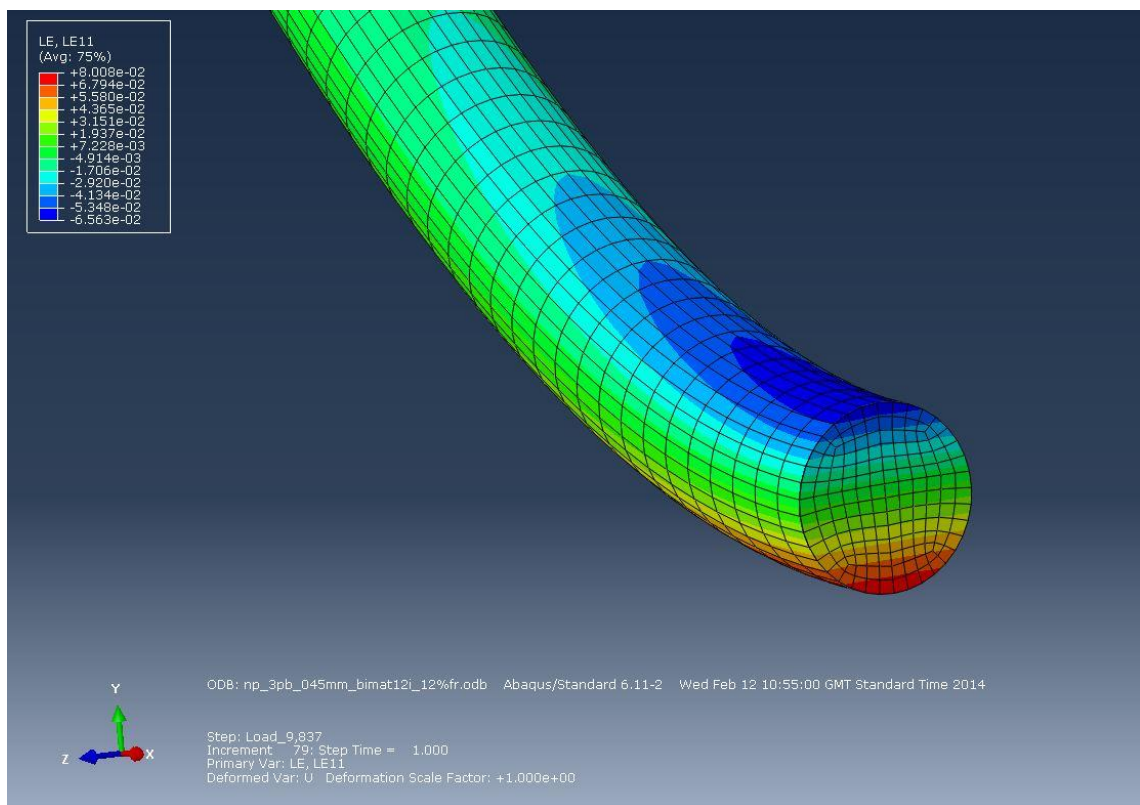
Figure 6-19: Simulation using 'bimat RTb' material model, of 0.45 mm wire at maximum 3-Point bending deflection (9.837 mm). The cut view shows the E_{11} strain distribution for the apex cross-section.

E$_{11}$ strains and 'y' distance from centerline were measured at all nodes around the wire surface of this cross-section and then plotted for comparison with the DIC overlay results of figure 5-22 from Chapter 5. The comparative results can be seen in figure 6-20 below.
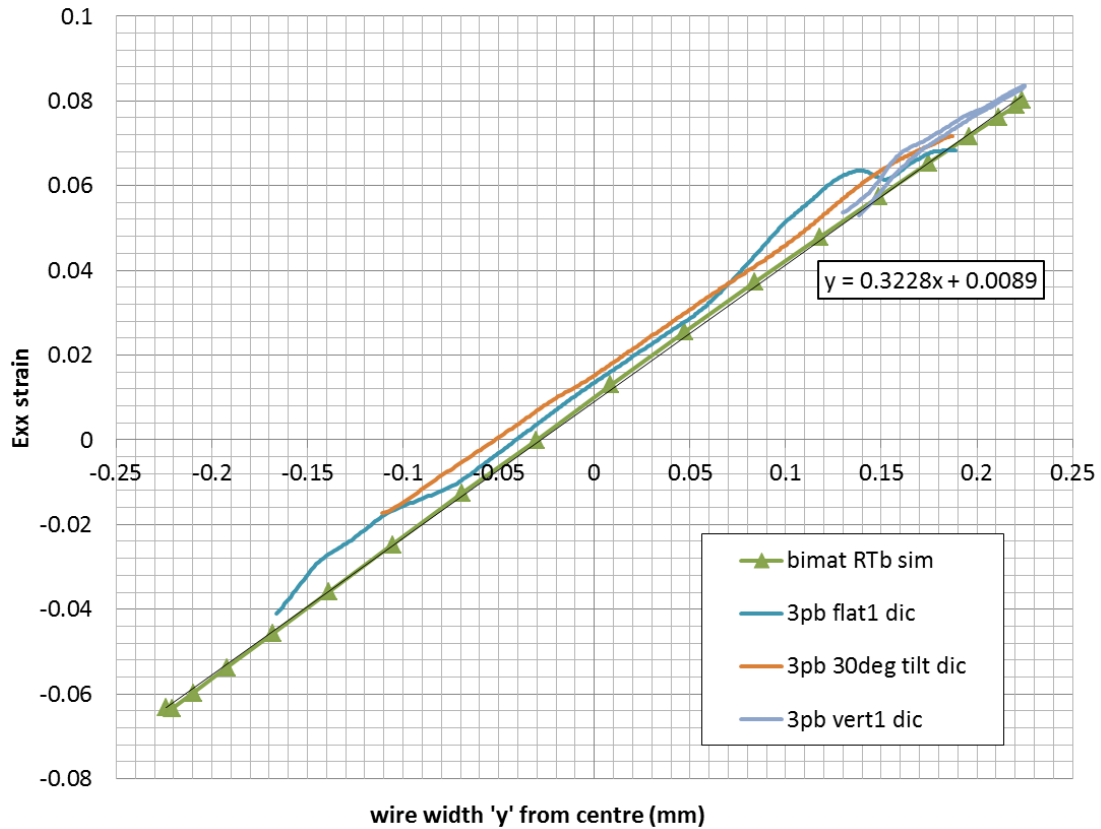
Figure 6-20: 0.45 mm wire 3-Point Bend simulation result, using bimat RTb, showing the bend apex cross-section strain distribution at 9.84 mm pin deflection, overlaid with the experimental DIC result from figure 5-22 (at max 3PB deflection)

Table 6-9 shows a summary of the key parameters from these results for comparison.

Parameter	Experimental DIC result	'Bimat RTb' simulation result
Strain gradient 'k'	0.31	0.3228
Neutral axis position	-0.048 mm	-0.03
Neutral axis pos. as % of wire diameter	10.66 %	6.66 %
Maximum tensile strain	8.4 %	8.0 %
Maximum compressive strain	Not measured (calculated from 'k' and NA position: 5.5 %)	6.3 %

Table 6-9: Bend apex surface strain distribution parameters from experimental and simulated 'room temp' 3-Point Bend test results, for 0.45mm wire at max deflection

The main finding from this comparison is that the Neutral Axis is less eccentric in the simulation model than in the experiment, showing less tensile-compressive strain asymmetry for the simulation. This can be attributed to the following features of the 'bimat' model compared to the experimental material (with reference to figure 6-12):

- 'E_A' tensile modulus is higher for bimat RTb
- 'E_M' 2nd loading modulus is considerably higher in tension for bimat RTb, while it is similar in compression to the experimental material
- The compressive load plateau is lengthened (extending to 4.8 % strain) in compression for bimat RTb

These features result in higher internal tensile stresses and lower internal compressive stresses than in reality for a given bend curvature, meaning less stress asymmetry and a more central Neutral Axis position. As a result, the 'bimat' model will under-predict maximum tensile strain and over-predict maximum compressive strain for large deflection bending.

The strain gradient 'k', indicating bend curvature, is very similar for the experimental and simulation result. The slightly lower 'k' value in the experiment suggests that

curvature was more evenly distributed at large deflections for the experimental material in 3-Point Bending.

Another strain validation of the 'bimat RTb' material model was performed using the 'Free Bend' strain results from Chapter 5 for comparison. Here, FEA was used to simulate the 0.45 mm wire bent into a constant curvature. A 'Python' script was developed by Martin van Zyl and David Bow at University of Strathclyde to perform the pre-processing for this bending simulation. Figure 6-21 shows the 'Free Bend' wire simulation with results for E_{33} (strains in the (axial) z direction).
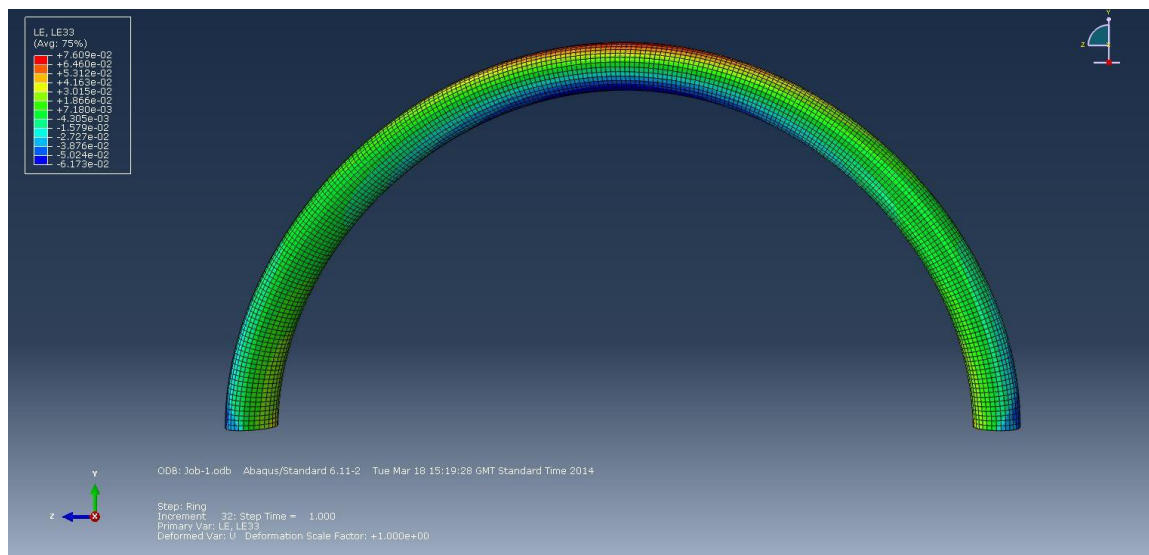
Figure 6-21: 'FreeBend' simulation for 0.45 mm wire (constant radius of curvature R=3.4 mm) showing E_{33} results (normal strain in z-direction). Note: plotting of max principal strain would show even strain distribution along the bending wire, due to the constant curvature 'R'.

Figure 6-22 shows a cut view of the central cross section of this simulated 'Free Bend' wire, showing the E_{33} strain distribution for the cross-section. From these simulation results, the E_{33} axial strains and 'y' distance from centerline were measured at all nodes around the surface of the central cross-section and then plotted for comparison with the

DIC overlay 'Free Bend' results from figure 5-75 of Chapter 5. Figure 6-23 shows the 0.45 mm wire simulation and experimental strain results for Bend Radius R = 3.4 mm. Table 6-10 then shows a summary of the key parameters from these results for comparison.
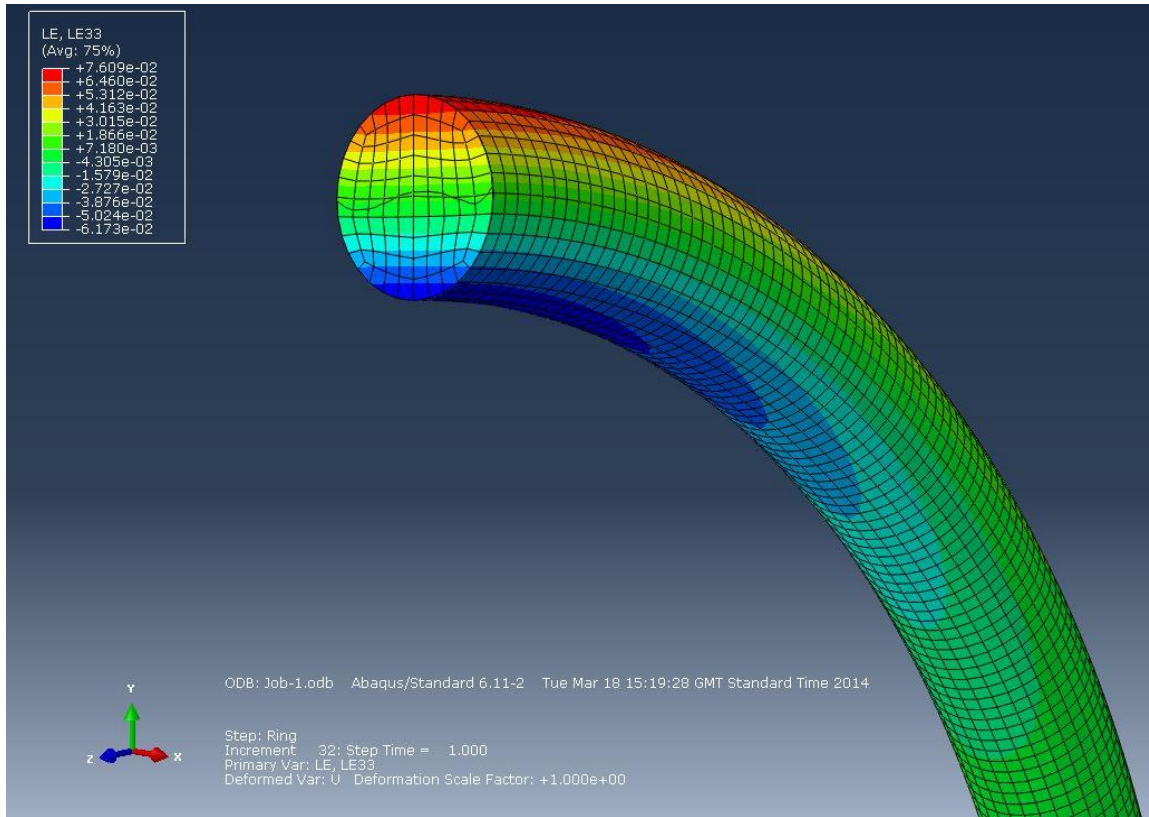
Figure 6-22: 0.45 mm wire at bend radius R = 3.4 mm, cut to show E$_{33}$ strain

distribution for central cross-section. 'Bimat RTb' material model has been used here.
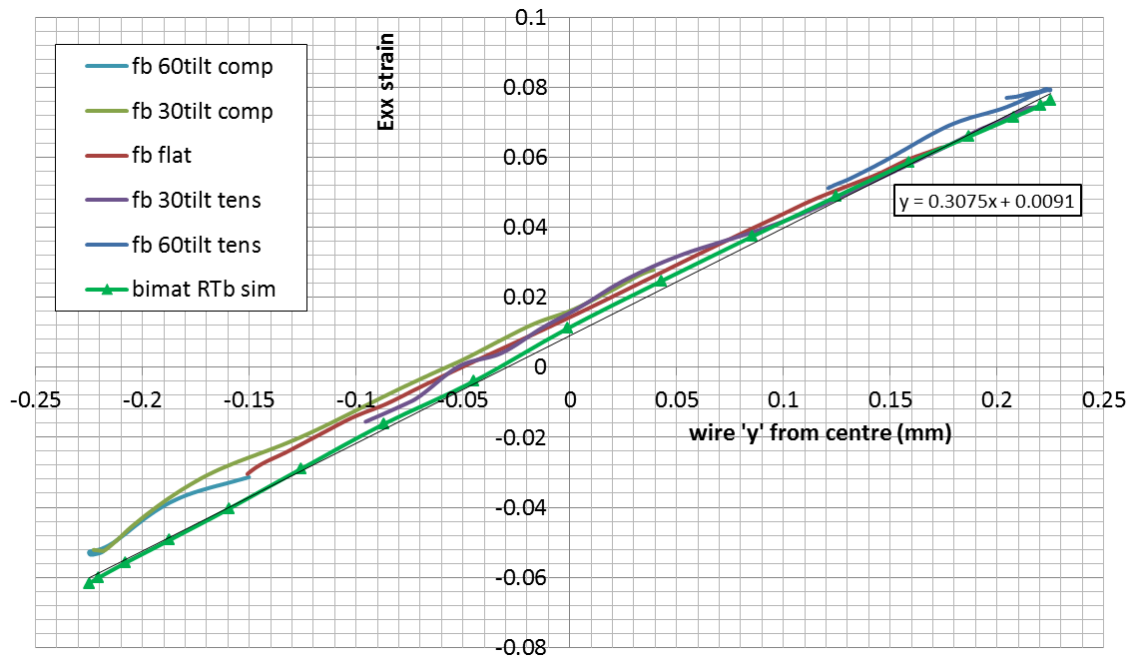
Figure 6-23: 0.45 mm wire 'Free Bend' simulation result, using bimat RTb, showing the bend apex cross-section strain distribution for bend readius R = 3.4 mm, overlaid with the experimental DIC result from figure 5-75 of chapter 5

Parameter	Experimental DIC result	'Bimat RTb' simulation result
Strain gradient 'k'	0.295	0.3075
Neutral axis position	-0.048 mm	-0.03 mm
Neutral axis pos. as % of wire diameter	10.66 %	6.66 %
Maximum tensile strain	8.0 %	7.61 %
Maximum compressive strain	5.3 %	6.17 %

Table 6-10: Cross-sectional surface strain distribution parameters from experimental and simulated 'Free Bend' test results for 0.45 mm wire at bend radius R = 3.4 mm, at room temperature

From the results comparison, it is seen that the 'bimat RTb' simulation gives a value for 'k' that is slightly higher. This suggests some inaccuracy in the FEA simulation results, as the experimental value for 'k' (0.295) closely matches the value found from beam-bending theory using k = 1/R (= 0.294). Indeed, the surface strain values in figure 6-23 taken from the simulation results do deviate slightly from the straight trend-line, showing some deviation from the expected 'planar' bending expected from the theory.

However, the more significant difference between experimental and simulation results is seen in the Neutral Axis position. As with the 3-Point Bend case, there is again less tensile-compressive strain asymmetry in the 'bimat RTb' simulation than for the experimental wire in bending. As a result, the model would be expected to under-predict maximum tensile strain and over-predict maximum compressive strain for compaction simulations.

From these comparisons of FEA bending simulations and experimental results, a detailed understanding of the capabilities and limitations of the 'room temperature' bimat models (RTa and RTb) in representing Vascutek's NiTi#1 wire at room temperature has been gained, with assessment of the ability of the underlying 'Auricchio-Taylor' constitutive model to represent key bending behaviours of the material. Attention will now turn to the 'body temperature' material models.

6.4.2.2 Body Temperature (37 C) Material Models Validation

The bimat 37a and 37b material models were applied to simulations of 0.14 mm wire in 3-Point Bending, based on the set-up used in Chapter 4 (see figure 4-4). Here, a single wire strand was used in the simulation, and then the Force output results were multiplied by 6 to get the '6 strand equivalent' results for validation comparisons. Figure 6-24 shows the simulation results for Load-deflection overlaid with the experimental results for 0.14 mm NiTi wire in 3-Point Bending at 37 C from chapter 4 (figure 4-7). Table 6-

11 then shows key parameters extracted from the results in figure 6-24, for comparison of the models with the experimental material.
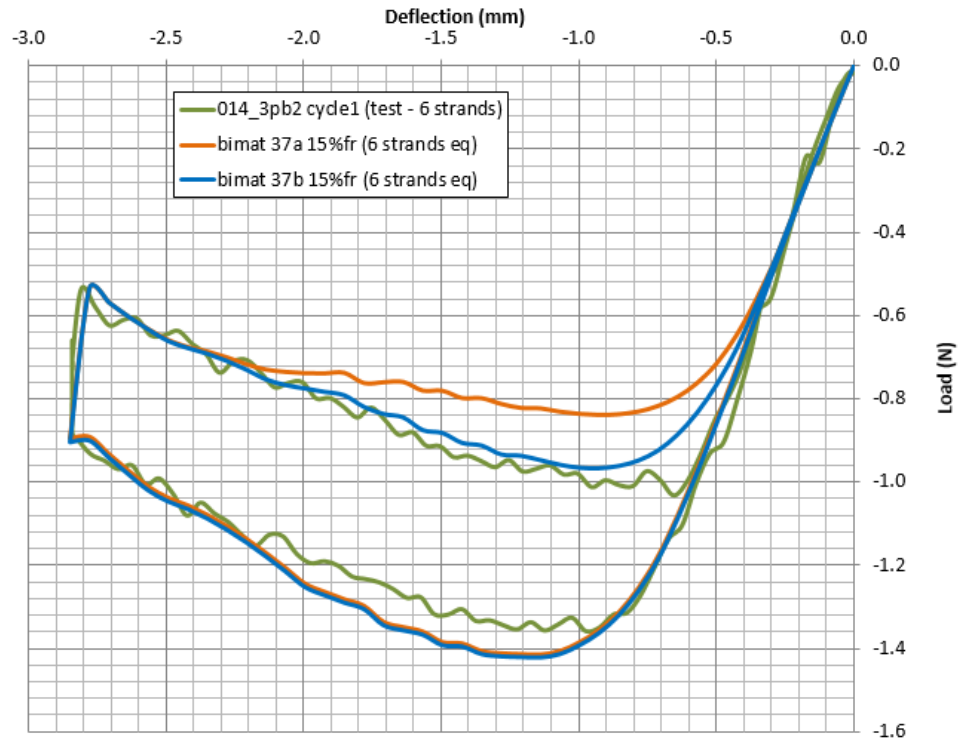
Figure 6-24: Load-deflection results from 0.14 mm wire 3-Point Bend simulations using bimats 37a and 37b, overlaid with experimental results at 37 C from chapter 4.

Parameter	Experiment value (6 strands)	Bimat 37a value (6 strands eq)	Bimat 37b value (6 strands eq)
Initial 'austenite' bend stiffness (N/mm)	1.8	1.7	1.7
Load plateau force (N)	1.36	1.41	1.41
Load plateau start deflection (mm)	0.9	1.1	1.1
Load drop due to friction @ 2.85 mm deflection (mm)	0.34	0.34	0.34
Unload plateau force (from 2.85 mm max deflection) (N)	1.0	0.84	0.96
Unload plateau end deflection (mm)	0.6	0.8	0.9

Table 6-11: Parameters from experimental and simulated 3-Point Bend test results for 0.14 mm NiTi wire at 37 C

Considering the results above, the bimat 37a and 37b models give a good representation of the L-D bending response in loading, showing similar initial stiffness and forces at large loading deflections, with slightly higher 'plateau' forces than the experimental results. The good match for bend stiffness at 37 C is important in terms of stent in-vivo loading simulations, as the material in a stent will be loading and unloading with small cyclic bend deformations in-service.

The force drop between load and unload matches well, showing that the 15% contact friction coefficient used for simulation again gives a good representation of contact conditions between wire and 3-Point Bend rig pins.

In unloading, very good validation results are obtained for the 'bimat 37b' material model, which closely matches the unload curve and unload plateau force of the test material. At unload deflections between 0.7 mm and 0.4 mm the comparison is poorer, with the bimat 37b model under-predicting forces. This may be due to the inability of the constitutive model to represent the localized bending behaviour of the material so that it does not show the sharp change in unloading stiffness seen for the experimental material. Generally, though the bimat 37b model would be very useful for predicting in-vivo unloading forces for a NiTi#1 wire stent component in bending. The bimat 37a model is less well matched, under-predicting the unloading force for intermediate deflections by approximately 16%. (It should be noted that bimat 37a still gives a closer match to the experimental results than 'unimat 37a' seen in figure 6-5.)

From these results, the 'bimat 37b' model shows the best validation against experimental data in terms of Force response to bend deflections in loading and unloading. As with the 'bimat RTb' model discussed previously, this material model compensates for limitations in the constitutive model by using raised unload plateau stress values (as shown in figure 6-13).

The above validation comparisons, both for 'room temperature' and 'body temperature' material models, have shown good results compared to experimental data, particularly in terms of Load-Deflection response. A standard method was used to determine suitable parameters for these models, as was detailed in table 6-4. This method is therefore recommended for future use in interpreting uniaxial tensile and compressive stress-strain results to obtain 'bimat' material model input parameters.

6.5 Further Investigation of Bending Behaviours using Bimat Models

Having performed validation for the 'bimat' material models and gained an understanding of the capabilities and limitations of the underlying constitutive model in representing bending behavior of NiTi#1 wire, it was decided to use FEA simulations with these models to further investigate the material behaviours discussed in chapters 4 and 5. Of particular interest were the load history effects on unloading strains and unloading forces, and the cycling behavior of Nitinol in bending.

6.5.1 FEA Investigation of Strain History for NiTi Wire at 37⁰C

Firstly, the strain history results from the 3-Point Bend simulation of 0.14 mm wire at 37 C were output. Figure 6-25 shows the strain-deflection results for bimats 37a and 37b.

In figure 6-25, each model exhibits a steeper unload path, with large strain recovery over a small deflection range (between 1.3 and 0.5 mm deflections), compared to a shallower loading path. This suggests more localized bending behaviour during unloading in the simulations, which is representative of the experimental behaviour seen in chapter 5 (see green unload plot in figure 6-17). It would be useful in future to obtain experimental DIC results at 37 C in order to validate this strain history behaviour of the 'body temperature' material models.

Figure 6-25 also shows load-unload hysteresis for the simulations between 0.5 mm and 1.6 mm deflections, meaning these material models will demonstrate load-history dependence of final strain state for bending simulations.
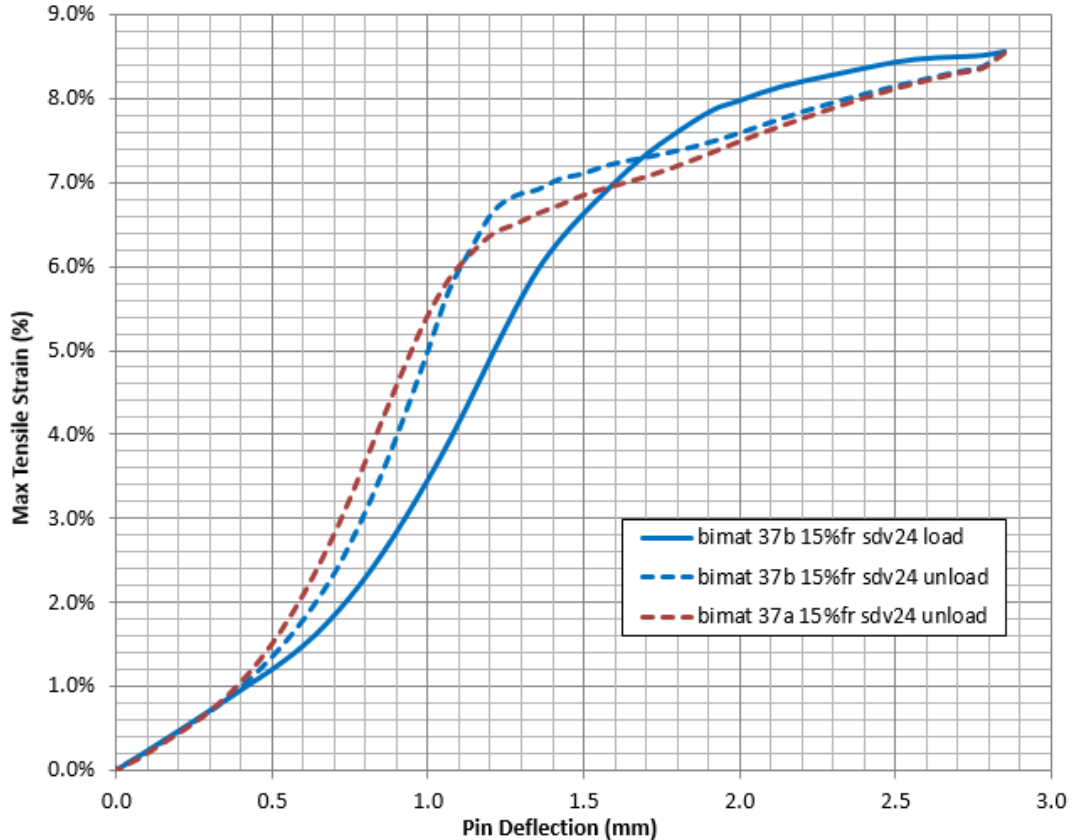
Figure 6-25: Strain-deflection results from simulation of 0.14 mm wire in 3-Point Bending at 37 C, using bimats 37a and 37b.

6.5.2 FEA Investigation of ΔD Cycling in Bending

Another important investigation was to simulate the 3-Point Bend testing reported in Chapter 4, section 4.4.4 for Δdeflection bend cycling during unloading at 37 C. The same cyclic bend deflections were used in the simulation as for the testing, and results were obtained to look at the Load-Deflection path of the material (figure 6-26) and also

the Strain-Deflection path (figure 6-27). This investigation is relevant to the bending behaviour of a Nitinol wire component as it will be deployed and cycled in-vivo.
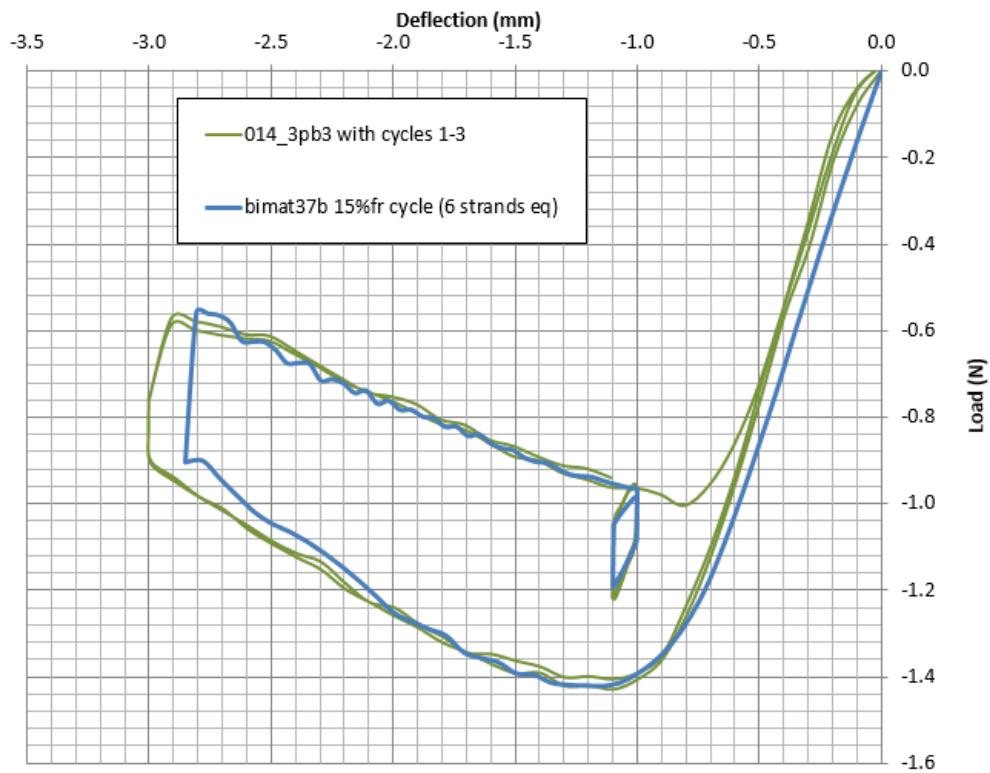
Figure 6-26: Load-Deflection results for 3-Point Bend simulation of NiTi wire (6 strands) at 37 C using bimat 37b model, with Δdeflection cycling (2 cycles) between 1.0 and 1.1 mm deflections during unloading. The simulation results are overlaid with the experimental results from figure 4-11 of chapter 4.

Figure 6-26 shows the Load-deflection results extracted from the simulation, overlaid with the experimental results from figure 4-11 of chapter 4 for comparison. As expected, the simulation shows the material reloading along a different path from its unload plateau path as ΔD cycling 'from below' commences. This re-load stiffness gives nitinol stents their in-vivo 'Radial Resistive Force' under cyclic loading by a vessel, limiting deformation.

The simulation results give a close match to the test results in terms of the Δdeflection bend cycling hysteresis loop shape, although it can be seen that the simulation is slightly underestimating the cyclic bending stiffness (seen by the gradients of the load and unload slopes). The lower bending stiffness (approximately 30% lower stiffness for the simulation, from average of loading and unloading slopes) is as expected from the previous discussion of the cycling moduli values from figure 6-14. As mentioned there, this is a conservative representation if the models were to be applied to in-vivo device simulations for fatigue analysis.

It should also be noted that figure 6-26 shows an excellent match between the loading and unloading plateau forces of the simulation and of this particular set of test results, again showing the validity of the input parameters for bimat 37b.

Figure 6-27 shows a plot of the max tensile strain vs. deflection for the wire in this simulation. The most important feature from this plot is that the 'reload' path for cycling during unloading is linear (with no hysteresis) and is different from the steep 'hinge unloading' path. This is important as it means the material does not 'hinge' during small $\Delta\varepsilon$ cycling, but instead loads and unloads elastically – with stiffness similar to the initial bending stiffness (see slope of cycling path). This means that the magnitude of $\Delta\varepsilon$ is limited for Δ deflection cycles, avoiding large $\Delta\varepsilon$ levels that could lead to early fatigue failure. This can clearly be seen in figure 6-27, where the change in strain between 1.1 mm and 1.0 mm deflections during 'hinge unloading' is 1 %, while the $\Delta\varepsilon$ for Δdeflection cycling between these same deflections is only 0.3 %.
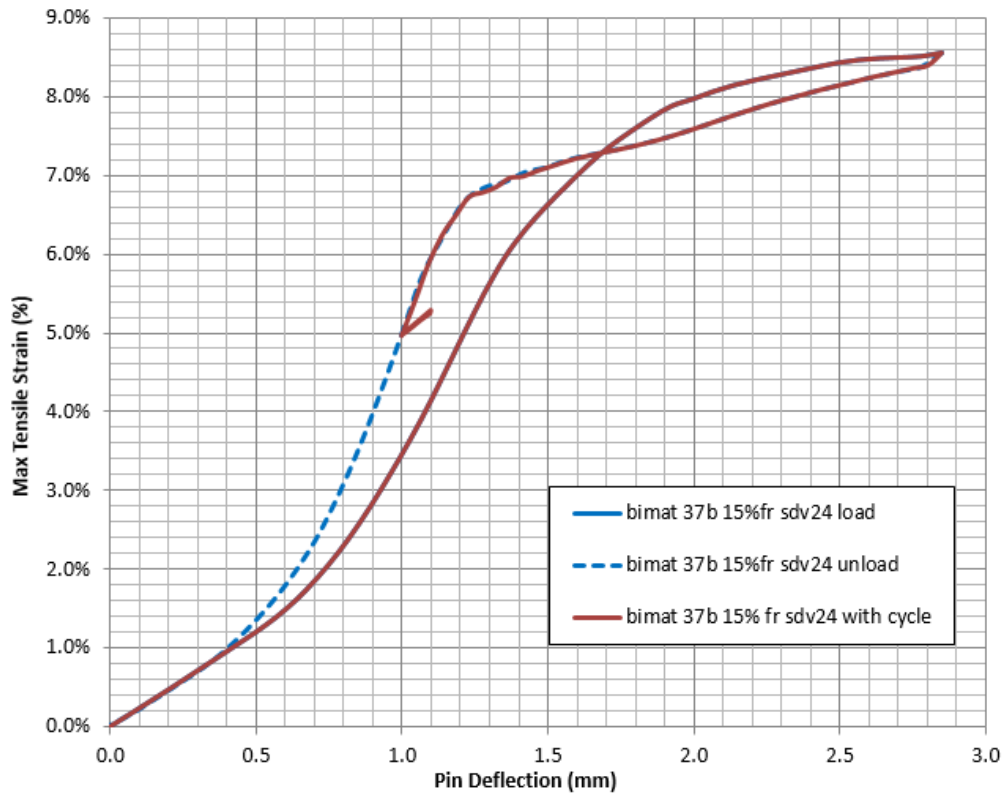
Figure 6-27: Strain-deflection results for 3-Point Bend simulation of 0.14 mm NiTi wire at 37 C using bimat 37b model, with Δdeflection cycling (2 cycles) between 1.0 and 1.1mm deflections during unloading

6.5.3 FEA Investigation of Load History Effects on Unloading Forces and Strains for Nitinol Wire in Bending

Using the room temperature 'bimat RTb' model, further investigation simulations were performed to provide supporting evidence for the 'strain history' discussion in section 5.5.3 of chapter 5. Figure 6-28 shows Strain-Deflection results for 0.45 mm wire in 3-Point Bending with different load-unload paths. These simulation results are overlaid with the experimental Strain-Deflection results from figure 5-35 in chapter 5.
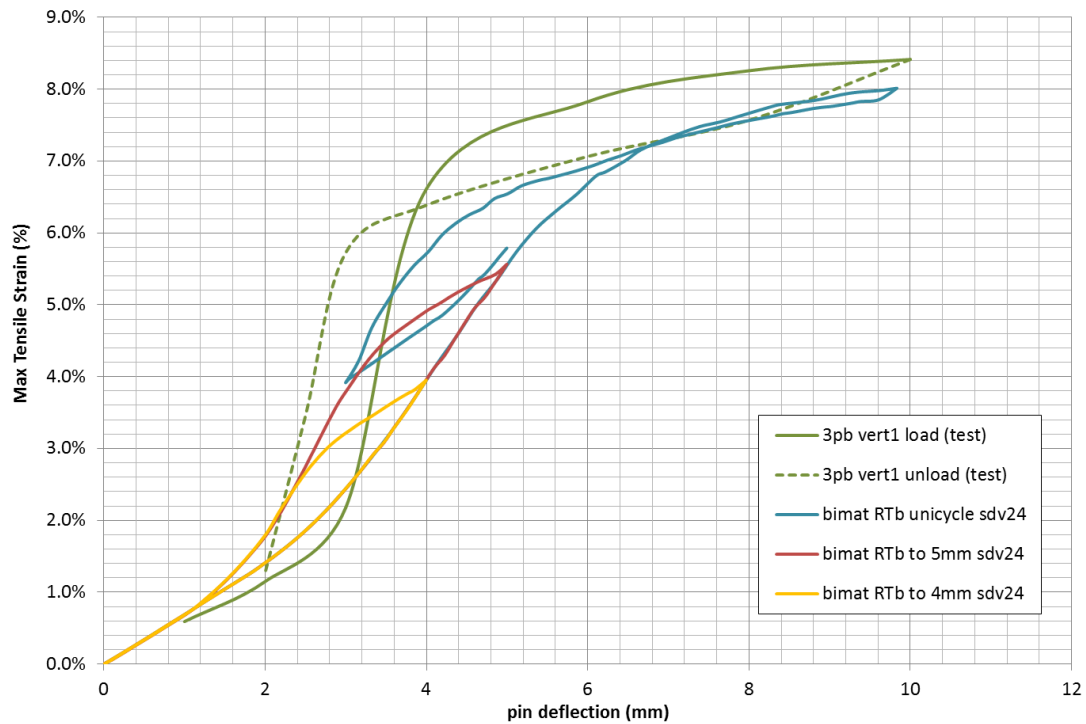
Figure 6-28: Strain-Deflection results from simulation of 0.45 mm wire in 3-Point Bending using bimat RTb, where simulations involve different load-unload deflections to investigate load-history dependence of strain paths. Simulation results are overlaid with the experimental Strain-deflection results from chapter 5 (green plot).

In chapter 5, the analysis of strain history effects involved plotting of 'expected' results for different load-unload deflections – see figure 5-70 of section 5.5.3. With reference to figure 6-28 above, the simulation results support these predictions in general terms, with the bending material following a unique Strain-Deflection unload path depending on the maximum deflection. For example, from figure 6-28 the maximum tensile strain during unloading at a deflection of 3.6 mm is 3.6 % for the yellow path (max load deflection = 4 mm) and 4.6 % for the red path (max load deflection = 5 mm). As discussed in Chapter 5, this behaviour is responsible for the load history effects on final strain state identified by van Zyl et al using FEA (ref 33).

Although the simulation captures this general behaviour, the less pronounced 'localised bending' behaviour compared to the experiment (seen in figure 6-28 by the shallower loading slope from 3 mm deflection and unloading slope down to 2 mm deflection) means that the load history effect on final strain state will be less pronounced for a small difference in maximum loading deflection.

The blue strain history path in figure 6-28 above shows a cycle involving re-loading from an intermediate deflection during unloading. As with figure 6-27 previously, this shows how the material re-loads elastically, limiting the $\Delta\varepsilon$ for a given Δdeflection. The slope of this elastic re-load path is similar to the elastic Strain-Deflection slopes (regions 1 and 5 in figure 5-35) of the experimental material, meaning that the simulation should give a good representation of $\Delta\varepsilon$ for a given small Δdeflection (for example, where $\Delta\varepsilon \leq$ 0.4 %). Beyond the 'elastic' re-load path of the blue line, the strain again starts to increase locally showing that 'hinge' deformation due to phase change is occurring. It can be seen from comparing the load-unload strain hysteresis loops of the simulation plots with the experimental plot in figure 6-28 that the simulation will over-predict the elastic $\Delta\varepsilon$ level prior to phase change (and localised bending) occurring. The experimental hysteresis loop and elastic deformation slope suggest that elastic strain during re-loading (and cycling) will be limited to $\Delta\varepsilon \leq 0.4$ %.

For the same 3-Point Bend load – unload simulations, the Load-Deflection results were plotted and overlaid with an experimental result from figure 4-5 in chapter 4. These results are shown below in figure 6-29, and are useful for investigating different load history paths of the material.
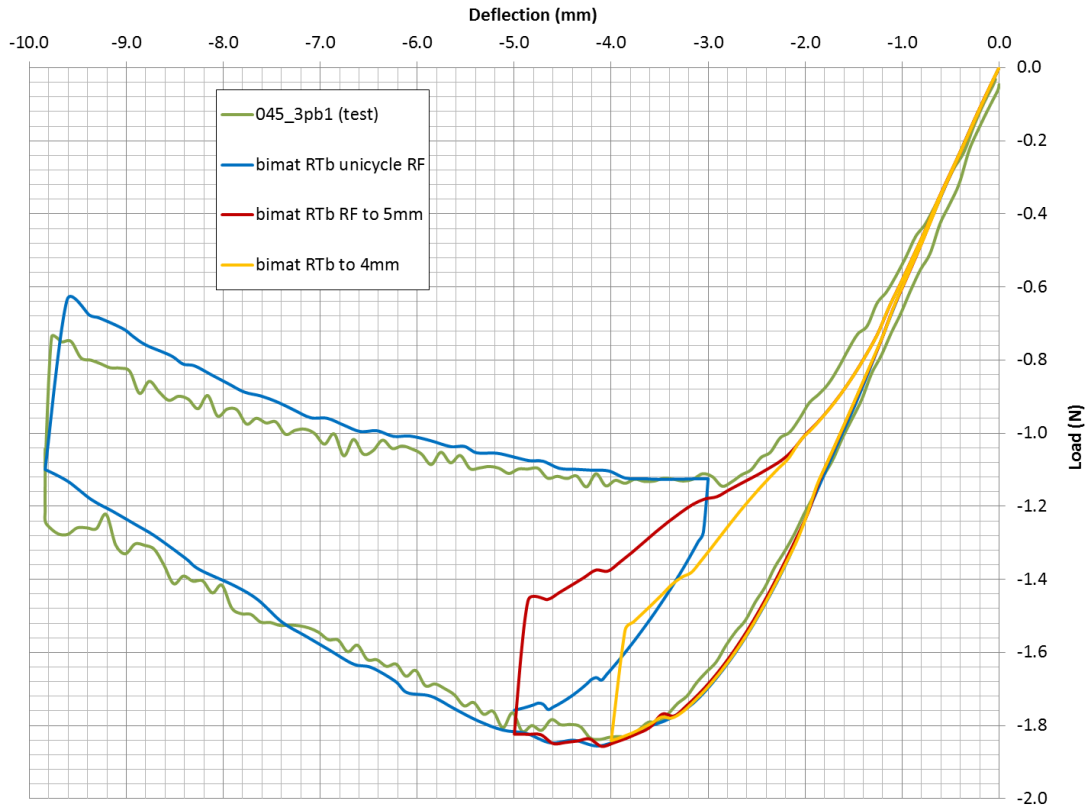
Figure 6-29: Load-Deflection results from simulation of 0.45 mm wire in 3-Point Bending using bimat RTb, where simulations involve different load-unload deflections to investigate load-history effects. Simulation results are overlaid with experimental Load-Deflection results from chapter 4 (green plot).

Of particular interest from figure 6-29 is the load-path dependency of the force during unloading, seen clearly from comparing the yellow, red and blue unloading paths at 3.5mm deflection. Each path shows a different force during unloading for this common deflection:

- yellow path (max deflection = 4 mm) shows force of 1.44 N
- red path (max deflection = 5 mm) shows force of 1.26 N
- blue path (max deflection = 9.83 mm) shows force of 1.12 N

This effect is considered to be due to the different stress state of the unloading wire in bending depending on the loading history, and could have important implications for

radial force (Chronic Outward Force) of a stent deployed in a vessel. The results suggest that collapsing and re-opening of an unsheathed ring stent during in-vivo re-positioning could actually increase its Chronic Outward Force. This load history effect on radial force would be an interesting area for future experimental investigation of Vascutek's Nitinol ring stents.

6.6 Discussion: Application of Material Models for Stent Component Simulations

In this chapter, the 'bimat' material modelling approach has been successfully applied to 2-D planar bending simulations involving minimal shear forces, in order to overcome limitations of using a single asymmetric UMAT 'unimat' material model for Nitinol. This 'bimat' method allows more definition to be given for compressive material modelling.

Application of the 'bimat' approach for stent component simulation would be more complex due to the involvement of 3-D bending deformations including shear and torsion. A more complex method would be required to instruct elements to use either the tension or compression UMAT model depending on their strain state. Also, the ability of 'bimat' models to represent shear and torsion behaviour of the NiTi#1 wire has not been investigated.

In the short term, therefore, it will be necessary to continue to use an asymmetric 'unimat' model for 3-D stent ring simulations, with an understanding of its inaccuracies in representing superelastic bending behaviour (as seen in figure 6-5). Longer term, the 'bimat' tensile and compressive parameters established in this chapter to represent NiTi#1 wire can hopefully be applied to stent simulations. This will depend on development of a suitable 'bimat' approach for 3D bending simulations, or introduction of a more advanced Nitinol constitutive model in FE codes that can better represent the tensile-compressive asymmetry of Nitinol.

In any case, the experimental data from chapters 3, 4 and 5 of this report have been shown to be useful for calibrating and validating material models of the NiTi#1 wire used in FE simulations, and for investigating the capabilities and limitations of the underlying constitutive model in representing the Nitinol material behaviour.

6.7 Conclusions

Uniaxial tensile and compressive results from chapter 3 were used to calibrate representative material models for FE simulations using the Abaqus UMAT constitutive model for Nitinol. In order to overcome limitations of a single asymmetric UMAT 'unimat' model, a 'bimat' approach was implemented. Here, separate models were created for tension and compression and then applied to different regions of a wire model for bending simulations. 'Bimat' models were successfully created to represent superelastic Nitinol mechanical behaviour both at room temperature and body temperature. Calibration of these models was performed against uniaxial plots from chapter 3.

3-Point Bend Load-Deflection results from chapter 4 were useful for validation of the 'bimat' models. Good comparison between experimental and simulated L-D results in loading was achieved for all models. For unloading, material models based on stress-strain curves from chapter 3 under-predicted the unloading forces for 3-Point Bending. Additional models, designed to compensate for limitations in modelling the unload stress-strain path by using raised unload stress plateaus, gave a close match to the experimental results.

Experimental strain results from chapter 5 were also used to validate the room temperature material models. These validations highlighted a limitation in the ability of the FE constitutive model to represent the highly localised bending (or 'hinging') seen in 3-Point Bend DIC testing of Nitinol wire. This will result in under-prediction of strains at intermediate deflections during loading and unloading. At high bend deflections, there

is better comparison for maximum 'bending' strains, although simulation accuracy was limited by under-representation of strain asymmetry by the 'bimat' models.

Having performed validation of the material models for bending simulations, the models were then used for further investigations.

Simulations to investigate load-history effects showed dependency of the Strain-Deflection unload path on the maximum strain during loading, with path shapes similar to those proposed in chapter 5 to explain the phenomenon reported by van Zyl et al (ref 33). The Load-Deflection results from these simulations were also interesting, showing dependency of the unloading force value on the loading history.

The material models were also used for simulation of cyclic 'ΔD' bending deflections during unloading, in order to better understand the in-vivo bending behaviour of stent components under pulsatile loading. This investigation demonstrated an important behaviour in terms of fatigue resistance, showing that the Δε is limited during small ΔD cycles as distributed, elastic bending will always precede localized bending during re-loading cycles.

The work in this chapter has validated the calibrated 'bimat' material models for use in 2-D planar bending simulations and provided understanding of limitations of the underlying constitutive model in representing NiTi#1 wire. For application to more complex 3-D bending simulations required for stent components, further development of the 'bimat' modelling approach will be required, or an alternative constitutive model with greater fidelity for describing compressive nitinol behaviour will need to be identified and implemented. In the short term, an asymmetric 'unimat' material model must be used in Abaqus, with an understanding of the inherent limitations when interpreting simulation results.

This chapter has highlighted the following features which should be kept in mind when using the in-built Abaqus superelastic model for simulating Nitinol stent behaviour:

- the model does not capture strain localisation behaviour. For simulations of stent in-vivo bend cycling, this means that for the regions of interest for fatigue analysis (ie. the maximum tensile strain regions) the mean strains will be higher in reality than those predicted by the FEA. For example, in figure 6-17 there was a difference of 1.6% strain between simulation and experimental results at certain bend deflections during unloading. Fortunately, though, mean strain is not the critical parameter for predicting fatigue safety of Nitinol, as the cyclic tensile stress range is approximately the same over a wide range of mean strains during unloading (due to the unload stress plateau).

- The model does capture the cyclic Δdeflection strain response of superelastic Nitinol during unloading, with elastic deformation for small ΔD values and strain hysteresis for larger ΔD values. Maximum tensile Δε (which relates to Δσ) is the critical parameter for predicting fatigue safety of Nitinol stents, and therefore the FEA model can be used for fatigue analysis of stents.

- The particular austenite and martensite modulus values used in this chapter meant that the material bending stiffness for Δdeflection (representing in-vivo pulsatile cyclic stiffness) was approximately 30% lower than those seen experimentally, which would give a conservative representation for fatigue analysis as the stent will be have less stiffness to resist cyclic deformation.

- The difficulty in accurately representing this bending stiffness derives from the inability to accurately describe the post-transformation load and unload behaviour using only a single value for martensite modulus in the model. The compromises caused by this for modelling the material also lead to under-representation of the tensile-compressive asymmetry at high bending deformations, and therefore lower maximum tensile strains than in reality. This needs to be taken into account when using the model for stent compaction

analysis. The method described in section 5.6.4 of Chapter 5 offers a useful alternative for compaction strain analysis.

- The model is very effective for simulating the forces required for superelastic bend deformation during loading, as seen by the L-D results of this chapter compared against test results. This may be useful for compaction analysis of stents into delivery catheters, although this is not a major application of FEA for stent design, as compaction forces can easily be measured experimentally.

- For unloading, there is a tendency for the simulation to under-represent the force applied by the material in bending at intermediate deflections, which is the bend deflection range that is most relevant for in-vivo stent behaviour. This means that radial force results from stent simulations using the Abaqus material model will be lower than reality for a given stent deformation in-vivo (ie. when oversized in a vessel). For fatigue analysis this is a conservative approach, as there will be less damping of the vessel from the stent, and therefore larger cyclic deformations of the stent by the vessel. In the preceding chapter, the material model unload plateaus stresses were modified (bimat RTb and 37b) to enable a more accurate representation of the bending forces during unloading.

As discussed, the limitations highlighted here do not preclude the Abaqus Superelastic constitutive model from being used effectively for fatigue analysis of stents, which is currently the main application of FEA for stent design. However, it would be a useful area of future work to investigate alternative constitutive model options that can more accurately capture the following behaviours in order to improve simulation fidelity:

- Compressive stress-strain response
- Strain localization
- unloading stress-strain paths both in tension and compression
- Post-transformation load-unload stress-strain behavior, both for tension and compression
- Different unloading paths due to plasticity

Chapter 7: Conclusions and Recommendations

7.1 Conclusions

This research project had the principal objective of experimentally characterizing the behavior of superelastic Nitinol wire in compression and bending, under conditions relevant to its in-service application in stent graft products, to provide improved understanding of the material for future analysis and optimization of device designs. It was vital that this experimental testing should provide useful data for input to and validation of FEA-based material models, as FEA has become a vital tool for the design of safety-critical Nitinol stent components.

In order to focus on the relevant in-service loading modes and conditions, the product life cycle for the Nitinol components was considered. This highlighted the following key areas for experimental characterization of superelastic Nitinol wire:

- bending to large deformations, with high maximum tensile and compressive strains, followed by unloading, as seen in device compaction and deployment
- large cyclic deformations (up to three cycles), representing multiple compactions during manufacture
- temperature dependence (Room Temperature, 37 C and 55 C), relevant to the different conditions seen during manufacture, sterilization and implantation
- small cyclic deformations during unloading, as seen in-vivo following implantation due to pulsatile cycling of the stent graft in the aorta
- load history effects on unloading behavior for bending wire, to account for the different maximum bend deformations that may be seen prior to final deployment depending on compaction and repositioning history
- load history effects on unloading behavior for wire in uniaxial tension or compression, to account for the different material load-unload paths throughout a wire in bending.

With these points in mind, a Literature Review was conducted. First of all this highlighted the importance of sample processing history, test temperature and strain rate for experimental work with Nitinol. As a result, test samples were specially sourced to have equivalent microstructure and mechanical property specification (given by the processing history) to the wire used in Vascutek's stent components. The Literature Review also provided a good understanding of the general qualitative behaviours of superelastic Nitinol in tension, compression and bending, including localization effects and cycling behavior in tension, and features of tension-compression asymmetry in stress-strain plots. Consideration of available FEA-based constitutive models for Nitinol was also addressed through the literature review, with focus on the superelastic model implemented in Abaqus and widely used for design and analysis of stent components in industry.

The review highlighted some notable gaps in knowledge. The only information found on testing of Nitinol wire (as opposed to other material forms with unrepresentative processing history) in compression was from the investigation by Henderson et al (23) at University of Strathclyde, and this did not focus on the relevant in-service conditions for stent graft products. Similarly, a lack of relevant experimental information for Nitinol wire in bending was found in the literature. No previous experimental work to measure strains of thin Nitinol wire in bending could be found, providing an exciting opportunity for novel investigation in the present work. Related to this, no experimental investigations of load history effects on unloading strains in bending were found, despite this interesting phenomena being reported by van Zyl et al (33) through FEA simulation work. Finally, no studies could be found on the accuracy of FEA-based Nitinol constitutive models (and in particular the widely-used Auricchio-Taylor model in Abaqus) for representing the strain state of superelastic Nitinol wire in bending.

In order to meet the objectives of relevant material characterization testing and provision of data for material modelling, it was therefore necessary to plan and execute a program

of compressive and bend testing. Using the specially sourced 'equivalent wire' samples, compressive tests were performed on 1 mm wire using the equipment developed by Henderson et al (23). By focusing on the in-service behavior of the material, this testing provided useful quantitative data, as well as improved understanding of the load history dependence of the unload path (showing that increasing plasticity results in lower unload stress plateaus) and the small cyclic deformation effects during unloading (showing stable elastic deformation from the first cycle for deformations representative of in-vivo pulsatile cycling). Comparison with tensile test data (from the material supplier and from previous in-house testing at Vascutek) also provided useful results in terms of quantifying the tensile-compressive asymmetry of the material. Finally, initial feasibility work was performed to develop an improved compression test method for Nitinol wire, to overcome limitations of the previous method.

For bend testing, two different experimental methods were developed, including design and build of bending rigs. The first method, using a Bose 3200 machine with low capacity load cells, was used to investigate 3-Point Bend Load-Deflection behavior of thin wires in large deformation bending. The second method used 3D microscopic DIC to measure the surface strain field of thin wires in bending and to investigate the Strain-Deflection behavior during loading and unloading. This DIC testing, which builds on the work of Reedlunn et al (34), is considered to be a key area of novelty in this research project.

The Load-Deflection bend testing, as well as providing quantitative data useful for material model validation, showed interesting behaviours relevant to in-service stent function. By unloading from different bend deflections, it was seen that the unloading force at a given bend deflection is load-path dependent. For stent graft products, this means that a higher in-vivo radial force from a stent ring may be achievable simply by partially collapsing and re-deploying the device following unsheathing. Small bend deformation cycling during unloading also gave useful evidence that in-vivo pulsatile

cycling of the material occurs elastically and has a stable Load-Deflection path from the first cycle.

The novel DIC test method utilized both a 3-Point Bend rig and a 'Free Bend' rig together with various mounting platforms in order to obtain a large amount of strain data for thin Nitinol wire in bending. By considering the cross-sectional strain distribution at a given bend deflection or radius, this provided values to describe the tensile-compressive asymmetry of the Nitinol stent wire in bending (including neutral axis eccentricity), as well as useful data for FEA model validation. The 3-PB Strain-Deflection results yielded the most interesting information, clearly showing the stiff-compliant-stiff behavior of Nitinol in bending and also showing load-unload hysteresis. This means that the bending wire undergoes localized bending deformations, and that it takes a different global shape during loading from that in unloading for a given intermediate deflection. Using elastic and plastic beam bending theory together with uniaxial tensile and compressive stress-strain results, these experimental Strain-Deflection results were analyzed to explain the load history effects on unloading strains in bending, as highlighted by Van Zyl et al (33) from FEA simulations. This strain dependence on the loading history was explained in terms of the internal stress-state of the material during bending, and was shown to result from the load-unload stress hysteresis of superelastic Nitinol material.

Having performed the experimental investigations, the final step of this research project was to use the experimental data for input to and validation of FE-based material models, in order to assess their suitability for application in stent design and analysis.. This work built on collaborative efforts between Vascutek and University of Strathclyde to develop FEA models of Nitinol stent graft components, using Abaqus software. This FEA software implements the Aurrichio-Taylor constitutive model for Nitinol (42) for its built-in superelastic UMAT model, which is calibrated by inputting a number of material-specific parameters from uniaxial stress-strain data. It is well known that this

UMAT model is limited in its ability to represent the compressive properties of superelastic Nitinol material, with its asymmetric tensile-compressive stress-strain behaviour. This was demonstrated by uniaxial and bending simulations with a 'unimat' model. For this reason, a 'bimat' material modelling approach was used which is well suited to planar bending simulations.

Using the compressive and tensile stress-strain data from Chapter 3, input parameters were derived for bimat material models at Room Temperature and at 37ºC (Body Temperature). The resulting material models were first applied to uniaxial tensile and compressive simulations for comparison against the experimental uniaxial results, showing good general agreement, despite limitations in representing the post-transformation stress-strain behavior. Although only elastic UMAT parameters were used here, it was noted that an important limitation of the built-in constitutive model is the inability to represent decreasing unload stress plateaus due to plasticity. This is an inherent limitation of the model for simulating stent radial force following compaction to maximum strains beyond the superelastic limit.

The bimat models were then applied to bending simulations for comparison against the experimental results of Chapters 4 and 5. In terms of 3PB Load-Deflection results, the simulations gave an excellent match to the experimental results for the loading part of the cycle. However, for unloading it was found that the UMAT model under-represents the bending forces, which was attributed to the model's simplification of the material's unloading stress-strain path both in tension and compression. The 3PB simulations showed that the load-history dependence on unloading force is captured by the FEA model (see figure 6-15) and that the small deflection cycling behaviour during unloading is also captured (see figure 6-26), although with slightly reduced cyclic stiffness.

The 3PB Strain Deflection results from the simulations were compared against the experimental data from Chapter 5 (see figure 6-17) and it was seen that the general

'hinging' and load-unload hysteresis behaviours were represented. For this reason, further 3PB simulations with the material models could be used for further analysis of load-history effects on unloading in Section 6.5, giving supporting evidence for the discussion in Chapter 5. Although the simulations represented the general load-unload bending behaviours for Strain-Deflection, the simulated bend behaviour was less localized than that seen in the experimental results. From numerous simulations with different material parameters, this was found to be an inherent limitation of the constitutive model, and was attributed to the model's inability to simulate localized phase change.

From 3PB and 'Free Bend' simulations using the bimat models, the cross-sectional strain distribution at the bend apex was also plotted for comparison against the experimental DIC results (see figures 6-20 and 6-23). These comparisons showed that the FEA simulations underestimate the neutral axis eccentricity (and so the tensile-compressive asymmetry) for these large bend deformations. This should be considered when interpreting results from FEA simulations of Nitinol component compaction, as it could lead to underestimation of the maximum tensile strain. The design tool presented in Section 5.6.4 of Chapter 5, derived from experimental strain measurements on representative Nitinol wire, is proposed as a useful alternative method to estimate maximum tensile and compressive compaction strains when bend curvature is known (for example, from micro-CT measurements of compacted components).

While the Bimat material models were useful for the planar bending investigations relevant to this research project, it was noted that considerable development would be required to apply this approach to the more complex 3-D case of Nitinol ring stent simulation.

Chapter 6 was concluded with a consideration of the applicability of the Abaqus superelastic model for use in design and analysis of Nitinol stent components. It was

noted that the main use of FEA in this context is for fatigue analysis, and that the model can be used for this purpose, where it will tend to give conservative results for in-vivo cyclic deformations. The key areas where improvements would be required for useful higher fidelity simulations were identified:

- improved representation of compressive stress-strain response
- inclusion of Strain localization
- more detailed representation of unloading stress-strain paths both in tension and compression
- more detailed representation of the post-transformation load-unload stress-strain behavior, both for tension and compression
- Different unloading paths due to plasticity

It can be concluded that the main objective of this research project has been met, as the compressive and bending behaviors of superelastic Nitinol wire material have been characterized under conditions relevant to its in-service application for stent components. This has included development of novel experimental methods for strain measurement, and has provided improved understanding of the material including load-history effects on unloading behavior in bending. The experimental testing has also provided useful data for input to and validation of the Abaqus FEA-based material model, allowing an assessment of the capabilities of this model for application to stent design and analysis.

7.2 Recommendations for Future Work

7.2.1 Compression Testing: Recommendations

It is recommended that future compression testing on Nitinol wire should focus on the alternative approach investigated at the end of Chapter 3, to eliminate the need for specimen support holders by using test specimens with a suitable diameter to length ratio. As shown in chapter 3, a 1mm diameter NiTi wire with length of 3mm can be compressed to superelastic strain levels without either buckling or barrelling effects.

Next steps would be to identify and implement a suitable specimen strain measurement method, with Digital Image Correlation of in-situ loading SEM images being an obvious candidate. Alternatively, a different uniaxial test machine could be used, with commercially available compression plates and displacement / strain measuring equipment. A review of suitable test equipment to meet the required specification for superelastic compression testing of ø1 mm x 3 mm NiTi wire samples yielded the following results (table 7-1).

Feature	Required Specification	Instron 5848 Micro Tester (ref 73)	Zwick 'Precision Line Automatic' (ref 74)
Stiff support frame	Electromechanical system (not hydraulic)	Electromechanical (8.32 kN/mm)	Electromechanical
Test type	(quasi) static	(quasi) static	(quasi) static
Max force	> 1.5 kN	2 kN	2.5 kN
Position control	< 3 μ (0.1 % strain)	±0.5 μ	±0.5 μ
Displacement measurement resolution	< 0.3 μ (0.01 % strain)	0.02 μ	0.12 μ
Minimum speed (for $10^{-4} s^{-1}$ strain rate)	0.018 mm/min	0.000024 mm/min	unknown
Operating temperature range	10 – 37 C (10 – 60 C preferred)	10 – 38 C	10 – 35 C

Table 7-1: Required specification of equipment for proposed 'small diameter, short sample' compression testing, and specification of suitable commercially available equipment

7.2.2 3-Point Bend Load-Deflection Testing: Recommendations

It is recommended that a useful first step in advancing the 3-Point Bend testing would be to try and minimize friction between the wire and support pins, which was still evident in the results despite the use of polished pins. One promising option would be to replace the support pins with rollers (mounted in roller bearings).

It would then be worthwhile performing further investigation of the wire's 3-Point Bending response, with testing focused on a smaller deflection range (up to 5mm for the 0.45mm wire; up to 1.5mm for the 0.14mm wire) in order to avoid the 'negative stiffness' effects from large deflections. These smaller ranges are still expected to subject the material to large compaction strains (~7% max tensile ε) in bending, based on FEA simulations.

With this improved set-up and method, useful future investigations would include:
- 3-Point bend testing at 55ºC, to investigate effects of sterilization temperature on the wire's bending behavior
- 3-Point bend load-unload testing to different maximum deflections, to further explore load path dependency effects. This would be relevant to the different bending unload paths that may be taken by a stent ring following unsheathing and following repositioning.

Additionally, it would be useful to investigate plasticity effects in bending, particularly in terms of the effects on unloading forces (which would be expected to reduce). This would be relevant to the unloading radial force of a ring stent from a highly compacted state. In order to achieve the higher strains in 3-Point bending while avoiding the 'negative stiffness' effects seen in Chapter 4, the span of the support pins could be reduced for these tests. FEA simulations with different support pin spans could be used to guide the design of the improved 3-Point Bend test set-up.

7.2.3 DIC Strain Characterization Testing: Recommendations

It would be useful to expand on the 'strain history' DIC investigation work by performing 3-Point Bend tests to different maximum deflections in the range 2 - 5 mm, thereby focusing on the range where localized bending occurs at the bend apex. This

would provide experimental validation of the theoretical 'expected' results shown in figure 5-52 of Chapter 5.

For future DIC testing, a number of improvements to the test set-up and rig design have been identified:

- Temperature monitoring near the wire sample surface, using a thermocouple
- Means of Force measurement for the 3-Point Bend loading rig, so that test deflections can be directly compared to applied loadImproved method of deflection measurement for the 3-Point Bend loading rig
- Sample locating features (e.g. recesses) on the 3-Point Bend pins to ensure that the wire sample is held horizontal across the pins and cannot move laterally during bending.

It is also recommended that the DIC method be used for further Nitinol wire characterization, such as measurement of the Poisson's ratio. In the testing performed, this was not possible as the 'DaVis' software could not correctly calculate the 'Eyy' strain (i.e. transverse engineering strain). However, this issue is due to be addressed in future versions of the software. Future versions are also anticipated to include updated strain calculations that will allow measurement of axial strains for out-of-plane bending regions, making analysis of the output results easier.

7.2.4 FEA Modelling: Recommendations

Having identified limitations of the constitutive model currently implemented in Abaqus (Auricchio-Taylor model) for stent component simulation, it is recommended that alternative models be investigated for their ability to offer improved simulation fidelity in the areas highlighted. In particular, the Auricchio-Souza model should be considered, as recent iterations offer improvements for Nitinol plasticity modelling, as seen from the literature review.

7.3 Final Words

This research project has successfully met its stated objectives of characterizing superelastic wire material in compression and bending under relevant in-service conditions, and of providing experimental data for evaluation of material modelling. Beyond this, the project has been of great value in terms of establishing a useful approach to material characterization, identifying a number of relevant experimental technologies and combining these with computational material modelling to gain an in-depth understanding of the material's mechanical behaviour. Indeed, the work presented here has provided a clear approach for ongoing Nitinol research between Vascutek and University of Strathclyde to build upon, and has already found useful application for Vascutek's stent graft development. Exploitation of the work to date includes FE material model input to ring stent fatigue life testing (performed by the author) to obtain fatigue safety limit results for the stent material, and 3-point bend Load-Deflection testing of alternative composition Nitinol material wires to investigate material optimization for stent radial force. Moving forward, it is hoped that the work presented here and the ongoing research effort that it supports will continue to positively impact the design of stent graft devices.

References

(1) *Biscarini, A. Mazzoliai, G. Tuissi, A. Enhanced Nitinol Properties for Biomedical Applications. Recent Patents on Biomedical Engineering, 2008: **1**, pp.180-196*

(2) *Pelton, A. DiCello, J. Miyazaki, S. Optimisation of processing and properties of medical grade Nitinol wire. Minimally Invasive Therapy & Allied Technology, 2000: **9**(1), pp. 107-118*

(3) *Shaw, J.A. & Kyriakides, S. Thermomechanical Aspects of NiTi. Journal of the Mechanics and Physics of Solids, 1995: **43**(8), pp. 1243-1281* (Figure 10 reprinted with permission of the rights holder, Elsevier)

(4) *Nemat-Nasser, S. & Guo, W.G. Superelastic and cyclic response of NiTi SMA at various strain rates and temperatures. Mechanics of Materials, 2006: **38**, pp. 463-474*

(5) *Schaffer, J. & Plumley, D. Fatigue Performance of Nitinol Round Wire with Varying Cold Work Reductions. Journal of Materials Engineering and Performance, 2009:**18**, pp.563-568*

(6) *Mehta, A. Gong, X. Y. Imbeni, V. Pelton, A.R. Ritchie, R. Understanding the Deformation and Fracture of Nitinol Endovascular Stents Using In Situ Synchrotron X-Ray Microdiffraction. Advanced Materials, 2007: **19**, pp. 1183-1186*

(7) *Pelton, A.R. Nitinol Fatigue: A Review of Microstructures and Mechanisms. Journal of Materials Engineering and Performance, 2011: **20**, pp613 - 617*

(8) *Pelton, A.R. Schroeder, V. Mitchell, M. Gong, X. Y. Barney, M. Robertson, S.W. Fatigue and Durability of Nitinol Stents. Journal of the Mechanical Behaviour of Biomedical Materials, 2008: **1**, pp. 153-164*

(9) Schaffer, J. (2012), Fort Wayne Metals. *Personal communication during Fort Wayne Metals seminar at MedTec, Stuttgart, February 2012*

(10) *Fonte, M. & Saigal, A. Effects of crystallographic texture directionality on the compressive stress-strain response of shape recovered polycrystalline nitinol. Scripta Materialia, 2010: **63**, pp. 320-323*

(11) *Perry, K. Labossiere, P. Steffler, E. Measurement of Deformation and Strain in Nitinol. Experimental Mechanics: 2007: **47**, pp. 373-380*

(12) *Churchill, C.B. Shaw, J. Iadicola, M. Tips and Tricks for Characterizing Shape Memory Alloy Wire: Part 2 – Fundamental Isothermal Responses. Experimental Techniques, 2009: **33** (1), pp. 51 - 62*

(13) *R-Phase.* [Online] (2013) [accessed 19th September 2013]. Available from: en.wikipedia.org/wiki/R-Phase

(14) *Pelton, A.P. DiCello, J. Miyazaki, S. Optimisation of processing and properties of medical grade Nitinol wire. Proceedings of the International Conference on Shape Memory and Superelastic Technologies SMST-2000* [Online] [accessed 20th September 2013]. Available from: www.nitinol.com/media/reference-library/027.pdf (Figure 5 reprinted with permission of the rights holder, ASM International)

(15) *Siddons, D.J. & Moon, J.R. Tensile and compression performance of superelastic NiTi tubing. Materials Science and Technology, 2001: **17**, pp. 1073 - 1078*

(16) *Zurbitu, J. Kustov, S. Zabaleta, A. Cesari, E. Aurrekoetxea, J. (2010) Thermo-mechanical behavior of NiTi at impact. Shape Memory Alloys, Corneliu Cismasiu (Ed.), ISBN 978-953-307-106-0, InTech* [Online] [accessed 20th September 2013]. Available from www.intechopen.com/books/shape-memory-alloys/thermo-mechanical-behaviour-of-niti-at-impact

(17) ASTM F2516-07, Standard Test Method for Tension Testing of Nickel-Titanium Superelastic Materials, ASTM International, West Conshohocken, PA, 2007, www.astm.org

(18) *Reedlunn, B. Churchill, C.B. Nelson, E. Shaw, J. Daly, S. Tension, Compression and Bending of Superelastic Shape Memory Alloy Tubes. Journal of the Mechanics and Physics of Solids, 2014: **63** (1), pp. 506 – 537* (Figures 4, 8, 10 ,16 reprinted with permission of the rights holder, Elsevier)

(19) *Chen, W. Wu, Q.P. Kang, J. Winfree, N. Compressive superelastic behavior of a NiTi shape memory alloy at strain rates of 0.001-750 s^{-1}. International Journal of Solids and Structures, 2001: **38**, pp. 8989 - 8998*

(20) *'Compression Test'* [Online] [Accessed 24th September 2013]. Available from http://www.instron.co.uk/wa/applications/test_types/compression.aspx (includes information on compression testing taken from *ASM Handbook, vol. 8, Mechanical Testing and Evaluation. ASM International, Materials Park, OH 44023-0002, pp. 32, 143, 146 - 147*)

(21) *Liu, Y. Xie, J. Van Humbeeck, J. Delaey, L. Asymmetry of Stress-Strain Curves Under Tension and Compression for NiTi Shape Memory Alloys. Acta Mater, 1998: **46** (12) pp. 4325-4338*

(22) *Painting, A.L. A study of the end effects in specimen cores under compression tests, with a view to the elimination of these effects. Journal of the South African Institute of Mining and Metallurgy, 1974: Apr, pp. 333-339*

(23) *Henderson, E. Nash, D. Dempster, W. On the experimental testing of fine nitinol wires for medical devices Journal of the Mechanical Behaviour of Biomedical Materials, 2011: **4** , pp. 261 - 268* (Figure 6 reprinted with permission of the rights holder, Elsevier)

(24) *Crystal Twinning* [Online] (2013) [accessed 25th September 2013]. Available from: en.wikipedia.org/wiki/Crystal_twinning

(25) *Rebelo, N. Zipse, A. Schlun, M. Dreher, G. A Material Model for the Cyclic Behaviour of Nitinol. Proceedings of the International Conference on Shape Memory and Superelastic Technologies SMST-2010 (Springer) ISBN 978-1-4614-0197-1; pp. 605 – 612* (Figure 2 reprinted with permission of the rights holder, Springer Nature)

(26) *University of Cambridge DoITPoMS website. Bending Moments and Beam Curvatures* [Online] (2004) [Accessed 28th August 2013]. Available from: www.doitpoms.ac.uk/tlplib/beam_bending/bend_moments.php (Content reproduced under Creative Commons license. ©2004-2018 University of Cambridge. Except where otherwise noted, content is licensed under a Creative Commons Attribution-NonCommercial-ShareAlike 2.0 UK: England & Wales License. https://creativecommons.org/licenses/by-nc-sa/2.0/uk/legalcode)

(27)   Efunda website. Beam Theory: Euler Beam Equation [Online] [Accessed 28th August 2013] Available from: www.efunda.com/formulae/solid_mechanics/beams

(28)   *Pelton, A.R. Rebelo, N. Duerig, T. Wick, A. Experimental and FEM Analysis of the Bending Behaviour of Superelastic Tubing. The 1st International Conference on Shape Memory and Superelastic Technologies, 1994, pp. 353 - 358* [Online] [accessed 29th August 2013]. Available from: www.nitinol.com/media/reference-library/041.pdf

(29)   *De la Flor, S. Urbina, C. Ferrando, F. Asymmetrical Bending Model for NiTi Shape Memory Wires: Numerical Simulations and Experimental Analysis. Strain, 2011: 47 (3), pp. 255 - 267*

(30)   ISO 15841:2006 Dentistry - Wires for use in orthodontics. Purchased online at https://www.iso.org/standard/38023.html

(31)   *Duerig, T. Pelton, A.R. Nitinol: The Book, Part 1 Mechanisms and Behaviour, Chapter 5 Monotonic Mechanical Properties (unpublished)* [Online][accessed 12th September 2013]. Previously available from www.asminternational.org *SMST e-Elastic newsletter October 2010*

(32)   *Gupta, S. Pelton, A.R. Weaver, J.D. Gong, X.Y. Nagaraja, S. High Compressive Pre-strain Reduces the Fatigue Life of Electropolished Nitinol Wire . SMST-2013 Proceedings of the International Conference on Shape Memory and Superelastic Technologies (ASM International) pp 255 – 256*

(33)   *Van Zyl, M. Dempster, W. Nash, D. McCummiskey, E. Load Path Dependency of Nitinol (Report 1) Unpublished Research Paper, University of Strathclyde (23 Mar 2011)*

(34)   *Reedlunn, B. Daly, S. Hector Jr., L. Zavattieri, P. Shaw, J. Tips and Tricks for Characterizing Shape Memory Alloy Wire: Part 5 – Full-Field Strain Measurement by Digital Image Correlation. Experimental Techniques, 2011: Experimental Characterization of Active Materials Series, pp.1 - 17*

(35)   *Rebelo N, Gong XY, Hall A, Pelton A, Duerig T. Finite Element Analysis on the Cyclic Properties of Superelastic Nitinol. Proceedings of the 2004 ABAQUS Users' Conference, 2004* [Online] [Accessed on 1st October 2013] Available from www.simulia.com/download/solutions/life_sciences_cust_references/life_stents_fea_auc04_americawest.pdf

(36)   *Schlun, M. Zipse, A. Dreher, G. Rebelo, N. Effects of Cyclic Loading on the Uniaxial Behaviour of Nitinol. Journal of Materials Engineering and Performance, 2011: 20(4), pp. 684-687* (Figure 5 reprinted with permission of the rights holder, Springer Nature)

(37)   *Launey, M. Ong, I. Pelton, A.R. On the Life Fatigue of Superelastic Nitinol. SMST-2013 Proceedings of the International Conference on Shape Memory and Superelastic Technologies (ASM International) pp. 251 – 252*

(38)   *Paiva, A. Savi, M. An Overview of Constitutive Models for Shape Memory Alloys. Mathematical Problems in Engineering, Volume 2006, Article ID 56876, pp 1-30*

(39)   *Lubliner, J. A Simple Model of Generalized Plasticity. International Journal of Solid Structures,1991: 28, pp. 769-778*

(40)   *Lubliner, J. Auricchio, F. Generalized plasticity and shape memory alloys. International Journal of Solid Structures, 1996: **33** (7) pp. 991-1003*

(41)   *Auricchio, F. Taylor, R. Lubliner J. Shape Memory Alloys: Macromodelling and numerical simulations of the superelastic behavior. Computer Methods in Applied Mechanics and Engineering, 1997: **146**, pp. 281-312 (Received July 1995)*

(42)   *Auricchio, F. Taylor, R. Shape Memory Alloys: Modelling and Numerical Simulations of the finite-strain superelastic behavior. Computer Methods in Applied Mechanics and Engineering, 1997: **143** pp. 175-194 (Received Jan 1996)*

(43)   *Auricchio, F. Sacco, E. A One-Dimensional Model for Superelastic Shape-Memory Alloys with Different Elastic Properties Between Austenite and Martensite. International Journal of Non-Linear Mechanics, 1997: **32** (6) pp. 1101 – 1114 (Received Oct 1996)*

(44)   *Auricchio, F. Sacco, E. A Superelastic Shape-Memory-Alloy Beam Model. Journal of Intelligent Material Systems and Structures, 1997: **8** (6) pp. 489-501*

(45)   *Auricchio, F. A Robust Integration-Algorithm for a Finite-Strain Shape-Memory-Alloy Superelastic Model. International Journal of Plasticity, 2001: **17** pp. 971-990 (Received June 2000)*

(46)   *Rebelo, N. Walker, N. Foadian, H. Simulation of Implantable Stents. Abaqus Users Conference 2001, pp 421-434*

(47)   *Abaqus Plasticity Model for Superelastic Materials* webpage on National University of Singapore website. [Online] [Accessed on 21st February 2018] Available from http://bobcat.nus.edu.sg:2080/English/SIMACAEMATRefMap/simamat-c-plastsuperelastic.htm

(48)   *Conti, M. Auricchio, F. De Beule, M. Verhegghe, B. Numerical simulation of nitinol peripheral stents: from laser-cutting to deployment in a patient specific anatomy. European Symposium on Martensitic Transformations (ESOMAT) 2009, Article ID 06008* [Online] [Accessed on 21st February 2018] Available from http://www-2.unipv.it/compmech/publications/2009_9p.pdf

(49)   *Rebelo, N. Fu, R. Lawrenchuk, M. Study of a Nitinol Stent Deployed into Anatomically Accurate Artery Geometry and Subjected to Realistic Service Loading. Journal of Materials Engineering and Performance, 2009: **18**, pp. 655-663*

(50)   *Lagoudas, D. (Editor). Shape Memory Alloys: Modeling and Engineering Applications. 2008 (Springer US)*

(51)   *Nematzadeh, F. Sadrnezhaad, S. Effects of material properties on mechanical performance of Nitinol stent designed for femoral artery: Finite element analysis. Scientia Iranica, 2012: **19** (6), pp.1564-1571*

(52)   *Gong, XY. Pelton, A. Duerig, T. Rebelo, N. Perry, K. Finite Element Analysis and Experimental Evaluation of Superelastic Nitinol Stent. SMST-2003 Proceedings of the International Conference on Shape Memory and Superelastic Technologies (ASM International)*

(53)   *Gong, XY. Pelton, A. Finite Element Analysis on Nitinol Medical Applications. Proceedings of International Mechanical Engineering Congress and Exposition*

*2002: **53**, pp1-2* [Online] [Accessed on 22nd February 2018] Available from https://pdfs.semanticscholar.org/2749/c2a53f453db5eba83738028058b07540aa80.pdf

(54)   *Souza, A. Mamiya, E. Zouain, N. Three-dimensional model for solids undergoing stress-induced phase transformations. European Journal of Mechanics - A/Solids, 1998: **17**, pp. 789-806*

(55)   *Auricchio, F. Petrini, L. Improvements and algorithmal considerations on a recent three-dimensional model describing stress-induced solid phase transformations. International Journal of Numerical Methods in Engineering, 2002: **55**, pp.1255-1284*

(56)   *Auricchio, F. Petrini, L. A three-dimensional model describing stress-temperature induced solid phase transformations. Part 1: solution algorithm and boundary value problems. International Journal of Numerical Methods in Engineering, 2004: **61**, pp. 807-836*

(57)   *Auricchio, F. Reali, A. Stefanelli, U. A three-dimensional model describing stress-induced solid phase transformation with permanent inelasticity. International Journal of Plasticity, 2007: **23**, pp. 207-226*

(58)   *Auricchio, F. Reali, A. Stefanelli, U. A Macroscopic 1D model for shape memory alloys including asymmetric behaviours and transformation-dependent elastic properties. Computer Methods in Applied Mechanics and Engineering, 2009: **198**, pp. 1631-1637*

(59)   *Arghavani, J. Auricchio, F. Naghdabadi, R. Reali, A. On the robustness and efficiency of integration algorithms for a 3D finite strain phenomenological SMA constitutive model. International Journal of Numerical Methods in Engineering, 2011: **85**, pp. 107-134*

(60)   *Barrera, N. Biscari, P. Urbano, M. Macroscopic modelling of functional fatigue in shape memory alloys. European Journal of Mechanics - A/Solids, 2014: **45**, pp. 101-109*

(61)   *Urbano, M. Auricchio, F. Modelling permanent deformations of superelastic and shape memory materials. Journal of Functional Biomaterials, 2015: **6**, pp. 398-406*

(62)   *Petrini, L. 'Modelling functional fatigue and plasticity of shape memory alloys: applications in the biomedical field.' Slides from 2017 presentation at Politecnico di Milano.* [Online] [Accessed on 22nd February 2018] Available from https://www.eventi.polimi.it/events/lorenza-petrini-modeling-functional-fatigue-and-plasticity-of-shape-memory-alloys-applications-in-the-biomedical-field/

(63)   *Auricchio, F. Conti, M. Morganti, S. Reali, A. Shape Memory Alloy: From constitutive modelling to Finite Element Analysis of Stent Deployment. Computer Modelling in Engineering and Sciences, 2010: **57** (3), pp. 225-243*

(64)   Instron 5960 Series manual. [Online] [Accessed on 23rd February 2018] Available from http://www.instron.co.uk/-/media/literature-library/products/2013/02/5960-series-dual-column-tabletop-5kn--50kn.pdf?la=en-GB

(65)   Deben Microtest 2000 datasheet. [Online] [Accessed on 23rd February 2018] Available from http://2z2w0i1ewkrx1owjm040i7ai.wpengine.netdna-cdn.com/wp-content/uploads/2011/08/DEB3416_DatasheetA4_TensileStages-MicrotestOverview_v2-5.pdf

(66)   *Brodie, R. Ashton, T. Stevenson, D. Dempster, W. Nash, D. Strain Characterization of Superelastic Wire in Bending Using Digital Image Correlation. SMST-2013 Proceedings of the International Conference on Shape Memory and Superelastic Technologies (ASM International)*

(67)   *Bow, D. Micro CT Compaction Strain Analysis of Anaconda One-Lok. Unpublished Vascutek Internal R&D Report No. 1530 Rev 01 (3 Dec 2014)*

(68)   *'Analytical rigid surface definition'. Simulia Abaqus 6.14: Abaqus Analysis User's Guide, Section 2.3.4.* [Online] [Accessed on 3rd March 2018] Available from http://abaqus.software.polimi.it/v6.14/books/usb/default.htm?startat=pt09ch40s05alm67.html

(69)   *'Solid (continuum) elements'. Simulia Abaqus 6.14: Abaqus Analysis User's Guide, Section 28.1.1.* [Online] [Accessed on 3rd March 2018] Available from http://abaqus.software.polimi.it/v2016/books/usb/default.htm?startat=pt06ch28s01ael03.html

(70)   *Bow, D. Nitinol Ring and Langwouters' Artery FEA Methodology and Validation. Unpublished Vascutek Internal R&D Report No. 2032 Rev 01 (20 June 2017)*

(71)   *'Frictional behaviour'. Simulia Abaqus 6.14: Abaqus Analysis User's Guide, Section 37.1.5.* [Online] [Accessed on 3rd March 2018] Available from http://abaqus.software.polimi.it/v2016/books/usb/default.htm?startat=pt09ch37s01aus171.html#usb-cni-afriction

(72)   *Bow, D. Brodie, R. Dempster, W. Van Zyl, M. Nash, D. Computer implemented method of simulating performance of e.g. endovascular stent-graft, involves partitioning model such that material models simulate material behavior in units of object model of superelastic tension and compression. Patent Application WO 2014184591-A1 WOGB051533, 20 Nov 2014.*

(73)   Instron Model 5848 Micro Tester manual. [Online] [Accessed on 23rd February 2018] Available from https://itll.colorado.edu/modular_experiments_dir/itll_modules/Instron%20Universal%20Testing%20Machine/InstronSpecs%20(5869).pdf

(74)   Zwick Precision Line Automatic manual. [Online] [Accessed on 23rd February 2018] Available from http://www.zwick.co.uk/en/products/static-materials-testing-machines/testing-machines-up-to-5-kn/precisionline-testing-machines.html

Appendix 1: Vascutek Wire Specifications for Nitinol wire, 0.22 mm ø

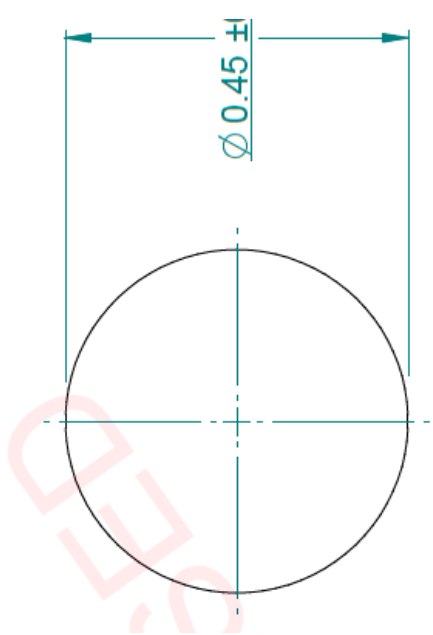(Typical specification for Vascutek Etched Nitinol Wire, diameter range 0.1 – 0.24mm, as used for stent rings)
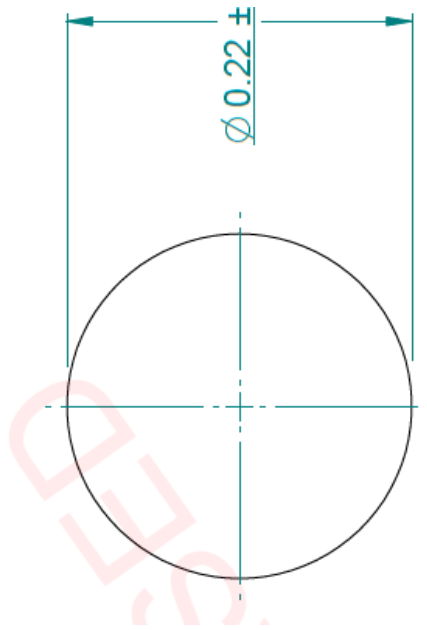
Specification drawing cropped to remove confidential information

Appendix 2: Vascutek Wire Specifications for Nitinol Wire, 0.45 mm ø

(As used for hook components, following additional Shape Set, Electro-Polish and Cutting processes)

$\varnothing\,0.45\,\pm$

Specification drawing cropped to remove confidential information

Appendix 3: Additional DIC Test Method Details

A3.1 Introduction

This appendix includes supplementary information to Chapter 5, section 5.3, in order to provide additional detail on certain steps in the DIC test method that was developed. This information will be useful if the present test method is used as a basis for further investigations of Nitinol wire bending strains.

## A3.2 Identification of 'in-focus' bending apex region: detailed steps

Further to section 5.3.7.6 of chapter 5, the steps below detail the approach used with the 'DaVis' software to identify the 'in-focus' bend region for 'tilt' and 'vertical' test results:

1. Extract Vz components of displacement vectors: figure A3-1 below shows a plot of the Vz results for a deformed wire on the 'tilt' platform.
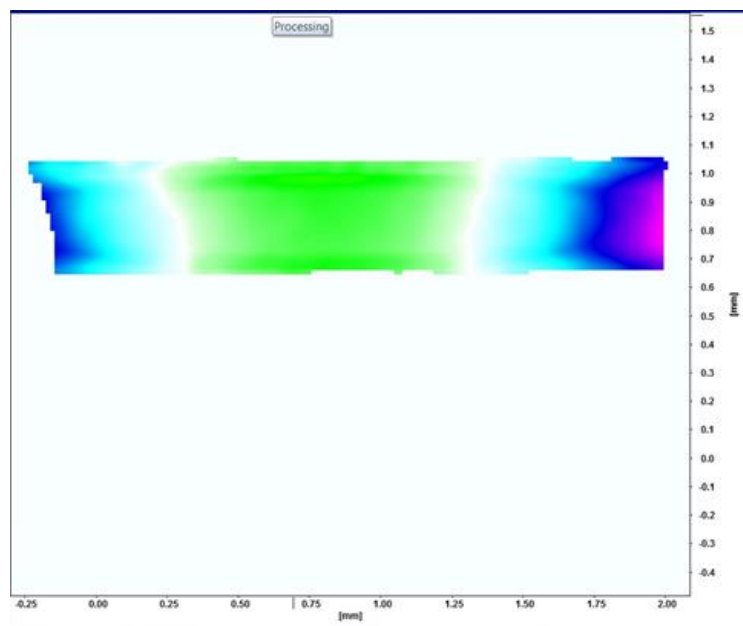


Figure A3-1: Displacement Field Plot of Vz displacement components(following rigid body motion removal) for wire with out-of-plane bending relative to x-y plane

2. Plot profile of Vz results: this shows the bend of the wire in the z direction – see figure A3-2 below.
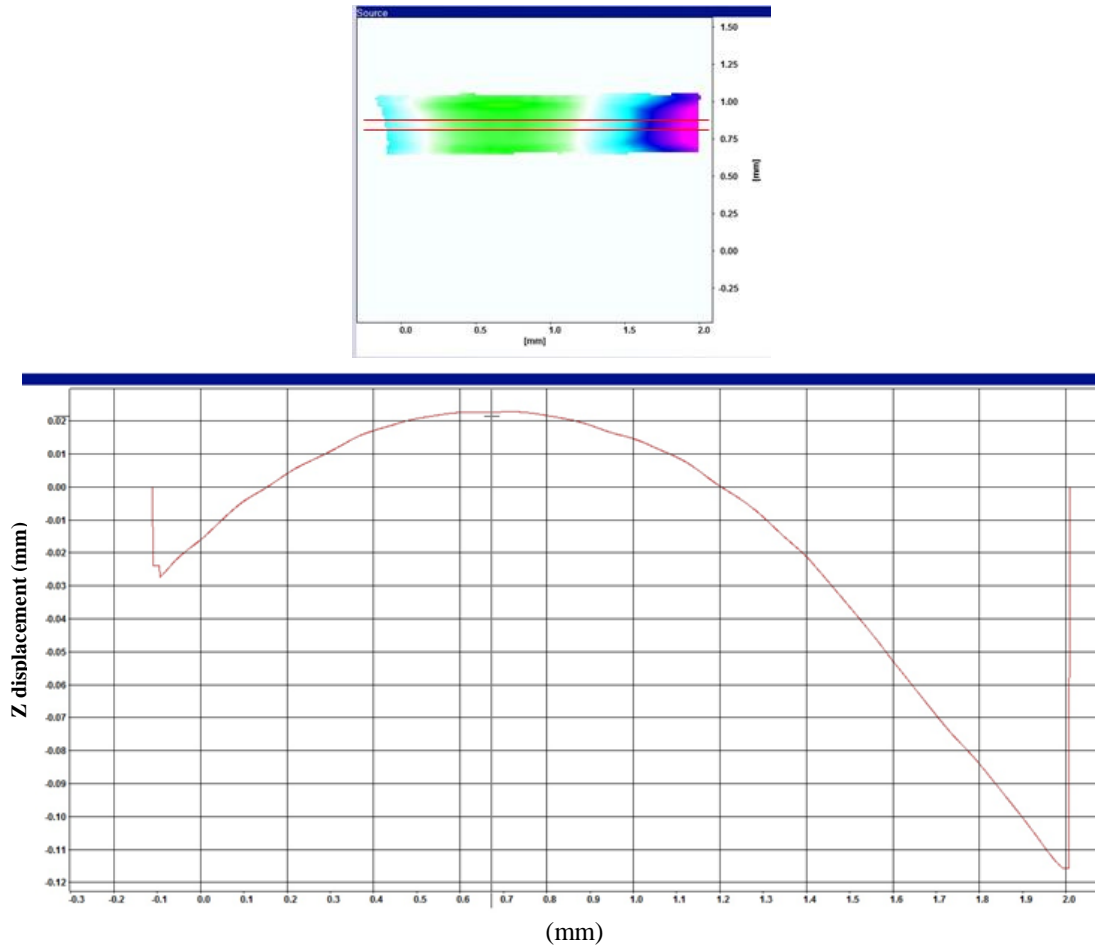
Figure A3-2: Profile plot (bottom) of Vz results, for region identified in the displacement field (top), showing out-of-plane bending displacements of the wire relative to x-y plane

3. Identify the 'in-focus' Vz bend apex region, which is axially parallel to the x-axis. In the example shown below (figure A3-3), this region is between 0.6 and 0.75 mm on the x-axis scale. This identified region will be used for extracting Exx strain and Height profiles for the deformed wire.
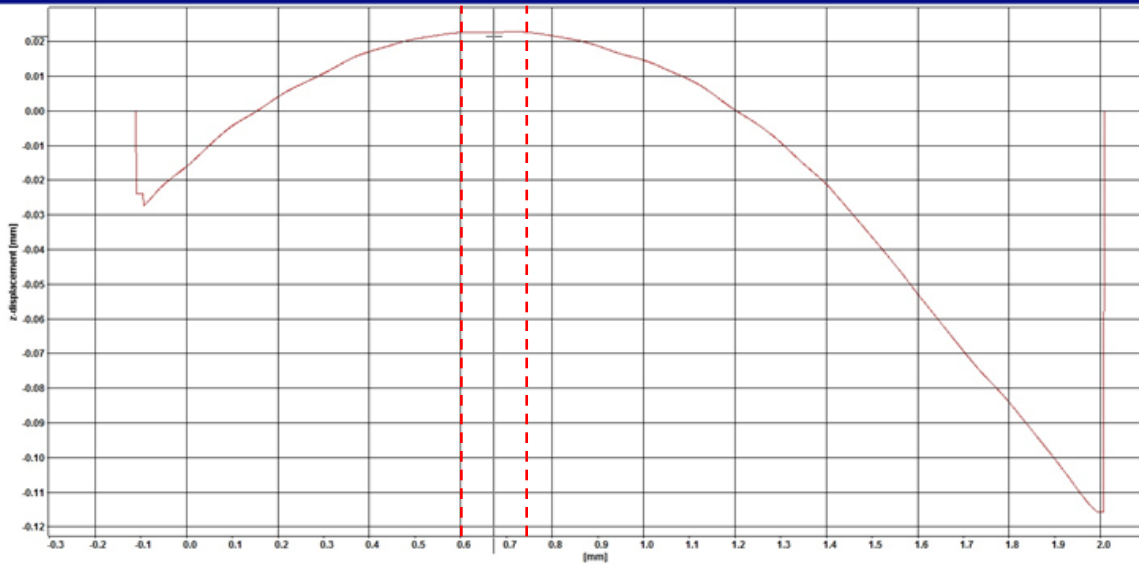
Figure A3-3: 'In-focus' region identified from Vz profile result, shown by red dashed lines

A3.3 Results Extraction and Plotting: detailed process

Further to section 5.3.7.7, the information below details the steps used to accurately plot the normal axial strain 'Exx' of the wire against the surface position for each bending deformation.

A3.3.1 Results Extraction: 'Exx strain' and 'Height' profiles

Once the correct 'in-focus' bend apex region has been identified, the Exx strain results and wire Height profile results are extracted for that region, in order to allow accurate location of the axial strains relative to the wire cross-section for the bend apex. The method below summarizes the process used for results extraction and export:

1. Extract Exx strain component for all deformation field results. Figure A3-4 shows the extracted Exx plot for a certain deformed wire position. (As described in section 5.3.7.6 of chapter 5, Exx is only useful for describing the normal axial strain in the identified 'in-focus' bend region.)
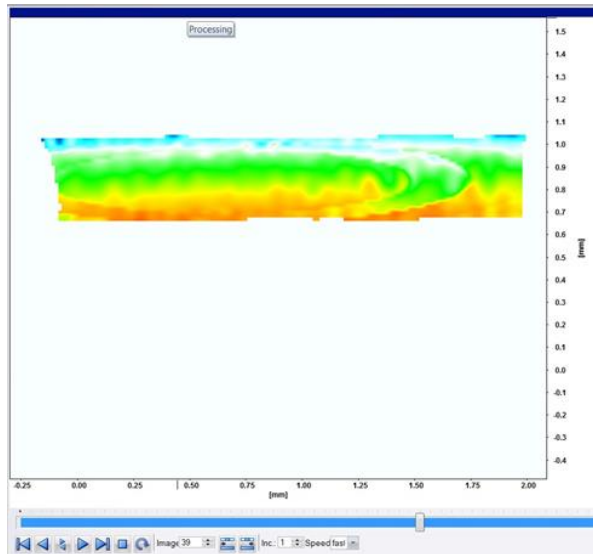
338

Figure A3-4: 'Exx' strain field plot for angle-mounted wire in bending. Only the 'in-focus' region results from this plot are accurate for describing normal axial strain

2. Plot profile of Exx results for the identified apex region (for tilt and vertical test results, this is the 'in-focus' region identified previously). The vertical lines in figure A3-5 below (top) are positioned to define the identified apex region and set the boundaries for the Exx strain extraction. Note that the results give the average Exx strain between the lines. The image in figure A3-5 (bottom) shows the plot of Exx strain profile across the wire width. Note that this plot does not extend to the very edges of the wire (i.e. plot width < wire diameter) as the 3-D DIC cannot measure displacements and strains at these regions of a round wire. For the 0.45 mm diameter round wire, it was found that the system was capable of measuring strains over a wire width of 0.3 mm, or ± 0.15 mm from the wire centreline. In other words, the measured strain field covered 66% of the wire's surface, and excluded the outer regions on either side of this measured area.
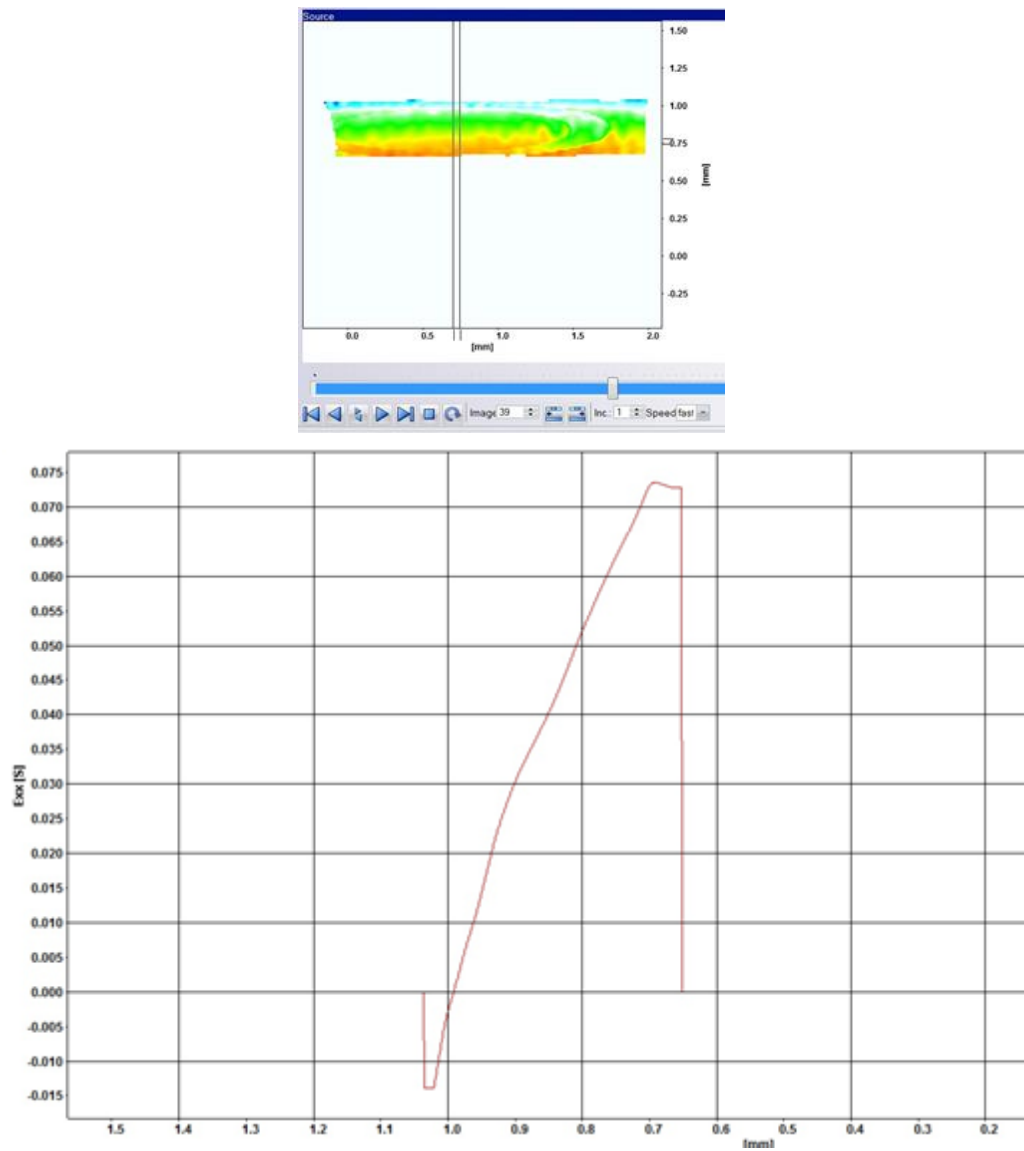
Figure A3-5: profile plot of 'Exx' strain (bottom) for identified in-focus apex region (top) of bending wire. For this plot from an 'angle-mounted' set-up, the 'Exx' strain values range from -1.2% (compressive) to 7.2% (tensile)

3. Extract 'Height' results for all deformation field results. The 'Height' plot shows the cross-sectional profile height of the wire along its length, as can be seen in figure A3-6. This height plot is calculated from a combination of the original

'undeformed' surface height profile and the Vz displacement vector components after Rigid Body Movement removal.
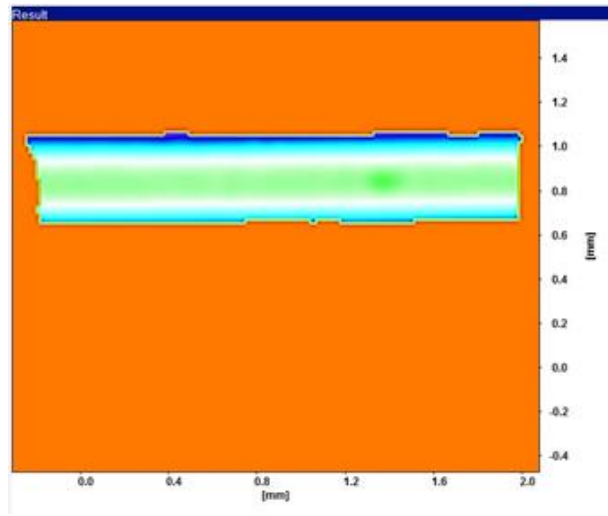
Figure A3-6: 'Height' plot for wire, giving cross-sectional profile heights along the wire.

4. Plot profile of Height results for the identified apex region (for tilt and vertical test results, this is the 'in-focus' region identified previously). The vertical lines in figure A3-7 (left) are positioned for the identified in-focus apex region and set the boundaries for the Height extraction. Note that the results give the average Height between the lines. The image in figure A3-7 (right) shows the plot of Height profile across the wire width. As with the Exx results plot above, this plot does not extend to the very edges of the wire (i.e. plot width < wire diameter) as the 3-D DIC cannot measure height profiles and displacements at the very edges of the round wire.
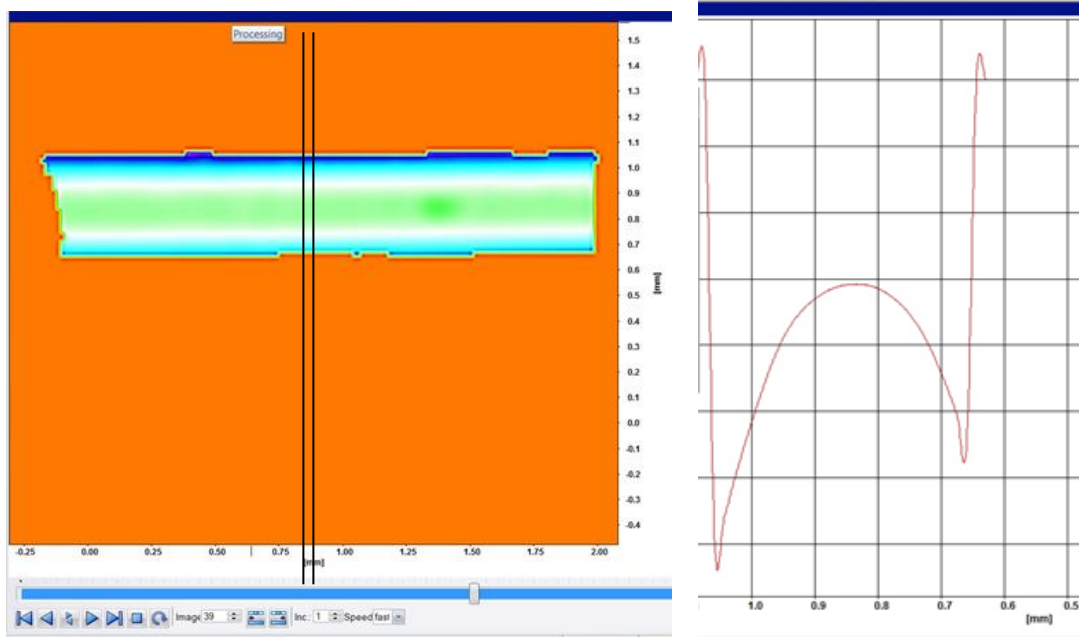
Figure A3-7: profile plot of ''Height' (right) for identified in-focus apex region (left) of bending wire.

5. Having extracted the apex Exx strain and Height profiles for every 3-Point Bend pin deflection position, the results are then exported as PRF files (ensuring that 'global options > dot' is selected, for easy compatibility with MS Excel). These data files can then be opened in Excel for manipulation and results plotting.

A3.3.2 Exx vs wire width: transform process for tilt / vertical test results

When the Exx strain results are initially plotted against cross-sectional position (using 'height' profile), the plot shape is determined by the angle of mounting platform that was used. Figure A3-8 below illustrates how different 'Exx vs wire width' plot shapes were obtained for flat, tilt and vertical mounted bend tests, due to differences in the wire bend direction relative to the camera viewing angle.
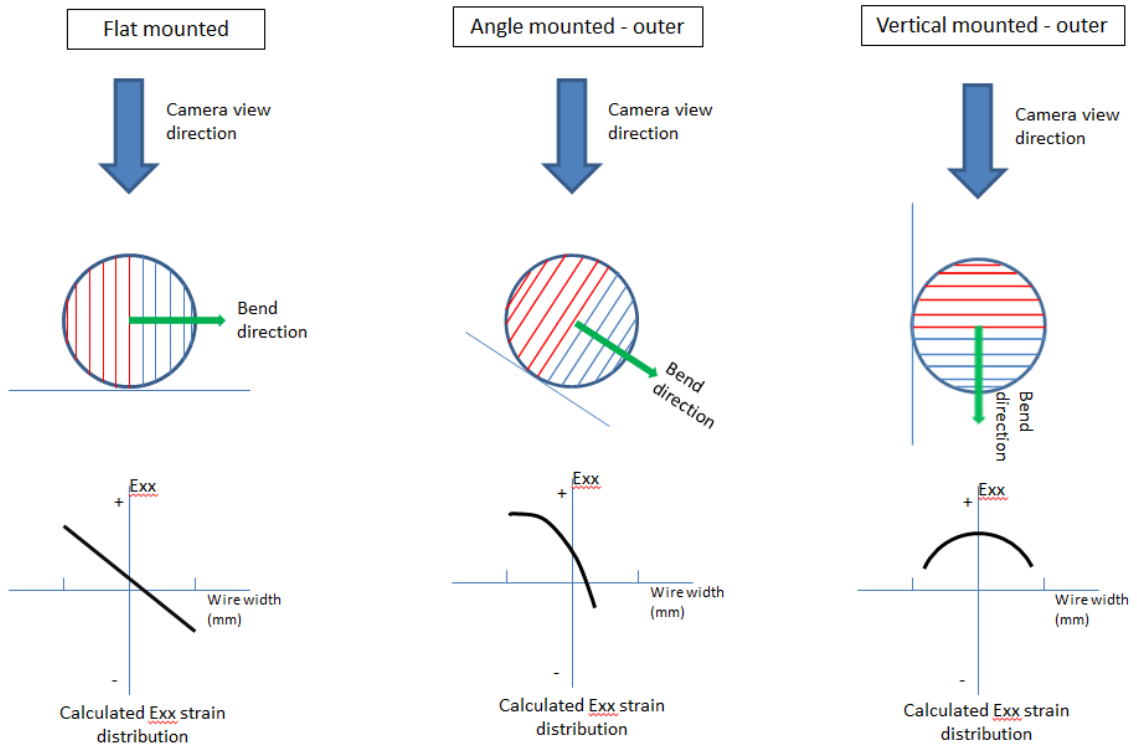
Figure A3-8: Effect of bend direction relative to camera view direction on the 'Exx vs wire width' plot shape obtained.

In order to obtain the correct strain distribution across the wire section due to bending, it was necessary to transform the wire width values from the tilt and vertical tests. This is illustrated in figure A3-9.
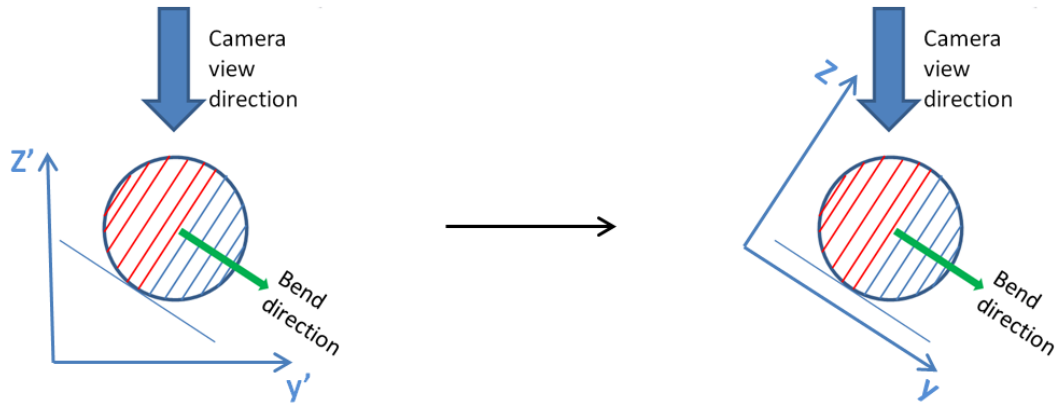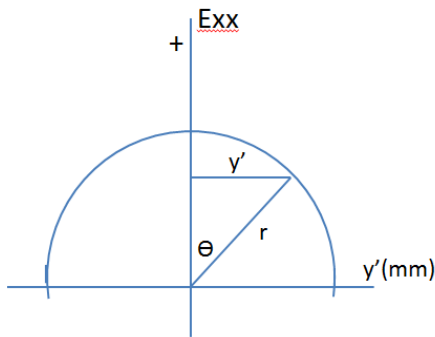
Figure A3-9: The 'Exx vs wire width' results from 'tilt' and 'vertical' tests must be transformed to obtain the correct strain distribution across the wire width 'y'

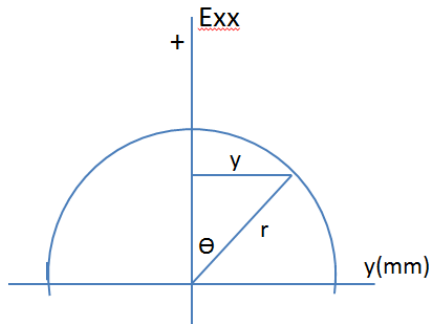The transform process involved the following steps:

1. Convert **Exx vs y'** results to **Exx vs θ** (including platform angle)

$$\Theta = \text{ASIN}(y'/r) + \textbf{platform angle}$$
$$r = 0.225mm$$

2. Convert **Exx vs θ** results to **Exx vs y**

$$y = r\sin\Theta$$
$$r = 0.225mm$$

A3.4 Wire deflection measurement from 'macro view' digital images: detailed steps

Further to section 5.3.7.7in Chapter 5, the information here details how measurements were made of the 3-Point Bend wire deflections from the 'macro view' images captured.

A3.4.1 Wire Deflection Measurement, flat mounted 3-Point Bend tests

The measurement method is described below, with example provided by figure A3-10.

Figure A3-10: zoomed-out 'macro' CCD images of wire in 3-Point Bending. Left image shows initial pin position; middle image shows known 'maximum deflection' pin position; right image shows interpolated intermediate pin position

For the 'zoomed-out' macro view images, the outer pins were just outside the field of view and the linear scale could not be seen. Therefore the following method had to be used to determine the maximum pin displacement and to determine the intermediate pin displacements using interpolation.

1. For the initial straight (undeformed) wire image (figure A3-10, left), the position of the top edge of the wire was noted (red arrow) using the grid value on the right side of the image (grid was displayed in mm for this purpose). This is the '0' pin position.

2. The maximum pin deflection for each test was known – in this case 10 mm. The 'maximum bend deformation' image was identified (figure A3-10, middle) and

the position of the top edge of the wire against the image grid noted (red arrow). This is the '10 mm' position.

3. For all other 'intermediate deformation' images (eg. Figure A3-10, right) the pin deflection was calculated by finding the top edge (blue arrow) grid position and then using the following equation:

$$d_{pin\ int} = (grid\ pos_{int} - grid\ pos_0) * max\ deflection\ /\ (grid\ pos_{max} - grid\ pos_0)$$

For the example shown in figure A3-10 , this gave an intermediate pin deflection ($d_{pin\ int}$) of 5.8 mm.

Using this method for flat-mounted 3-Point Bend tests, the maximum pin deflection is known from the test plan and is therefore an accurate value. However, the method for calculating intermediate pin deflections during loading and unloading involves some error for these flat mounted test sets (note: none of the other test sets used this method). As a conservative estimate, these calculated intermediate pin deflection values are considered to be accurate to within ± 0.3 mm, as it is known that the pins were moved in approximately 0.3 mm increments to deform the wire during testing, and the incremental image number of each 'macro' photograph is known in each case. This allowed a check of the calculated intermediate pin deflections by comparing against the expected pin deflection from the cumulative incremental deflections.

A3.4.2 Wire Deflection Measurement, angle and vertical mounted 3-Point Bend tests

For the angle and vertical mounted tests, the linear displacement scale (with 1 mm gradations) on the 3-Point Bend test rig could be clearly seen in the 'macro' images taken with the digital camera (see figure A3-11). The pin displacement was found from the position of the slider against the linear scale. This is shown by the red lines in figure A3-11.
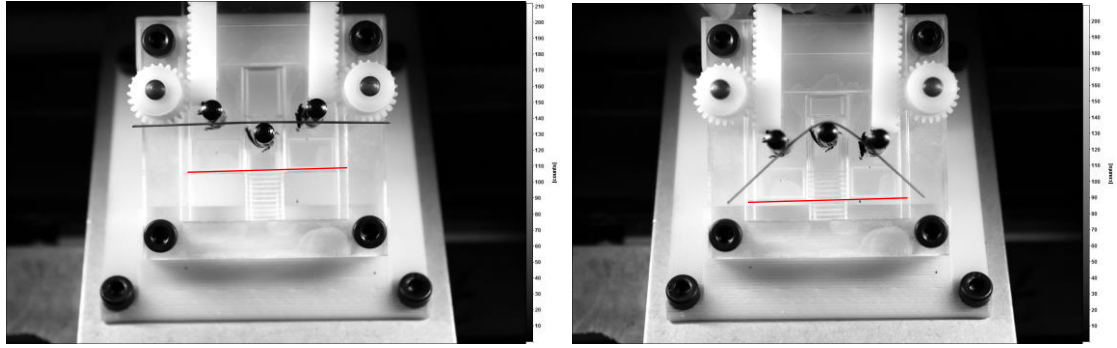
Figure A3-11: digital camera images of wire in 3-Point Bending, used to measure pin deflection. For the left hand image, deflection = 0 mm; for the right hand image, deflection = 6.3 mm (shown by red lines against linear scale)